Manipulation of molecular motion using a high-energy chirped laser system

Nicholas Peter Coppendale

Submitted for the degree of Doctor of Philosophy

Department of Physics and Astronomy University College London

October 2011

Declaration

I, Nicholas Peter Coppendale confirm that the work presented in this thesis is my own. Where information has been derived from other sources, I confirm that this has been indicated in the thesis.

Nicholas Peter Coppendale _____

Abstract

This thesis reports on the development of a laser system for the manipulation of molecules using the optical dipole force. The centre-of-mass motion of molecules within the deep optical lattices created by the laser system, was probed using coherent Rayleigh scattering (CRS) and compared with simulations of these processes.

The laser system was constructed to produce two, temporally coincident, pulsed beams with durations of hundreds of nanoseconds. The frequency difference between the two beams was controlled to be on the order of 1 GHz. This frequency control was produced by the construction of a low power (20 mW) Nd:YVO_4 microchip-type laser which was frequency chirped by rapidly changing cavity length via an intra-cavity electro-optic crystal. The deleterious effects of intensity modulation induced by this process, were overcome by the design of an injection locking system with a free running semiconductor diode laser. This master slave laser system was pulse amplified to the required intensity in a fibre amplifier and a Nd:YAG flash-lamp pumped amplifier system with a total gain of 10^9 maintaining the frequency characteristics of the low power laser system.

The motion of molecules trapped in the optical lattice produced by the laser system was probed using CRS. Long pulse CRS was performed on xenon and octane gases utilising 100-200 ns pulses with a flat-top profile.

Contents

Acknowledgements

I would like to thank my supervisor Professor Peter Barker for his supervision, guidance and support over the course of my PhD. I would also like to thank my colleagues, particularly Dr Peter Douglas and Conor Maher-McWilliams for providing me with their recent results which demonstrated the use of my laser system. I would like to thank them, as well as other members of the group past and present, including Lei Wang, Dr Simon Purcell and Alexandros Gerakis for providing assistance, insight and also conversation over the past few years.

I am extremely grateful to my friends and family for all of their financial and emotional support throughout my PhD which has been invaluable, particularly during the more difficult and frustrating periods.

Publications

1. N. Coppendale, L. Wang, P. Douglas, P. F. Barker, *"A high-energy, chirped laser system for optical Stark deceleration"*, Applied Physics B, **104**, 569-576, (2011).

2. P. F. Barker, S. M. Purcell, P. Douglas, P. Barletta, N. Coppendale, C. Maher-McWilliams and J. Tennyson, *"Sympathetic cooling by collisions with ultracold rare gas atoms, and recent progress in optical Stark deceleration"*, Faraday Discussion, **77**, 063409, (2008).

Chapter 1

Introduction

1.1 Motivation

1.1.1 Introduction

The creation of trapped cold and ultra cold molecules is of great interest as they offer the potential to observe properties and interactions normally masked at higher temperatures. There is no strict definition for the cold regime, however it is typically 1 K > T > 1 mK and the ultra cold is T $\leq$ 1 mK [1, 2, 3].

Cold and ultra cold molecules have many possible applications including high resolution spectroscopy which may allow for measurements of parity violation and time variation of the fundamental constants. They also allow experiments which may put limits on the magnitude of the electron electric dipole moment. Cold trapped molecules offer the possibility of studying many interactions and at temperatures where the de Broglie wavelength becomes comparable to the molecular size and therefore where quantum effects may dominate intermolecular interactions. High resolution collision experiments made possible by the ability to control collision energies at low temperatures are also starting to provide information on the molecular structure, including collisional cross sections at well defined energies.

1.1.2 High Resolution Spectroscopy

Often, spectroscopic resolution is limited by the interaction time between the particles being studied and the laser field used to probe them. The use of slowed molecules to resolve hyperfine transitions has been demonstrated [4]. Measurement of the fluorescent decay of Stark decelerated and electrostatically trapped CO molecules has been used to measure the difference in the lifetimes between rotational states [5] and in a similar way precision measurements have been made of the vibrationally

excited OH radicals [6]. Photoassociative spectroscopy [7] of cold molecules, enables observation of small vibrational and rotational spacings of long range molecular intervals [8, 9]. In all these cases it is primarily the longer interaction time made possible with cold trapped molecules that enables the higher resolution measurements.

Electron electric dipole moment and parity violation

There is great potential to use cold molecules for precision spectroscopic measurements that put limits on the magnitude of the electron electric dipole moment. A large non-zero dipole moment of the electron implies through CPT theory both violation of time reversal symmetry and parity [10, 11].

To measure the electron dipole moment (e.d.m.), unpaired electrons are required, since otherwise the e.d.m.'s will cancel and cannot be observed. The ability to measure the e.d.m. is limited by the size of the applied electric field (ϵ), and more importantly, the effective electric field (ϵ_{eff}) from the molecule, as experienced by the unpaired electron. The ratio of these fields, $\epsilon/\epsilon_{\text{eff}}$ is known as the enhancement factor. This enhancement factor is proportional to the degree of polarisation by the external field which for cold heavy polar molecules can be up to 10^3 times greater than for atoms where the magnitude is limited by the external field. Thus the energy shift in the levels due to the e.d.m. and the applied field can be up to 10^3 times greater in molecules.

High resolution spectroscopy of cold chiral molecules [12] may allow for detection of parity violation by the measurement of the small energy conversion (10^{-11} J mol^{-1}) between the R and S enantiomers of the ground state [13]. This measurement could be improved by the use of cold, trapped molecules.

Internal state interferometry (Stückelberg Interferometry) with ultra cold Cs_2 molecules has been demonstrated by Mark et al. [14] with a possible application to detecting parity violation. This has allowed the precise determination of the difference in energy between two states of the molecule. This technique can measure energy scales below $h \times 1$ Hz, where h is Planck's constant, which is in the region of the feeble interactions between molecular states, such as non-conserving parity interactions.

Time variation of fundamental constants

The consensus is that the physical constants do not change with time. However it has been theorised that this may not be the case [15] within the context of the Kaluza-Klein models [16]. These suggest that there may be more than the usual

four dimensions that we observe (space and time) which allow for the variation of the physical constants in our own four-dimensional world.

The use of high resolution spectroscopy to measure the difference between closely spaced levels between, for example vibronic and a fine structure level, offers the possibility of measuring the fine structure constant α and the ratio $m_{\mathrm{p}}/m_{\mathrm{e}}$ to high precision [17]. It has also been proposed to use laser spectroscopy on ultra cold molecules to test the time dependence of the electron and nuclear mass by comparing the frequencies of different transitions in the ground electronic state [18].

High precision measurement of the Λ-doublet microwave transitions in Stark decelerated OH molecules could, if compared to measurements of OH megamasers in interstellar space, give a sensitivity of 1 part per million for changes in the fine structure constant over a time of 10^{10} years [19].

1.1.3 Many body interactions

At cold temperatures dipole-dipole interactions which are both spatially anisotropic and long range can become significant. There have been many studies of magnetic dipole-dipole interactions between atoms [20, 21] however these interactions are considerably weaker than in electric-dipoles in cold molecules, which can be tuned by an applied electric field.

The creation of a quantum degenerate molecular gas requires the production of ultra cold molecules at sufficient phase space densities, since dipole-dipole interactions scale as $1/r^3$. Whilst samples of molecular gases have been produced which approach quantum degeneracy [22, 23], dipole-dipole interactions between molecules have not yet been observed.

A dipolar molecular gas would provide a quantum mechanical model of solid state materials, including investigations of spin waves, quantum phase transitions and large interaction strengths.

Cold atoms have led to the observation of the first Bose Einstein condensate [24], the first Fermi gas [25] and the first observation of a phase transition from an incompressible superfluid to Mott insulator [26]. Exotic quantum phases have been demonstrated with cold atoms loaded into a 3D optical lattice [27] and proposed for cold polar molecules [28, 29] including quantum magnetism [30] which involves long range dipole-dipole ordering of polar molecules.

Molecular Bose Einstein condensates have also been produced more recently using Feshbach resonances [31, 32], which will be discussed in detail later. This has been achieved by creating ultra cold Fermi gases of atoms, and then tuning an external magnetic field over a Feshbach resonance where a weakly bound molecule

can form from constituent atoms. Qian et al. describe a scheme to produce a polar molecular BEC from ultra cold atoms [33] by tuning a laser over a photoassociative resonance, which offers the advantage of greater flexibility and control than magnetic fields.

1.1.4 Cold chemistry

At ultra cold temperatures, chemical reactions can become quantum mechanical in their nature. Instead of the reaction rate continuing to drop with lower temperatire, the reaction rate may increase as quantum tunnelling can overcome the repulsive barrier [34]. At cold and ultra cold temperatures, complete control over chemical reactions is possible [35], where control of the quantum state, such as the spin state can allow or prevent a reaction from taking place [36]. This contrasts with 'normal chemistry' where reactions are due to the average of many-particle interactions. The high resolution offered by cold trapped molecules also enables a more precise measurement of the Stark shifts by weak electric fields where hyperfine effects must be incorporated. Such measurements could be used to assess first and second-order perturbation theory approximations to Stark shifts [37].

1.1.5 Collisions

Control over the velocity of cold molecules allows high resolution studies of collisional processes, and the testing of potential energy surfaces (PES's) with high precision, especially at long range [38, 39, 40]. Early experiments involving crossed beams of molecules tuned the collisional energy by varying the intersection angle between the beams. This allowed studies of the reaction barrier for reactive scattering [41, 42] and measurement of the threshold behaviour of rotational energy transfer [43, 44, 45].

The resolution was limited by the relatively large spread in velocities of the beams ($\Delta v/v \approx 10$ %) [46]. Sawyer et al. describe an experiment where Stark decelerated OH molecules were trapped in a permanent magnetic trap at a temperature of 70 mK [47]. They were then collided with velocity-tunable supersonic beams of atomic He and molecular D_2 at tunable, collisional center of mass energies of between 60 cm^{-1} - 230 cm^{-1} and 145 cm^{-1} - 510 cm^{-1}. The resolution was still limited by the velocity spread of the supersonic beams of atomic He and molecular D_2, (T > 1 K). Resonant and quantum threshold effects were demonstrated.

Comparison of these high resolution experiments with theory increases our insight into elastic and inelastic scattering in the presence of applied fields. This is important in predicting collisional cooling in electromagnetic traps as well as calcu-

lating trap loss [48], and for testing molecular structure calculations [49, 50].

1.2 Techniques for producing cold molecules

1.2.1 Introduction

There are a variety of techniques that have been employed or are being pursued to produce cold and ultra cold molecules. These can be grouped broadly into the two main categories of associating cold atoms to form molecules [51] and phase space filtering which involves selecting a small region of phase space, corresponding to a small energy spread [52]. These can then be trapped and cooled to the cold and ultra cold regime, where further cooling may take place [53]. The production of cold molecules from ultra cold atoms is currently able to reach the lowest temperatures, in the < 1 mK regime, however, these techniques are limited to particular species where their exists a Feshbach or photoassociative resonance.

1.2.2 Laser cooling

Conventional laser cooling is not generally applicable to molecules, due to a lack of a closed cycle laser transition. This type of dissipative cooling requires many cycles of excitation via a pump laser and then spontaneous emission to the same state. However, a molecule may decay into many rotational or vibrational channels, causing the species to fall out of resonance with the pump laser and therefore prevent further cooling of the molecule unless other pump lasers are available to re-pump into an excited state. The practical difficulties in having many lasers operating at a variety of frequencies generally prohibit this.

There are however some schemes that overcome this problem. For example Bahns et al. [54] describe a novel scheme in which a single laser generates a spectrum of stimulated Raman sidebands which are sequentially amplified and selected in order to continue to cool the molecules as they change state and the resonant frequency changes. More recently, Shuman et al. [55] describe direct laser cooling of SrF molecules to the mK regime, choosing excited states where the vibrational and rotational decay channels are restricted or eliminated. Just three lasers are required, including a primary pump and two vibrational re-pumping lasers making this method experimentally feasible.

1.2.3 Feshbach resonances and photoassociation

Resonant laser fields, and external magnetic and electric fields can be used to induce Feshbach resonances and control reactions and scattering lengths between colliding atoms or molecules [56, 57, 58, 59]. This occurs due to the modification of the internal energies of the species due to the interaction with the external optical or electric/magnetic fields. In this way Feshbach resonances can be used to produce a bound state from two colliding atoms to form a weakly bound molecule [60]. Here the translational temperature of the molecules is comparable to the temperature of the constituent atoms, and therefore can be in the μK regime in the case of Cubizolles et al. who produced ultra cold Li_2 dimers [61].

Photoassociation has been extensively used with a laser tuned to a resonance such that two or more atoms may form a bound, excited state molecule [62] with a translational temperature comparable to the initial temperature of the constituent atoms. For example Haimberger et al. produced NaCs molecules in an excited state, at a few hundred μK which decayed into their electronic ground state through spontaneous emission [63]. The technique has been developed using additional lasers to produce ground state molecules. For example Nikolov et al. produced potassium molecules in the $X^1\Sigma_g^+$ electronic state by first using photoassociation to produce a weakly bound excited state, and then to shorter range Rydberg states using an additional laser and eventually by radiative decay to the final ground state [64]. Other similar techniques for obtaining molecules which are in a ground state have been described. These usually involve photoassociation of atoms to form an excited molecule and often via an intermediate stage, to a ground state molecule via radiative decay [65, 66].

1.2.4 Photodissociation

A novel technique developed in Durham called 'Photostop' uses the recoil velocity of NO when dissociated from NO_2 to cancel out the molecular beam velocity [67] for a portion of the molecules. Estimated densities of 10^7 cm^{-3} per quantum state, and translational temperatures of 1.6 K have been observed. A dye laser which can be tuned between 380 and 400 nm is used to dissociate the NO_2 molecules and a second laser is used to ionise for detection and measurement of the velocity spread of the ensemble.

1.2.5 Buffer gas and sympathetic cooling

The use of a buffer gases such as helium, is often used to bring a molecular sample down to the 100 mK - 1 K regime [68, 69]. Elastic collisions between the buffer gas and the atomic/molecular sample dissipates translational, vibrational and rotational energy from the hotter species where they can be trapped in a conservative field, for example in a magnetic trap [70]. The effectiveness of this method and the time required for thermalisation depends on the elastic collisional cross-section of the cooling species with the buffer gas as well as the buffer gas density. It is not dependent on the particular energy levels of the system [70], except where this affects the ratio of inelastic and elastic collisions, and the elastic collisional cross-section. It is therefore a relatively general technique for a great variety of atoms and molecules. This technique is accompanied by effective cooling of the rotational and vibrational degrees of freedom [70, 68, 71]. Weinstein et al. have demonstrated the magnetic trapping of calcium monohydride molecules which were first cooled through elastic collisions with a buffer gas of He [72].

Sympathetic cooling is essentially an extension of the buffer gas cooling technique but using colder, laser cooled atoms, in the μK regime, to thermalise another atomic or molecular species. This is suitable for species which may not be cooled using standard laser cooling techniques. For example ^{6}Li fermions [73] have been evaporatively cooled with the ^{7}Li boson isotope and ^{41}K [74] has been evaporatively cooled with rubidium. To achieve thermalisation, the two species must be trapped together for a long enough time that sufficient collisions occur between the ultra cold species and the hotter species. Both species will therefore tend towards the same common temperature.

There are several schemes for using sympathetic cooling to produce cold and ultra cold molecules which may allow the production of cold molecules below the usual limit of $>$ 10 K. One of the most important calculations for these schemes is the collisional cross section between potential candidates for cooling [75, 53, 76], which determine the thermalisation time. This must be within the lifetime of the trap.

1.2.6 Cavity cooling

Atoms which are strongly coupled to a high finesse cavity can be subjected to a dissipative friction force which dampens the motion and results in cooling [77, 78, 79]. This arises from the finite time needed for a cavity to adjust to a change in optical path length due to the motion of an atom within it. Dissipation of kinetic energy

is via cavity loss of blue shifted photons rather than spontaneous emission, making this an attractive prospect for molecules, since no closed laser transition is required. It also avoids or reduces other problems associated with laser cooling, such as atom recoil and photon re-absorption.

The use of cavity assisted cooling has also been proposed for atoms and molecules [78, 80, 81]. Wallquist et al. compare various schemes for electrostatically trapped polar molecules, which are strongly coupled to a microwave cavity. This enhances spontaneous emission of the excited rotational states and cools the molecule.

1.2.7 Zeeman and Stark deceleration

Time varying, inhomogeneous electric fields can be used to decelerate polar molecules [82, 83, 84]. Bethlem et al. describe the deceleration of metastable CO molecules from 225 ms^{-1} to 98 ms^{-1} and have since decelerated a number of molecules to rest. This technique employs the Stark effect which is induced by the applied electric field. Since it is not possible to create an electrostatic maximum in free space [85], it is generally weak field seekers that can be efficiently decelerated, although there are some techniques to avoid this problem [86, 87, 88]. As a weak-field seeker approaches the electrodes, the Stark shift in the energy levels causes a gain in potential energy and a resultant loss in kinetic energy. If the field was kept on, then the particle would lose potential energy and regain its kinetic energy as it exited the electrodes. Instead, the electric field is switched off at the maximum gain in potential energy. Since the amount of kinetic energy that can be extracted in each stage is limited, many stages are required [89].

The principle limitation of this technique is that only molecules with a permanent dipole moment can be slowed. Also, as all ground state molecules are high-field seeking, for the simplest configuration of Stark deceleration the molecules must first be excited into a low-field seeking state. The first implementation of the Stark effect was to decelerate CO molecules which had been excited into the metastable state [89].

Rydberg molecules are of great interest since their large dipole moment made them ideal candidates for Stark deceleration [90]. This has been implemented with supersonic beams of Ar [91, 92] and H in the Rydberg state with principle quantum number in the 15-25 range. The advantage of the larger dipole moment is that the fields required are much smaller, for example a few kV/cm are required to decelerate H from 750 ms^{-1} to rest. Tunable microwave electric fields for Stark deceleration have also been proposed by Enomoto et al. [93]. A wider range of polar molecules could be made available with tunable microwave sources.

The Stark effect has also been employed in velocity selection of molecules, for example using an electrostatic quadrupole to filter out molecules with smaller transverse and longitudinal velocities [94, 95]. In this way, slow ND_3 and H_2CO molecules with a longitudinal velocity of a few K have been guided in a vacuum chamber from a room temperature reservoir.

The use of pulsed magnetic fields and the Zeeman effect is analagous to the use of electric fields and Stark effect. In this technique, paramagnetic molecules gain potential energy as they approach each stage of the magnetic coils, losing kinetic energy. The fields are then switched off in sequence, so that the molecules do not regain their potential energy. Most molecular radicals have a permanent magnetic moment, however molecular oxygen is unique in being paramagnetic in the ground state. It is partly for that reason that it was chosen as a candidate by Narevicius et al. [96] who used pulsed electromagnetic coils to decelerate molecular oxygen from 389 to 83 ms^{-1}.

1.2.8 Optical Stark deceleration

The use of the optical Stark effect for deceleration [52, 97, 98] and focusing [99, 100] of neutral molecules in a molecular jet, including benzene, NO and xenon, has been demonstrated by Fulton et al [97]. This uses the deep ($E/k_\mathrm{B} > 100$ K) periodic potentials (optical lattice) produced by interfering two intense far off-resonance optical fields in the 10^{16} W m^{-2} range which induce a dipole moment in a polarisable species. This in turn interacts with the applied optical field. Up until now, a constant velocity lattice, set at half the speed of the jet has been used to decelerate benzene molecules to rest.

Like Stark and Zeeman deceleration, molecules must first be cooled from room temperature before they can be manipulated by the optical fields. They are first cooled by a supersonic expansion into a primary vacuum chamber (2×10^{-7} Torr) via a pulsed valve with a 500 μm orifice. This supersonic jet has a mean velocity of ≈ 400 ms^{-1}, for example and a translational temperature of $\approx 1 - 2$ K. A skimmer then selects the central portion of the molecular beam with minimal radial velocity where they then enter the secondary chamber, which is kept at 4×10^{-7} Torr. In this chamber, they interact with the laser beams used to form an optical lattice, which decelerates them.

Molecules which interact in such a lattice undergo oscillations in phase space, in terms of their position and velocity. The pulses are temporally shaped such that they switch off after molecules have undergone a half rotation in phase space and therefore experience greatest deceleration. More recently the technique was refined

to decelerate benzene from a xenon-backed jet velocity of 420 ms^{-1} to rest [101].

The main advantage of this technique is that it is entirely general since any molecule is polarisable and is limited only by the polarisability to mass ratio of the species and the available intensities/energies of the laser beams used to create the optical lattice.

Chapter 2

Modelling deceleration of atomic and molecular species

2.1 Introduction

Optical Stark deceleration uses intense optical fields to induce a dipole moment which then interacts with the field that created it to produce an optical potential. The gradient in the optical potential has sufficient force to manipulate the centre-of-mass motion of molecules and atoms which can be used to slow atoms and molecules in a molecular beam. In an inhomogeneous optical field ϵ the instantaneous optical potential U experiences by molecules, with polarisability α is given by [97],

$$U = -\tfrac{1}{2}\alpha\epsilon^2. \tag{2.1}$$

We consider that our beams, which are at $\lambda = 1064$ nm, are far detuned from any transitions in our molecular species and therefore the interaction is due only to the static polarisability of the species.

The force that can be applied to molecules is therefore proportional to the intensity gradient such as exists in a tightly focused laser beam [100]. A larger gradient can be created by the interference pattern formed by two near counter-propagating laser beams. The optical potential formed by the interaction of the interference pattern with the polarisability of the molecules, produces a periodic potential called an optical lattice.

For two counter-propagating beams with wave vectors $\mathbf{k}_1, \mathbf{k}_2$ where we only consider the wave vectors as being in the $\boldsymbol{x}$ direction, with a radial intensity profile in the r direction, the two optical fields, ϵ_1 and ϵ_2 that form the optical lattice are

given by,

$$\begin{aligned}\epsilon_1(r,\boldsymbol{x},t) &= E_1(r,t)\sin\left(\mathbf{k}_1\cdot\boldsymbol{x}-\phi_1(t)\right)\\ \epsilon_2(r,\boldsymbol{x},t) &= E_2(r,t)\sin\left(\mathbf{k}_2\cdot\boldsymbol{x}-\phi_2(t)\right),\end{aligned} \tag{2.2}$$

where E_1 and E_2 are the amplitudes of the electric fields, $\phi_{1,2}(t) = \int \omega_{1,2}(t)\mathrm{d}t$ are the instantaneous phases of the beams that create the lattice, and $\omega_{1,2}(t)$ are the instantaneous angular frequencies of each beam.

For simplicity we also assume here that the instantaneous phases are constant, such that $\phi_{1,2}(t) = \omega_{1,2}(t)$.The total electric field $\epsilon = |\epsilon_1 + \epsilon_2|$ is therefore given by,

$$\begin{aligned}|\epsilon|^2 = \frac{1}{2}\left(E_1^2+E_2^2+E_1^2\cos\left[2\mathbf{k}_1\cdot\boldsymbol{x}-2\omega_1 t\right]+E_2^2\cos\left[2\mathbf{k}_2\cdot\boldsymbol{x}-2\omega_2 t\right]\right)\\ + E_1E_2\cos\left[(\mathbf{k}_1+\mathbf{k}_2)\cdot\boldsymbol{x}-(\omega_1-\omega_2)t\right]+E_1E_2\cos\left[(\mathbf{k}_1-\mathbf{k}_2)\cdot\boldsymbol{x}-(\omega_1+\omega_2)t\right].\end{aligned} \tag{2.3}$$

We simplify this by removing the terms which are oscillating at twice the optical and spatial frequencies, $2\mathbf{k}_{1,2}$ and $2\omega_{1,2}$ to give,

$$\begin{aligned}|\epsilon|^2 = \frac{1}{2}\left(E_1^2+E_2^2\right)+E_1E_2\cos\left[(\mathbf{k}_1+\mathbf{k}_2)\cdot\boldsymbol{x}-(\omega_1+\omega_2)\,t\right]\\ + E_1E_2\cos\left[(\mathbf{k}_1-\mathbf{k}_2)\cdot\boldsymbol{x}-(\omega_1-\omega_2)\,t\right].\end{aligned} \tag{2.4}$$

We are only interested in the slowly varying optical potential for molecular transport, therefore we can also neglect the second term which will be oscillating more than the optical frequency to give,

$$|\epsilon|^2 = E^2\left(1+\cos\left[(\mathbf{k}_1-\mathbf{k}_2)\cdot\boldsymbol{x}-(\omega_1-\omega_2)\,t\right]\right), \tag{2.5}$$

where we have also assumed that $E_1 = E_2 = E$.

More generally, the $(\omega_1-\omega_2)\,t$ term can be replaced by the instantaneous phase difference $\phi_1(t)-\phi_2(t)=\phi(t)$ such that,

$$|\epsilon|^2 = E^2\left(1+\cos\left[(\mathbf{k}_1-\mathbf{k}_2)\cdot\boldsymbol{x}-\phi(t)\right]\right), \tag{2.6}$$

Finally this can be substituted into equation (2.1) to give the slowly varying optical lattice potential U_L, produced by the interaction of the optical lattice produced by fields ϵ_1 and ϵ_2, with a molecule of polarisability α as [97],

$$U_L(r,x,t) = -\frac{1}{2}\alpha E^2(r,t)\cos\left[qx - (\phi(t))\right], \tag{2.7}$$

where q is the amplitude of the lattice wave vector also defined as $q \equiv |\mathbf{k}_1 - \mathbf{k}_2|$ and $x = |\boldsymbol{x}|$. We have also neglected the constant term which is an offset to the optical lattice.

It is assumed here, and throughout this thesis that the wave vector q is a constant. In order to verify this note that,

$$q \equiv |\mathbf{k}_1 - \mathbf{k}_2| = 2\pi \sin\left(\frac{\theta}{2}\right)\left(\frac{1}{\lambda_1} + \frac{1}{\lambda_2}\right), \tag{2.8}$$

where θ is the angle of separation between the two counter propagating beams that create the optical lattice and λ_1, λ_2 are the respective wavelengths. This can be rewritten, considering that the lattice wave vector and frequencies of the beams may have a time dependence as,

$$q(t) = \frac{2\pi \sin\left(\frac{\theta}{2}\right)}{c}\left(f_1(t) + f_2(t)\right), \tag{2.9}$$

where f_1, f_2 are the frequencies of each beam. This implies that $\Delta q/q = \Delta f/f$, where $\Delta q = q(t = t_0) - q(t = t_{chirp})$ and $\Delta f = f(t = t_0) - f(t = t_{chirp})$. Here t_{chirp} is the duration of the frequency sweep. For a maximum required chirp of ≈ 1 GHz, $\Delta q/q = 1 \times 10^9/2.8 \times 10^{14} \approx 10^{-6}$. This justifies the assumption that q remains essentially constant for the duration of the chirp, and therefore has no time dependence. Therefore $q = \frac{4\pi \sin(\theta/2)}{\lambda}$, $\lambda_1 \approx \lambda_2$.

Using equation (2.7), the dipole force, $F(x,t) = -\nabla U_L(x,t)$ is given by [101],

$$F(x,t) = -F_0 \sin\left[qx - \phi(t)\right], \tag{2.10}$$

where F_0 is the maximum force that is applied to the molecules and is given by [101],

$$F_0 \equiv \frac{1}{2}\alpha q E^2. \tag{2.11}$$

In the case of a simple linear chirp from an initial frequency difference ω_0 and a chirp rate $\beta(t) = \mathrm{d}\omega(t)/\mathrm{d}t$, where $\omega(t) = 2\pi f(t)$, the force is given by,

$$F(x,t) = -F_0 \sin\left[qx - \left(\omega_0 t - \frac{1}{2}\beta t^2\right)\right]. \tag{2.12}$$

As we are generally interested in the motion of an ensemble of molecules, one way to model the motion of the ensemble is by solving the Boltzmann equation. In 1-dimension this is given by [102],

$$\frac{\partial g}{\partial t} + v\frac{\partial g}{\partial x} + \frac{F(x,t)}{m}\frac{\partial g}{\partial v} = \left(\frac{\partial g}{\partial t}\right)_{\mathrm{c}}, \tag{2.13}$$

where the velocity distribution function $g = g(x, v, t)$, $(\partial g/\partial t)_{\mathrm{c}}$ is the collision integral (the rate of change of the distribution function), $F(x,t)$ is substituted by the optical dipole force in equation (2.12) and m is the molecular mass. In the collision free regime, $(\partial g/\partial t)_{\mathrm{c}} = 0$ and this can be numerically integrated to predict the dynamics of an ensemble of molecules using, for example, the MacCormack finite difference method [102, 103]. The measurements of laser intensity and measured temporal profile can be input into the scheme.

A fixed frequency difference between the two beams will create a constant velocity lattice which has been used to decelerate molecules, using a half oscillation of the molecules in phase space which are trapped in the deep optical lattice [97]. The lattice velocity, v_{L} created by two beams with an angular frequency difference $\Delta\omega$ and wave vector q is given by,

$$v_{\mathrm{L}} = \frac{\Delta\omega}{q}. \tag{2.14}$$

2.2 Constant velocity optical lattice deceleration

In previous deceleration experiments, constant velocity lattices were used to slow nitric oxide (NO) and benzene (C_6H_6) molecules in a molecular jet to rest in a backing gas of xenon [97, 52, 104]. The formation of such an optical lattice is shown in figure 2.1. To produce the optical lattices, two single-mode injection-seeded, Q-switched, Nd:YAG lasers were used. The two beams were focused down to a full-width half maximum (FWHM) of 60 μm and intersected at $\theta = 167.5°$ to produce a periodic potential with a period of approximately 532 nm and intensities of approximately 10^{12} W cm^{-2}. The FWHM duration of the lattice pulse was 5.8 ns.

In order to produce a constant velocity lattice, the lasers were temperature tuned to produce the required frequency difference. It was found that a lattice velocity set at half the molecular beam velocity (≈ 400 ms^{-1}) could produce a proportion of stationary molecules in the laboratory frame. Since molecules in a periodic potential will undergo oscillatory motion, to slow molecules, the field is switched off when the molecules have undergone a half rotation or a half rotation plus an integer number of oscillations. In the case of benzene molecules with mass 78 a.m.u. and static polarisability of $\alpha = 11.6 \times 10^{-40}$ cm^2 V^{-1} , and an optical lattice created by two fields of intensity $I = 2.2 \times 10^{12}$ W cm^{-2}, this created an oscillation period of 2.0 ns.

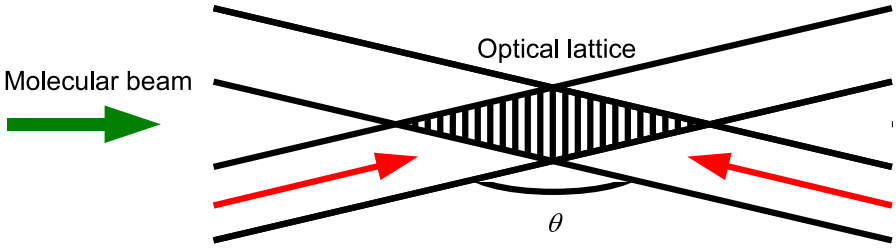

Figure 2.1: Formation of optical lattice with intense infrared laser beams with angle of intersection θ

This scheme, although successful, is limited to creating slowed molecules ensembles with an energy spread that is comparable to the initial spread of the molecular beam, while the required fast switching of the optical field is technically challenging. A narrower energy spread centered at 0 ms^{-1} can be created by trapping these molecules with a lower trap depth than the decelerating potential, however it is not suitable for high resolution collision studies at arbitrary velocities which require a narrower energy spread.

In this thesis, I explore the creation of ensembles with energy spreads that are much narrower, using chirped optical Stark deceleration.

2.3 Motivation and requirements for chirped optical Stark deceleration

The creation of a narrower energy spread of molecules is required to improve the resolution of collisional experiments, as well as producing a colder distribution of decelerated molecules, making them more suitable for trapping and sympathetic cooling. A scheme that uses a decelerating optical lattice has been described theoretically [105, 102]. The dynamics in this scheme occur over a much longer period (20-1000 ns) when compared to the constant velocity scheme, allowing for slower switching of fields. Despite the lower intensities required, relatively large energies are still required, (up to 0.5 J per pulse), due to the longer pulse durations.

The slowly varying lattice potential $U_L(x,t)$ for a linearly decelerating/accelerating lattice from equation (2.7), without the constant offset, can also be written as [52],

$$U_L(r,x,t) = \frac{-\alpha}{\epsilon_0 c}\sqrt{I_1(r,t)I_2(r,t)}\cos(qx - (\omega_0 t - \tfrac{1}{2}\beta t^2)), \tag{2.15}$$

where α is the polarisability of the species, $I_1(r,t)$ and $I_2(r,t)$ are the intensities of the two laser beams which create the lattice, $q = \frac{4\pi\sin(\frac{\theta}{2})}{\lambda}$ is the wave vector,

$\omega_0 = 2\pi f_0$ is the initial angular frequency difference. The chirp rate, $\beta = \Delta\omega/\Delta t$, is determined by the angular frequency excursion $\Delta\omega$ and the chirp duration is Δt. A decelerating lattice would be represented by $-\beta$ and an accelerating lattice by β.

The optical lattice velocity is controlled by sweeping the relative frequency of the two beams (chirping). For deceleration from a molecular beam of xenon, the lattice velocity must change from 400 ms^{-1} to zero velocity. Since the difference in frequency as a function of time of the lattice is, $f_{\mathrm{L}}(t) = \frac{2v_{\mathrm{L}}(t)\sin(\theta/2)}{\lambda}$, where $v_{\mathrm{L}}(t)$ is the instantaneous lattice velocity, λ is the wavelength of the laser beams, and θ is the angle between them, this implies that we need to start with an initial frequency difference of $\approx$ 750 MHz for near counter-propagating beams. Given that other backing gases such as argon may be used where jet velocities may be up to 560 ms^{-1}, this frequency difference can be even larger. For deceleration times in the range 20-1000 ns, the required chirping rate is therefore in the range of $1 - 40$ GHz $\mu\mathrm{s}^{-1}$.

Another major requirement for the laser pulses is that they ideally have a flat temporal profile, with a relatively fast rise and fall time. The depth of the potential experienced by a molecule is proportional to the square root of the product of the intensities of the laser, as shown by equation (2.15), therefore any decrease would cause a loss of population from the optical wells. An increase in intensity over the duration of the pulse would also be sub-optimal, because you would simply deepen the potential well of already confined molecules. This would waste the finite amount of energy available in the amplifying rods and due to the increased width of the potential, there would be unwanted heating of the decelerated distribution.

As the required laser system for chirped decelerating was not available commercially, a significant part of this thesis is dedicated to its design and construction.

In chapters 3-5 I will describe the development of this unique, high energy, chirped laser system suitable for the deceleration of molecules in a molecular jet.

2.4 Phase space diagrams

To investigate the trajectories of accelerated or decelerated particles within an optical lattice we consider their motion relative to a moving lattice. We work in the reference frame of the lattice, since for the purposes of this thesis, we are only interested in trapped molecules which move at the same centre of mass velocity as the optical lattice and not the molecules which just have their velocities perturbed by it.

Using equation (2.12) the equation of motion for a particle in a linearly chirped lattice is given by [105],

$$\ddot{x}(x,t) = -a(t)\sin\left(qx + \frac{1}{2}\beta t^2 - qv_0 t\right), \tag{2.16}$$

where $a(t) = \frac{1}{2}\alpha q E_0(t)^2/m$ is the maximum force per unit mass supplied by the lattice, v_0 is the initial lattice velocity and $\beta(t) = \mathrm{d}\omega_2(t)/\mathrm{d}t$ is the frequency chirp.

In the reference frame of a decelerating lattice, we replace position and velocity, with the dimensionless quantities of phase, θ and phase velocity η, where $\theta = qx + (\beta/2)t^2 - qv_0 t$ and $\eta = (q\dot{x} + \beta t - qv_0)/\sqrt{\beta/2}$. The critical points are found from the equations of motion for the particles where [102],

$$\frac{\mathrm{d}\eta}{\mathrm{d}T} = 2 - \frac{2}{\psi}\sin\theta, \frac{\mathrm{d}\theta}{\mathrm{d}T} = \eta, \tag{2.17}$$

where $T \equiv \sqrt{\beta/2}\ t$ is the dimensionless time and $\psi \equiv \beta/aq$ which physically is a measure of the effective depth of the potential well of the lattice. The two critical points of this system are given by [102], $[\theta_1, \eta_1] = [2n\pi - \sin^{-1}\psi, 0]$, which are stable points where n is an integer, and $[\theta_2, \eta_2] = [(2n-1)\pi + \sin^{-1}\psi, 0]$ which are saddle points.

The potential as a function of the phase in the moving reference frame is $U(\theta) = -\int m/q^2 \mathrm{d}^2\theta/\mathrm{d}t^2 \mathrm{d}\theta$ [105], which from equation (2.17) gives,

$$U(\theta) = -\frac{m\beta}{2q^2}\left(\frac{2}{\psi}\cos\theta + 2\theta\right). \tag{2.18}$$

The depth of a potential well, ΔU, is the difference between a saddle point and the stable equilibrium given by [102],

$$\Delta U = \frac{ma}{q}\left[2\cos\left(\sin^{-1}\psi\right) - \psi\left(\pi - 2\sin^{-1}\psi\right)\right]. \tag{2.19}$$

Equation 2.19 shows that no potential can exist for $\psi \geq 1$ since mathematically, there is no value for $\sin^{-1} x$, where $x > 1$. Physically this implies that no potential well exists when the chirp rate is too high compared to the maximum force per unit mass supplied by the optical lattice to the polariseable particle. Since $\psi = \beta/aq$,

$$\frac{\beta}{aq} < 1 \tag{2.20}$$

The potential $U(\theta)$ is plotted in figure 2.2 for three values of $\psi = 0.3, 0.5, 0.8$, presenting three depths of the optical potential for a decelerating lattice. In the case of 0.8 the potential is relatively shallow, which would therefore trap the smallest proportion of molecules. At the opposite extreme, where $\psi = 0.3$ represents a decelerating lattice with a lower chirp rate, or one with larger intensity beams,

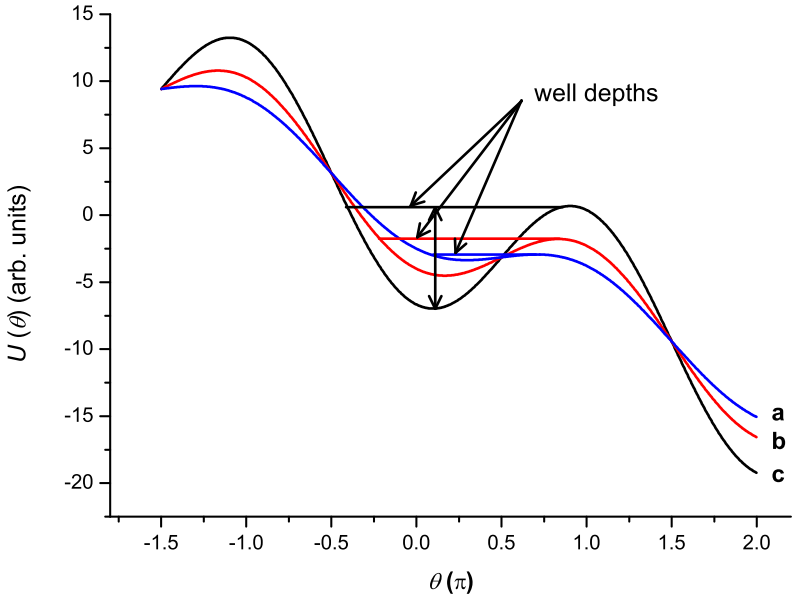

Figure 2.2: This plot is the potential as a function of phase, $U(\theta)$, for three ratios of chirp rate to intensity, (a) $\psi = 0.8$, (b) $\psi = 0.5$ and (c) $\psi = 0.3$. It can be seen that the effective well depth decreases as the parameter ψ increases, which represents either an increasing chirp rate or decreasing laser beam intensity. This is calculated using the relationship, $U(\theta) \propto \left(\frac{2}{\psi}\cos\theta + 2\theta\right)$.

where the chirped lattice potentials are much deeper.

The equations of motion given by (2.17) can be solved numerically to produce phase space plots that map out trajectories of phase velocity and phase position, as shown by figure 2.3. Here the trajectories of 15 particles are mapped out in the phase space, with the x-axis representing the phase relative to the reference frame, θ of the lattice and the y axis representing dimensionless phase velocity η which can be related to the actual velocity as $v = \eta\frac{\sqrt{\beta/2}}{q}$. The particles start with a variety of initial velocities and phases. The tear drop shaped trajectory, which is almost a closed orbit maps out the separatrix between particles which are trapped by the optical lattice and the un-trapped particles. In dimensional units this critical velocity is given by [102],

$$v_c(\theta) = V\left[\cos\theta - \cos\left(\pi - \sin^{-1}\psi\right) + \psi\left(\theta + \pi + \sin^{-1}\psi\right)\right]^{1/2}, \tag{2.21}$$

where $V = 2\sqrt{(\beta/2)/\psi}/q$.

The particles mapped out by the closed, elliptical trajectories are particles starting with zero velocity relative to the lattice, and sufficiently close to the centre of the lattice site to remain confined. They also indicate the positions of the centres of the lattice sites, where two lattice sites can clearly be seen. The rest of the par-

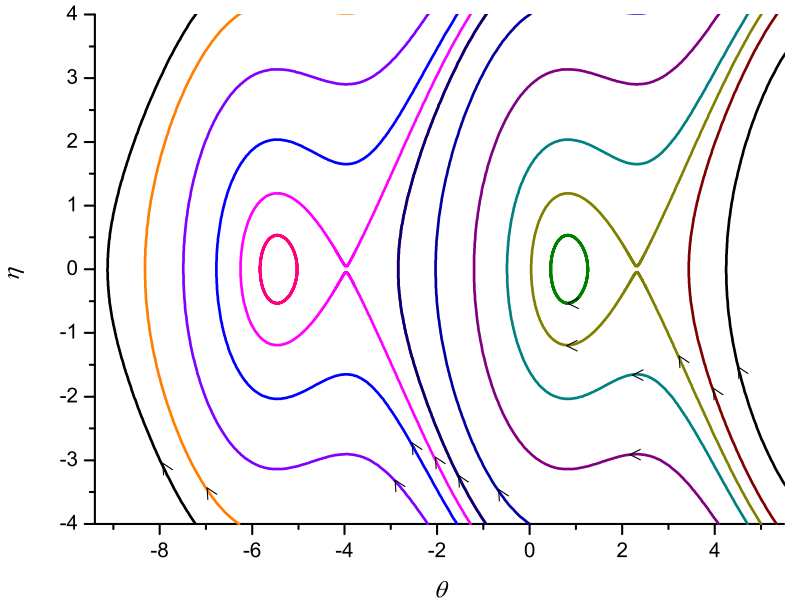

Figure 2.3: Trajectories of molecules over two lattice sites, for various initial phase positions and phase velocities for $\psi = 0.735$. The tear drop shaped, almost closed trajectory represents the separatrix between molecules which are trapped by the optical potential. Outside this region, are the trajectories of particles which are just perturbed by the lattice.

ticles shown start with velocities of $\eta = -4$ and various phase positions. They are perturbed by different degrees according to how close they pass to the centre of the lattice sites.

The dimensionless phase velocity as a function of time can be converted back to dimensionless units, according to $\eta = vq/(\beta/2)^{0.5}$. The evolution of velocity over the duration of the chirp for various benzene molecules with different initial velocities is shown in figure 2.4 and 2.5. Their initial phase position is chosen so that the molecules are at the centre of a lattice site, where v_c has its maximum value. Figure 2.4 shows the trajectories of 5 particles with different initial speeds, that remain trapped over the duration of the pulse. The turquoise trace represents a weakly confined molecule, and the pink and lime traces represent more strongly confined molecules. It can be seen that the period of oscillation decreases for stronger confinement. The black trace shows the evolution of a decelerating lattice velocity. The blue and red traces show the limits of the minimum and maximum velocity that a molecule may have in order to be confined by the lattice. For $\psi = 0.5$ the critical velocity is $\pm$ 25.71 ms^{-1}. This is the maximum/minimum initial velocity a benzene molecule can have relative to the velocity of the optical lattice .

Figure 2.5 shows the trajectories of molecules which are not confined by the optical lattice, but have their velocities perturbed. Once again the lattice velocity is

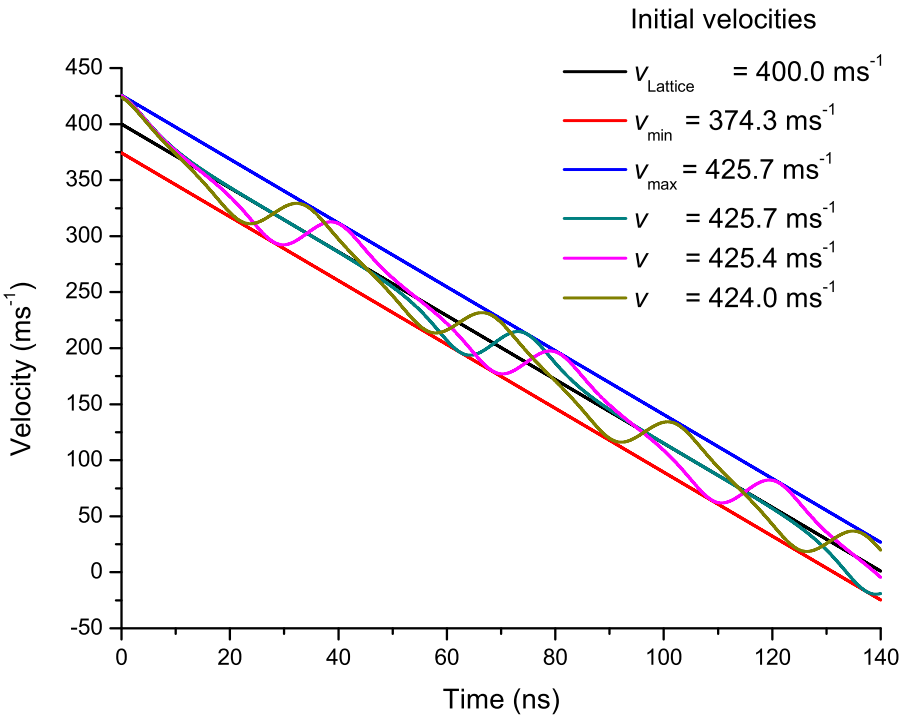

Figure 2.4: A plot of the trajectories of the benzene molecules initially at different velocities but with the same phase so that they are at the centre of the potential well, for $\psi = 0.5$, representing a chirp of 750 MHz in 140 ns, decelerating from 400 ms^{-1} to rest. The blue and red lines represent the velocity spread of confined benzene molecules at $\pm$ 25.7 ms^{-1} compared to the lattice velocity. These lines represent the maximum and minimum initial velocities at $t = 0$ to be confined by the optical potential. The turquoise trace represents a molecule which is just confined by the potential. The pink and lime green trace represents more strongly confined molecules, where the period of oscillation decreases, for greater confinement, that is where the initial velocity is closer to the velocity of the optical lattice.

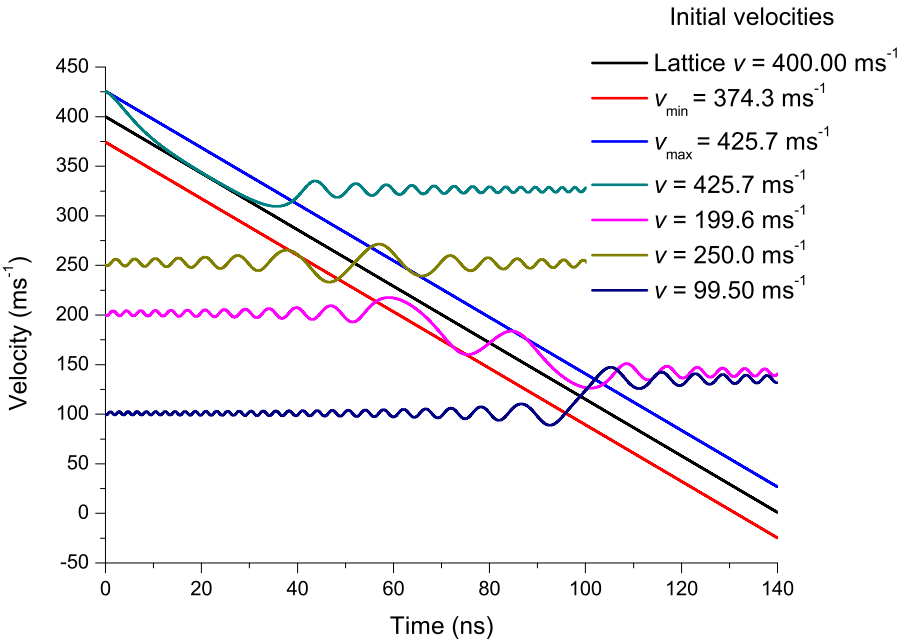

Figure 2.5: Trajectory of benzene molecules initially at different velocities but with the same phase so that they are at the centre of the potential well, for $\psi = 0.5$ for a chirp of 750 MHz down to 0 MHz in 140 ns, decelerating from 400 ms^{-1} to rest over 140 ns. The blue and red lines represent the velocity spread of confined benzene molecules at $\pm$ 25.7 ms^{-1} compared to the lattice velocity, which also represents the maximum and minimum initial velocities at $t = 0$ to be confined by the optical potential. The turquoise trace represents a molecule which escapes the optical potential after 40 ns because its initial velocity is slightly above the upper limit. This initial perturbation creates a small oscillation in velocity which damps out over the duration of the pulse. The lime green trace represents a molecule with an initial velocity much lower than the optical lattice velocity, which remains largely unperturbed in terms of mean velocity, other than a small oscillation in velocity. The pink and navy traces represent molecules which are strongly perturbed, the former decelerated by approximately 60 ms^{-1} and the latter accelerated by 40 ms^{-1}.

shown by the black trace, and the critical velocities by the red and blue traces. The turquoise trace shows the trajectory of a molecule with an initial velocity slightly too high and escapes the optical lattice after $\approx$ 40 ns. The other traces show trajectories of particles with initial velocities that are much lower than the lattice velocity. They are perturbed as the lattice velocity approaches their own. It is interesting to note that the period of oscillation of the molecules, caused by the interaction with the optical lattice, changes before and after the strong interaction which occurs when the lattice velocity decelerates to be comparable to that of the molecule.

The fraction of particles (capture efficiency), κ which can be trapped and decelerated by the optical field is given by the number of particles, initially in thermal equilibrium which overlap the trapped region as shown by the phase space plot in

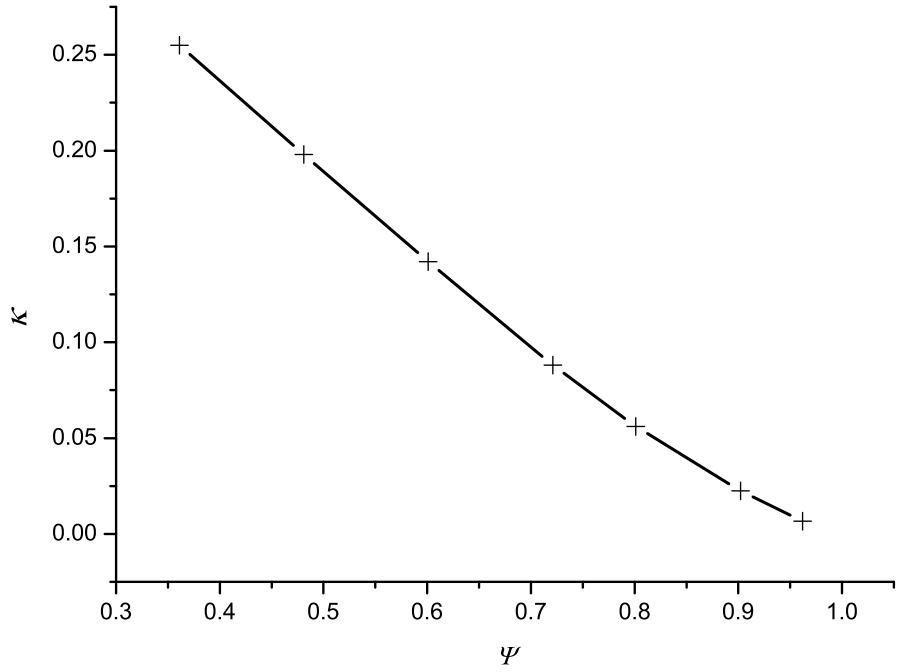

Figure 2.6: Proportion of trapped benzene molecules, κ, for various values of $\psi \equiv \beta/aq$.

figure 2.3 is given by [102],

$$\kappa = \frac{1}{2\pi} \int_{\Theta_1}^{\Theta_2} \int_0^{v_c(\theta)} \sqrt{\frac{m}{2\pi kT}} e^{-mv^2/2kT} \mathrm{d}v \mathrm{d}\theta, \tag{2.22}$$

where Θ_1 , Θ_2 are critical points of equation (2.17) and v_c is given by equation (2.21).

For benzene, with mass 78 a.m.u. with polarisability of $\alpha = 11.6{\times}10^{-40}$ C m^2 V^{-1} with intensities in both beams of 0.75×10^{14} W m^{-2}, with a chirp of 750 MHz, over 140 ns and parameter $\psi = 0.962$ gives a capture efficiency $\kappa = 0.67$ % according to equation (2.22). Figure 2.6 shows the capture efficiency κ for various values of ψ.

2.4.1 Radial motion in lattice beams

Trapped molecular motion in an optical lattice is not only in the direction along the optical lattice wave vector. Transverse motion is created by the radial intensity gradient in a Gaussian beam. This potential takes the form [106], $U(r) = 1/2\alpha I_0/\epsilon_0 c \ \exp\left[-2r^2/\omega_0^2\right]$, where I_0 is the maximum intensity and ω_0 is the beam waist, and the force is given by, $F(r) = -\nabla U(r)$, therefore the force can be written as,

$$F(r) = -2\alpha I_0 r/(\epsilon_0 c \omega_0^2) \ \exp\left[-2r^2/\omega_0^2\right] \tag{2.23}$$

Assuming small oscillations and therefore simple harmonic motion we perform a second order Taylor expansion of this to give the force near the centre of the beam, $F(r) = (-2\alpha I_0 r)/(c\epsilon_0\omega_0^2)$.

Since the period oscillation of a simple harmonic oscillator experiencing a force $F(r) = -kr$, is $P = 2\pi\sqrt{m/k}$ [107], the period of oscillation in our beams is given by,

$$P = 2\pi\sqrt{\frac{mc\epsilon_0\omega_0^2}{2\alpha I_0}} \tag{2.24}$$

For deceleration experiments with intensities of $I_0 = 1 \times 10^{14}$ W m^{-2}, beam waist $\omega_0 = 50$ μm and using benzene as an example, with mass 78 a.m.u and polarisability $\alpha = 11.6 \times 10^{-40}$ C m^2 V^{-1}, this gives $P = 9.7\mu$s. This is several orders of magnitude longer than the duration of the decelerating pulse which validates the approximation of our quasi 1-dimensional model for most situations. To estimate the acceleration of particles in the radial direction and the distance they may move over the duration of the pulse, we consider that the maximum force occurs at,

$$\nabla \cdot F(r) = F(r)/r - 4r/\omega_0^2 F(r) = 0 \tag{2.25}$$

Maximum force is therefore at $r = \pm\,\omega_0/2$, where $F_{\max} = I_0\alpha/(c\epsilon_0\omega_0)\exp(-1/2)$. For the worst case scenario, we consider a particle with twice the most probable speed at 1 K, where $v_{\rm p} = \sqrt{2RT/M}$, where T is the temperature, M is molar mass and R is the gas constant.

For benzene, and with the same intensity, $I_0 = 1 \times 10^{14}$ W m^{-2} as before and given $2 \times v_{\rm p} = 0.9$ ms^{-1} then this gives the maximum force as $F_{\max} = 5.37 \times 10^{-19}$ N, and the corresponding maximum acceleration $a_{\max} = 4.1 \times 10^6$ ms^{-2}. For a 140 ns pulse , the change in velocity is 0.57 ms^{-1} and total distance traveled is 170 nm. This distance is relatively small compared to the interaction region.

2.5 Numerical modelling of deceleration and acceleration

The simulations up to this stage are for the simplest case of constant intensity beams and linear chirps, however we may also want to simulate the transport of atomic and molecular species using realistic and actual experimental parameters, such as the temporal profile of the laser beams and non-linear chirps.

We therefore performed numerical simulations by solving two coupled equations

of motion for each individual particle,

$$\frac{\mathrm{d}v(x,t)}{\mathrm{d}t} = -F_0 \sin(qx - \phi(t))$$
$$\frac{\mathrm{d}x}{\mathrm{d}t} = v(x,t), \tag{2.26}$$

where $F_0 = \alpha q I(t)/(m\epsilon_0 c)$ and $\phi(t)$ is the relative phase between the two beams. The Runge-Kutta method was used to solve these equations, which was implemented using the ODE45 function in Matlab with variable time steps to optimise the calculation time.

The calculation was then performed for each of a large number of particles (e.g. 20000) to build up a distribution of positions and velocities, since we assume that the particles do not interact with each other over the duration of the pulse.

We assumed various initial conditions, such as an initial Maxwell Boltzmann velocity distribution associated with a temperature input by the user and a random distribution in position over 20 μm. The program then read in the measured temporal profile of a typical pulse (code therefore assumes both pulses have the same temporal profile) and measurement of the instantaneous phase $\phi(t)$ and frequency $f(t)$.

In all of our simulations we have assumed a 1-dimensional problem. Although we have calculated that the radial forces are negligible for typical pulse durations in terms of motion in the transverse direction, our simulation does not take into account the particles which are trapped or perturbed in the region outside the central region of maximum intensity. Since these particles will be trapped in a smaller potential, the overall final temperature of the decelerated/accelerated ensemble may actually be lower than simulated.

2.6 Numerical modelling of cold stationary molecules

2.6.1 Idealised temporal intensity profile and linear chirp

For an idealised case, with a perfectly linear chirp from 750 to 0 MHz in 140 ns, molecules can in principle be decelerated from 400 to 0 ms^{-1}.

Figure 2.7 illustrates a linear chirp, represented by the blue trace, with flat top temporal profiles represented by the black trace. This pulse has an artificially square temporal profile, and has been modelled with a super-Gaussian function of the form $I(t) = \exp[-((t_0 + t)/\Delta t)^{100}]$. This pulse has a rapid rise time, from zero to half

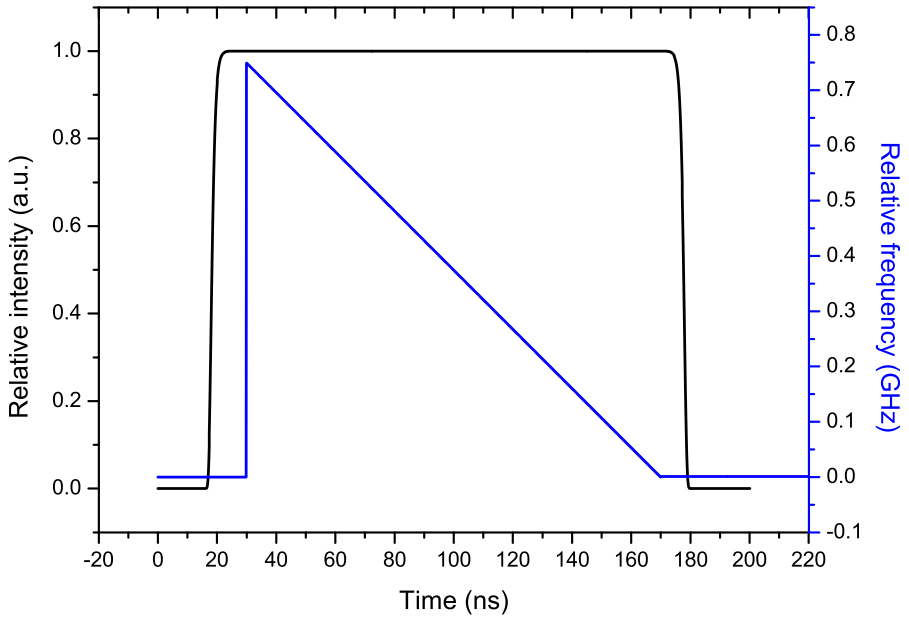

Figure 2.7: Constant linear chirp from 750 to 0 MHz, represented by the blue trace, corresponding to a lattice acceleration from 380 ms^{-1} to rest in 140 ns for near counter propagating beams which have a simulated, super-Gaussian temporal profile of the form $I(t) = \exp\left[-((t_0 + t)/\Delta t)^{100}\right]$, with a half maximum rise time of ≈ 2 ns.

maximum in ≈ 2 ns and a flat profile for a duration of ≈ 170 ns. In this idealised situation, initially both beams have the same frequency, and therefore the optical lattice is stationary until the intensities of the beams have reached their maximum value. The frequency chirp then begins after maximum intensity has been reached and is maintained for the duration of the chirp.

We study the deceleration of molecules in a molecular beam with an initial temperature of 2 K, and a corresponding FWHM velocity spread according to $v = \sqrt{\frac{8\ \ln 2\ k_{\mathrm{B}}T}{m}}$ as shown by figure 2.8.

Figure 2.9 shows the final distribution of velocities when the decelerating optical lattice is applied to an ensemble of 20000 benzene molecules, with polarisability $\alpha = 11.6 \times 10^{-40}$ C m^2 V^{-1}, and mass $m = 80$ a.m.u..

We study deceleration using maximum intensities in the $(0.75-1.4)\times 10^{14}$ W m^{-2} range. The simulations show that as the intensity is reduced, the final velocity spread generally decreases along with the number of particles captured. The mean velocity for the decelerated molecules is, ≈ -15 ms^{-1} which is probably due to the sudden change in potential that they experience on switch off. This will be explored in the next set of simulations, where a temporal profile will be modelled with a slower rise time. The lowest intensity for successful deceleration of benzene molecules is $\approx I_{\mathrm{max}} = 0.75 \times 10^{14}$ W m^{-2}. Here, approximately 140 (0.7 %) molecules have been decelerated, with a FWHM velocity spread of ≈ 7 ms^{-1} representing a tempera-

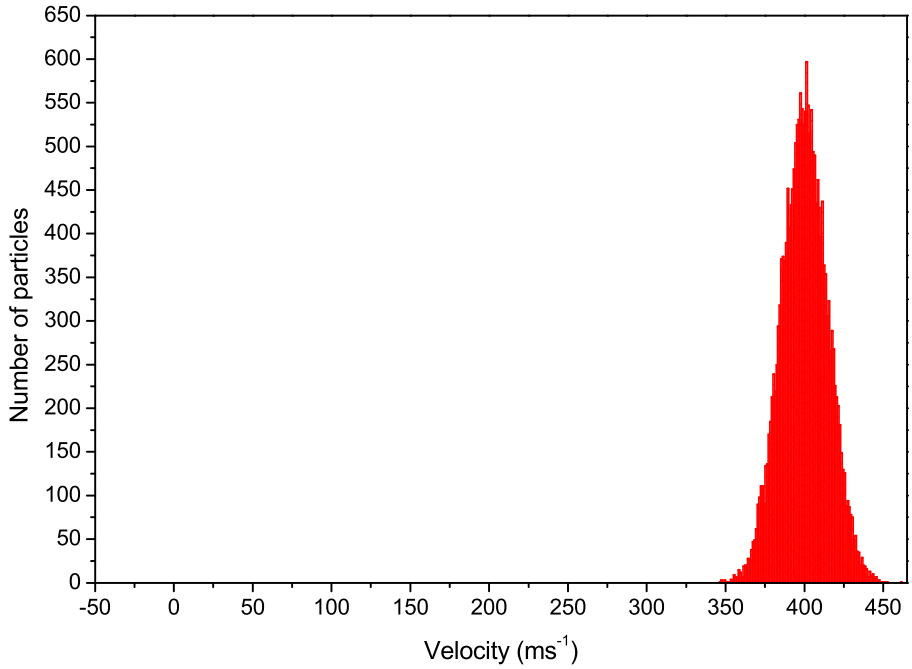

Figure 2.8: Initial distribution of benzene molecules, with an initial temperature of 2 K, and a corresponding FWHM velocity spread of 34 ms^{-1}.

ture of $\approx$ 0.2 K. This is not actual temperature, but represents an energy spread in K according to $\Delta \mathrm{T} = \frac{1}{2}m(\Delta v)^2/k_{\mathrm{B}}$ and will be given in subsequent decelerated/accelerated decelerations.

For $I_{\mathrm{max}} = 1 \times 10^{14}$ W m^{-2}, where approximately 1900 (9.6 %) molecules were decelerated, the FWHM of the velocity spread was $\approx$ 34 ms^{-1} representing a temperature of $\approx$ 5.5 K. For $I_{\mathrm{max}} = 0.9 \times 10^{14}$ W m^{-2} approximately 2400 (11.9 %) molecules were decelerated, the FWHM of the velocity spread was $\approx$ 21 ms^{-1} representing a temperature of $\approx$ 2.1 K. For $I_{\mathrm{max}} = 0.8 \times 10^{14}$ W m^{-2} approximately 400 (2 %) molecules were decelerated, the FWHM of the velocity spread was $\approx$ 12 ms^{-1} representing a temperature of $\approx$ 0.7 K. For $I_{\mathrm{max}} = 0.7 \times 10^{14}$ W m^{-2}, no molecules were decelerated.

For $I_{\mathrm{max}} = 1.0 \times 10^{14}$ W m^{-2}, figure 2.6 which showed the theorectical capture efficiency κ for benzene for various values of the parameter ψ, predicts $\approx$ 8 % of molecules which would be trapped and decelerated by the optical lattice. This compares well with the simulation, where $\approx$ 9.6% were decelerated. For comparison, at $I_{\mathrm{max}} = 0.8 \times 10^{14}$ W m^{-2}, figure 2.6 predicts $\approx$ 1.8 % which also compares well with the 2 % which were decelerated in the simulations.

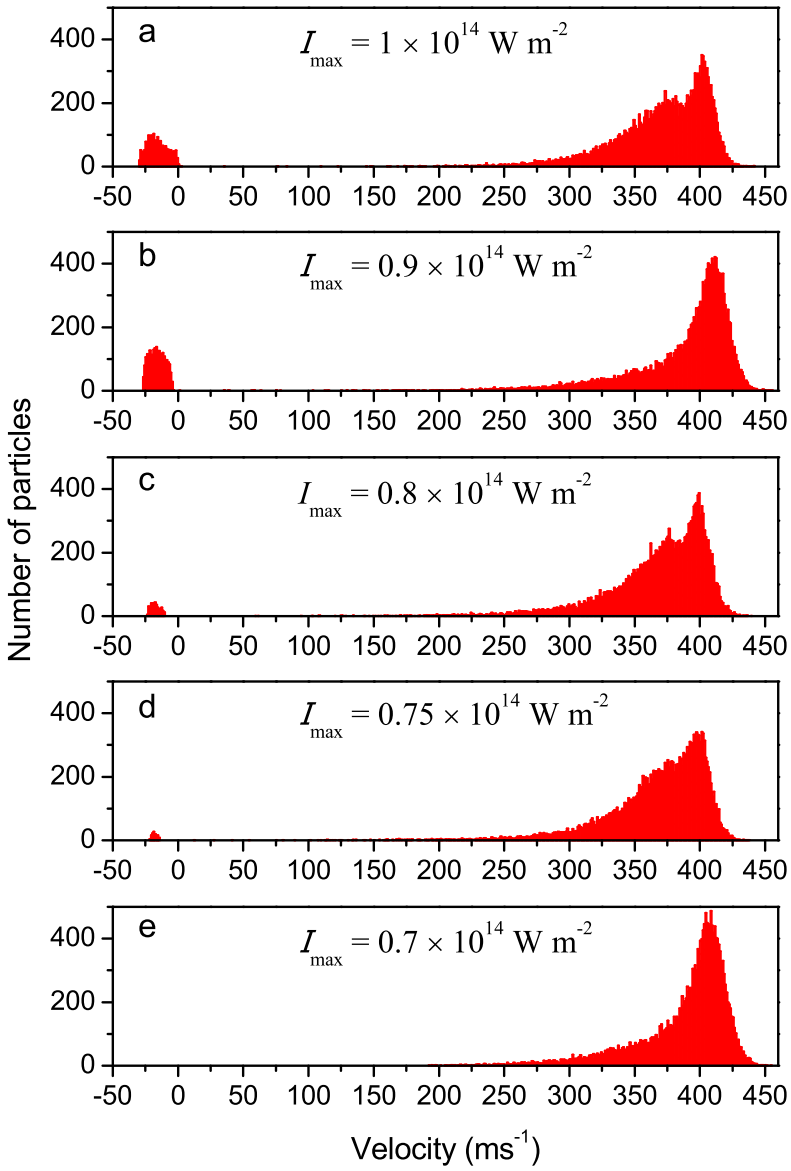

Figure 2.9: The resultant distribution of velocities when the decelerating optical lattice described in figure 2.7 is applied to an ensemble of 20000 benzene molecules for various maximum intensities for each beam. (a) $I_{max} = 1.0 \times 10^{14}$ W m^{-2}, (b) $I_{max} = 0.9 \times 10^{14}$ W m^{-2}, (c) $I_{max} = 0.8 \times 10^{14}$ W m^{-2}, (d) $I_{max} = 0.75 \times 10^{14}$ Wm^{-2}, (e) $I_{max} = 0.7 \times 10^{14}$ W m^{-2}.

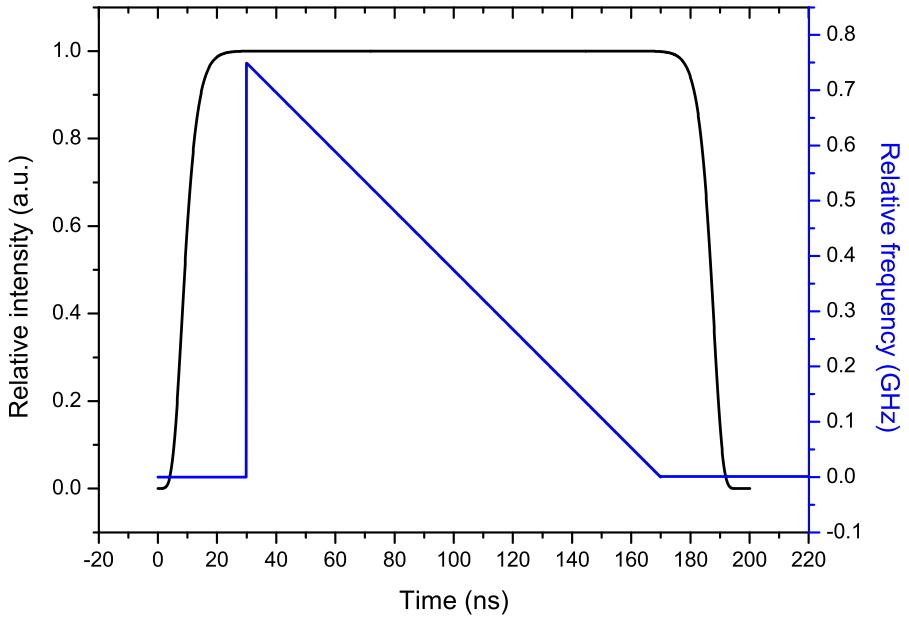

Figure 2.10: Constant linear chirp from 750 to 0 MHz, represented by the blue trace, corresponding to a lattice deceleration from 400 ms^{-1} to rest in 140 ns, for near counter propagating beams which have a simulated, super-Gaussian temporal profile of the form $I(t) = \exp[-((t_0 + t)/\Delta t)^{30}]$, with a half maximum rise time of $\approx$ 10 ns, comparable to typical rise times achievable with our laser system.

2.6.2 Slower rise time intensity and linear chirp

In order to investigate the effect of a slower rise time, a super-Gaussian pulse, of the form $I(t) = \exp[-((t_0 + t)/\Delta t)^{30}]$ with a half maximum rise time of $\approx$ 10 ns was modelled and used in the simulation. This is closer to typical rise times achievable in a laser system. This profile is shown, overlaid with the same linear chirp, as in figure 2.10.

Figure 2.11 shows the resultant distribution of benzene molecules at 2 K with this new temporal intensity profile, but with the same maximum intensity as before. The mean velocity of the decelerated molecules is now approximately 0 ms^{-1} indicating that it was indeed the rapid switch off that caused an undesirable 'kick' to the velocity spread of the particles. For the threshold intensity for deceleration of $\approx I_{max} = 0.75 \times 10^{14}$ W m^{-2}, approximately 250 (1.3 %) molecules were decelerated with a FWHM velocity spread of approximately $\approx$ 10 ms^{-1} representing a temperature of $\approx$ 0.5 K. This is more particles than in the previous case, with a slightly wider velocity spread. The number of particles and their energy spread (K) is very sensitive to the intensity. A 10 % decrease in intensity from $I_{max} = 1.0 - 0.9 \times 10^{14}$ W m^{-2} results in a 35 % decrease in temperature.

For $I_{max} = 1 \times 10^{14}$ W m^{-2} approximately 3700 (18.5 %) molecules were decel-

erated, the FWHM of the velocity spread was $\approx$ 22 ms^{-1} representing a temperature of $\approx$ 2.3 K. For $I_{\max} = 0.9 \times 10^{14}$ W m^{-2}, approximately 2300 (11.3 %) molecules were decelerated, the FWHM of the velocity spread was $\approx$ 18 ms^{-1} representing a temperature of $\approx$ 1.5 K. For $I_{\max} = 0.8 \times 10^{14}$ W m^{-2}, approximately 770 (3.8 %) molecules were decelerated the FWHM of the decelerated molecules was approximately $\approx$ 14 ms^{-1} representing a temperature of $\approx$ 0.9 K. For $I_{\max} = 0.75 \times 10^{14}$ W m^{-2} approximately 250 (1.3 %) molecules were decelerated, the FWHM of the decelerated molecules was approximately $\approx$10 ms^{-1} representing a temperature of $\approx$ 0.5 K. For $I_{\max} = 0.7 \times 10^{14}$ W m^{-2} no particles were decelerated except for some deposited at higher velocites and spread over a large velocity range.

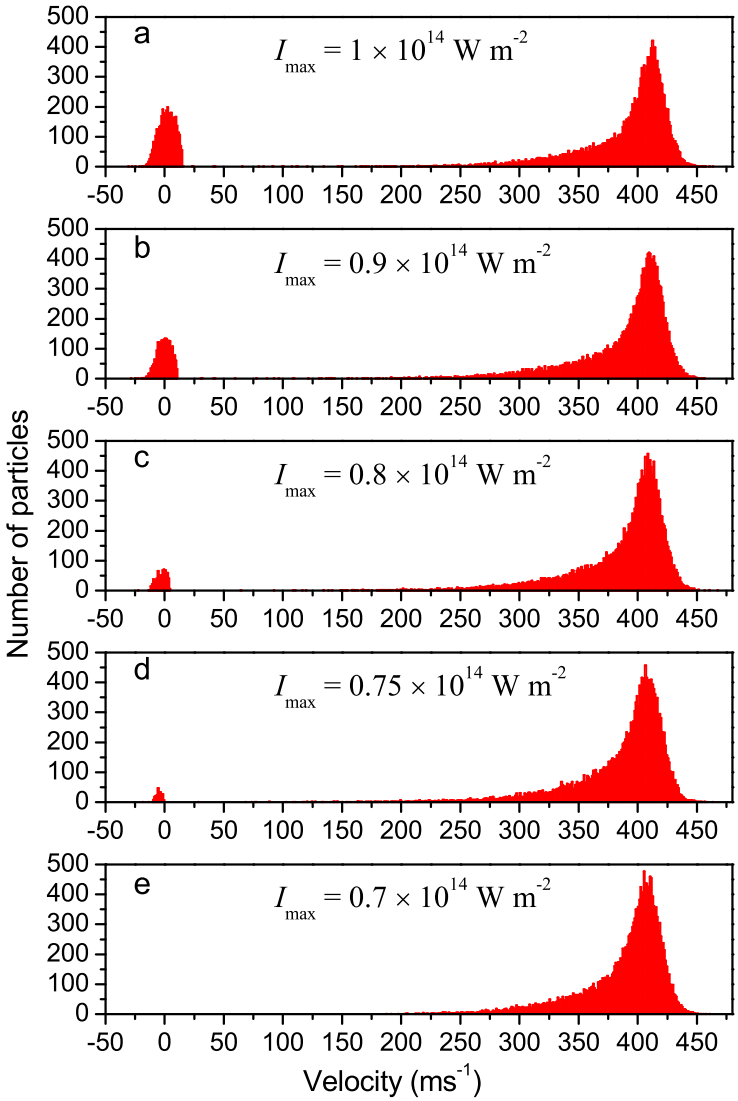

Figure 2.11: The resultant distribution of velocities when the decelerating optical lattice described in figure 2.10 is applied to an ensemble of 20000 benzene molecules with a temperature of 2 K (FWHM 34.3 ms^{-1}) for various maximum intensities for each beam. (a) $I_{\max} = 1.0 \times 10^{14}$ W m^{-2}, (b) $I_{\max} = 0.9 \times 10^{14}$ W m^{-2}, (c) $I_{\max} = 0.8 \times 10^{14}$ W m^{-2}, (d) $I_{\max} = 0.75 \times 10^{14}$ W m^{-2} and (e) $I_{\max} = 0.7 \times 10^{14}$ W m^{-2}.

The temporal intensity profile and linear frequency chirp shown by figure 2.10 is then applied to NO molecules, with polarisablity $\alpha = 1.9 \times 10^{-40}$ C m^2 V^{-1}, mass, $m = 30$ a.m.u. and an initial temperature of 2 K (FWHM 55.3 ms^{-1}). This distribution will be similar to that shown in figure 2.8 however with a slightly wider FWHM. The resultant distribution is shown in figure 2.12 when applied to an ensemble of 20000 NO molecules, with a maximum intensity in the $1.7 - 1.9 \times 10^{14}$ W m^{-2} range. As expected, the number and velocity spread of particles which are decelerated decreases with decreasing intensity. Approximately 320 particles (1.6 %) with a velocity spread of 9 ms^{-1} are decelerated (0.15 K) for $I_{\max} = 1.75 \times 10^{14}$ W m^{-2}. This is the threshold intensity for successful deceleration of molecules. This is lower but of the same order of magnitude as achieved with benzene ($I_{\max} = 0.75 \times 10^{14}$ W m^{-2}). The ratio of these threshold intensities is comparable to the ratio of α/m for nitric oxide versus benzene, as one would expect since the potential well is proportional to both the intensity and α/m. The larger threshold intensity required in this case when compared to the ideal Gaussian pulse is consistent since there is the same frequency excursion over a shorter duration, i.e. a faster deceleration. A greater deceleration reduces the effective well depth, and therefore the required laser intensity is higher.

For $I_{\max} = 1.9 \times 10^{14}$ W m^{-2} approximately 650 (3.2 %) molecules have been decelerated, the FWHM of the velocity spread was ≈ 15 ms^{-1} representing a temperature of ≈ 0.41 K. For $I_{\max} = 1.8 \times 10^{14}$ W m^{-2}, where approximately 270 (1.3 %) molecules were decelerated, the FWHM of the velocity spread was ≈ 11 ms^{-1} representing a temperature of ≈ 0.22 K. For $I_{\max} = 1.7 \times 10^{14}$ W m^{-2}, there were essentially no decelerated molecules which have been decelerated, (the inset indicates just 12 molecules at small negative velocities, or < 0.1 % of the initial distribution).

As with benzene, small changes in intensity result in large changes in the velocity spread of the decelerated particles. A 9 % decrease in intensity from $I_{\max} = 1.9 - 1.75 \times 10^{14}$ W m^{-2} results in a decrease in energy spread (K) of 60 %. This relationship is comparable to benzene.

We cannot compare to the confinement efficiency κ shown in figure 2.6, since this contained physical parameters relating only to benzene. Similar modelling for NO predicts $\kappa \approx 0.8$ %, which compares well to the 1.3 % of NO molecules that were decelerated in the numerical simulations for $I_{\max} = 1.8 \times 10^{14}$ W m^{-2}. For comparison, for $I_{\max} = 1.9 \times 10^{14}$ W m^{-2}, we would predict that $\kappa \approx 1.6$ % of NO molecules would be trapped, which is the right order of magnitude as the 3.2 % which were decelerated in the simulation. It would be expected that the decelerated number of particles could be greater than the predicted proportion which are trapped

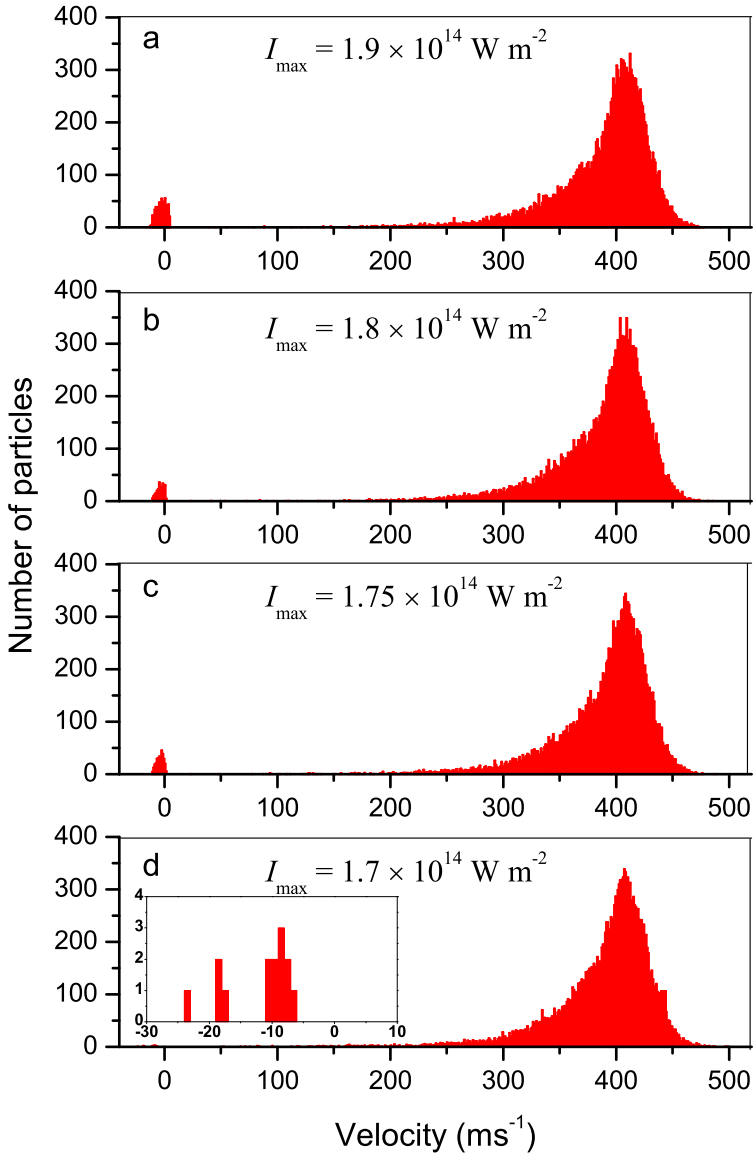

Figure 2.12: The resultant distribution of velocities when the decelerating optical lattice described in figure 2.10 is applied to an ensemble of 20000 NO molecules with a temperature of 2 K (FWHM 55.3 ms^{-1}) for various maximum intensities for each beam. (a) $I_{max} = 1.9 \times 10^{14}$ W m^{-2}, (b) $I_{max} = 1.8 \times 10^{14}$ W m^{-2}, (c) $I_{max} = 1.75 \times 10^{14}$ W m^{-2}, (d) $I_{max} = 1.7 \times 10^{14}$ W m^{-2}.

by the optical lattice, since some particles can be significantly perturbed without being trapped.

2.7 Conclusions

The variety of idealised simulations that have been modelled gives us some greater insight into requirements of our laser system, such as minimum laser intensity and

the temporal profile of the pulses. A fast rise time (or fall), whilst convenient for timing of a continuously varying chirp can cause an unwanted 'kick' to the particles, resulting in a less than ideal deceleration.

If working close to threshold intensity, precise timing of the beginning of the chirp relative to the beginning of the pulse will also clearly be important. If, for example a linear chirp is allowed to start too soon, before the optical potential is sufficient to trap a proportion of the particles, then by the time the intensity has reached its maximum level, the velocity of the optical lattice will already be too different from the initial velocity of the particles. Ideally we would create a voltage waveform which had a flat region before the linear ramp, which would ensure overlap with the beginning of the pulse. This would manifest in a region of constant or zero lattice velocity at the beginning and end of the chirp and pulse. Otherwise precise and systematic adjustment of the phase of the chirp may be necessary to optimise the experiment.

Chapter 3

Microchip laser

3.1 Introduction

Optical Stark deceleration requires intense optical fields whose frequency and intensity can be well controlled. Of particular importance to chirped acceleration and deceleration is to have the frequency difference between the fields rapidly chirped over 1 GHz while maintaining a flat top temporal profile over 100's of ns.

A well established technology [106, 108, 109] based on Nd:YAG or Nd:YVO_4 exists which, through pulsed amplification, can provide the high intensities ($10^{10} - 10^{11}$ W cm^{-2}) over pulse durations of 20-1000 ns with the narrow linewidth that we require at a wavelength of $\lambda = 1064$ nm. This wavelength also full-fills the other requirement that the fields are far off resonance, in order to prevent excitation or ionization of the species. We also require a system with a relatively small cavity (mm), such that the free spectral range (FSR) is $>>$ 1 GHz to ensure single mode operation while scanning across frequencies (chirping).

3.2 Rapidly chirped laser systems

There are basically three main methods for changing the frequency of a laser. These are a change in the gain profile or cavity length as a function of time [110]. We can select the frequency which is reflected back into the cavity using a wavelength specific mirror, for example, a diffraction grating [111]. The frequency of the laser can also be changed by modulating the phase of the output as a function of time [112]. Examples of these techniques can be found below. Of course, combinations of these techniques can also be employed to combine the speed and range of different methods.

3.2.1 Phase modulation of laser output

Conceptually speaking, the most straightforward technique to frequency chirp a laser is to modulate the phase. For example, this can be performed with a fibre-based phase modulator and self-injection-locked diode laser as described by Troger et al. [112]. This was further developed using an electro-optic (e.o.) waveguide based element by Rogers et al. [113]. In the latter, light at $\lambda = 780$ nm is passed through a fibre based phase modulator and a fibre delay line before being used to frequency lock a free running diode laser. Some of the output of this laser is passed through the fibre modulator/delay line again and re-injected into the diode laser. Large changes in phase can be accumulated through multiple passes through the fibre based modulator, and the output power of the laser maintained by the free running laser diode. Chirp excursions of ≈ 2 GHz at rates ≈ 40 GHz $/\mu$s are demonstrated. One of the biggest challenges with this technique is the precise timing of the phase modulation that is required due to the accumulation of any error during every cycle.

3.2.2 Cavity length change

The use of an intra-cavity e.o. crystal to modulate the optical cavity length in an extended cavity diode laser has been described many times [110, 114, 115, 116]. The advantage of an e.o. crystal within the cavity of a laser to change the cavity length rather than to modulate the phase of the laser output is that voltage requirements are much less. The use of an e.o. device to modulate the phase and amplitude is described by Bakos et al. [117] who describes chirps at 780 nm and chirp modulations of 50-150 MHz over nanosecond durations [118].

Electro-optic modulation of an optically pumped $NdYVO_4$ microchip-type laser is described at modulation frequencies of 1-100 GHz over periods of 17 ps to 1000 ps by Li et al. [119]. Here a voltage is applied to a $LiNbO_3$ crystal which causes a change in the refractive index, and consequently a change in the resonant frequency of the cavity. Linear voltage ramps are investigated and also sinusoidal modulation at various frequencies. The tunability, $f_V \equiv \Delta f/\Delta V$, where Δf is the frequency excursion and ΔV is the total voltage change, was found to be a function of frequency. The tunability increased considerably when the voltage applied to the e.o. crystal was modulated with an amplitude of 40 V at frequencies around the FSR of the cavity compared to modulation frequencies far from the FSR. For example, at modulations of 50-60 GHz, the tunability $f_V = 28 - 45$ MHz/V representing chirp rates of $(1.1 - 2.2) \times 10^5$ GHz/μs. The tunability decreased to $f_V = 16$ MHz/V at modulation frequencies far from the FSR. For a modulation at 1 GHz for example,

this represented a chirp rate of 1.3×10^3 GHz/μs. The use of e.o. tuning will be discussed further in section 3.3 for our laser system.

The use of current modulation to chirp a diode laser was used by Wright et al. [120] to investigate ultra cold collisions with atoms at a range of internuclear separations and its use in photo-association of cold atoms was discussed by Luc-Koenig et al [121].

3.2.3 Frequency selective feedback

The use of a diffraction grating for frequency selective feedback is normally achieved in the Littrow configuration [111, 122, 123, 124], where the first order diffracted light is coupled back into the laser diode, and the zeroth order used as the output beam. Since the angle of diffraction is wavelength dependent, there are various techniques used to compensate for changes in the output angle of the beam [111]. Another commonly used technique is the Littman technique, which uses a rotating mirror to tune the cavity length and the grating feedback wavelength simultaneously [125].

Repasky et al. [126] describe an external cavity diode laser which can be mechanically tuned by up to 20 nm by rotation of an external feedback grating and then rapidly tuned through the application of a voltage on an e.o. crystal. Chirps of 800 MHz over durations of between 3 and 337 μs at a wavelength of 793 nm are demonstrated. This has applications in optical coherent transient (OCT) processing and computer memory. Frequency chirping for OCT requires a linear chirp, on the μs time scale. This is so that there is sufficient time, at a particular frequency, for the material to interact and react to [127, 128].

Frequency tuning of a AlGaAs/GaAs diode laser with an external cavity is described by Kazharsky et al. [129]. Here excursions of more than 200 GHz, and a chirp rate of 11.1×10^4 GHz s^{-1} at 850 nm was achieved. Here piezo-actutators are used to change the length of the external cavity. A cavity grating was used to separate out the correct cavity mode. The pumping current was simultaneously modulated to achieve continuous tuning greater than the external cavity eigenmode interval alone.

3.2.4 Combination of these methods

Current modulation of diode lasers

Rapid frequency modulation of external cavity diode lasers, where changing the current has the effect of changing the operating temperature and therefore the stable operating frequency of the diode, has been implemented to produce chirp excursions

of 1 GHz and chirp rates of 15 GHz/μs [130]. For higher frequencies, above 10 MHz, modulation of the refractive index by modification of the carrier density [131] is the dominant frequency modulation mechanism.

Modulation of the pump power of a microchip solid state laser can cause a change in the frequency of the laser output [132]. Changing the current to the pump diode causes a change in the heating of the gain medium, which can cause a change in refractive index and physical cavity length. Both these effects cause a change in the optical path length of the cavity, and therefore a change in the resonant frequency of the cavity, and therefore the output frequency of the laser.

Pump power modulation has generally been considered too slow for applications such as frequency locking a laser, due to the finite time it takes for the gain medium to thermalize after a change in the heating due to a change in current. It also has the un-desireable effect of causing a simultaneous modulation in the amplitude of the output. Zayhowski et al. [132] has investigated the frequency response of this method of frequency chirping and found that for sufficiently small cavities, this method of frequency chirping of microchip lasers (in this case Nd:YAG) was suitable for many applications which require a relative fast frequency chirp. Modulation frequencies from 1 Hz to 10 kHz were tested with frequency excursion of between 0.6 and 150 MHz for an applied pump power modulation of 8 mW.

As discussed, mechanical manipulation of gratings can be used to tune over large ranges, i.e. many nm, developed for atomic-spectroscopy applications, however they are necessarily slow. Faster tuning can be obtained through piezo-actuators however the range is much reduced and still not fast enough. The use of e.o. crystals gives the ability to rapidly tune with a high degree of reproducibility, not obtainable with mechanical means. The maximum frequency excursion is however limited to the free spectral range of the cavity, which can be increased by making the cavity as short as possible. Ménager et al. [133] describes a design whereby the e.o. crystal is cut into the shape of a prism. When light hits the prism at an angle, it is refracted onto a grating which transmits a particular wavelength, depending on the incident angle. When a voltage is applied to the e.o. crystal, the optical path length changes, causing the laser cavity frequency to chirp, however the incident angle of the light to the grating also changes and thus the grating feedback frequency changes simultaneously. Frequency excursions of over 10 GHz were achieved over ms to μs chirp durations, which is greater than several free spectral ranges of their cavity. A total chirping range of 14 nm using a chirped grating fabricated with holographic techniques is described by Duval et al. With this configuration, chirping is achieved by translation of the grating [134].

3.2.5 Summary

In this work we chose to used a neodymium based microchip laser, which is attractive for two main reasons. Firstly they are compact, with cavity lengths typically of a few mm or less. This ensures a large theoretical cavity free spectral range, which we require in order for our laser to remain single mode over a chirp of over 1 GHz. Secondly since our pulsed amplification consists of Nd:YAG flash-lamp pumped rods, then good overlap between the seed wavelength and the gain curve of the amplification system should be assured. Frequency chirping using an intra-cavity e.o. crystal offers the required frequency excursion in excess of 1 GHz, with realistic voltages (< 100 V) producing the required chirp rates of 10's GHz / μs. Although such laser systems have been demonstrated [119], they are not commercially available.

3.3 Microchip laser

To provide a chirped master laser for amplification to the energies required for optical Stark deceleration, we have built a short cavity (4.5 mm), single frequency Nd:YVO_4 laser, operating at a wavelength of 1064 nm as shown in figure 3.1 and detailed in the schematic in figure 3.2. The cavity consists of a 500 μm thick Nd:YVO_4 microchip (CASIX) with a high reflecting reflective coating for 1064 nm and an anti-reflection coating for the pump wavelength of 808 nm on one side of the microchip and an anti-reflection coating for 1064 nm and 808 nm on the other. The microchip was thermally attached to a copper block, the temperature of which was controlled to within 10 mK by a Peltier cooler. A 94 % reflective plane mirror forms the output coupler of the cavity. An intra-cavity e.o. ($LiTaO_3$) crystal (n=2.2) of length 3 mm is placed in the centre of the cavity. When a voltage is applied, the change in optical path length allows a rapid change in the frequency.

Figure 3.3 is an image of the output of the microchip beam $\approx$ 50 cm from the cavity. The $1/e^2$ radius at this point was 0.64 ± 0.02 mm. The profile is relatively poor, however this will be decoupled from the beams used to make the optical lattice due to the various stages of injection locking and fibre coupling which will be described in due course. However, the effect of this profile may be poor mode matching during injection locking.

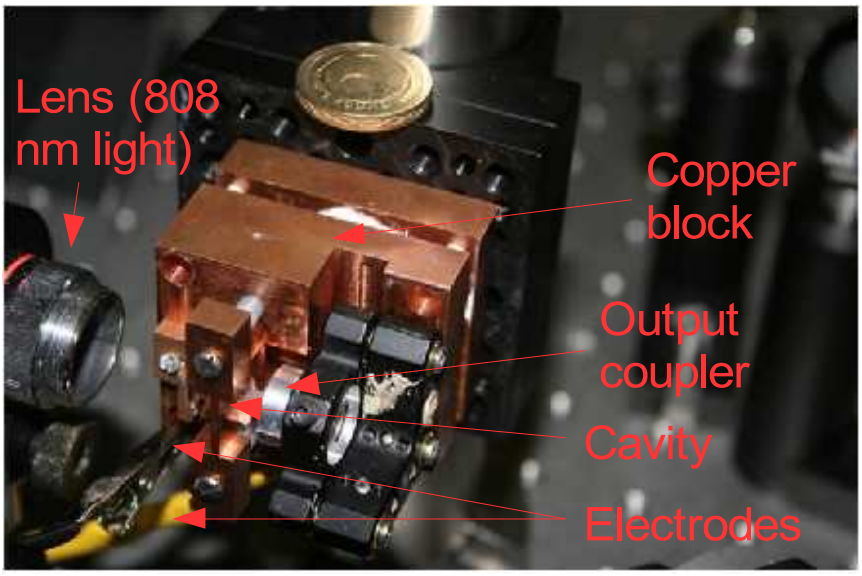

Figure 3.1: Photo of the microchip system. The cavity is located in the region between the electrodes which provide the voltage for chirping. To the left is the lens which focuses 808 nm light onto the Nd:YVO_4 chip and on the right the output coupler can be seen on the mirror mount. The copper block, to which the cavity is thermally attached, is controlled by a Peltier cooler to within 10 mK.

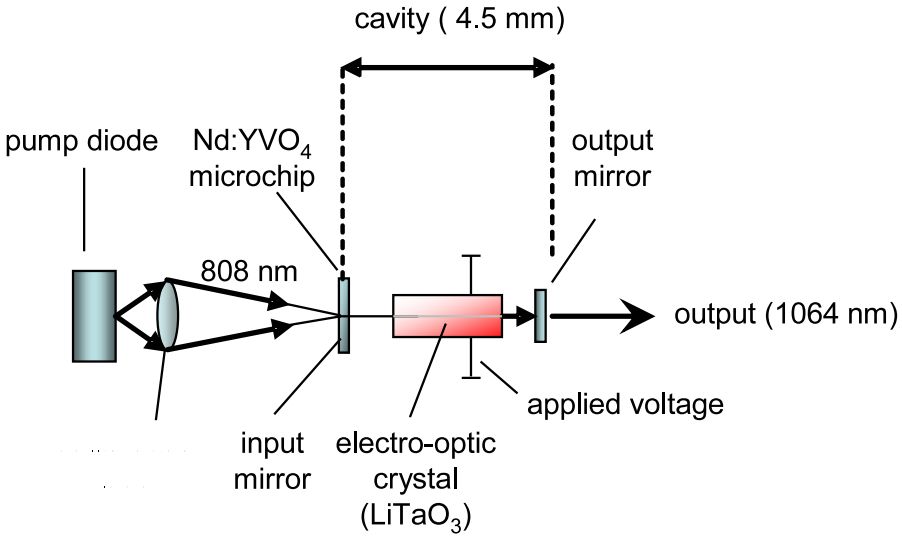

Figure 3.2: A schematic of the microchip type laser. The cavity is formed by a 500 μm thick Nd:YVO_4 microchip with a high reflecting coating for 1064 nm and anti-reflection coating for the pump wavelength of 808 nm. A 94 % reflective output mirror forms the output coupler of the cavity. An intra-cavity e.o. crystal ($LiTaO_3$), with a refractive index, n_1=2.2 of length 3 mm is used to rapidly change the optical path length.

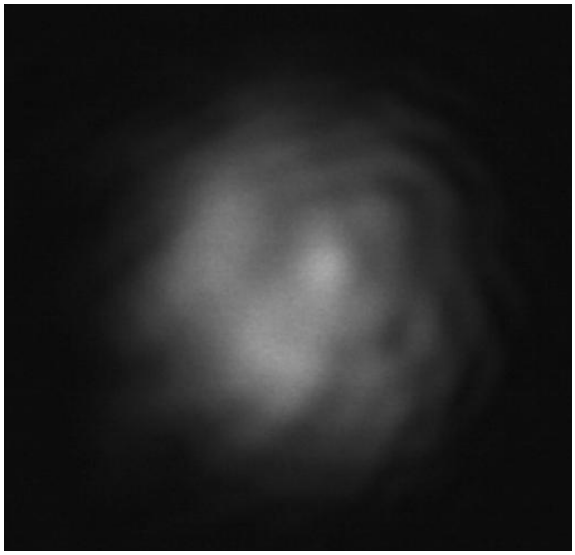

Figure 3.3: The beam profile of the Nd:YVO_4 beam. $1/e^2$ radius of 0.64 ± 0.02 mm.

3.3.1 Cavity optimisation

The lens used to focus the pump onto the Nd:YVO_4 crystal is a 3 x objective lens, mounted onto a translation stage. The output coupler is mounted on a mirror mount, allowing the angle to be adjusted. By adjusting these in turn, the output can be optimized. The temperature of the pump can also be adjusted to optimize the pump with the absorption profile of the Nd:YVO_4 gain medium.

The system was also further optimized further by tuning the temperature of both the pump diode to optimize the wavelength and also of the microchip, to maximize the position and overlap with the Nd:YVO_4 gain curve [135], [136].

Figure 3.4 is a plot of the output power at 1064 nm as a function of applied pump power at 808 nm. The linear fit indicates a slope efficiency (gradient of output power versus pump power) of 7.5 %. Efficiencies of approximately 30 % have been achieved in similar Nd:YVO_4 microchip-type lasers, [137, 138, 139]. Normally, it is the short length of the Nd:YVO_4 crystal, required to ensure a large FSR, and therefore single mode operation, that limits the efficiency of these systems due to excessive thermal lensing and therefore satuaration effects. Our low efficiency may indicate poor alignment of the cavity or poor overlap of the pump wavelength with the Nd:YVO_4 crystal absorption band which has a laser gain bandwidth of $\approx$ 250 GHZ [140]. However, it is believed to be due to greater losses in the cavity than estimated.

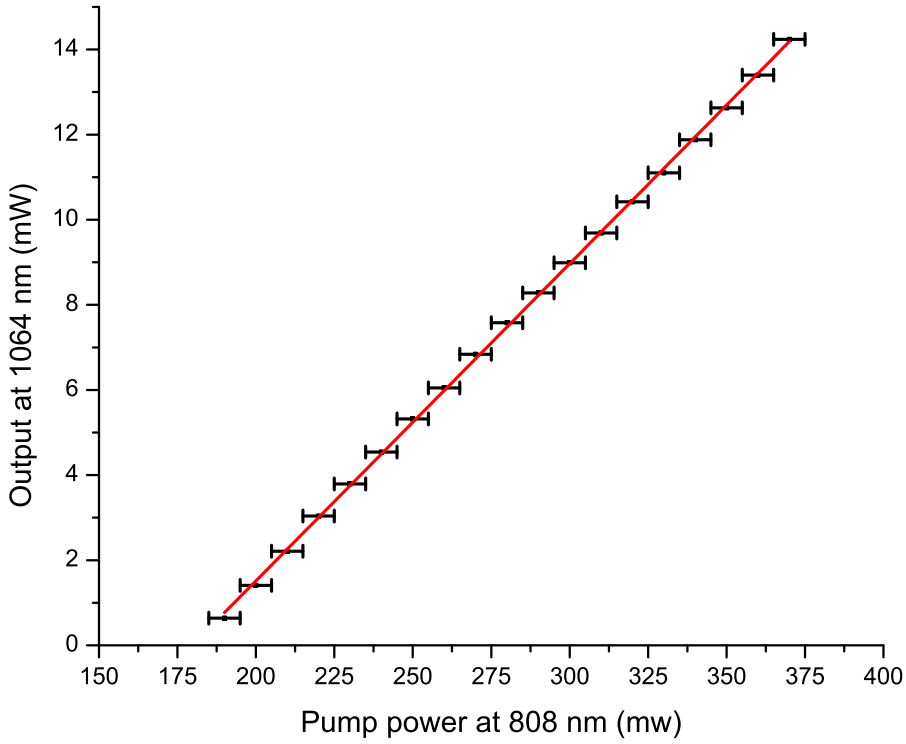

Figure 3.4: The output power at 1064 nm as a function of 808 nm pump power. The line of best fit has a gradient of 0.0745 ± 0.0003 with an intercept of -13.4 ± 0.09. This implies a slope efficiency of ≈ 7.5 % (gradient of pump power, versus output power) and a threshold pump power of 180 mW. At a typical operating power of 7 mW, with a pump power of 270 mW, the optical conversion efficiency is 2.6 %.

3.3.2 Electro-optic tuning

The frequency change δf of the laser with an applied voltage δV to the electrodes of the intracavity $LiTaO_3$ crystal is given by [126],

$$\delta f = \frac{\eta n_1^2 r_{33} f_{\text{opt}}}{2d} \frac{n_1 l_1}{n_1 l_1 + n_2 l_2 + n_3 l_3} \delta V \tag{3.1}$$

where l_1, l_2 and l_3 are the respective lengths of the $LiTaO_3$ crystal, the Nd:YVO_4 crystal and the air gap. The overlap efficiency between the electric field and laser cavity mode is given by η and d is the thickness of the $LiTaO_3$ crystal, which is 1 mm for our system. The refractive index of the extraordinary wave in the $LiTaO_3$ crystal is $n_1 = 2.2$ and the refractive index of the π polarisation component Nd:YVO_4 is $n_2 = 2.2$. The refractive index of air is n_3. The e.o. coefficient of the $LiTaO_3$ crystal along the cavity axis is r_{33} (30.4 pm/V at 1064 nm) and f_{opt} is the frequency of the optical wave. Using equation (3.1), and the known values for our microchip laser and assuming $\eta = 1$ we predict a tunability of 15.7 MHz/V.

As we require a continuous tuning range of approximately 1 GHz for molecular deceleration and operation on a single longitudinal and transverse mode, the shortest possible cavity length maximizes the mode hop free tuning range. Having a larger e.o. crystal which forms the majority of the cavity length ($n_1 l_1 >> n_2 l_2 + n_3 l_3$) increases the frequency change per voltage which is applied to the crystal (tunability, f_{V}). The maximum value tends toward, $\delta f / \delta V = (\eta n_1^2 r_{33} f_{\text{opt}})/(2d)$, which for our laser is 20.7 MHz/V. Increasing the length of the crystal also reduces the mode hop free tuning range for a particular pump intensity. The only way to increase this tunability further would therefore be to decrease the thickness of the e.o. crystal.

We determine the tunability of the laser by measuring the change in laser frequency as a function of applied voltage for three different temperatures. Whilst the temperature controller is connected primarily to control the $NdYVO_4$ microchip, the $LiTaO_3$ crystal is in thermal contact and is therefore affected by the operating temperature.

The tunability f_{V} was measured for three temperatures in the range at which the cavity is normally operated. A Fabry-Perot interferometer (FPI) was used to measure the relative frequency of the single mode peak of the operating master, and its movement in response to the applied voltage recorded, and analyzed to deduce the frequency change. This was achieved by measuring the horizontal shift of the single mode peak relative to the known FSR of the interferometer. Figure 3.5 indicates some variation in the tunablity, from $f_{\text{V}} = (14.0 \pm 0.2)$ MHz / V at 18 °C, $f_{\text{V}} = (15.2 \pm 0.2)$ MHz / V at 17.5 °C and $f_{\text{V}} = (14.7 \pm 0.1)$ MHz / V at

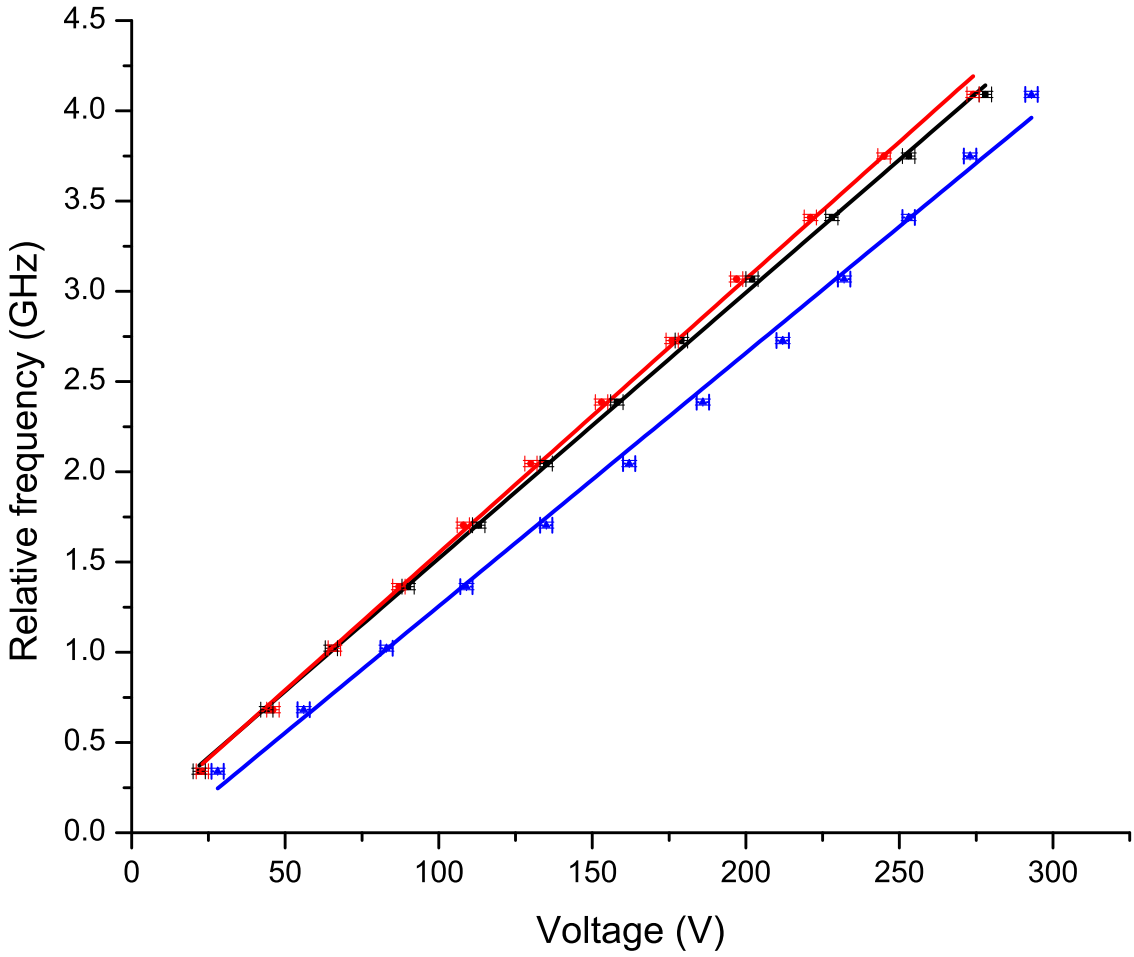

Figure 3.5: The relative frequency as measured by position of single mode peak on a Fabry-Perot interferometer for three temperatures. Linear fits are applied to the data indicating $f_V = (14.0 \pm 0.2)$ MHz/V at 18.0 °C, $f_V = (15.2 \pm 0.2)$ MHz/V at 17.5 °C and $f_V = (14.7 \pm 0.2)$ MHz/V at 16.95 °C.

16.95 °C. This variation may be due to temperature induced stress on the clamped e.o. crystal [139].

We find that our cavity with a 3 mm e.o. crystal remains single mode up to ≈ 1100 V which corresponds to a d.c. frequency shift of 16.8 GHz and a tunability, f_V of 15.4 MHz/V. This is within the theoretical mode hop free $F.S.R. = c/2l$ for our cavity of ≈ 22 GHz. We have not measured the linewidth of our laser since it is below the resolution of our Fabry-Perot interferometer (7 MHz).

3.4 Pump power and temperature tuning

The cavity can also be tuned by varying its temperature and also the power (current) of the pump diode which has the same effect. In general, heating may cause the op-

tical path length of the cavity to change, due to a temperature dependent refractive index, a thermal, stress-induced change in refractive index and a physical change in the length of the crystal caused by thermal expansion. It has been shown that the stress induced refractive index change is much less than the other two effects [132]. It is also the case that for large current modulation frequencies, above 10 MHz, a fourth frequency modulation effect can become significant, due to modulation of the carrier density [131].

The tuning rate with temperature, $\delta f_c/\delta T$, where f_c is the resonant frequency of the cavity and T is the cavity temperature, can therefore be approximated by [139],

$$\frac{\delta f_c}{\delta T} = -f_c \frac{(\delta n/\delta T)\, l_{rod} + \alpha_1 n l_{rod}}{n l_{rod} + l_{air}}, \tag{3.2}$$

where $\alpha = (1/l_{rod}(\delta l_{rod}/\delta T)$ is the thermal expansion coefficient of the laser rod, l_{rod} is the physical length of the laser medium, n is the refractive index of the laser rod, and l_{air} is the length of the air spacing between the laser medium and the coupling mirror. We assume the change in cavity length is small compared to the total cavity length. Hansen et al. investigates the frequency tuning and stability of a Nd:YVO_4 laser in a dual coupled cavity [139], and studies the theoretical configuration ratio of air gap to Nd:YVO_4 rod length for continuous tuning without mode hops.

They find for Nd:YVO_4, that $n = 2.165$, $\alpha = 4.43 \times 10^{-6}$ K^{-1}, and $\delta n/\delta T$ = 3.0 $\times 10^{-6}$ K^{-1} [139]. Lithium tantalate has an α of 1.6×10^{-5} [141], $\delta n/\delta T$ = -3.27 $\times$ 10^{-5} K^{-1} and $n = 2.2$ [142]. These values predict a relative tuning rate of 6.9 GHz/ °C for our system.

Figure 3.6 indicates a tuning rate of (9.28 ± 0.08) GHz/ °C which is comparable to the predicted rate and confirms that an increase in temperature causes an increase in frequency. As the temperature changes, the centre of the gain curve, f_0, will also change. For Nd:YVO_4, $\delta f_0/\delta T = -0.53\times 10^9$ Hz K^{-1}, therefore, if the temperature change is large enough, the laser may jump onto a neighbouring longitudinal mode, if the gain of that mode is larger. Even without a mode jump, the operating frequency of the laser will always be pulled away from the natural cavity frequency and towards the middle of the gain curve of the gain medium. This process is known as mode pulling [106, 143].

In a similar way, by considering the absorption of the pump power, and the resultant heating, the tuning rate due to the heating could be predicted [132]. For a continuous modulation of the pump power, the tuning rate is a function of the modulation frequency because of the finite time to heat the medium.

Figure 3.7 indicates a tuning rate of (64.6 ± 0.6) MHz/mW of pump power. This

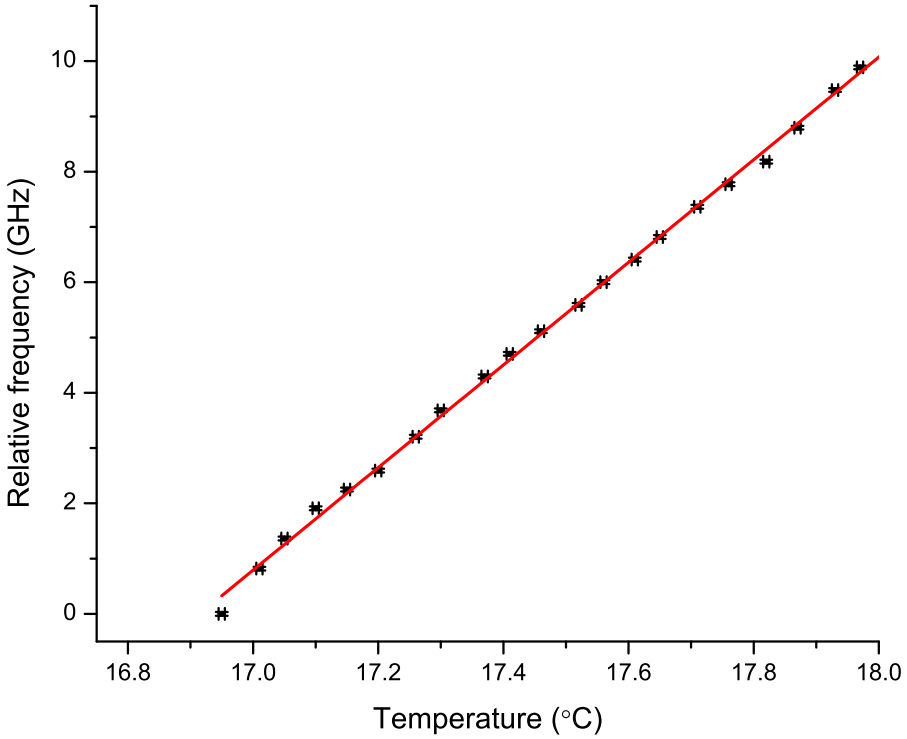

Figure 3.6: The relative frequency change as a function of cavity temperature as measured by a Fabry-Perot interferometer. A linear fit indicates a tuning rate of (9.28 ± 0.08) GHz / °C.

data was taken by manually changing the power output of the pump laser and then measuring the relative frequency of the single mode peak on the FPI. The tuning rate as function of pump power is also dependent on the modulation frequency [132]. In this paper the tuning rate is 18.75 MHz/mW for 1 Hz power modulation dropping to 0.070 MHz/mW for 10 kHz power modulation. This dropped at higher frequencies because the heating mechanism is too slow and cannot keep up with the modulation of the pump power. Given that our modulation frequency needs to be > 1 MHz, this method appears to be too slow for our purposes without prohibitively large pump power modulations.

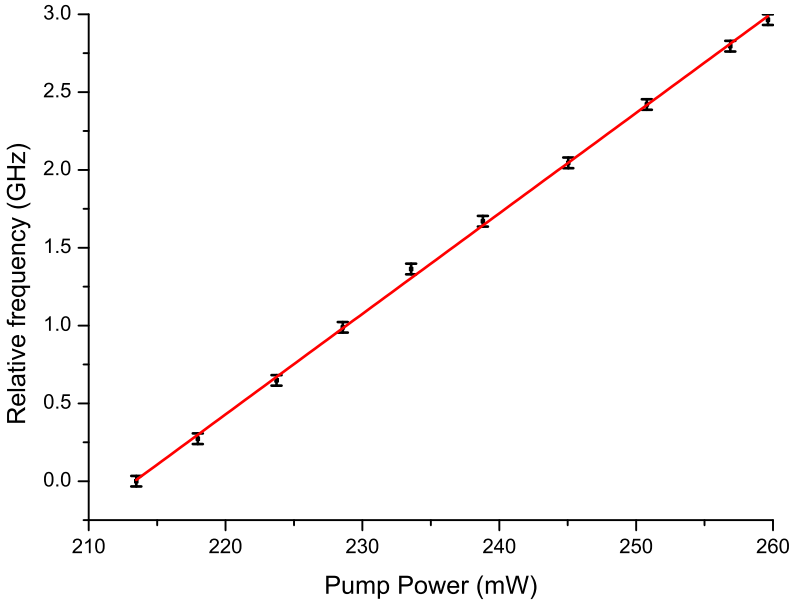

Figure 3.7: The relative frequency change as a function of pump power. A linear fit indicates a tuning rate of (64.6 ± 0.6) MHz / mW of pump power, for the case of d.c power modulation.

3.5 Rapid chirping

We then tested the ability of the laser to be rapidly chirped over 1 GHz frequencies, on a time scale of 100's of ns. Initially we used a frequency generator to produce a sinusoidally changing voltage with a frequency of 1.82 MHz. This gives the maximum voltage change over 275 ns, which is of the right time scale required for our chirp. The maximum output of the frequency generator was 20 V which given a tunability of ≈ 15 MHz/V, would only give us a chirp of 300 MHz. We used a tank circuit to amplify this to ≈ 70 V. This circuit is shown in figure 3.8.

As with previous measurements of our laser system, in order to investigate the rapid chirp of the laser we used a Fabry-Perot interferometer (FPI). When the sinusoidally changing voltage was applied, the single peak indicating single mode operation of the laser widened to the characteristic 'bat-wing' shape as observed by Troger et al. [112]. This shape is due to the FPI scanning at a constant rate and the voltage/frequency at the top and bottom of a sine wave changing at a slower rate; the FPI therefore spends more time on average at the extremes of the frequency excursion. The result of applying a 1 GHz sinusoidal voltage with a peak to peak amplitude of 67.5 V is shown in figure 3.9. This indicates a tunability of ≈ 14.8 ± 0.4 MHz/V, in reasonable agreement with the d.c tunability already calculated for 16.95 °C.

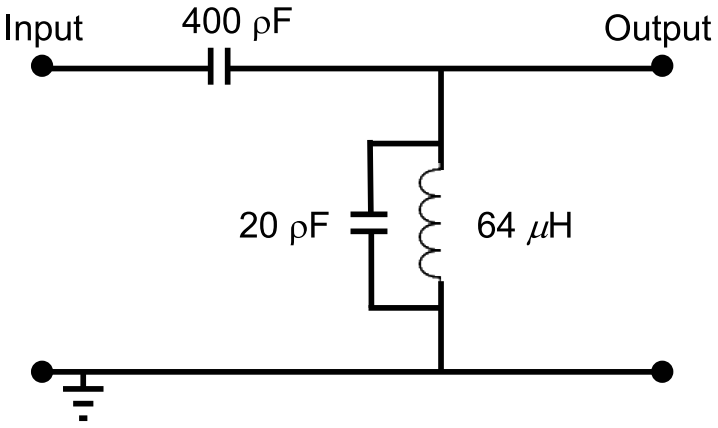

Figure 3.8: A tank circuit, designed to amplify a sinusoidal voltage from 20 to 70 V at ≈ 1.82 MHz.

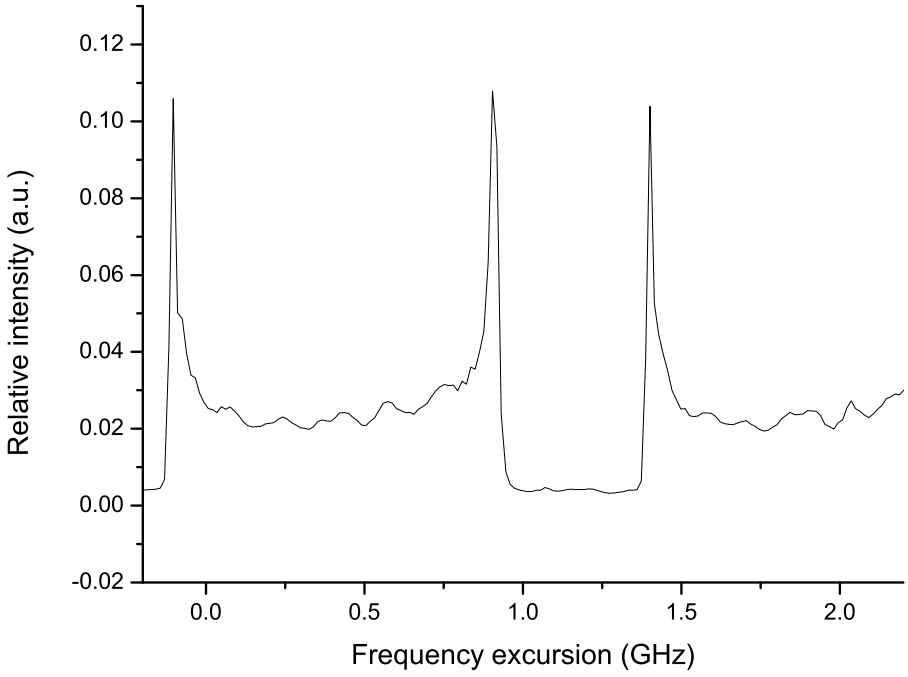

Figure 3.9: The signal from the Fabry-Perot interferometer when the laser is rapidly chirped with a sinusoidal voltage with modulation frequency 1.82 MHz, and peak to peak amplitude of 67.5 V. The x-axis has been calibrated by measurement of the distance between two identical points on adjacent 'bat-wings' and comparing it to the known free-spectral range which was 1.5 GHz. The frequency excursion is measured to be $\approx 1.00 \pm 0.03$ GHz indicating a tunability f_{V} of 14.3 ± 0.4 MHz/V.

3.6 Intensity oscillations

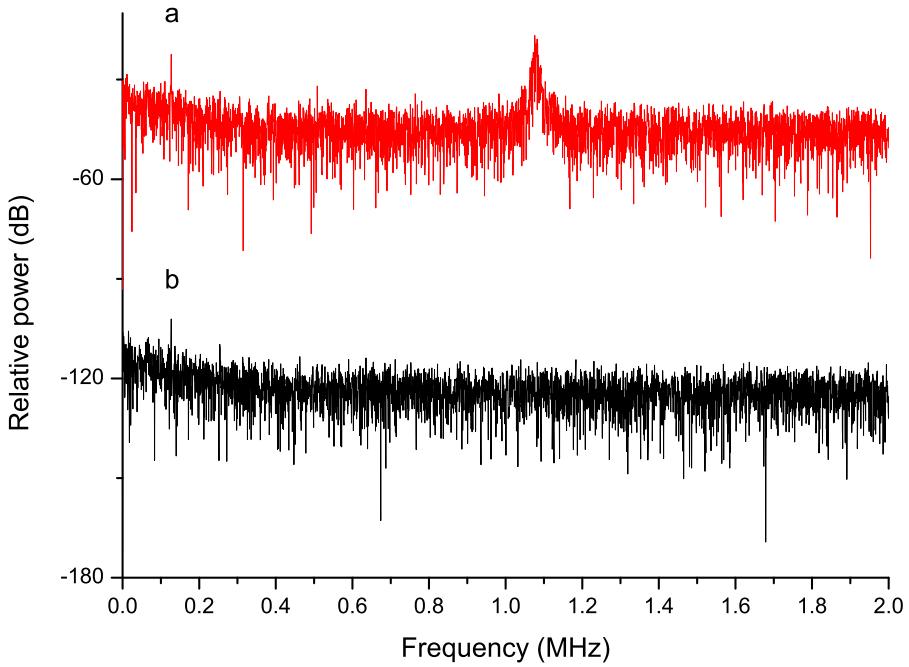

Figure 3.10: Instantaneous Fourier transform of the signal on a photodiode. (a) The unchirped relaxation oscillation peak centred at ≈ 1.1 MHz. (b) Background signal taken by blocking the photodiode.

We have now demonstrated that our microchip laser can be rapidly chirped by up to 1 GHz, as required for deceleration of molecules in a molecular jet. We also require the microchip laser to have a constant intensity as a function of time, particularly over the 100's of nanosecond range which will be amplified later, in order to produce the required intensities for optical Stark deceleration.

After measuring the output power of our microchip laser, it was immediately clear that there were small (< 5 %) oscillations at around 1.1 MHz, as shown by figure 3.10 which is the instantaneous Fourier transform of the signal on a photodiode. After investigation of similar systems it was found that a common source of intensity noise is from relaxation oscillations. These can arise, in the case of a system like ours, from the large difference between the lifetime of the cavity (ps) and laser transition (ms). This can be better understood mathematically through analysis of two, coupled, single-mode, single-atomic-level rate equations.

The cavity photon number $n(t)$ in the oscillating mode, which is proportional to the intensity $I(t)$, can be written as [106],

$$\frac{\mathrm{d}n(t)}{\mathrm{d}t} = KN(t)n(t) - \gamma_c n(t), \tag{3.3}$$

and for the population inversion $N(t)$,

$$\frac{\mathrm{d}N(t)}{\mathrm{d}t} = R_\mathrm{p} - \gamma_2 N(t) - KN(t)n(t), \tag{3.4}$$

where $\gamma_\mathrm{c}, \gamma_2$ are the cavity and atomic decay rates respectively, and R_p is the pump rate of the 808 nm diode and K is a measure of the off-resonance coupling efficiency between the two levels, which increase to a maximum where the resonant frequency of the cavity ω_i is equal to the atomic transition frequency ω_a. This is given by [106],

$$K(\omega_\mathrm{i}) = K_0 \times \frac{1}{1 + [2(\omega_\mathrm{i} - \omega_\mathrm{a})/\Delta\omega_\mathrm{a}]^2}, \tag{3.5}$$

where K_0 is the on-resonance coupling efficiency, given by $K_0 \equiv K(\omega_\mathrm{a}) \equiv 3^*\gamma_\mathrm{rad}/p$. γ_rad is the purely radiative decay rate, and the cavity mode number p is given by,

$$p \equiv \tfrac{4\pi^2 V_\mathrm{c}}{\lambda^3} \tfrac{\Delta\omega_\mathrm{a}}{\omega_\mathrm{a}}, \tag{3.6}$$

where V_c is the cavity volume and λ is the wavelength of the transition. The cavity mode number is the effective number of laser cavity modes which lie within the atomic transition linewidth $\Delta\omega_\mathrm{a}$.

There are no simple analytic solutions to these equations, but they can be solved numerically. Figure 3.11 shows an example of typical evolutions of $n(t)$ and $N(t)$ for $\gamma_\mathrm{c} \approx 10^5\ \gamma_2$, which is similar to our system, where the atomic decay rate is $\approx 1.1 \times 10^4\ \mathrm{s}^{-1}$, and the cavity lifetime based on a cavity of length $L = 4.5$ mm cavity, with a reflectivity a of 94%, is calculated from the cavity decay rate, $\gamma_\mathrm{c} = \frac{c(1-a)}{L} = 4 \times 10^9\ \mathrm{s}^{-1}$.

When the laser is initially switched on there is a build up in $N(t)$. As the population inversion $N(t)$ approaches the threshold population, N_th, the cavity population $n(t)$ begins to rise as the laser gain exceeds losses. The build up time for photons is typically much faster ($\tau_\mathrm{c} \approx 100$'s ps), than the build up of the excited population (100's μs) and may reach an observable photon output of 10^8 to 10^{10} in less than 10 ns [106]. As soon as the cavity photon number exceeds the steady state oscillation level n_ss, the cavity photons begins to induce stimulated decay of the excited population at a faster rate than it is being re-populated by the pump diode. The cavity population still rises rapidly due to stimulated emission until the population $N(t)$ falls to the threshold level N_th. This corresponds to the maximum cavity population number $n(t)$ which begins to fall rapidly until the n_ss cavity photon population is reached. At this point the re-population of the excited state exceeds the stimulated emission, and $N(t)$ begins to rise.

After a certain time, characterised by a relaxation oscillation decay rate $\gamma_{sp} \equiv r\gamma_2/2$, where r is the ratio of the pump rate to threshold pump power for lasing, an unperturbed cavity will reach a steady state value for the excited state population. This is equal to the threshold population, N_{th} and the steady state cavity photon number n_{ss}. It can be shown that the threshold population is given by,

$$N_{th} = \gamma_c/K \text{ and } n_{ss} = R_p/KN_{th} - \gamma_2/K = (r-1)\gamma_2/K, \tag{3.7}$$

where K is the coupling coefficient of the laser transition and R_p is the pump rate. In our system, the cavity was observed not to reach a steady state value. Due to the very large difference in time scales between our cavity lifetime and excited atomic state lifetime, i.e. $\tau_c/\tau_2 \approx 4 \times 10^5$, it is extremely difficult to model the relaxation oscillations using all the experimental parameters required such as the pumping rate. By making some approximations we can deduce some analytical relationships which give some insight into the behaviour or the laser system. The relaxation oscillation frequency (ω_{sp}) is given by the geometric mean of the atomic lifetime $\tau_2 \equiv 1/\gamma_2$ and the effective build up time of the cavity $(r-1)/\tau_c$ as [106],

$$\omega_{sp} = \sqrt{\frac{r-1}{\tau_c} \times \frac{1}{\tau_2}}. \tag{3.8}$$

This equation predicts a relaxation oscillation frequency of 750 kHz for $r = 1.5$ for our laser. This represents a period of ≈ 1.3 μs. This is the right order of magnitude as the observed relaxation frequency of 1.1 MHz.

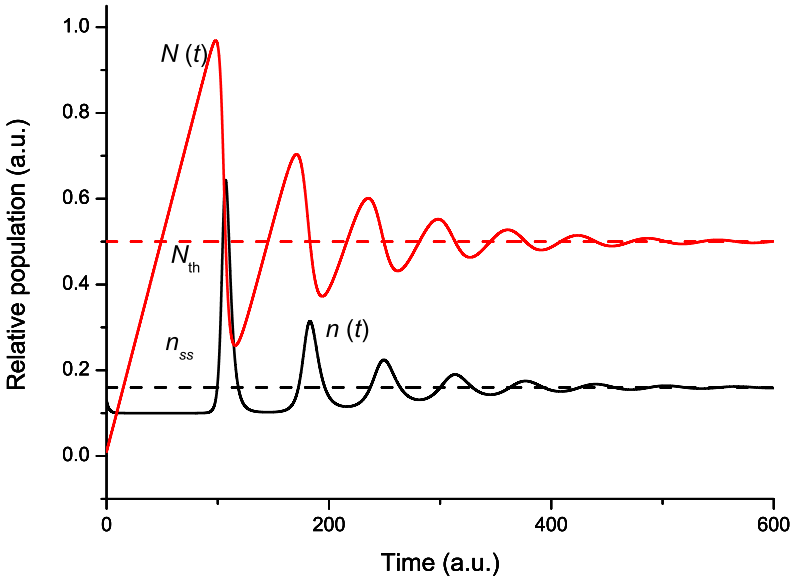

Figure 3.11: The dynamics of a diode pumped microchip-type laser after the pump is instantaneously switched on and the cavity photon population. $N(t)$ is the evolution of the excited state population, and $n(t)$ is the cavity photon number. The excited state builds up initially, past the threshold value N_{th}, at which point the cavity photon number $n(t)$ begins to build up exponentially and the gain exceeds cavity losses. The population inversion $N(t)$ reaches a maximum, at which point stimulated emission caused by the large cavity photon population exceeds the re-population from pumping and $N(t)$ rapidly decreases. The population $n(t)$ continues to rise rapidly due to stimulated emission, until $N(t)$ falls below the threshold population N_{th} at which point $n(t)$ falls rapidly. The two populations will continue to oscillate around the steady state values, N_{th} and n_{ss}.

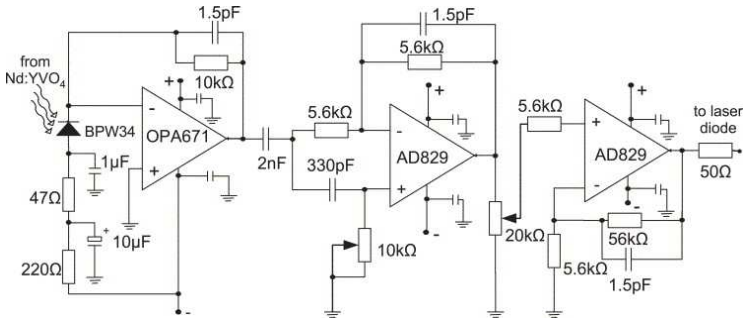

Figure 3.12: The tunable electronic feedback circuit for suppression of relaxation oscillations [144]. The + and - which connect to each amplifier in the circuit were connected to 9 V batteries, in order to avoid power line noise.

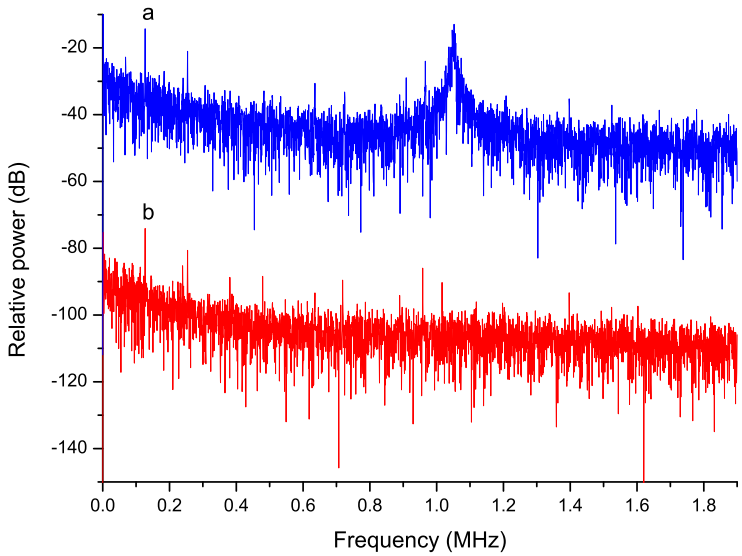

Figure 3.13: (a) A Fourier transform of the intensity output from the laser without feedback. We can observe a dominant intensity oscillation peak at 1.05 MHz. (b) Fourier transform of the output of the master laser with electronic feedback switched on. The oscillation peak has been suppressed by ≈ 30 dB, which is equivalent to 99.9 % suppression.

3.6.1 Suppression of relaxation oscillations

Initially, we tried to suppress these oscillations using electronic feedback to the current of the pump diode described in [144]. The circuit for this is shown in figure 3.12. A photodiode was used to monitor a portion of the output of the laser and an inverted signal was sent back to the RF input of the laser diode. In other words, an increased current was output to the laser diode if the intensity decreased and vice-versa. This was successful in suppressing an intensity modulation of up to 10 %. Figure 3.13 indicates a suppresion of the 1.1 MHz relaxation oscillation peak by 30 dB, equivalent to 99.9 % suppression.

3.7 Intensity oscillations during chirping

It was found that when we chirped the microchip laser, the intensity modulation increased dramatically. At 1.82 MHz frequency modulation for example, the amplitude modulation was ≈ 30 %. This is shown in figure 3.14a. Figure 3.14b show the frequency of the intensity oscillation as 1.82 MHz, equal to the modulation frequency of the chirp demonstrating the direct effect of our perturbation of the cavity. It was found that electronic feedback was not sufficent to suppress this larger intensity modulation.

As this method was insufficient to remove these oscillations, a different technique was required. Suppression of intensity oscillations in diode laser systems was reported by Wright et al. [130] which used a free running 'slave' diode, which was injection locked to a 'master' laser, and therefore we have developed a similar system for $\lambda = 1064$ nm light.

In this system, the frequency is determined by the master laser but the intensity is determined by the slave. To avoid inducing the relaxation oscillations in the slave, we also choose a free running semiconductor diode laser which had typical relaxation oscillation frequencies in the GHz regime [106]. These are much larger than those at MHz frequencies in the Nd:YVO_4 master laser. To get this scheme to work so that the slave locks to the master, they must be operating within a few GHz of each other [145]. The intensity oscillations of the slave have been shown to be several orders of magnitude less than the oscillations of the master using this scheme [130].

3.7.1 Injection locking to the slave laser

A detailed schematic of the injection locking section our laser system is shown in figure 3.15. The output of the microchip laser (master), which is operated in continuous wave (cw) mode and output intensity of ≈ 10 mW, is directed via mirrors 1-3 into a free running, semiconductor (slave) diode laser. Good spatial overlap can be achieved by overlapping the master and collimated output of the slave over a distance of several metres. Both the microchip laser (master) and slave are operating at approximately 1064 nm, however for injection locking, they must operate within a few GHz of each other [145]. A half wave plate (h.w.p.) 1 is used to rotate the polarisation of the master to horizontal polarisation such that it is transmitted through the polarising beam splitter into the slave. H.w.p. 2 and Faraday isolator 1, (E.O.T., CR1064, 30 dB extinction) are used such that in one direction the polarisation of light ends up rotated to the orthogonal linear polarisation (i.e. the h.w.p. adds to the rotation of the isolator) and in the other direction ends up unaffected

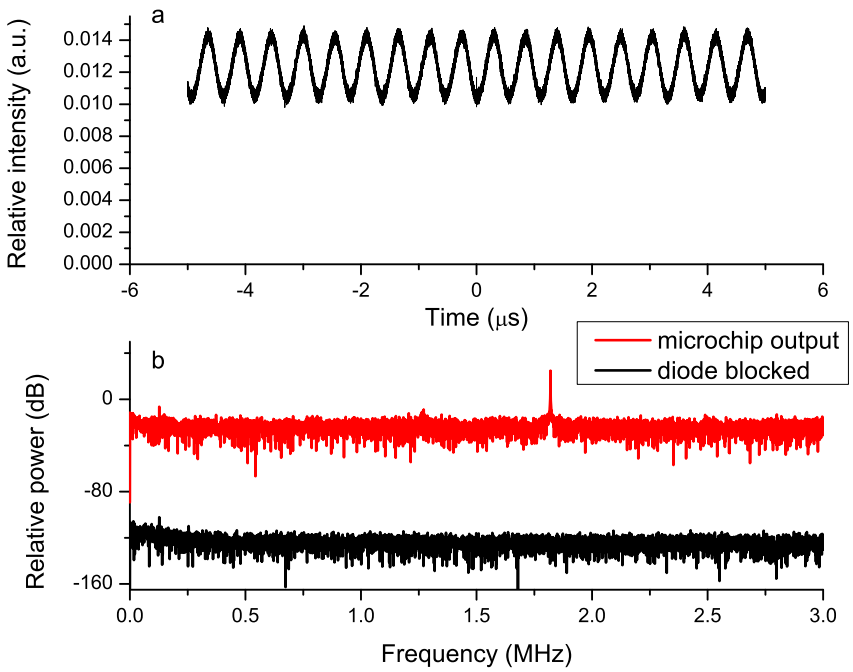

Figure 3.14: (a) The signal from the microchip laser when chirped with a modulation frequency of 1.82 MHz, with amplitude 67.5 V. There is a periodic modulation of 30 %. (b) The Fourier transform of (a) showing the relaxation oscillation peak at 1.82 MHz.

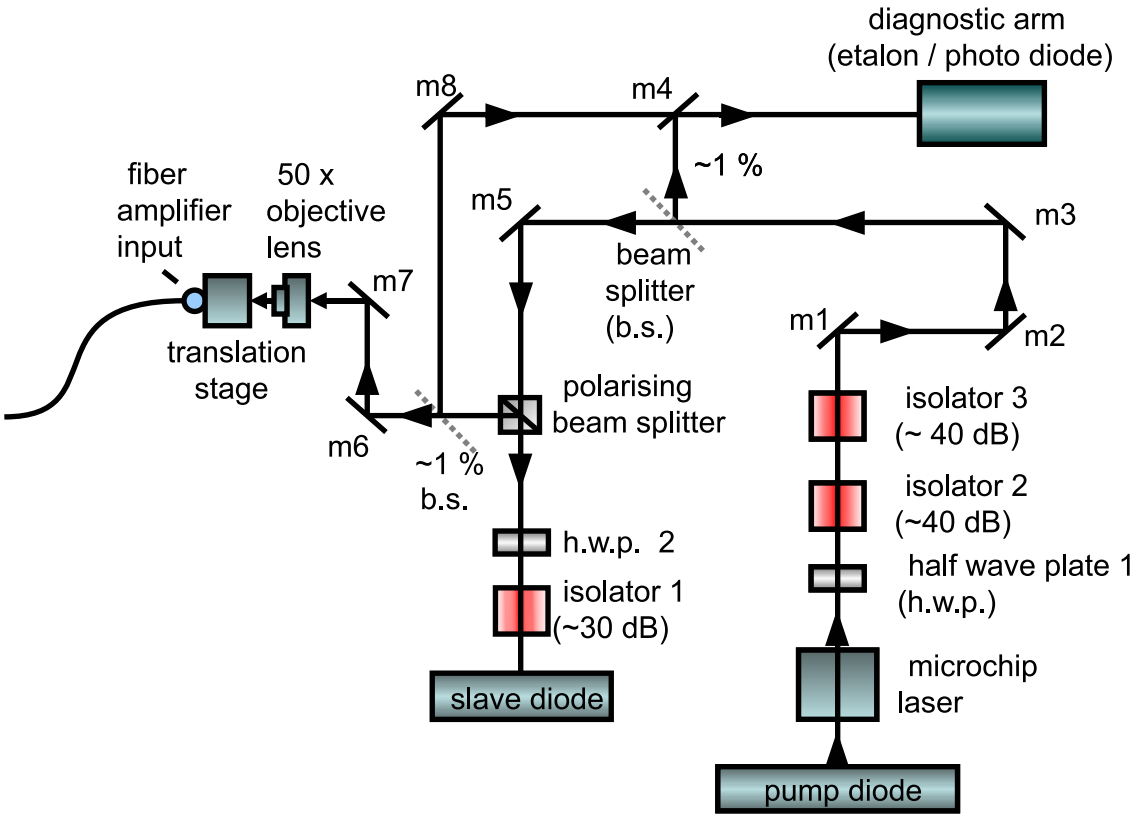

Figure 3.15: Detailed injection locking setup

(i.e the h.w.p. rotates in the opposite sense to the isolator). In this way the output of the slave is rotated to the vertical polarisation and is reflected by the polarising beam splitter. The slave output ($\approx$ 20 mW) is then directed onto mirror 6 and 7 which are used to couple the beam into the fibre amplifier. The input of the fibre amplifier is mounted on a translation stage, which can be moved relative to a 50 x objective lens to a resolution of a few μm. This is also mounted on the translation stage. Optical isolators 2 and 3 (OFR, IO-2.5-1064-VLP, 40 dB extinction) are required to provide further isolation of the master from the slave and ensure that light cannot travel back to the master from the slave, since the efficiency of the extinction of the polarising beam splitter was not 100 %. In total there is 110 dB of isolation. Approximately 1% of the output of the slave and the master are directed onto a Fabry-Perot interferometer (SA201) with a free spectral range of 1.5 GHz, a resolution of 7.5 MHz and a finesse of 200. This is used in order to provide information on the mode output and locking status.

Once the spatial overlap was achieved, the lasers were spectrally overlapped. Using a wave-meter (WavePro 7300) we tuned the wavelengths of the master laser and the slave laser to the same wavelength, limited by the 0.1 nm resolution of the wave-meter. This was done by adjusting the temperature of the Nd:YVO_4 microchip and the slave diode laser as well as fine tuning of the slave current. In order to re-optimise the spectral overlap of the master pump wavelength and the absorption of the microchip, the temperature and current of the master pump diode laser were re-adjusted.

The frequency of the free running slave still needed to be brought within a few GHz of the master's frequency [145] by systematically adjusting the slave and master current. If a stable, single mode locking position could not be found then the temperature of the slave and master could be adjusted. In order to know when locking was achieved, several techniques were employed at various times. For example, observing the output of the slave through the interferometer on an oscilloscope (Lecroy 5500) the position of the mode(s) of the slave could be measured. When the slave injection locked to the master, the mode jumped to the position of the master. When the master was then blocked and unblocked the mode position jumped back and forth. Another technique involved reducing the slave current close to threshold for lasing. When injection locking occurs, the output of the slave as viewed through a 'viewer' would immediately brighten and lase.

It will also be necessary to overlap the frequency of the master/slave system with the gain curve of the Nd:YAG pulsed amplification in order to maximise the output energies of the pulses. This will be described in chapter 5.

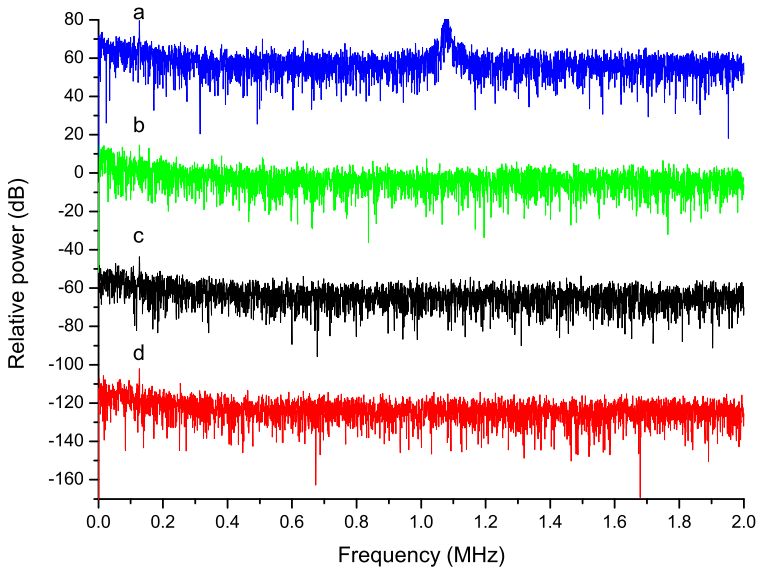

Figure 3.16: The signal on a photodiode of the slave and master when unchirped. (a) Master, (b) unlocked slave, (c) locked slave, (d) background noise, when the diode is blocked.

3.8 Results with injection locking

3.8.1 Unchirped master laser

We first tested the injection locking technique for the unchirped case. Figure 3.16a shows the relaxation oscillations of the master laser when unchirped, indicating a relaxation oscillation frequency of (1.08 ± 0.01) MHz. Figure 3.16b is the unlocked slave for reference. The 3 GHz limit of the oscilloscope was insufficient to observe the oscillations which we would expect to exist in a semiconductor laser and therefore scans at the 3 GHz range are not shown here. Figure 3.16c is the locked slave showing that the peak at 1.08 MHz has been removed completely, to the limit of the noise of the measurement. Other features, such as the small peak at ≈ 120 kHz are found to be due to electronic noise in the detection system, rather than a real signal from the light. This was verified by blocking the detector from the light, as shown by figure 3.16d where the peak is still evident.

3.8.2 Chirped operation with injection locking

We then tested the injection locking techniques for various chirp modulation frequencies with an amplitude of 67.5 V, since, as will be discussed in due course, the magnitude of the intensity oscillations can change dramatically depending on the modulation frequency. The results with injection locking are shown in figures 3.17, 3.18, 3.19, 3.20.

Figure 3.17a represents the Fourier transform of the master signal, for data taken up to 3 MHz. There are three peaks, a 32 dB peak at 900 kHz, 33 dB peak at 1.8 MHz, and 17 dB peak at 2.7 kHz. The induced intensity oscillations therefore follow the driving voltage modulation frequency, and its 2nd and 3rd harmonic. It is possible that these higher order harmonics are due to the non-linearity of the photodiode and not a real intensity oscillation [146, 147]. Figure 3.17b represents the Fourier transform of the injection locked slave. The three peaks have been removed to below the level of the noise, representing an improvement of at least 1600 times for the 900 kHz, at least 2000 times for the 1.8 MHz peak and at least 50 times for the 2.7 kHz peak. The background noise with detector blocked is shown in Figure 3.17c. This was used to ensure that only intensity oscillations were being analysed.

Figure 3.18a represents the Fourier transform of the master taken with a voltage modulation frequency of 1.82 MHz. There is a large, 42 dB peak at 1.82 MHz. Figure 3.18b represents the Fourier transform of the injection locked slave. The 1.82 MHz peak has been reduced by 25 dB, representing a reduction of at least 320 times. The background is shown in figure 3.18c.

Figure 3.19a represents the Fourier transform of the master signal taken with a voltage modulation frequency of 2.3 MHz. There is a 41 dB peak at 2.3 MHz and a 10 dB peak at 1.24 MHz, and a 5 dB peak at 1.06 MHz. Figure 3.19b represents the Fourier transform of the injection locked slave. The 2.3 MHz peak has reduced by by 18 dB, however the other two peaks appear to have joined to form a peak at 1.15 MHz, 100-400 times larger. The competition between these two peaks in the master is why in the slave, the oscillations have increased in magnitude. In fact, the single new peak seen in the slave is a combination of the other two observed in the slave. This is also the frequency of the unchirped, natural relaxation oscillation frequency. Once again, the background is shown in Figure 3.19c.

Figure 3.20a represents the Fourier transform of the master signal taken with a voltage modulation frequency of 1.0 MHz. There are many peaks, the major ones being a 50 dB peak at 1.0 MHz, 41 dB at 2.0 MHz, 30 dB at 3.0 MHz, 17 dB at 4.0 MHz, 14 dB at 5.7 MHz, and 15 dB at 7.7 MHz. Figure 3.20b represents the

Fourier transform of the injection locked slave. The 1 MHz peak has been reduced by 27 dB, or 500 times, and the other peaks have been reduced into the noise, representing improvements of between 25 and 4000 times for the 5.7 MHz peak and 2 MHz peak respectively. Once again the background is shown in Figure 3.20c.

In all cases the intensity of the slave diode was approximately ten times that of the master laser. Therefore the reduction in the absolute intensity oscillations in the slave are actually even higher.

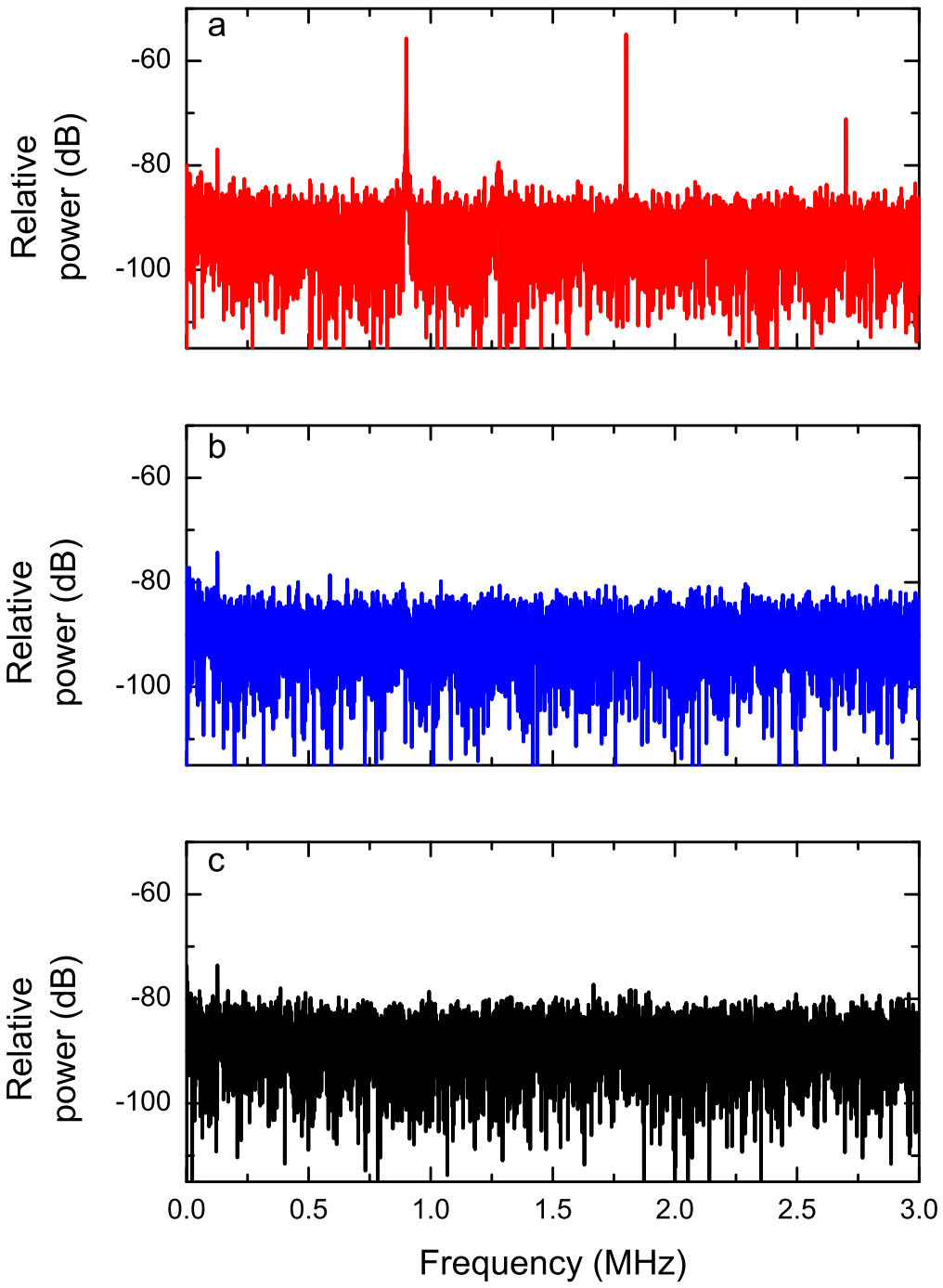

Figure 3.17: (a) The upper trace represents the Fourier transform of the master signal, for data taken up to 3 MHz, taken with a voltage modulation frequency of 900 kHz. There are three peaks, a 32 dB peak at 900 kHz, 33 dB peak at 1.8 MHz, and 17 dB peak at 2.7 MHz. (b) The Fourier transform of the injection locked slave. The three peaks have been removed to below the level of the noise, representing an improvement of at least 1600 times for the 900 kHz, at least 2000 times for the 1.8 MHz peak and at least 50 times for the 2.7 kHz peak. (c) Background noise, when the diode is blocked.

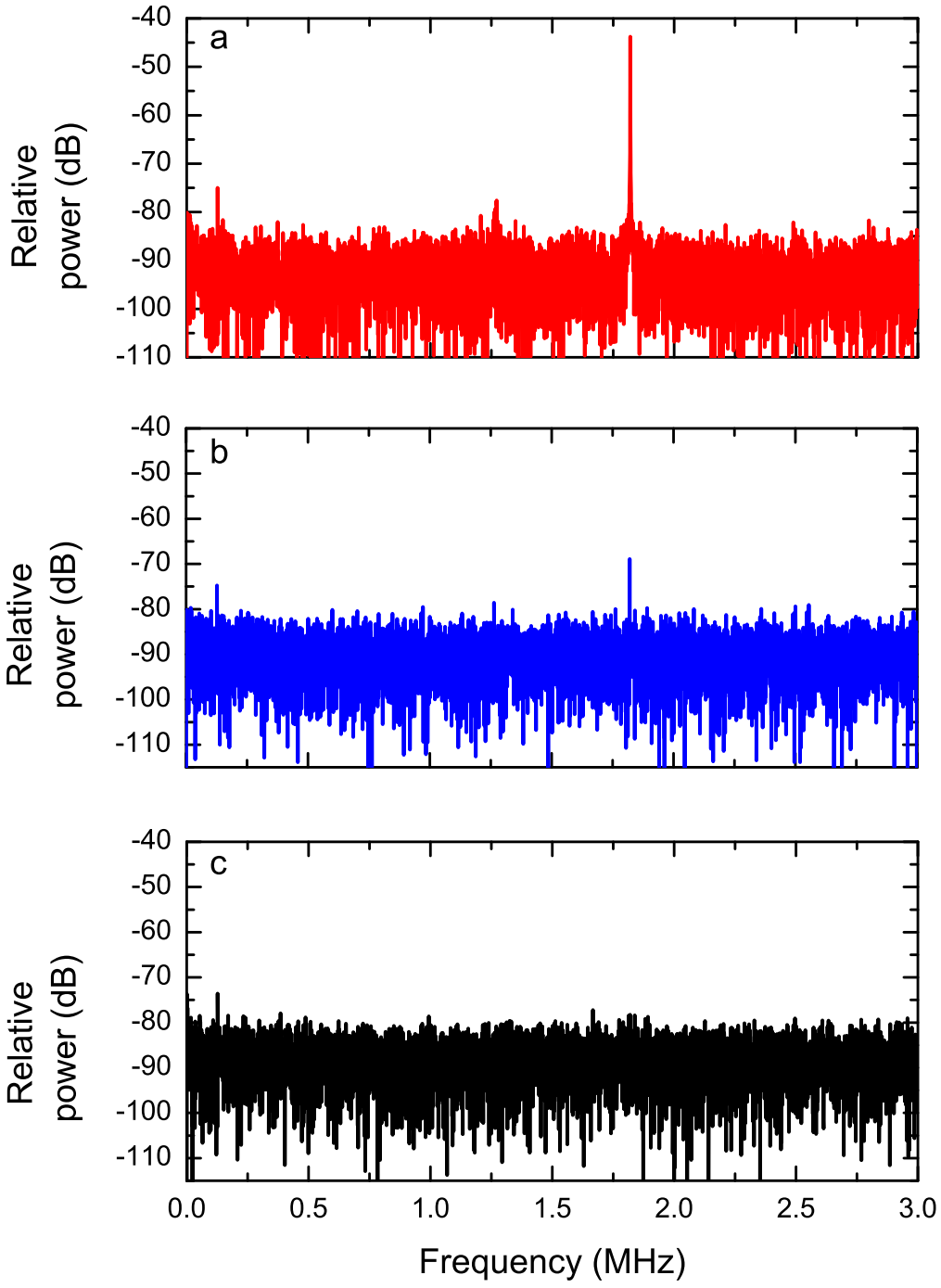

Figure 3.18: (a) The Fourier transform of the master taken with a voltage modulation frequency of 1.82 MHz for data taken up to 3 MHz. There is a large, 42 dB peak at 1.82 MHz. (b) The Fourier transform of the slave output, where this peak has reduced by 25 dB, representing a reduction of at least 320 times. (c) Background noise with detector blocked.

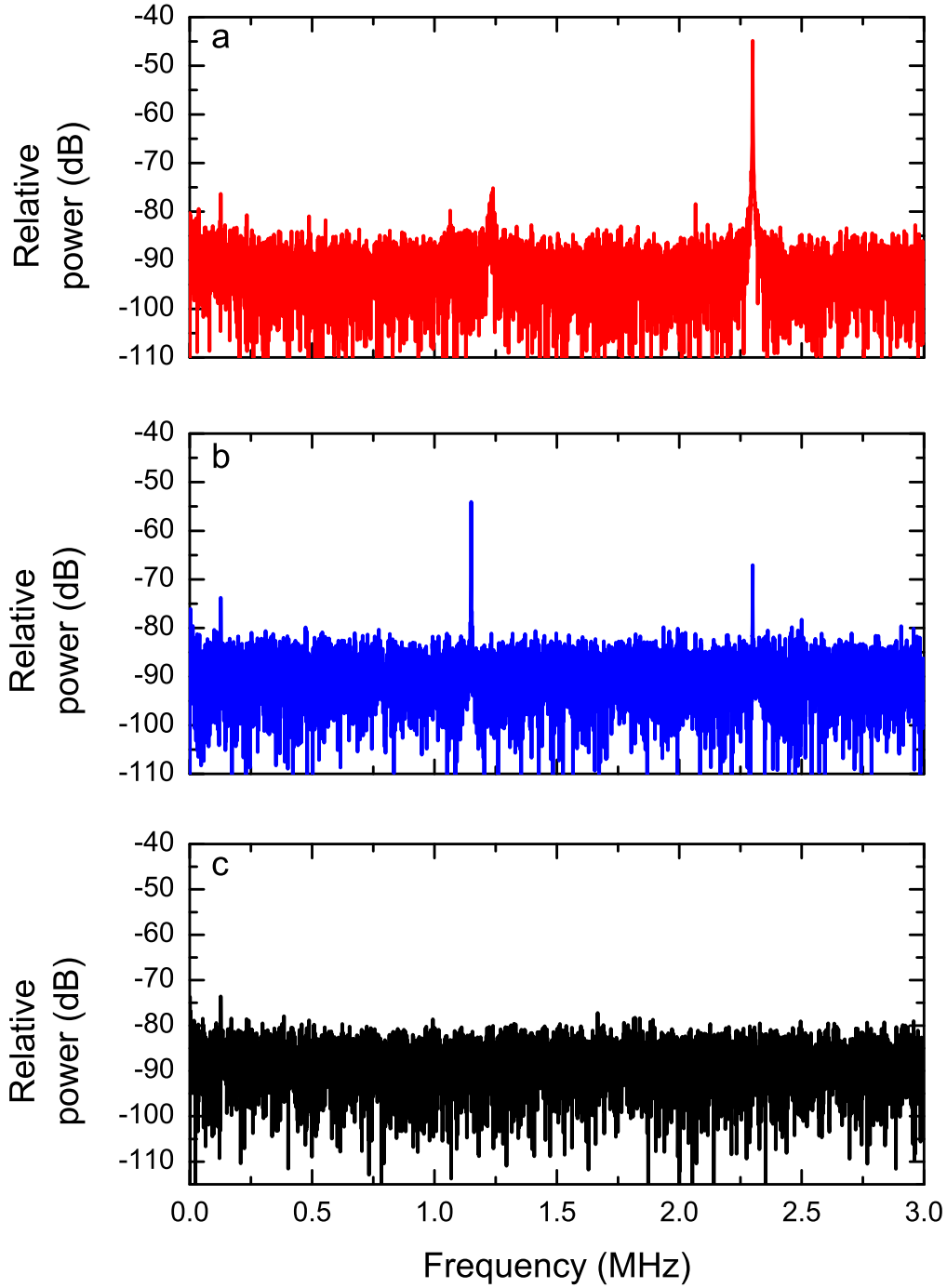

Figure 3.19: (a) The Fourier transform of the master signal taken with a voltage modulation frequency of 2.3 MHz for data taken up to 3 MHz. There is a 41 dB peak at 2.3 MHz and a 10 dB peak at 1.24 MHz, and a 5 dB peak at 1.06 MHz. (b) The Fourier transform of the slave output, where the 2.3 MHz peak has reduced by 18 dB, however the other two peaks appears to have joined to form a peak at 1.15 MHz, 100-400 times larger. (c) Background noise with detector blocked.

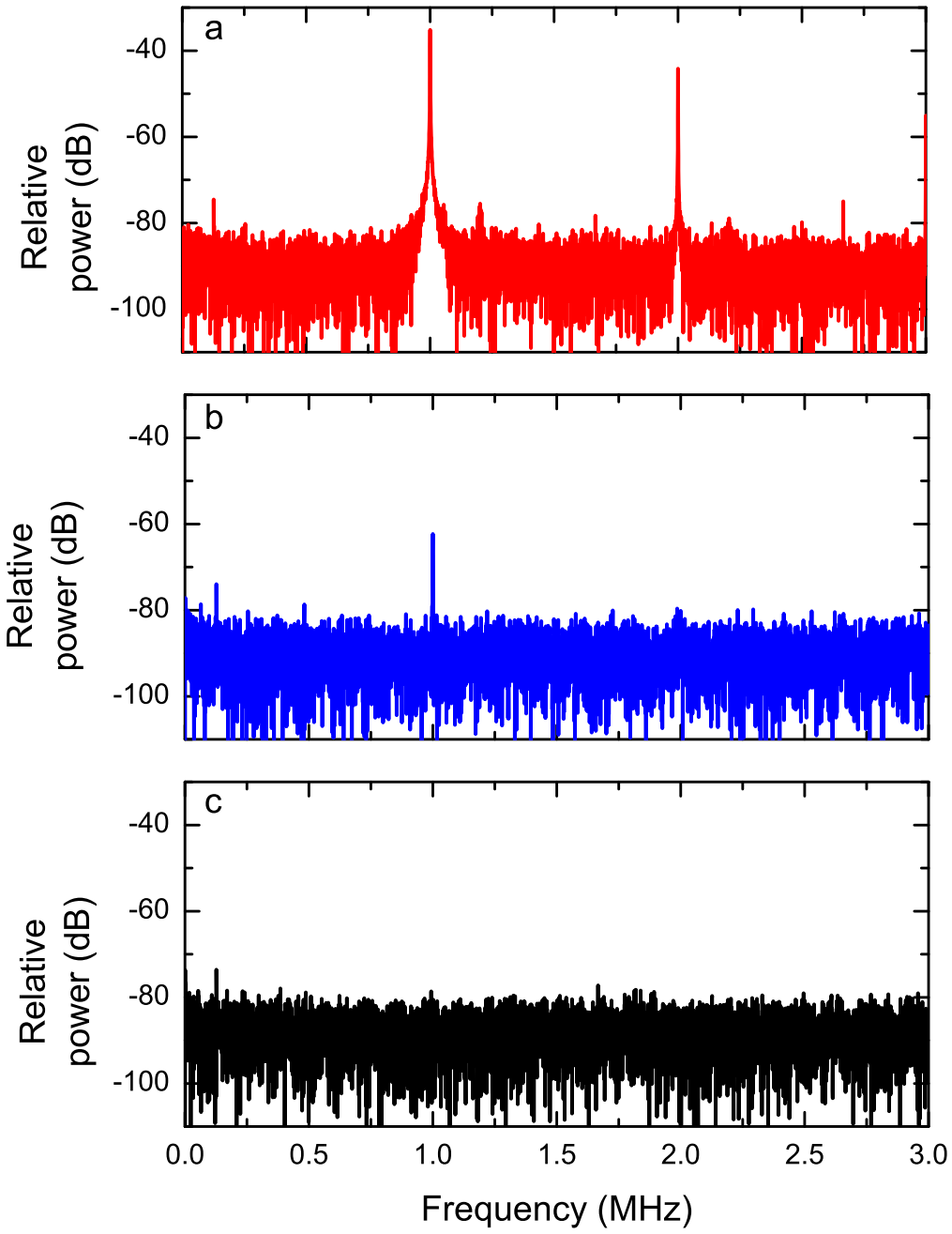

Figure 3.20: (a) The Fourier transform of the master signal taken with a voltage modulation frequency of 1.0 MHz. There are many peaks, the major ones being a 50 dB peak at 1.0 MHz, 41 dB at 2.0 MHz, 30 dB at 3.0 MHz. (b) The Fourier transform of the slave output, where the 1 MHz peak has been reduced by 27 dB, or 500 times, and the other peaks have been reduced into the noise, representing improvements of between 25 and 4000 times for the 5.7 MHz peak and 2 MHz peak respectively. (c) Background noise with detector blocked.

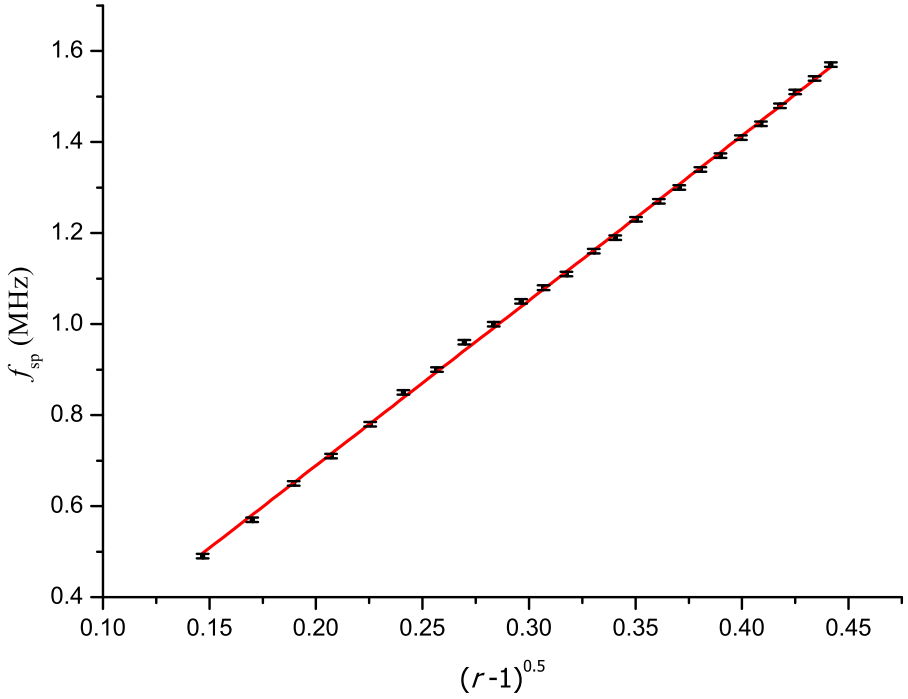

Figure 3.21: The variation of relaxation oscillation frequency f_{sp} with pump power of 808 nm light. r is the ratio of pump power/threshold pump power. A linear fit gives $f_{\mathrm{sp}} = \omega_{sp}/2\pi = 3.52 \pm 0.02\ (r-1)^{0.5}$ MHz.

3.8.3 Variation of relaxation oscillation frequency with pump power

Equation (3.8) indicates that there is also a dependence of the relaxation oscillation frequency on the pump power, where $\omega_{\mathrm{sp}} \propto \sqrt{(r-1)}$. Figure 3.21 shows the relaxation oscillation frequency $\omega_{\mathrm{sp}}/2\pi$ as a function of $\sqrt{(r-1)}$. The linear fit indicates that ω_{sp} is $2\pi \times 3.52 \pm 0.02$ MHz, which according to equation (3.8) implies that $\tau_{\mathrm{c}}\tau_2 = 2.04 \times 10^{-15}$ s^2. This technique can therefore be used to give a lifetime of one of the quantities if the other is already known. In this case, the lifetime of the transition τ_2 is known to be $\approx 90 \pm 8$ μs however the lifetime of the cavity was estimated to be 250 ps, based on a 4.5 mm cavity with a reflectivity of 94 %. In fact this data implies that $t_{\mathrm{c}} = (23 \pm 2)$ ps, an order of magnitude lower. This suggests that there are greater losses than included in the calculation.

3.9 Chirped intensity oscillations

To better understand the intensity oscillations when chirping the laser, it was decided to extend Siegman's treatment of relaxation oscillations [106] to take into account changes in the laser modulation frequency (chirping) which induce large os-

cillations. For our deceleration experiments, the laser will be chirped continuously, i.e. a modulated voltage will be applied to the crystal, rather than a d.c. voltage. When chirping at 1.82 MHz, we are perturbing the cavity on comparable time scales ≈ 1 μs, to the natural relaxation oscillation frequency, and much less than the time to reach steady state. This further complicates finding solutions to the rate equations. In Siegman's treatment of this system [106], a frequency response due to pump power modulation is deduced. This shows a resonance when the modulation frequency approaches the un-modulated oscillation frequency, $\omega_{\mathrm{m}} \approx \omega_{\mathrm{sp}}$. A similar relationship can be deduced for chirping the laser. Changing the frequency of the laser is equivalent to modulating the coupling coefficient K since it depends on the detuning of the cavity frequency ω_{i} from the atomic frequency ω_{a}, as shown in equation (3.5).

We extend the approach developed by Siegman [106] which assumes the modulation of the cavity population from its steady state value n_{ss} and the threshold excited state population N_{th} are small, to include a modulation in the coupling coefficient $K(t)$. This is equivalent to changing the resonant frequency of the cavity (chirping) since coupling coefficient K depends on the detuning of the cavity frequency ω_{i} from the atomic frequency ω_{a}, as shown in equation (3.5). Therefore assuming all are modulated at the angular frequency ω_{m},

$$\begin{aligned} n(t) &= n_{\mathrm{ss}} + Re\left[\tilde{n_1} e^{\mathrm{i}\omega_{\mathrm{m}} t}\right] && \text{where,} \quad |\tilde{n_1}| << n_{\mathrm{ss}} \\ N(t) &= N_{\mathrm{th}} + Re\left[\tilde{N_1} e^{\mathrm{i}\omega_{\mathrm{m}} t}\right] && \text{where,} \quad \left|\tilde{N_1}\right| << N_{\mathrm{th}} \\ K(t) &= K_0 + Re\left[\tilde{K_{\mathrm{p1}}} e^{\mathrm{i}\omega_{\mathrm{m}} t}\right] && \text{where,} \quad \left|\tilde{K_{p1}}\right| << K_0, \end{aligned} \tag{3.9}$$

where $\tilde{n_1}$, $\tilde{N_1}$ are the amplitudes of the modulations of the cavity photon population and population inversion respectively and $\tilde{K_{\mathrm{p1}}}$ is the amplitude of the modulation of the coupling coefficient $K(t)$ from its un-modulated value K_0. By substituting these into equations (3.3) and (3.4) and by dropping small product terms such as $\tilde{n_1}\tilde{N_1}$, and using the steady state values in (3.7), we can obtain a linear transfer function of the frequency response of the modulation of K and the amplitude of the modulation of the cavity population, $\tilde{n_1}$, to give

$$\frac{\tilde{n_1}}{\tilde{K_{\mathrm{p1}}}} = \frac{n_0 N_0 - (r-1)\gamma_2 n_0 N_0}{\omega_{\mathrm{sp}}^2 - \omega_{\mathrm{m}}^2 + \mathrm{i} r \gamma_2 \omega_{\mathrm{m}}}. \tag{3.10}$$

The calculated frequency response and phase relationship is shown by figure 3.22. As with pump power modulation, when the modulation frequency, ω_{m} approaches the

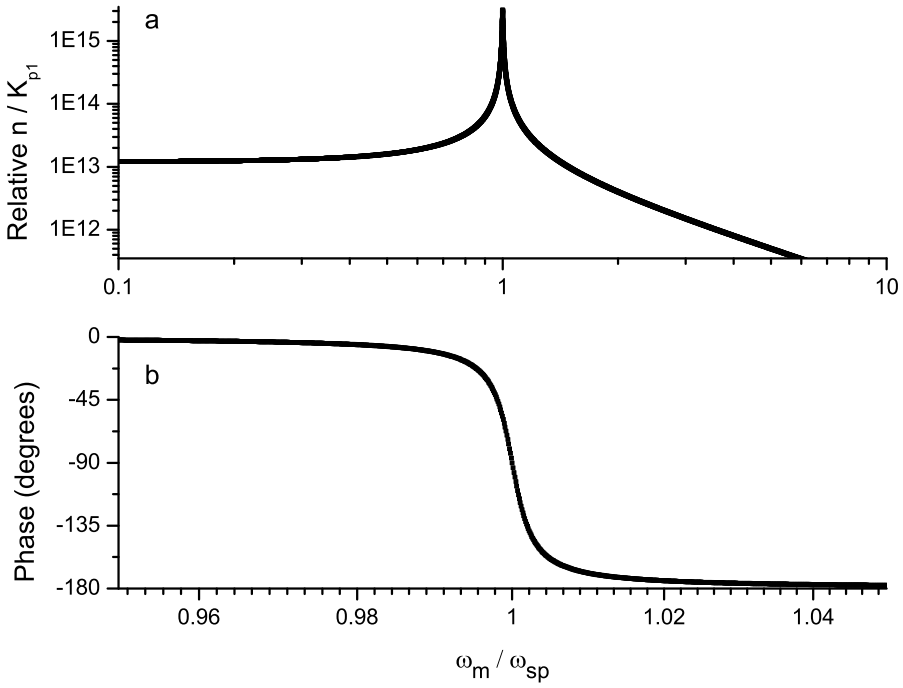

Figure 3.22: (a) The frequency response for K modulation, (b) the phase relationship with frequency as calculated by equation (3.10).

unchirped relaxation oscillation frequency $\omega_{\rm sp}$, there is a resonance in the magnitude of the intensity oscillation. In this regime, the phase between the driving frequency and the intensity oscillation also changes.

Equation (3.10) can also be used to deduce a relationship between the power modulation and the effect on the population. For our system it can be shown that for just 2 % modulation of the coupling coefficient, i.e. $\tilde{K_{\rm p1}}/K_0 = 0.02$, the ratio of the modulated cavity population to its steady state value, $\tilde{n_1}/n_{\rm ss} = 0.52$ when $\omega_{\rm sp} = \omega_{\rm m}$. This confirms the observed effect that when our laser was chirped at 1.82 MHz, the intensity modulation of the master was greatly increased in magnitude compared to unchirped modulation and why the modulation can increase further when, $\omega_{\rm m} \approx \omega_{\rm sp}$, which in the case of our cavity is ≈ 1.1 MHz.

Figure 3.22a assumes that there is equal modulation of the optical path length at all frequencies, however there are many piezo-electric acoustic resonances in the e.o. crystal where the mechanical response at particular well defined frequencies is greatly enhanced [108]. The piezo-electric effect causes a physical length change in the material proportional to the applied voltage which therefore also changes the optical path length. This modulation is much greater at the acoustic resonances than due to the electro-optic effect alone. This would manifest in figure 3.22a as narrow spikes on top of the predicted frequency response. These acoustic resonance typically occur above 80 kHz and have been observed up to 25 MHz [108].

Figure 3.23 shows data taken at three modulation frequencies where such acoustic resonances were observed and demonstrates that the modulation of the voltage applied to the e.o. crystal to frequency chirp the laser does indeed have a big effect on the magnitude of the intensity oscillations. At these frequencies, the intensity modulations due to relaxation oscillations were up to 100 % of the output intensity. We can reduce the effect of these intensity modulations by choosing a modulation frequency that does not overlap with these resonances. On these resonances, the voltage induced refractive index changes, and therefore the tunability, exceeds that induced by the electro-optic effect alone. A variation in tunabilty f_V is shown by figure 3.24, where for voltage modulations above 2.2 MHz, the tunablity increases from $\approx$ 15 MHz/V, to $\approx$ 28 MHz/V. This data was taken by measuring the width of the spectrum ('bat-wings') taken with the Fabry-Perot interferometer, as shown in figure 3.9. These data were taken by applying a sinusoidally varying voltage to the e.o. crystal, with a peak to peak amplitude of 67.5 V for various modulation frequencies around 1 MHz. These frequencies are in the regime of what is required to chirp the laser for deceleration experiments.

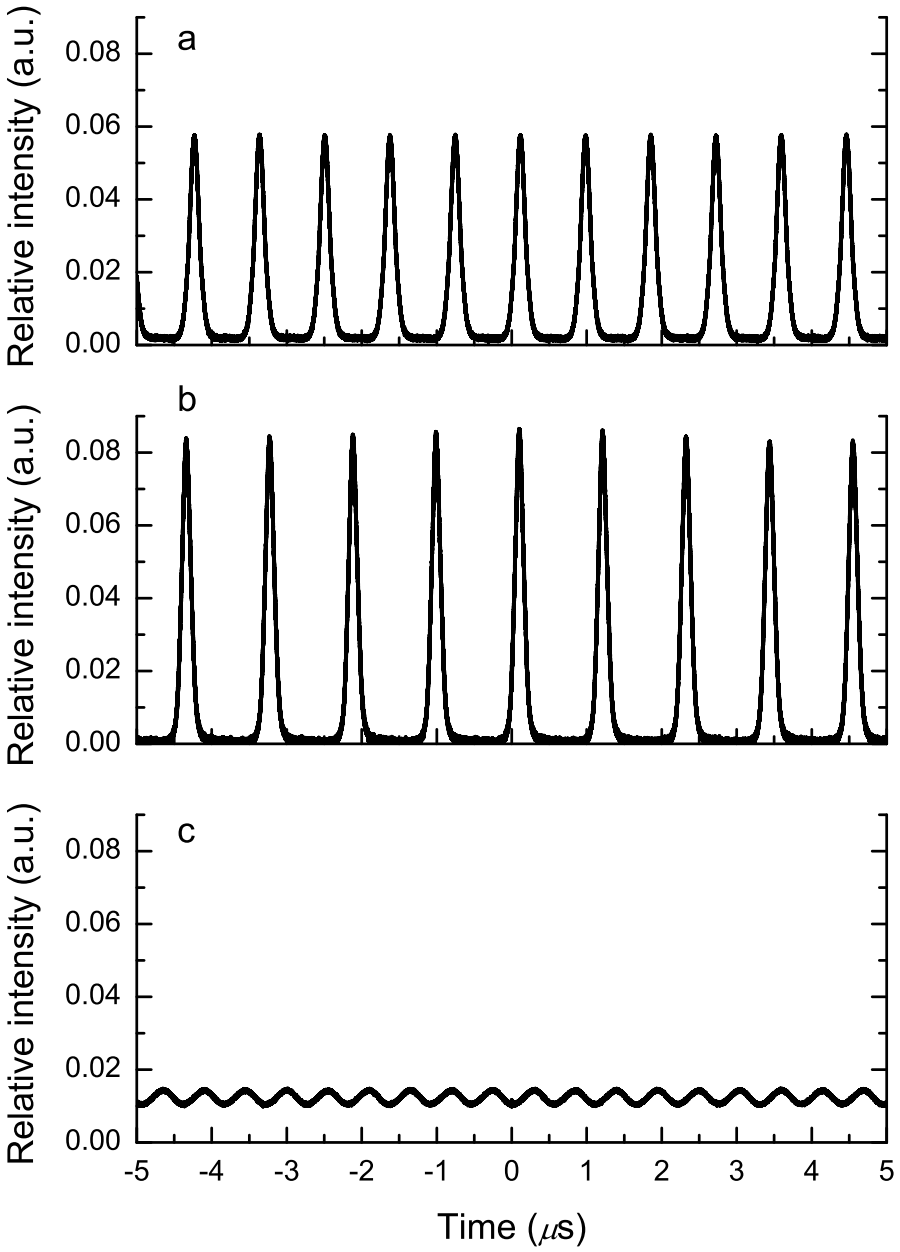

Figure 3.23: The intensity oscillation data taken at three frequencies where acoustic resonance were observed, when the voltage was modulated at (a) 2.3 MHz, (b) 900 kHz, where the intensity modulation was ≈ 100 % and (c) 1.82 MHz where the intensity modulation was ≈ 30 %.

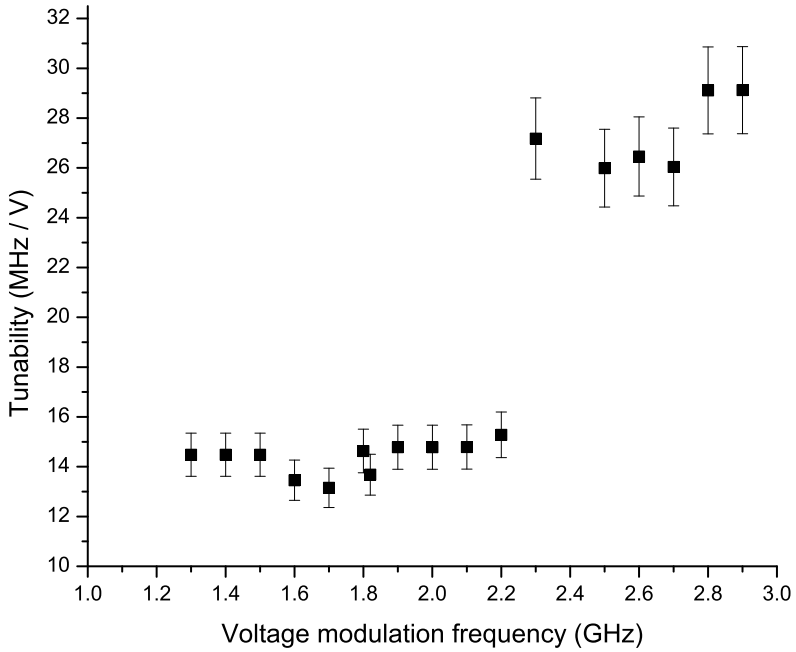

Figure 3.24: The tunability f_V for various modulation frequencies based on measurements of width of spectrum taking with a Fabry-Perot interferometer. For modulations between 1.3 and 2.2 MHz, f_V is in good agreement with d.c. operation ≈ 15 MHz / V. Above 2.3 MHz, the tunability increases to 28 MHz/V, perhaps due to overlap with a fundamental acoustic resonance within the crystal.

3.10 Summary

We have described a low power, continuous wave (cw) laser system, with a constant intensity output of approximately 20 mW, at $\lambda = 1064$ nm, where intensity oscillations have been suppressed by injection locking to a slave diode laser. This system is single mode and can be tuned up to ≈ 1 GHz, and remain single mode, by the application of a voltage across an electro-optic crystal within the cavity of our microchip laser. We can also rapidly tune up to 1 GHz by applying a sinusoidally varying voltage with a modulation frequency of 1.82 MHz, which is generated by a frequency generator, before being amplified by a tank circuit. This laser was then amplified to 1 W in a commercial fibre based amplifier.

Chapter 4

Low power CW heterodyning

4.1 Introduction

In the previous chapter, the development of a Nd:YVO_4 based continuous wave (CW) laser system was described, which could be rapidly chirped in excess of 1 GHz over durations of 100's ns. In this chapter I will describe how the output of this laser system was split into two, which we require in order to create the two beams which produce our optical lattices. A time delay was introduced between the two arms, in order to create a frequency difference as a function of time which allowed us to create stationary and accelerating/decelerating optical lattices for optical Stark deceleration.

4.2 Generating a frequency difference

The time delay between the two arms was produced by coupling the output beams into two fibres of different lengths (10 m and 65 m) which were then fed into our Nd:YAG pulsed amplification system. This scheme is summarised in figure 4.1. The operation of this pulsed amplification system will be described in the following chapter.

The time delay between each arm of the laser system therefore creates a frequency difference between the high energy outputs of arm A and B when the master laser is chirped. If a square wave voltage was applied to the master, there would only be a frequency difference for a maximum of the total time delay introduced by the 55 m difference in length between the two fibres, i.e. 275 ns before the frequency from the longer fibre changes to match the shorter one.

Apart from creating a time delay, the fibres also enabled us to physically isolate the Nd:YVO_4 master/slave lasers from the pulsed amplification system by mounting

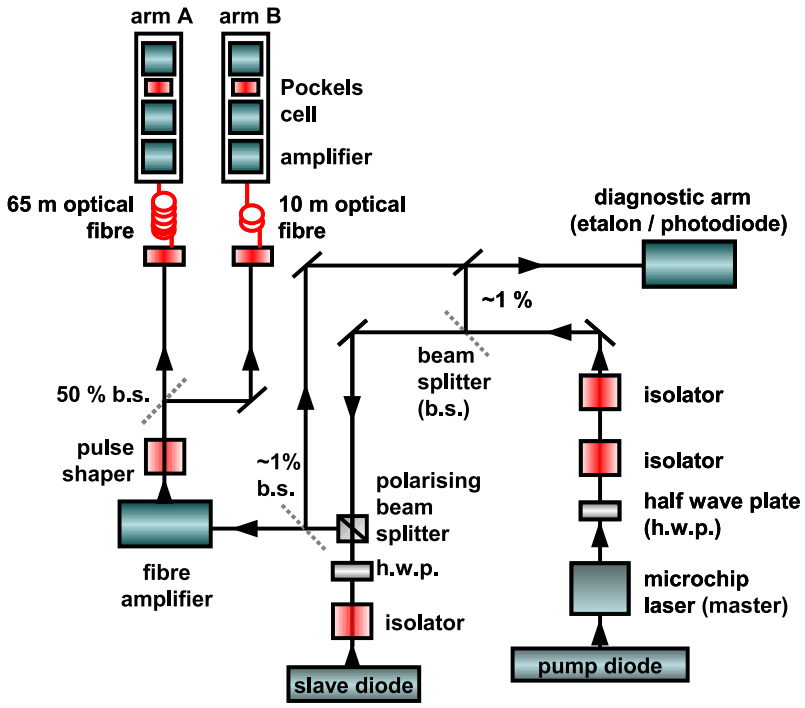

Figure 4.1: A microchip laser (master) injection locks a free running 'slave' laser diode. Isolators are used to ensure that the output of the slave laser cannot reach the master. The output is then coupled into a fibre amplifier where it is amplified up to 1 W. A pulse shaper creates pulses in the 10-1000 ns range and then the beam is split into two 'arms' and coupled into two optical fibres of different lengths. These outputs are fed into each arm of our pulsed amplification scheme.

it on a separate table. Initially, when the master was set up on the same table, the vibrations caused by the 10 Hz flashlamps destabilised the $NdYVO_4$ cavity.

For coupling into the fibres, we used a translation stage and a fibre port, both with μm resolution. We found that whilst the translation stage was much more intuitive to couple light into the fibre, the fibre port was more stable over time. In both cases coupling efficiencies of up to 50 % were achieved, providing 200-250 mW of power at the exit of each fibre for $\approx$ 500 mW input into each fibre. The fibres (Thorlabs - 1060XP) used were single mode, designed for use with wavelengths of $\lambda = 980 - 1600$ nm. One end of each fibre was supplied with an angled face, in order to prevent back reflection coupling into the system. Since they were not polarisation maintaining, we had to correct the polarisation to make it linear, and of the correct orientation for introduction of the light into the pulsed amplifier system. For this we used a 3-paddle polarisation controller (Thorlabs - FPC560) for each fibre, which adjusted the polarisation through stress induced birefringence. By iteratively adjusting each paddle, any arbitrary output polarisation could be produced from an arbitrary input polarisation state.

4.3 Rapid chirping

To measure an induced chirp we heterodyned the output of the two fibres. Due to the difference in their length, there was a time delay, and therefore a frequency difference, between the two beams at the fibre outputs when the master laser was chirped. To illustrate this, figure 4.2 shows the theoretical frequency shift induced by the applied voltage at the output of each fibre. This chirp was simulated by considering a sinusoidal voltage of amplitude 67.5 V applied to the electro-optic crystal at a frequency of 1825 kHz. Due to the time delay (275 ns) introduced by the difference in fibre lengths, there is a π phase shift between these waveforms. The third trace represents the frequency difference between these two beams that would be observed by heterodyning the two outputs. The maximum frequency difference between the two outputs is 1040 MHz based on a tunability of 16 ± 0.5 MHz/V. At approximately 140 ns and 420 ns, the relative frequency between the two arms goes to zero.

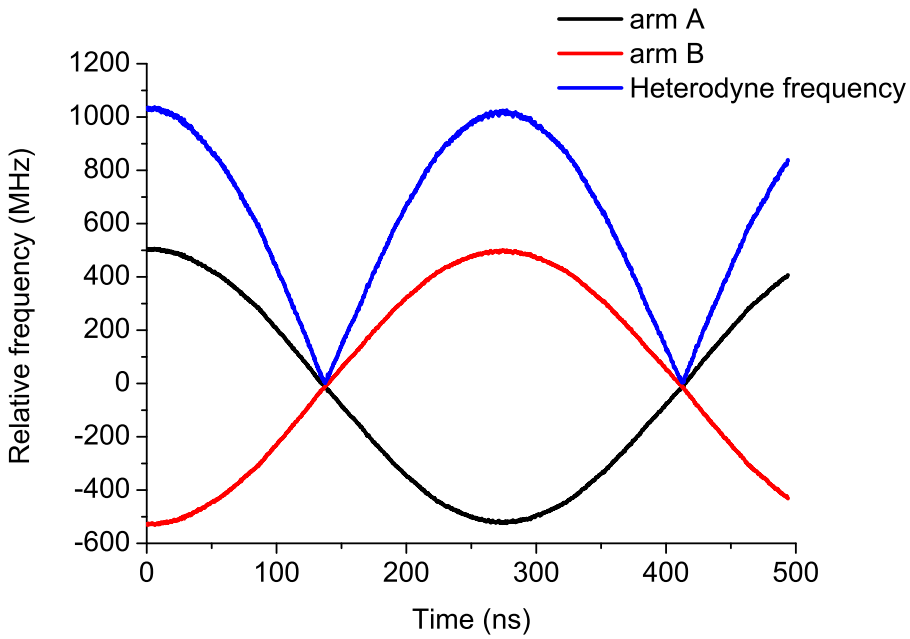

Figure 4.2: A theoretical rapid frequency chirp of 1040 MHz is shown, which would be produced from a sinusoidally varying voltage with amplitude 67.5 V and modulation frequency 1.82 MHz, applied to the e.o. crystal. A π phase delay between the sinusoidally varying frequency of each arm results from the difference in fibre length.

4.3.1 Heterodyning the laser outputs

To heterodyne (beat) the outputs from each fibre, we combined both beams onto a beam-splitter and focused these overlapped beams onto a fast photodiode with a bandwidth of 2 GHz, as shown in figure 4.3. In low power CW operation (up to 1 W), the half wave plates in the pulse shaping section and the custom amplifier system are adjusted to allow light to pass through. Flip mirrors m1a and m1b are raised to direct the beam onto photodiodes (p.d.) 1 and 2 for measurement of their individual temporal profile or the combined heterodyne signal. Similarly p.d. 2 allowed for the measurement of the pulse amplified beam, which is extracted via the 5 % beam splitters bs3 and bs4. This allowed for continuous and simultaneous measurement of the high power pulsed beam heterodyne signal during experiments. A camera (Thorlabs DCC1545M) allowed for measurement of the spatial profile of both beams. Both beams were attentuated further using neutral density filters, before heterodyning and before the camera, to ensure they were of similar and safe intensities to avoid damage to the sensors or saturation of the signals.

The photodiode signal was recorded on an oscilloscope with a 3 GHz bandwidth. A frequency difference between the two beams, which changed as a function of time if chirped, was manifested in the heterodyne (beat) frequency, $\omega_{\mathrm{m}}(t) = |\omega_2(t) - \omega_1(t)|$.

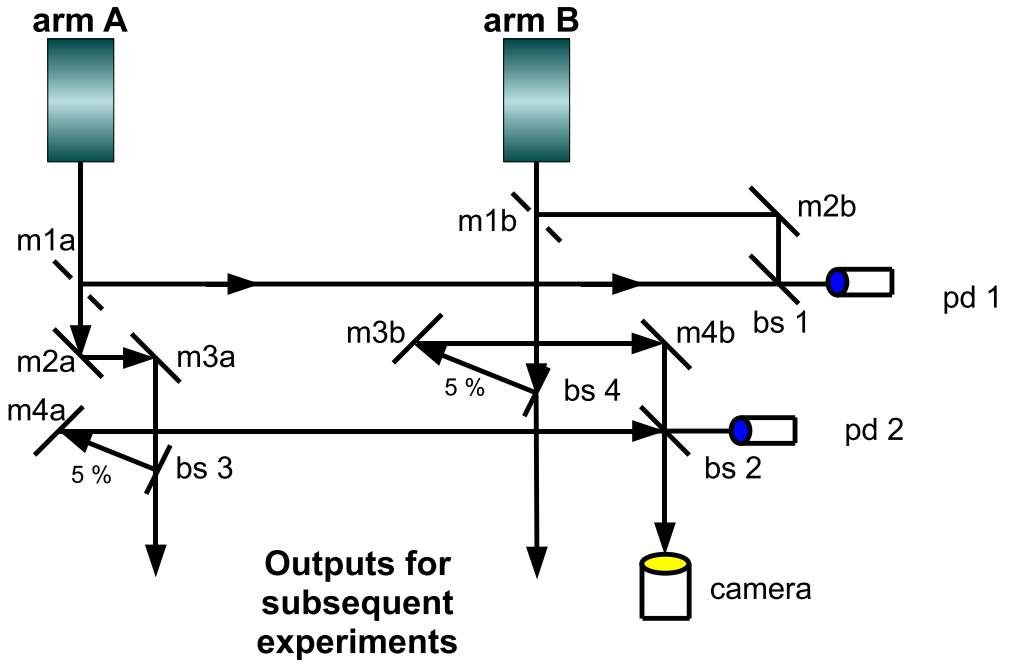

Figure 4.3: The optical setup at output end of Nd:YAG system for heterodyning. Photodiode (p.d) 1 allows for the measurement of the CW beam profile when one of mirrors, m1a or m1b, is raised to redirect the beam. When both are raised, the heterodyne can be measured. P.d 2 receives light from the 5 % beam splitters, bs3 and bs4 for measurement in the pulse amplified case. This is used because during amplification mirrors m1a and m1b would direct too much light onto p.d. 1 causing damage. The camera allows the spatial profile of each beam to be measured. Attenutation of the beams before the photodiodes and camera is also necessary to prevent saturation of the signal or damage to the sensors.

Maximum modulation depth would occur where the two intensities of the two beams are the same and where, at least over the area of detection, both beams were of equal size.

This signal is shown in figure 4.4a and the sinusoidal voltage which was applied to the electro-optic crystal, with a peak-to-peak amplitude of 74 V and frequency 1.82 MHz, as shown by the overlaid black line. The maximum beat frequency occurred at minimum (or maximum) applied voltage corresponding to 0 and 280 ns where the amplitude modulation is at a minimum. The variation in modulation contrast as a function of frequency was due to the non-linearity of the frequency response of the photodiode. This was determined by measuring the modulation depth as a function of a fixed frequency difference.

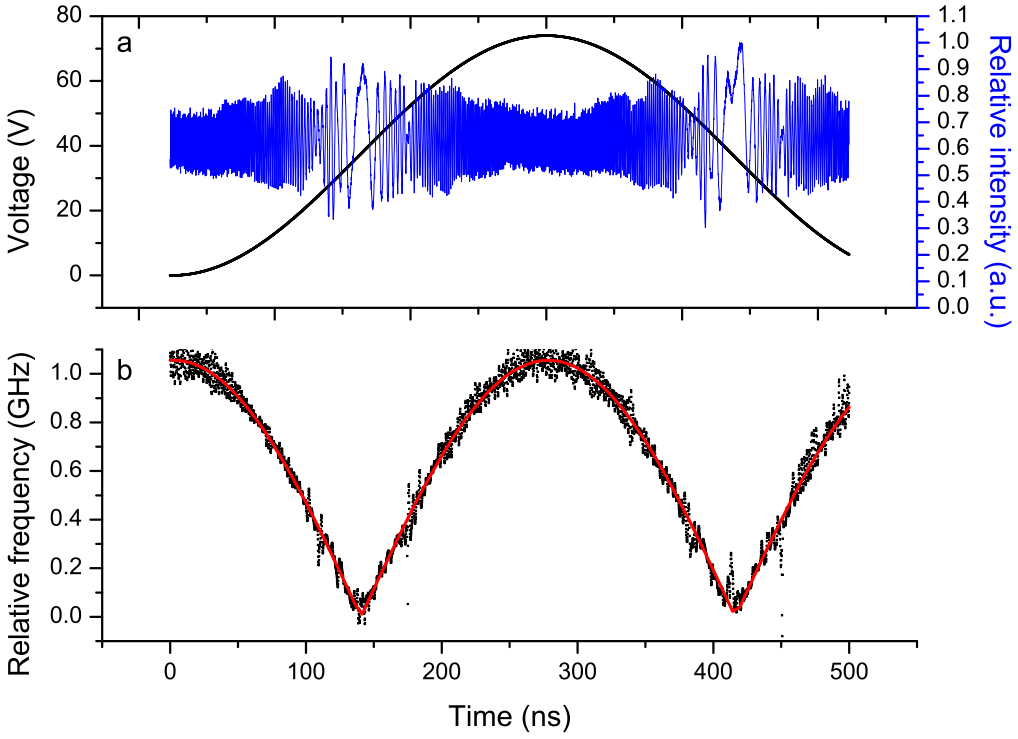

Figure 4.4: (a) The heterodyne signal measured on a photodiode between the two arms when a sinusoidal voltage is applied to the e.o. crystal of 74 V. (b) The derived instantaneous frequency difference $f(t)$ overlaid with a red trace which is a fit of function, $f = f_V V|\cos \omega t|$. This indicates a tunablity f_V of 14.3 ± 0.2 MHz/V at a modulation frequency of 1825 kHz.

4.3.2 Extraction of the instantaneous frequency difference as a function of time, $f(t)$.

Measuring the instantaneous frequency as a function of time, $f(t)$, which is the time derivative of the instantaneous phase of the complex amplitude, $\phi(t)$, is not straightforward. Usually pulsed lasers are simply characterised in terms of their temporal and spectral intensity profiles. Fluctuations in the frequency of pulsed lasers are measured in order to quantify their effect on the shape and spectral position of two photon spectra [148]. They showed that the variation in the laser frequency (chirp) over the duration of a measurement is the principle uncertainty in their measurement of the hydrogen $1S$ Lamb shift [149].

Generally such fluctuations are observable only through the broadening of spectral lines above the Fourier transform limit. However, this does not give the dynamics of such frequency changes (or chirping). In our case we want to measure a controlled frequency chirp, and also to verify that no additional chirp was introduced during the pulsed amplification stage. This problem was demonstrated in the work of Fulton [150]. His results showed that the Nd:YAG laser, used as one of the beams to create the constant velocity lattice for molecular deceleration, exhibited a chirp of up to 100 MHz over the duration of the pulse ($\approx$ 20 ns). These were caused by temperature and gain variations in the Nd:YAG amplifying rods. It was important to quantify these frequency variations, as they would cause fluctuations in the lattice velocity, and therefore the dynamics of the molecules trapped in the optical lattice.

We assume the electric fields of arm A and B of our low power CW and pulse amplified beams are given by, $E_{\mathrm{A,B}}(t) = E_{\mathrm{A0,B0}}(t)\exp\left[\mathrm{i}\left(\phi_{\mathrm{A,B}}(t) + \omega t\right)\right]$, where $E_{\mathrm{A0,B0}}$ are the electric field amplitude of each arm oscillating at the same optical frequency ω, with a time dependent phase $\phi_{\mathrm{A,B}}(t)$ whose derivative with time gives the instantaneous frequency change. To determine the frequency difference between the two beams as a function of time, we used the method of Fee et al. [148], where the heterodyne (beat) signal from the two beams recorded by the photodiode can be written in the time domain form as,

$$V \propto |E_{\mathrm{A}}(t)|^2 + |E_{\mathrm{B}}(t)|^2 + E_{\mathrm{A}}(t)E^*_{\mathrm{B}}(t)\exp\left[\mathrm{i}\left(\phi_{\mathrm{A}}(t) - \phi_{\mathrm{B}}(t)\right)\right] + \mathrm{c.c.} \tag{4.1}$$

Our aim is to separate out the third 'mixing' term from the first two intensity terms, in order to extract and measure how the phase is changing with time, on top of its oscillation every 2π. Once we can measure how the instantaneous phase as a function of time $\phi(t)$ is changing we can find the rate of change to find the instantaneous frequency $f(t)$.

In order to separate the terms we Fourier transform the time domain data into frequency space. When the beat frequency between the two beams is higher than the Fourier components of the first two terms in the equation above, we can apply a bandpass filter to extract only the higher frequency Fourier components of the third term in the equation above. This filtered signal in the frequency domain is transformed back into the time domain and the instantaneous phase is obtained by finding the phase angle of this term to give $\phi(t)$. The instantaneous frequency difference $f(t)$ is determined from its time derivative, $2\pi f(t) = \mathrm{d}\phi(t)\ \mathrm{d}t$. This was implemented with Matlab using the 'fft' and '$ifft$' functions to Fourier transform and reverse transform the data, '*angle*' to extract the phase angle of the third term and '*gradient*' to find the gradient of the phase term $\phi(t)$ to give $f(t)$.

To understand this better, figures 4.5 and 4.6 show the different steps used in the Matlab program. Figure 4.5a shows a simulated signal with an initial heterodyne frequency of 100 MHz chirping up to 600 MHz after 240 ns. Some white noise has also been applied. The form of noise was random, with a normal distribution, and a maximum amplitude of $\pm$ 5 % applied to the signal, $I(t)$. This data is Fourier transformed and then multiplied by a bandpass filter (the mask) which separates out the lower frequency components. When this is reverse Fourier transformed, if the mask has been applied correctly, we obtain the $E_{\mathrm{A}}(t)E^{*}_{\mathrm{B}}(t)\exp\left[\mathrm{i}\left(\phi_{\mathrm{A}}(t) - \phi_{\mathrm{B}}(t)\right)\right]$ 'mixing' term. Figure 4.5b shows the extracted temporal profile of the pulse calculated by taking the absolute value of the mixing term. The heterodyne signal with the first two components in equation 4.1 removed is shown in figure 4.5c.

The phase angle of this is then calculated by the program in order to obtain the instantaneous phase difference $\phi(t)$, as shown in figure 4.6a. This is shown as being periodic, since Matlab assumes phase to be periodic between $-\pi$ and π. We therefore have to unwrap this to reflect the fact that we know the phase is continuing to change in one direction, this is shown in figure 4.6b. Finally the gradient of this function is taken and scaled to give the instantaneous frequency difference $f(t)$ in figure 4.6c.

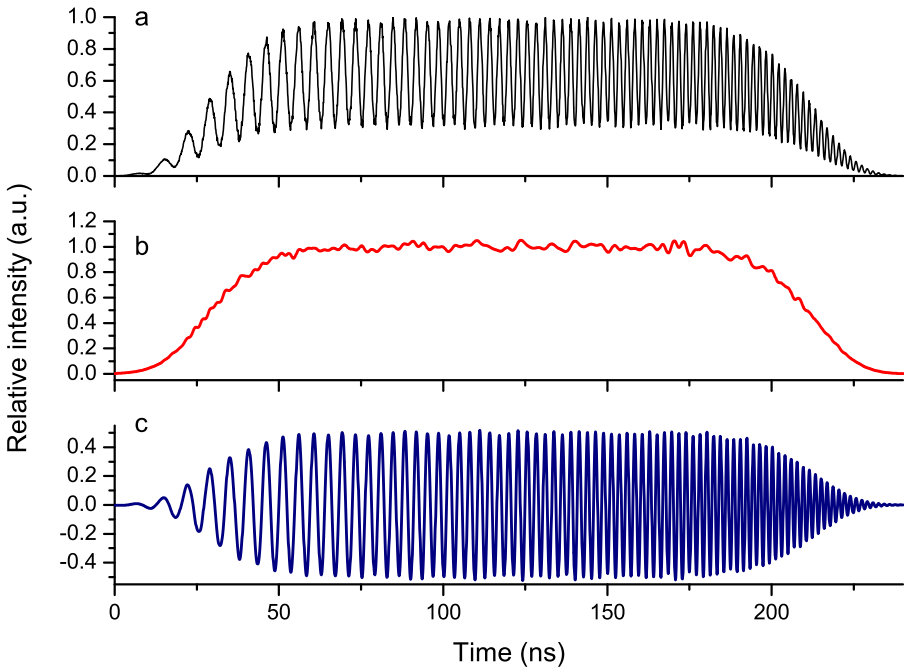

Figure 4.5: (a) Input signal, (b) Extracted temporal intensity profile $I(t)$, (c) Extracted heterodyne signal.

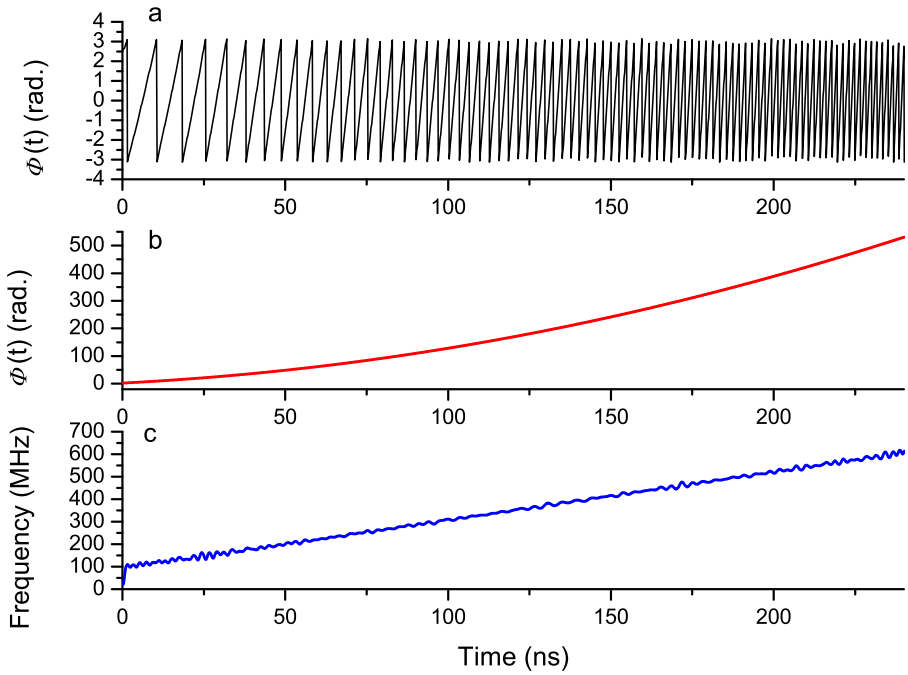

Figure 4.6: (a) Periodic phase ($\phi(t)$ obtained by extracting the angle from the 'mixing term' of equation (4.1), (b) Unwrapped phase ($\phi(t)$), (c) Frequency $f(t)$ obtained by taking the gradient of (b).

4.3.3 Bandpass filters

The type of bandpass filter used is important, as it determines how well we can separate out the frequency chirp components. In most cases we found that a 'super-Gaussian' of the form, $\exp\left[-1 \times ((-f_0 + f)/\Delta f)^{x>>2}\right]$ is effective since the large power ensures an extremely sharp rise and fall in the bounds of the mask, and good exclusion of lower intensity components.

Figure 4.4b represents the instantaneous frequency difference as a function of time determined from the data shown in figure 4.4a. We cannot determine the instantaneous frequency difference when the beat frequency components of the Fourier transform cannot be well separated from the low frequency components that result from the finite sampling window. At frequencies above 100 MHz, the instantaneous frequency difference can be determined within ± 10 MHz. A chirp in excess of 1000 MHz is more than sufficient for our purposes since it is equivalent to a lattice velocity of > 530 ms^{-1} for counter propagating beams. This velocity is greater than the initial velocity of cold molecules produced by a xenon buffer gas jet. We then fit the function $f = f_{\mathrm{V}} V |\cos \omega t|$ to the derived instantaneous frequency difference, as shown by the red trace in figure 4.4b, and determined a tunability of $f_{\mathrm{V}} = 14.3 \pm 0.2$ MHz/V at a modulation frequency of 1825 kHz which is in reasonable agreement with d.c. measurements for 16.95 °C, as shown in chapter 3.

White et al. [151] uses a similar Fourier transform method (FTM) devised by Fee et al. which we have employed, and compares it to two additional techniques for determining the instantaneous, time dependent frequency. The first of these extracts the time dependent phase from the amplitude and intensity components using the least squares fit method. This reconstructs the temporal profile of the pulse, and then subtracts it from the beat pattern of the waveform to leave only the phase term. The other method uses a matched pair of electronic mixers to introduce the modulation and beat frequencies into the mixer inputs. The inter-modulation output gives the quadrature phase information from which the instantaneous frequency difference is derived.

In the FTM, it was found that the Tukey filter yielded the smallest error, when compared to two types of Blackman filter.

4.4 Analysis of bandpass filters using simulated chirped data

Whilst a super-Gaussian bandpass filter was used to produce figure 4.4, other filters were investigated, including a standard Gaussian or in the simplest case, a rectangular filter. In order to investigate the effectiveness of different masks, simulated constant frequency difference (constant velocity) and linear chirps (linear deceleration/acceleration) were modelled. A constant frequency difference has the functional form $I(t) \propto \sin(f_0 t)$, and a linearly chirped frequency difference has the form $I(t) \propto \sin\left(f_0 t - \frac{\beta}{2}t^2\right)$, where f_0 is the initial or fixed frequency difference, and $\beta = \Delta f/\Delta t$ is the chirp rate, Δf is the frequency excursion and Δt is the pulse/chirp duration. A 1 GHz linear chirp over 137.5 ns was modelled.

4.4.1 Applying analysis to simulated data

It was found that a super-Gaussian (a Gaussian raised to the power 20) was the best compromise in terms of efficient cut-off of the chirp frequencies and the low frequencies which derive from the temporal profile of the pulse. It was important to capture the lowest range of the frequency chirp however this increased the likelihood of overlap with the temporal intensity components. Oscillations over the duration of the chirp, known as Gibb's oscillations [152], are due to the discontinuity and cut-off of the mask in Fourier space, which restricts the range of frequencies. This phenomenon is commonly discussed in Fourier analysis [151, 148, 153, 154].

To simulate a pulsed heterodyne signal we apply a Gaussian mask to a beat signal with a super-Gaussian intensity envelope in the time domain as shown in figure 4.7a. This is done in order to reduce the sharp edges created by the finite width of the data window. Sharp edges are known to induce Gibb's oscillations in the Fourier transform [153, 154]. In order to inform our understanding of our spectral analysis of the beat signals we also added white noise to the simulated data. The form of noise was random, with a normal distribution, and a maximum amplitude of $\pm$ 5 % applied to the signal, $I(t)$. This is not necessarily of the same form as the real noise in data taken in the laboratory, but will give us some greater understanding of the effects of noise on this analysis.

Our simulated data was sampled over 300 ns which gives a frequency resolution of $1/(300 \times 10^{-9}$ s) = 3.3 MHz. Given that the FWHM of the frequency peak is $<$ 1 MHz, then it is not going to be well resolved by our Fourier transform and therefore the centre of the peak will also not be well mapped out, which is why the

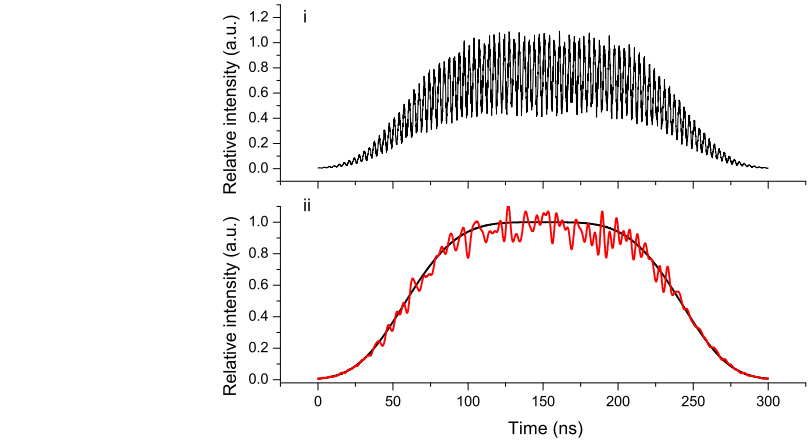

(a)

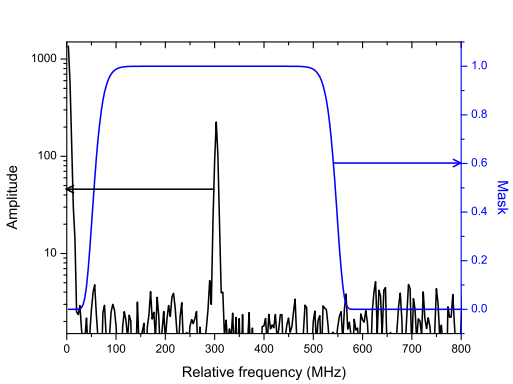

(b)

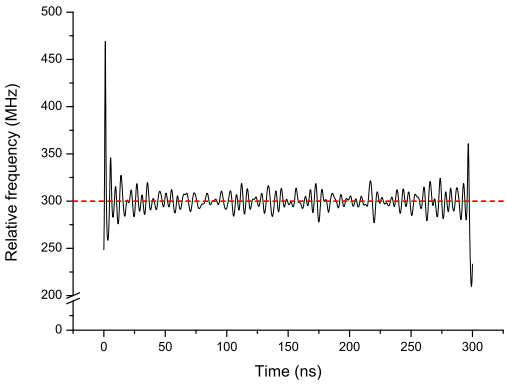

(c)

Figure 4.7: Simulations of the process for determining the instantaneous frequency difference $f(t)$. (a) i: The simulated heterodyne signal with a random normal distribution of noise with a maximum amplitude of 5 % , ii: black trace represents the Gaussian temporal intensity profile overlaid with the red trace which is the extracted intensity profile extracted from the beat signal. This shows modulation of $< \pm$ 5 % due to the added noise. (b) The Fourier transform of signal with overlaid super-Gaussian mask, including frequencies between $\approx$ 75 and 525 MHz (FWHM of mask). (c) The derived instantaneous frequency difference $f(t)$. After an initial overshoot, after 20 ns the oscillations in $f(t)$ are $< \pm$ 20 MHz.

peak is off centre to the mask which is centred on 300 MHz. The sampling rate, given that the simulated data had a data-interval of 0.1 ns, which was also the data interval of data taken with the oscilloscope, gives a Nyquist sampling frequency limit of 5 GHz. This is well above frequencies of interest to us.

Figures 4.7 demonstrates the use of a super-Gaussian mask which cuts off frequencies below $\approx$ 75 MHz. The the noise added to the data can be seen in the time domain (a) i, the extracted pulse shape (a) ii, and also in the Fourier domain (b) and the derived instantaneous frequency difference $f(t)$ (c). For example figure 4.7b shows many low amplitude frequency components over the displayed frequency range due to the presence of noise. The mask used included frequencies from 75 to 525 MHz. The oscillation of $f(t)$ around the actual value of 300 MHz in figure 4.7c is approximately $\pm$ 10-20 MHz, after an initial overshoot of approximately 170 MHz, and an undershoot of 70 MHz at the end of the data window.

The oscillation of $f(t)$ in figure 4.8c has been reduced to approximately $\pm$ 2 MHz, within the expected limit of certainty, due to the width of the data window. The modulation in the extracted intensity in figure 4.8a (ii) has been reduced from $\approx$ 10 % in figure 4.7a (ii) to 5 %, due to the narrower mask suppressing the noise and included frequency range.

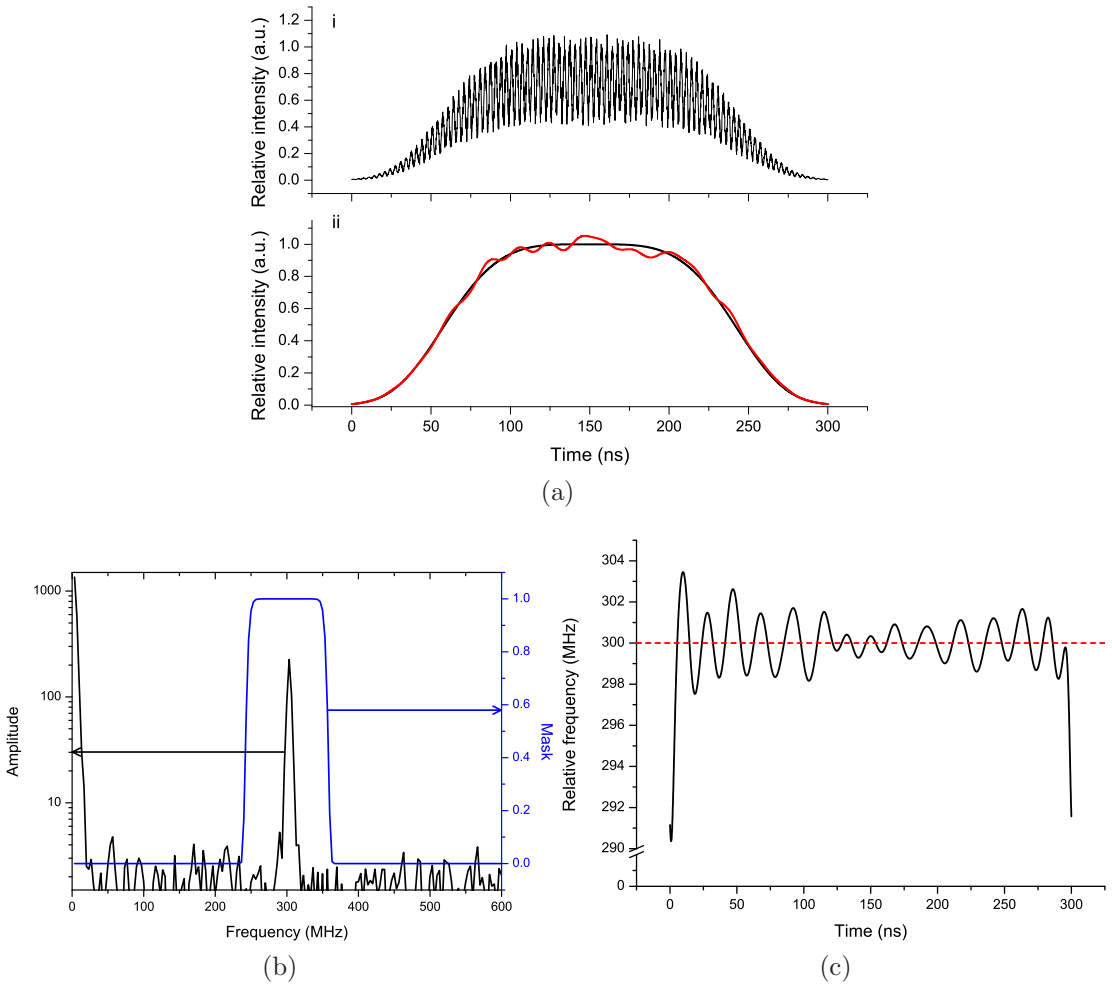

Figure 4.8: Simulations of the process for determining the instantaneous frequency difference $f(t)$ with a different mask applied in the Fourier domain. (a) i: The heterodyne signal as in figure 4.7, ii: black trace represents the Gaussian temporal intensity profile overlaid with the red trace, which is the intensity profile extracted from the heterodyne signal showing a reduction to 5 % modulation. (b) The Fourier transform of signal overlaid with super-Gaussian mask including frequencies between $\approx$ 250 and 360 MHz (FWHM of mask). (c) The derived instantaneous frequency difference $f(t)$. For the majority of the chirp the oscillation is $\approx \pm$ 0.2 MHz.

4.4.2 Summary

A super-Gaussian mask offered the best compromise between ease of implementation, having a rising edge which is not too steep, and having a good cut-off between beat frequencies and frequencies due to the temporal profile of the pulse. Having a clear separation is important since we need to isolate the instantaneous phase term, $\phi(t)$, as given in equation (4.1) in order to differentiate to derive the instantaneous frequency difference, $f(t)$. It clear at this stage, that noise has a significant effect on the uncertainty of the derived $f(t)$. Any high frequency noise in the phase $\phi(t)$ will be greatly magnified when differentiated, leading to large modulations in $f(t)$.

Other bandpass filters such as Blackman and Tukey can also be employed, which can be used to correctly separate the frequency term [148, 151] from the intensity components in Fourier space. The simplest, rectangular filter has the advantage that there is zero attenuation in the region of interest, and the cut-off is optimal, however the sharp edges cause significant spectral leakage, which become apparent in the time domain, due the higher frequency components contained in a sharp rising edge which can overlap with the chirp frequency components. There is therefore a trade off in the smoothness and flatness of a band-pass filter used.

Our analysis shows however, that for our purposes, a super-Gaussian provides sufficient accuracy to derive the instantaneous frequency difference as a function of time, and it is other sources of error, such as noise and data window width that will be of greater significance.

4.4.3 Linear chirp simulations

In order to test the method for extracting the instantaneous frequency difference as a function of time, $f(t)$ for a linear chirp, a Gaussian envelope was applied as before in the time domain, with a half maximum rise time of ≈ 50 ns. The chirp phase was adjusted so that the maximum chirp occurs at 50 ns and chirps down to 0 frequency difference at 190 ns as shown by the dashed red trace in figure 4.9c. Outside this range the mathematical function used to generate the simulated chirp continues, as shown by the beat pattern in figure 4.9a (i). However, as we are only interested in how well the derived instantaneous frequency difference is extracted over a particular time range we only plot it in the range from 50-190 ns as shown in figure 4.9c. The mask used in Fourier space is shown in figure 4.9b. In the first case this included all low frequencies close to 0 MHz up to the maximum. The extracted pulse shape shown in figure 4.9a (ii) shows modulation of the amplitude which implies that we have not correctly separated the Fourier components. The derived $f(t)$ shows very

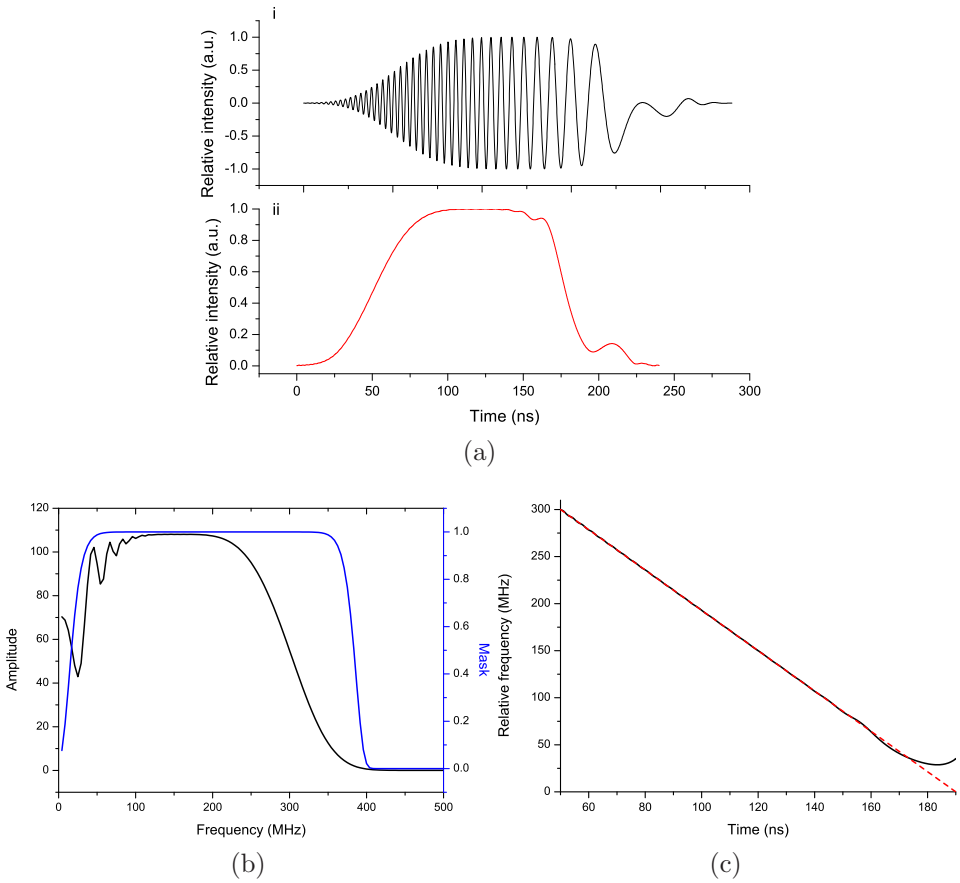

Figure 4.9: Simulations of the process for determining the instantaneous frequency difference $f(t)$ using a simulated linear chirp. (a) i: The simulated heterodyne signal, ii: black trace represents the Gaussian temporal intensity profile overlaid with the red trace which is the intensity profile extracted from the heterodyne signal. It shows a good extraction of the smooth intensity profile with some larger modulation of up to 10 % at the end of the pulse. (b) The Fourier transform of signal overlaid with super-Gaussian mask including frequencies down to the minimum of $\approx$ 10 MHz up to 380 MHz. (c) The derived instantaneous frequency difference $f(t)$. Oscillations around the predicted frequency are $\pm < 0.5$ MHz until after 175 ns when $f(t)$ deviates more.

little modulation, $\pm < 0.5$ MHz around the predicted frequency. The penalty for this is the limit on the extraction of lower frequencies, where after 175 ns, $f(t)$ deviates sharply away from the predicted value, with a final value of $\approx$ 35 MHz above the predicted 0 MHz value for the end of the chirp.

4.4.4 Offset and noise

To overcome the difficulty of accurately resolving higher frequencies, without compromise on extracting lower frequencies, we can simulate an offset in the frequency of one the arms our our laser system, resulting in a chirp which does not approach 0 MHz, which in an experimental situation could be achieved by the use of an A.O.M. in one of the arms in the heterodyning. The extracted Gaussian temporal profile in figure 4.10a has modulation of up to 5 % is without unwanted modulation and the derived instantaneous frequency difference in figure 4.10c follows the predicted frequency accuracy to less than 10 MHz limit down to the minimum value of the offset of 100 MHz. The Fourier components due to the temporal profile are not visible in figure 4.10b.

4.4.5 Conclusions

Determining frequencies from the beat (heterodyne) pattern of the two laser beams using the mathematical algorithm detailed in section 4.3.2 requires the careful separation in Fourier space of the chirp and temporal intensity components in order to give the accurate measurement of the instantaneous phase $\phi(t)$ and frequency $f(t)$ as a function of time. Issues arise with the extraction of low frequencies, where if you need to resolve below 50 MHz, the uncertainty of the derived instantaneous frequency difference $f(t)$ increases over the whole chirp. We found that it is better to cut off lower frequencies, and infer them by applying a fit, or by splitting the data and analysing higher and lower frequencies separately. Alternatively an A.O.M could be used to offset the frequency of one of the beams before heterodyning and therefore avoid the problem of deriving these lower frequencies.

A high signal to noise is also important since it can introduce uncertainties in $\phi(t)$, which when differentiated are magnified to introduce large uncertainties in $f(t)$.

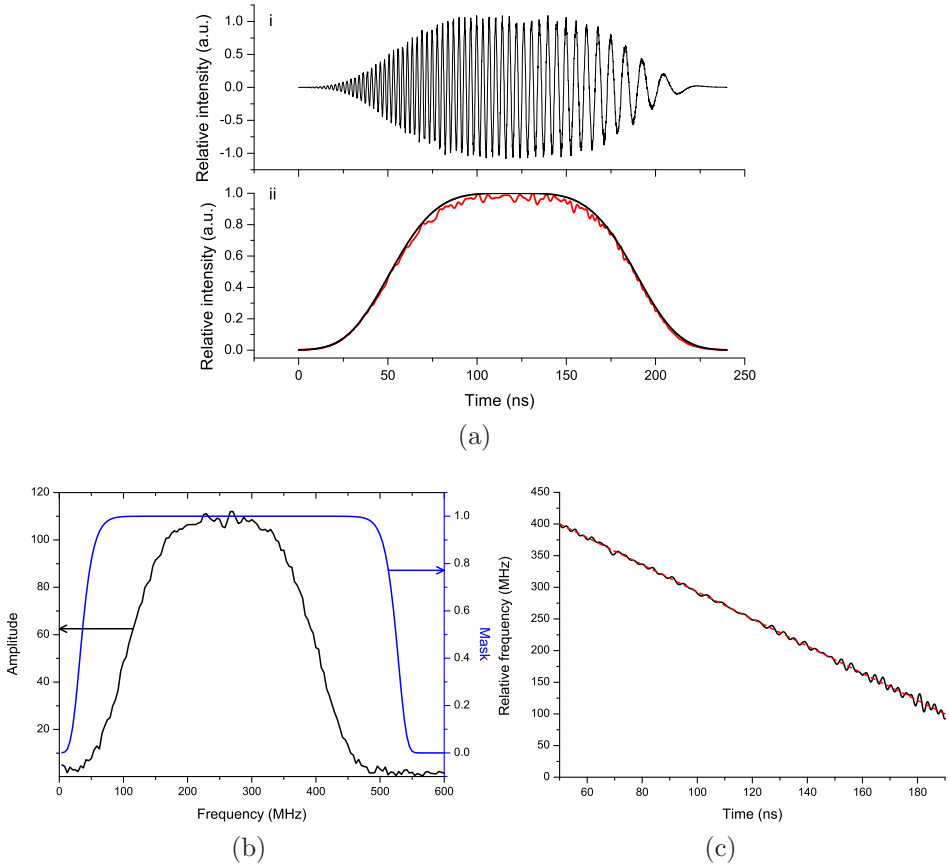

Figure 4.10: Simulations of the process for determining the instantaneous frequency difference $f(t)$ using an offset to the initial frequency. (a) i: The heterodyne signal of a 400 MHz down to 100 MHz chirp with a normal random distribution of noise, with a maximum amplitude of 5 % to the heterodyne signal, ii: the red trace is the extracted intensity temporal profile which shows a smooth intensity profile as shown by the overlaid black trace which is the input Gaussian profile. (b) The Fourier transform of signal overlaid with super-Gaussian mask including frequencies down to the minimum of ≈ 40 MHz up to 530 MHz. (c) The derived instantaneous frequency difference $f(t)$. Oscillations around the predicted frequency are $< \pm$ 10 MHz.

4.5 Constant velocity lattice heterodyne signals

We have now analysed the implementation of masks to separate the phase components from the temporal intensity components in Fourier space for simulated data. Once we have extracted the instantaneous phase difference as a function of time $\phi(t)$ we can derive the instantaneous frequency difference as a function of time $f(t)$ and therefore infer the lattice velocity $v(t)$. This method was then implemented with experimental heterodyne data for a constant velocity lattice, since it is the simplest case to begin with. Although the primary aim of our laser system is to produce a decelerating lattice with the two arms of the system, constant velocity lattices may also be created by applying a periodic square wave voltage to the e.o. crystal.

Applying a single square voltage pulse to the e.o. crystal would obviously only create a frequency difference between the two arms for the time delay due to the difference in length in the two fibres. After this point, the frequencies would be the same, since the frequency of the longer fibre would 'catch up' to the frequency of the shorter fibre. Instead, a periodic square wave was applied using a arbitrary waveform generator (TTi: TGA12101), which was limited to providing waveforms with 20 V peak to peak. It was set so that the voltage is on for 275 ns, and then off for 275 ns. After switch on, this caused a delayed shift in the frequency in each arm, as illustrated by figure 4.11. Figure 4.11a shows a simulated periodic square pulse, and figures 4.11b and c show the resultant relative frequency that would be observed at the end of each fibre. The outputs are π radians out of phase with each other due to the time delay introduced by the difference in lengths between the two fibres.

If the output of each of the fibres in this situation were interfered to create an optical lattice, a constant velocity lattice would be produced, due to the fixed frequency difference. After 275 ns, the direction of the moving lattice will swap, but with the same magnitude of velocity, given by the voltage, multiplied by the tunability f_{V}. To create a lattice moving at, for example half the velocity of the molecular jet, we would have to ensure that the right part of the cycle was used, otherwise the relative difference in velocity would be one and a half times the jet velocity and the lattice would be moving in the opposite direction to the jet. As discussed, a linear voltage ramp will eventually be the desirable waveform in order to create a constantly decelerating lattice. Whilst not of sufficient amplitude to produce the required frequency sweep to decelerate molecules in a molecular beam, a triangular waveform can be programmed to produce a linear ramp, with a maximum amplitude of 20 ± 0.5 V over a duration of 137.5 ns.

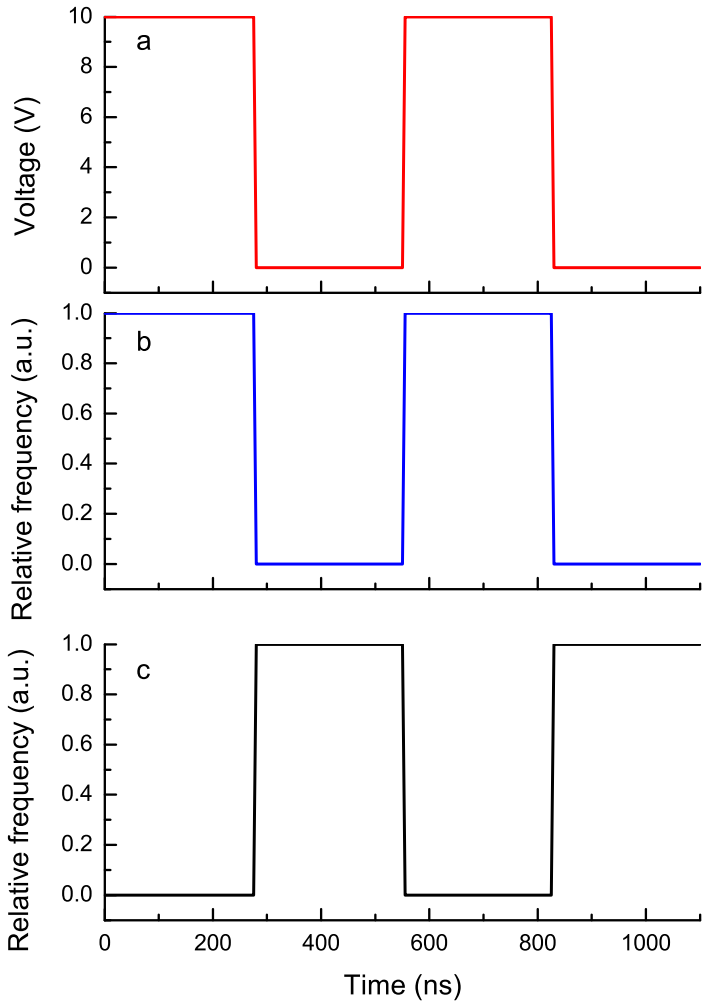

Figure 4.11: Creating a constant velocity lattice. (a) Shows the required input pulse from the voltage source. The period is such that the voltage is applied for 275 ns before switching off for 275 ns. This is the maximum use of the available fibre length. Even if the period was longer, the output of the longer fibre would catch up with the output of the shorter fibre after 275 ns which is the time delay induced by the 55 mm meter difference. (b) and (c) show the relative frequency which would be observed at the output of the two fibres compared to the normal output for zero volts. They are out of phase by π radians due to the time delay.

4.5.1 Square pulse: experimental data

Figure 4.12 shows the trace of a square wave voltage with amplitude 20 V programmed to be on for 275 ns, and then off for the same duration on the arbitrary waveform. The noise is probably due to the mis-match in the impedences of the scope and chirping crystal. The slope indicates that the half maximum rise time is ≈ 5 ns. The slope means that for a finite time, the frequencies on each arm approach each other during the part of the sequence where the voltage swaps from maximum to minimum voltage, or from minimum to maximum. Figures 4.13a-d shows the result of heterodyning the output of each fibre when a 20 ± 0.5 V periodic square pulse applied is applied to our laser system, with the voltage on for 275 ns and off for the same duration.

The area of ill-defined frequency in the middle of the pulse is due to the finite rise time of the square pulse. It was hoped that, if this was sufficiently rapid, i.e. the voltage generator generated a square pulse very accurately, with close to zero rise time, that it would be possible to measure the time it takes for the cavity to change to a new frequency. It has been found that the time that a cavity can follow an applied modulation is in the regime of the inverse of the cavity free spectral range [119]. In our case this is 22 GHz, which means that we would have to have a resolution in our analysis of the derived instantaneous frequency difference $f(t)$ of < 0.1 ns, which is unrealistic based on our analysis of simulated chirps in section 4.4. The area of ill-defined frequency is much larger, indicating that the limiting factors are the analysis technique, and also the finite time for the voltage to swap from maximum to minimum.

Figure 4.13a shows the voltage applied to the e.o. crystal (i), the heterodyne beat pattern recorded on the photodiode (ii) and the extracted intensity profile (iii). There is a great deal of intensity modulation up to 10 % increasing to 20 % close to the areas of ill-defined frequency at 110 and 380 ns. Figure 4.13b shows the Fourier transform of the heterodyne signal, overlaid with the mask which included frequencies from 70 to 230 MHz. Figures 4.13c (i) and (ii) shows $f(t)$ and $\phi(t)$ respectively. The instantaneous frequency difference $f(t)$ shows modulation of $\approx \pm$ 10 MHz overlaid with a linear fit which implies a tunablity $f_{\mathrm{V}} = 14.6 \pm 0.40$ MHz/V. The fit is applied to the data, omitting regions of ill defined frequency at 110 and 380 ns, and the edges of the data window. $\phi(t)$ is much smoother and is linear to a slope error of < 0.1 %, although there are some discontinuties evident at the times which $f(t)$ deviates greatly from predicted. The instantaneous phase $\phi(t)$ is shown for this data to demonstrate the effect that small discontinities result in large oscillations in $f(t)$. As previously explained, one of the important issues with any error due to

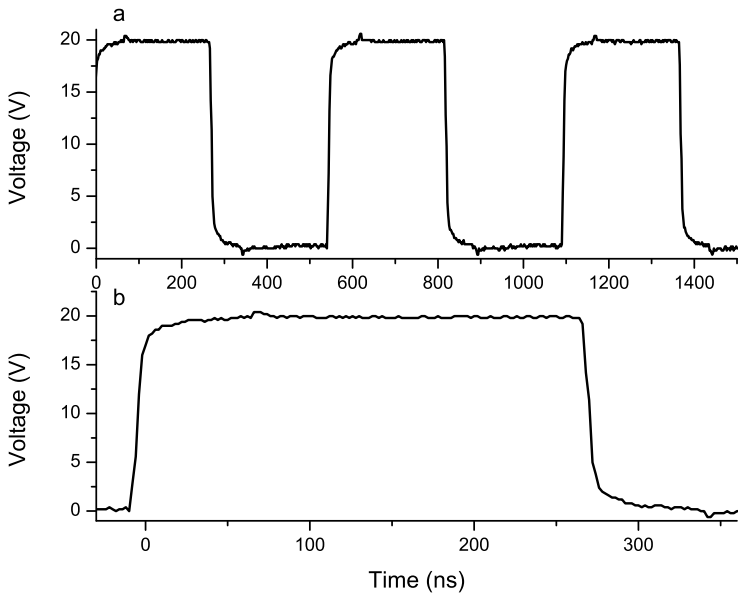

Figure 4.12: Measuring the output of the arbitrary waveform generator set to produce a periodic square pulse. (a) The periodic square pulse output of arbitrary waveform generator with output set to 20 V. Magnitude of output is 20 ± 0.5 V with some noise on the 'flat' sections of the pulse evident in (b) which is the same data with a different x-scale. There is a finite half maximum rise time of ≈ 5 ns.

noise in the instantaneous phase $\phi(t)$, is that taking the time derivative of phase will amplify any error when converting to frequency, $f(t)$.

Figure 4.13d shows the derived $f(t)$ when the analysis is applied to the middle section of the data in figure 4.13 between the two sections of ill-defined frequency. The same range of frequencies was included by the mask.

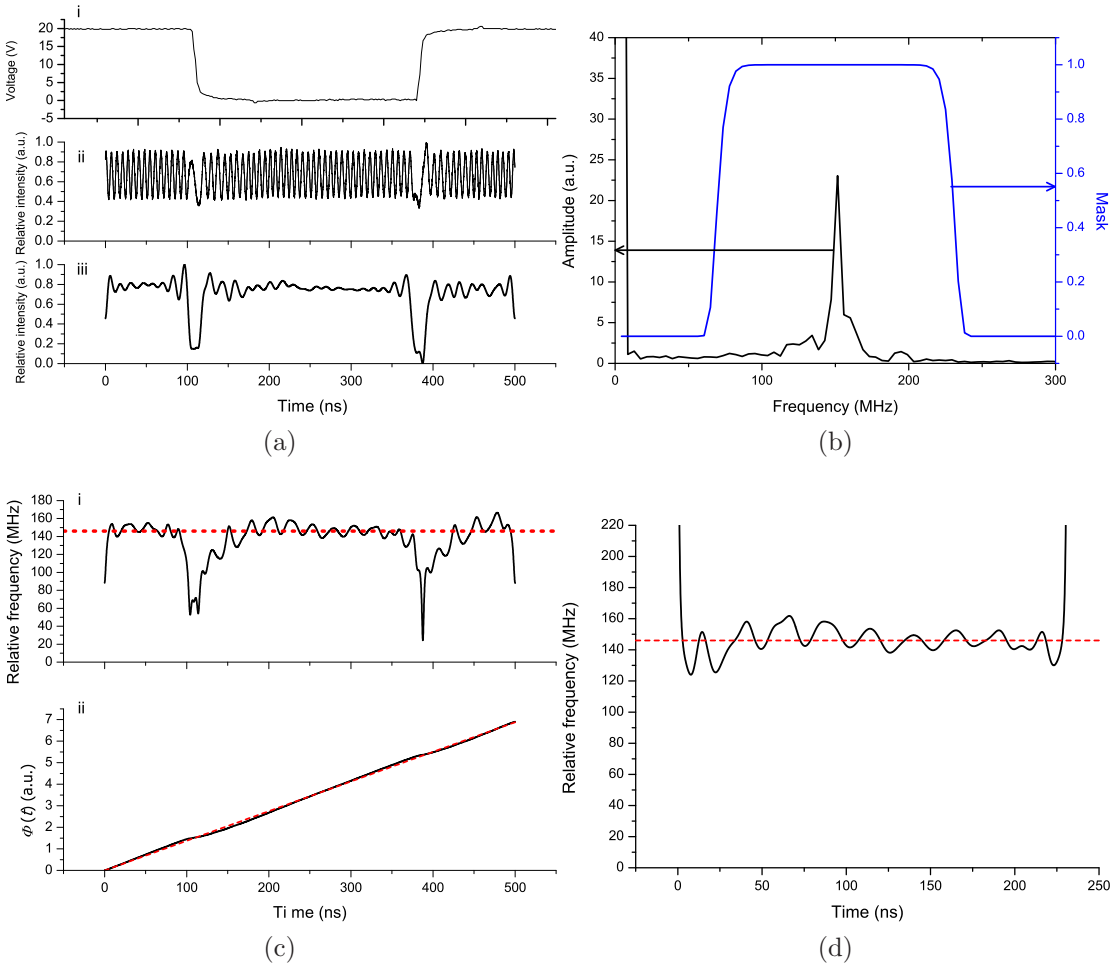

Figure 4.13: Analyzing heterodyne signal measured on a photodiode when a periodic square pulse is applied to the e.o. crystal, to determine the instantaneous frequency difference $f(t)$ (a) i: The periodic square voltage applied to the e.o. crystal, ii: The heterodyne signal, iii: extracted intensity temporal profile. There is intensity modulation of up to 10 % for most of the chirp, increasing to 20 % close to the areas of ill-defined frequency at 110 and 380 ns. (b) The Fourier transform of signal overlaid with super-Gaussian mask including frequencies down to the minimum of $\approx$ 70 MHz up to 230 MHz. (c) i: The derived instantaneous frequency difference $f(t)$ overlaid with a linear fit (applied to central data) which implies, given a voltage of 20 ± 0.5 V, a tunablity of $f_V = 14.6 \pm 0.4$ MHz/V. Oscillations around the predicted frequency are $\approx \pm$ 10 MHz. ii: The instantaneous phase $\phi(t)$ is linear and modulation is < 0.1 % althought there are some discontinuities evident at the times at which $f(t)$ deviates greatly from the fit. (d) As with (c) however when the analysis was applied to the middle section of (a). The applied fit implies a tunablity of $f_V = 14.6 \pm 0.4$ MHz/V, with oscillations around the fit of $\approx \pm$ 10 MHz.

4.6 Linear chirps

4.6.1 Introduction

Up to this point the required linear chirps have been investigated up to ≈ 400 MHz equivalent to a lattice velocity of 213 ms^{-1}. This is much less than required to capture molecules in a molecular jet (400 ms^{-1}) and is limited by the maximum voltage output of the arbitrary waveform generator. The practical difficulty with producing the linear frequency sweep is in producing a linear voltage sweep of approximately 70 V in ≈ 140 ns. A linear change over this period will contain high frequencies, and therefore place high demands on a voltage amplifier. In this regime the design and construction of a circuit is crucial where inductive effects from the wiring can play a dominant role. We investigated a tank circuit, as described in chapter 3, to verify that the maximum required chirp can be achieved with our microchip laser, which can amplify a sinusoidal waveform with a resonance centred around a particular frequency.

A linear circuit is still the ultimate goal. A linear ramp from the maximum frequency difference, equivalent to the optical lattice being equal to the jet velocity down to zero, is the optimum use of the pulse energy. In a sinusoidal ramp, the function changes more slowly at the beginning and the end of a downward change from maximum to minimum. We therefore investigated the linear voltage ramp up to 20 V, whilst considering that in the future further amplification may be needed to reach the required lattice velocity.

4.6.2 Triangular waveform data

We applied a triangular waveform to the arbitrary waveform generator to investigate a continuous linear frequency change. The measured input to the crystal is shown in figure 4.14. There is some rounding off at the top of the function, due to the intrinsic difficulties with producing such discontinuous waveforms, and noise up to ± 0.25 V.

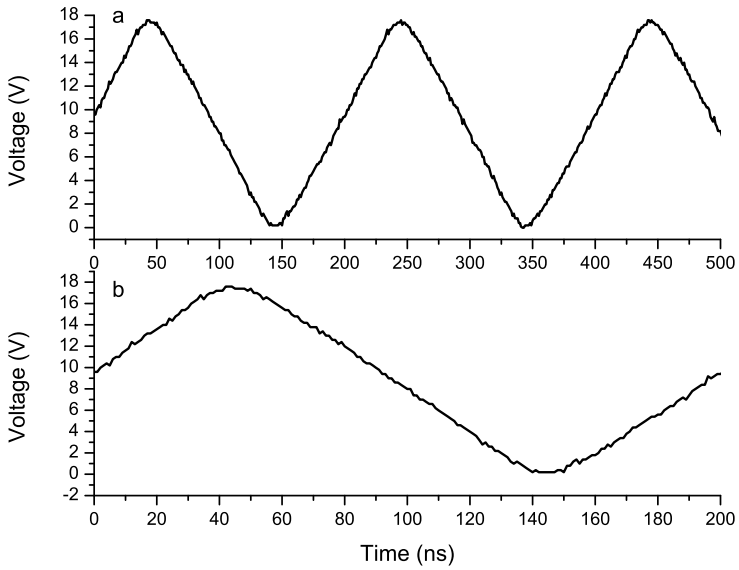

Figure 4.14: (a) The triangular, linear pulse output of the arbitrary waveform generator with output set to 20 V. The magnitude of output is just 18 V however there is some additional, random noise evident in (b) which is the same plot with a different x-scale, along the linear ramps and therefore the error is estimated to be $\pm$ 0.5 V.

4.6.3 Linear chirp analysis

Figures 4.15a (ii) shows the result of heterodyning the output of each fibre when the waveform described in figure 4.14 and 4.15a (i) is applied to the e.o. crystal of our laser system. There is a lot of modulation in the extracted intensity profile shown by figure 4.15a (iii), indicating overlap of the intensity and chirp frequency components in Fourier space. The mask applied in Fourier space included frequencies between 25 and 300 MHz is shown in figure 4.15b. The derived instantaneous frequency difference $f(t)$ and the instantaneous phase $\phi(t)$ is shown in figure 4.15c (i) and (ii) respectively. The modulation in $f(t)$ is $< \pm$ 10 MHz at lower frequencies and up to 20 MHz at higher frequencies. The phase $\phi(t)$ is much smoother. Once again, a small error or noise in the extracted phase is greatly magnified in the derived $f(t)$. A linear fit is overlaid on each individual section of the triangular waveform. The maximum frequency was approximately 276 ± 10 MHz. Given that the maximum voltage applied during the linear ramp was 18 ± 0.5 V according to figure 4.14 this implies that $f_{\mathrm{V}} = 15.3 \pm 0.7$ MHz/V. There is no statistically significant difference between this value and the one derived from the sinusoidal waveform shown in figure 4.4 where $f_{\mathrm{V}} = 14.3 \pm 0.2$ MHz/V. The crystal temperature at which this data was taken (16.95 °C) was the same in both cases, although a period of time had elapsed. It may be that the crystal characteristic had changed slightly over the period between which the data was taken. The other possibility is that the difference is due to

the different modulation frequencies contained within each waveform. Whilst the period of the waveforms are equivalent, a triangular waveform contains much higher frequencies, as discussed in chapter 3. This demonstrated that the tunability f_V can vary greatly for different frequencies. This could be an issue for a linear chirp if the tunability changes over the course of the ramp, however within the limits of the noise which are discussed, this does not appear to be the case. If this is actually responsible for this noise it may be an argument for using a sinusoidal wave-form, despite the disadvantages.

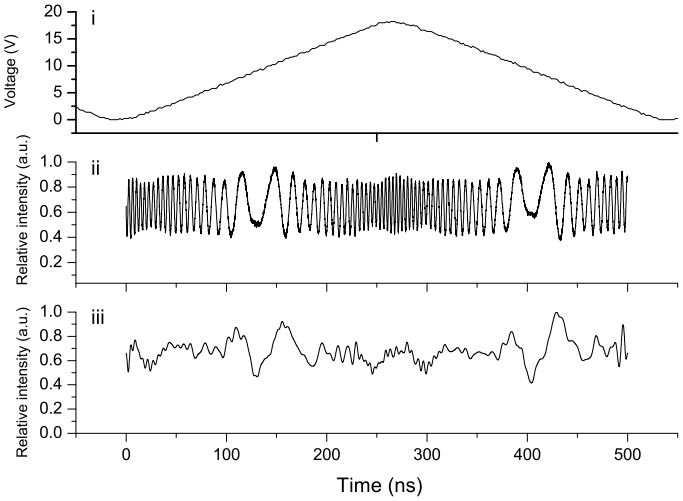

(a)

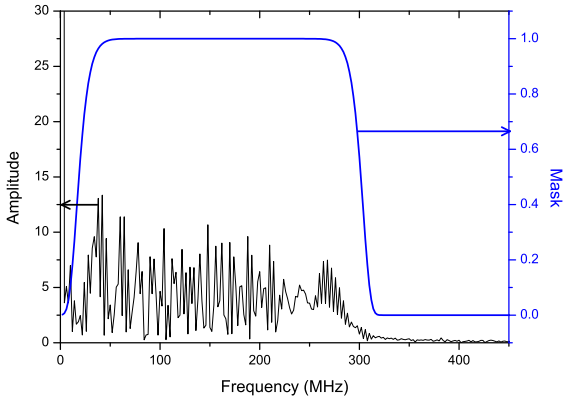

(b)

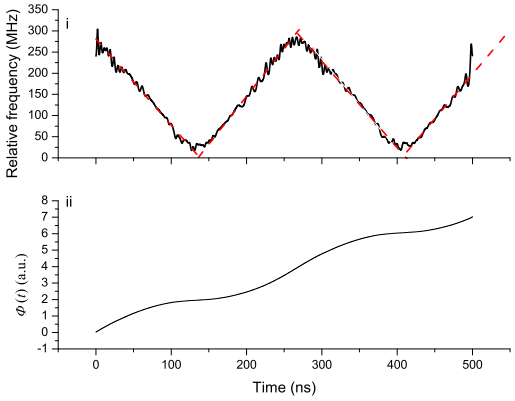

(c)

Figure 4.15: Analyzing heterodyne signal measured on a photodiode when a periodic linear ramp pulse is applied to the e.o. crystal, to determine the instantaneous frequency difference $f(t)$. (a) i: The triangular, linear pulse voltage which was applied to the e.o. crystal, ii: The heterodyne signal, iii: extracted intensity temporal profile. There is intensity modulation of up to 20 %. (b) The Fourier transform of signal overlaid with super-Gaussian mask including frequencies down to the minimum of $\approx$ 25 MHz up to 300 MHz. (c) i: The derived instantaneous frequency difference $f(t)$ overlaid with a linear fit, with phase adjusted for fit and a chirp duration of 137.5 ns. The modulation around this fit is within $\pm \approx 10$ MHz at lower frequencies and up to 20 MHz at higher frequencies, ii: the instantaneous phase $\phi(t)$ has no modulation to the limits of the accuracy of the plot.

4.7 Conclusions

We have demonstrated that our laser system can be chirped using a variety of waveforms. A constant frequency difference was created using a periodic square voltage applied to the e.o. crystal as well as rapid chirps using linear and sinusoidal waveforms. In all cases, the frequency of our laser system follows the applied voltage. Therefore, by simply shaping the applied voltage pulse, we can produce any form of chirp required for our deceleration and acceleration experiments. This is only limited by the speed and amplitude limitations of our voltage source, which we apply to the e.o. crystal.

The analysis on experimental data shows that the type of mask used is still very important in the extraction of the instantaneous frequency difference $f(t)$. The greater amount of noise present in the real data, compared to simulated data, means that there are many more components in Fourier space, making separation from the chirp components both more difficult, and therefore more critical. It seems relatively easy to reduce oscillations to within $\pm$ 10 MHz and this we believe demonstrates that the chirp of the laser follows the waveform of the applied voltage to this degree of accuracy.

To reduce oscillations further, we can exclude lower frequencies more, however this is at the expense of a higher limit to the lowest frequency that can be analysed. Once again, shifting the frequency of one of the arms for heterodyning, using a device such as an A.O.M., would be one way of ensuring that the minimum frequency has less overlap with the other components in Fourier space. Given that the limit of accuracy of the frequency given by the width of the data window is $\approx$ 3.3 MHz, there is little to gain in restricting the window to reduce oscillations below this.

It is very clear that maximising the signal to noise ratio is also crucial in enabling better separation in frequency space of the chirp and temporal intensity components. This could be achieved by ensuring a larger amount of optical signal. In addition, ensuring maximum modulation due to heterodyning by ensuring good spatial overlap of the two beams and matching of beam size will improve the signal. Reducing electronic noise by using double shielded co-axial cable would also help.

In the next chapter, this analysis will be used to derive the instantaneous frequency difference $f(t)$ for the pulse amplified data and compared to CW data, in order to verify that no additional chirp is imparted during pulsed amplification in the Nd:YAG rods.

Chapter 5

Pulsed Amplification

5.1 Introduction

The output from the slave diode laser is coupled into a fibre amplifier (IPG: YAR-1K-LP-SF), where it is amplified from 100-1000 mW, depending on requirements. This part of the laser system is described in chapters 3 and 4. As we require intensities on the order $10^{14} - 10^{15}$ W m^{-2} for deceleration and acceleration of molecules, we must amplify the output of the fibre amplifier in a pulsed amplifier for pulse durations in the 100's ns regime and pulse energies of $\approx$ 300-500 mJ per pulse as shown in figure 5.1. Before pulsed amplification, the output of the fibre amplifier is passed through a pulse shaper, consisting of a Pockels cell and polariser, which will later be used to chop the beam up into pulses for pulsed amplification.

5.2 Producing pulses from the continuous wave (cw) laser

We only need to amplify for the duration of the pulse (20 - 1000 ns). To do this we chop the cw beam into pulses of the required duration using a pulse shaper consisting of a Pockels cell (Kentech, provided by Continuum Lasers) and a polarising beam splitter, as shown by figure 5.1. The Pockels cell is used to rotate the polarisation of the light by an amount which depends on the voltage applied. The pulse shaper is set up so that the polarisation of the light that is output from the fibre amplifier is rejected by the polariser, sending it into a beam dump. When a larger voltage is applied, the polarisation rotates such that an increasing amount of light is able to pass through the polariser up to a maximum value of > 99 % of the total input power. A computer is used along with software provided by Continum, (Pulse 16.exe) to program the pulse shaper to apply a continuous range of voltages to the

Pockels cell in the pulse shaper. This rotates the polarisation from its original state to an orthogonal or any intermediate state, allowing almost continuous attenuation. Since for most purposes we require flat-top temporal profiles at the output of the pulsed amplification system, we must shape the input pulses to compensate for the non-linear gain of the Nd:YAG amplifying rods.

In some situations for example, alignment of the laser system, or monitoring of cw beams without pulsed amplification, the half-wave plate must be rotated so that light is transmitted by the polarising beam splitter when the Pockels cell is switched off.

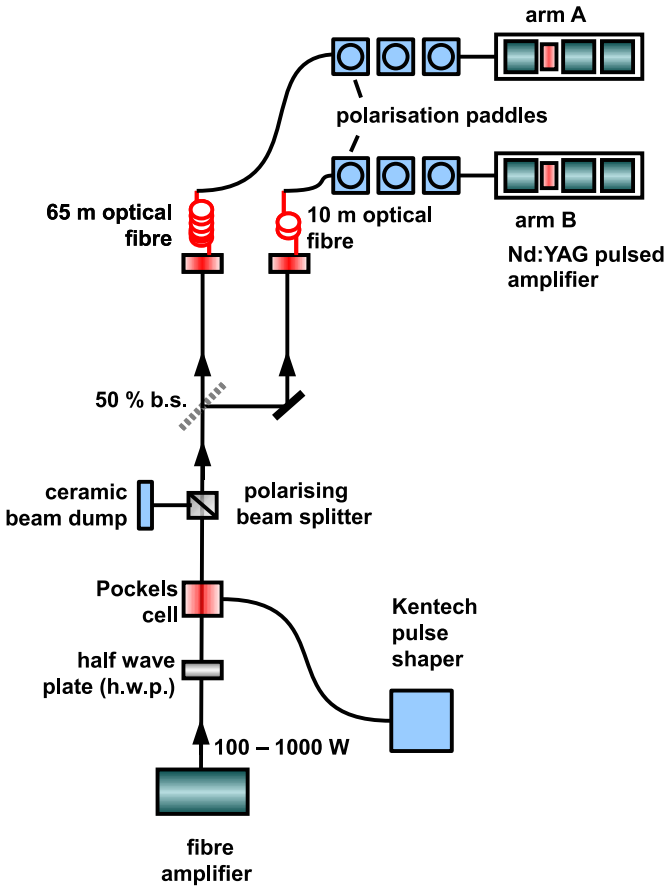

Figure 5.1: Detailed schematic of the laser system after cw amplification in the fibre amplifier up to the pulsed amplification stage. This includes the pulse shaping section and paddles which use stress induced birefringence to correct the polarisation, scrambled during passage through the fibre, for correct operation in the Nd:YAG amplifier system.

5.3 Pulsed amplification

5.3.1 Introduction

There are three stages of amplification in each arm, each one consisting of 100 mm long, 6 mm diameter Nd:YAG rods. These are flash lamp pumped at 10 Hz, which are triggered from an internal clock in the power supplies provided by Continuum. When seeded by our cw system, there is large amplification caused by the stimulated emission from the Nd:YAG gain medium at the same frequency as the seed (master microchip laser). Before the first stage of amplification there are two high power isolators in each arm (EOT: CR1064, and EOT: 04-00842, both with $\approx$ 30 dB extinction) which prevent light from traveling backwards from the amplifiers to the seed, which would cause considerable damage to the fibre ends, or to preceding optical apparatus. After the second stage of amplification there is a high voltage Pockels cell ($\approx$ 1.5 kV) and polariser combination which is used to prevent light from passing through the third stage of amplification, except when triggered to do so. This serves the primary purpose of preventing the build up of spontaneous emission, and stopping amplified light traveling in the opposite direction, back through the other amplifiers and causing run away amplification. We can also use the Pockels cell to sharpen the rise time of the pulses.

5.3.2 Pulse shaping requirements

Due to the time varying gain $G(t)$ in the Nd:YAG amplifying rods during amplification, we must shape the input pulses $I_{\text{in}}(t)$ in order to produce output pulses of the correct shape and length $I_{\text{out}}(t)$. The relationship between the input and output temporal profiles, assuming large signal can be written as

$$I_{\text{out}}(t) = I_{\text{in}}(t) \times G(t), \tag{5.1}$$

where the time dependent gain can be described by [106],

$$G(t) = \frac{G_0}{G_0 - (G_0 - 1)\exp\left[-U_{\text{in}}(t)/U_{\text{sat}}\right]}, \tag{5.2}$$

and $U_{in,out}(t) \equiv \int_{t_0}^{t} I_{\text{in,out}}(t)dt$. G_0 and U_{sat} are constants for the initial gain and a saturation intensity respectively. If we require a flat top output intensity then this means that I_{out} is a constant k and therefore $U_{\text{out}} = k\ t$.

If we want to specify the required gain profile $G(t)$ for a given output pulse shape,

then this can be alternatively written in the presence of saturation as [106]

$$G(t) = 1 + (G_0 - 1) \exp\left[-U_{\text{out}}(t)/U_{\text{sat}}\right]. \tag{5.3}$$

Since all other variables are constant this implies that

$$G(t) = 1 + (G_0 - 1) \exp\left[-k\ t/U_{\text{sat}}\right]. \tag{5.4}$$

The gain is therefore at a maximum at $t = 0$ when $G(t) = G_0$.

Substituting this into (5.1) implies that we need to provide an exponentially increasing intensity of light $I_{\text{in}}(t)$ in order to produce a constant $I_{\text{out}}(t)$ in order to compensate for the exponentially decreasing gain.

By adjusting the shape and controlling the switch-on of the Pockels cells to nanosecond resolution, the output intensity profile can then be fine tuned.

5.3.3 Overlapping of two pulses

Due to the time delay in the two arms of the laser, caused by the difference in fibre lengths, two pulses must be produced before the beam is split, and two sent into each fibre in such a way that the first pulse exiting the long fibre overlaps with the second pulse exiting the shorter fibre. The first pulse from the short fibre is blocked by the Pockels cells in the pulsed amplification system, and therefore not amplified. The second pulse from the longer fibre is discarded as it does not temporally overlap with the beams which form the optical lattice. Since the gain in each arm is not necessarily the same, due to the Nd:YAG rods and flashlamps, the two pulses can, and may need to be shaped differently in order to create the required flat-top temporal profile of the amplified pulses.

5.3.4 Modeling the gain of our system

By measuring the input pulse on a photodiode, and calibrating it according to the total energy as measured by a power meter, we calculated the temporal profile of the input beam $I_{\text{in}}(t)$. By comparing it to the output pulse that has been measured and calibrated in the same way, we can calibrate the gain $G(t)$ using equation (5.1). Figure 5.2a is a plot of the flat top temporal profile $I_{\text{in}}(t)$ and figure 5.2b shows the resultant amplified $I_{\text{out}}(t)$. Figure 5.2c shows the calculated $G(t)$. For a given input/output pulse there will be a unique $G(t)$ since there is a dependence implicit on the input intensity as shown by equations (5.2) and (5.3).

By applying an iterative fit using the program Origin, with the function given

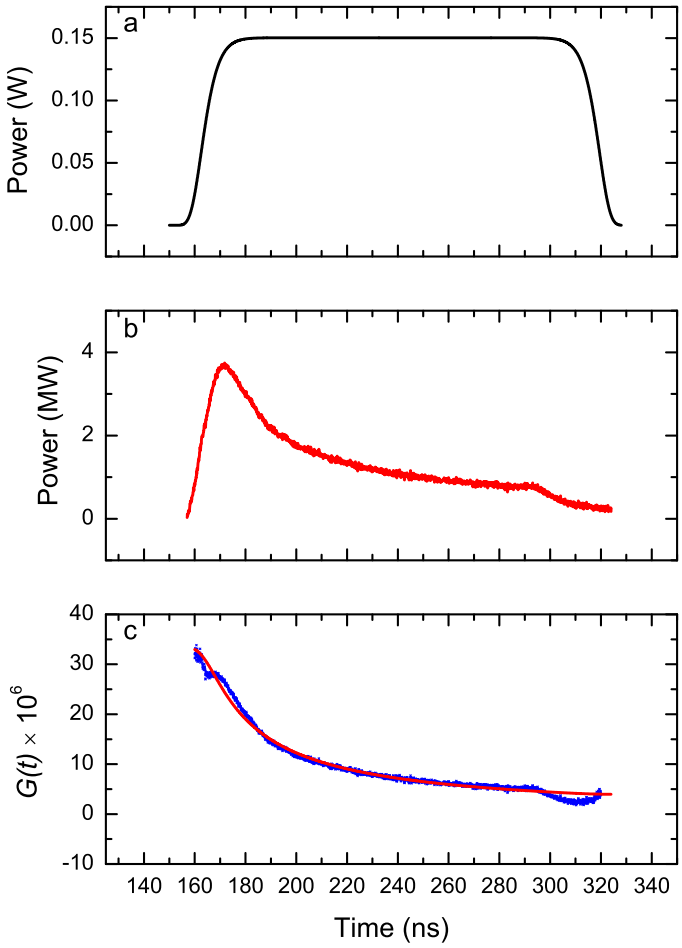

Figure 5.2: (a) The flat top temporal profile of the low power input beam, $I_{\text{in}}(t)$ calibrated for the power axis by dividing the total measured energy per pulse (power of cw beam over the time of the pulse) by the integrated signal as measured by the photodiode. (b) The measured amplified pulse $I_{\text{out}}(t)$ and (c) the calculated time dependent gain profile $G(t)$ with overlaid red trace which is an exponential fit of the form given by equation (5.4). It was found that for this case, $G_0 = 4.6 \times 10^7$, $U_{\text{sat}} = 0.11$ J m^{-2}.

by equation (5.3), the constants G_0 and U_{sat} can be estimated. This fit is shown by the red trace in figure 5.2c. In this case it was found that $G_0 = 4.6 \times 10^7$ and $U_{\text{sat}} = 0.11$ J m^{-2}. Now, by reversing this process we can calculate the required $G(t)$ needed to give a flat top $I_{\text{out}}(t)$ from equation (5.3), since as already stated $U_{\text{in/out}}(t) \equiv \int_{t_0}^{t} I_{\text{in/out}}(t)dt$. Finally from the inverse of equation (5.1) we can calculate $I_{\text{in}}(t)$ from the required $I_{\text{out}}(t)$ and the $G(t)$ just calculated.

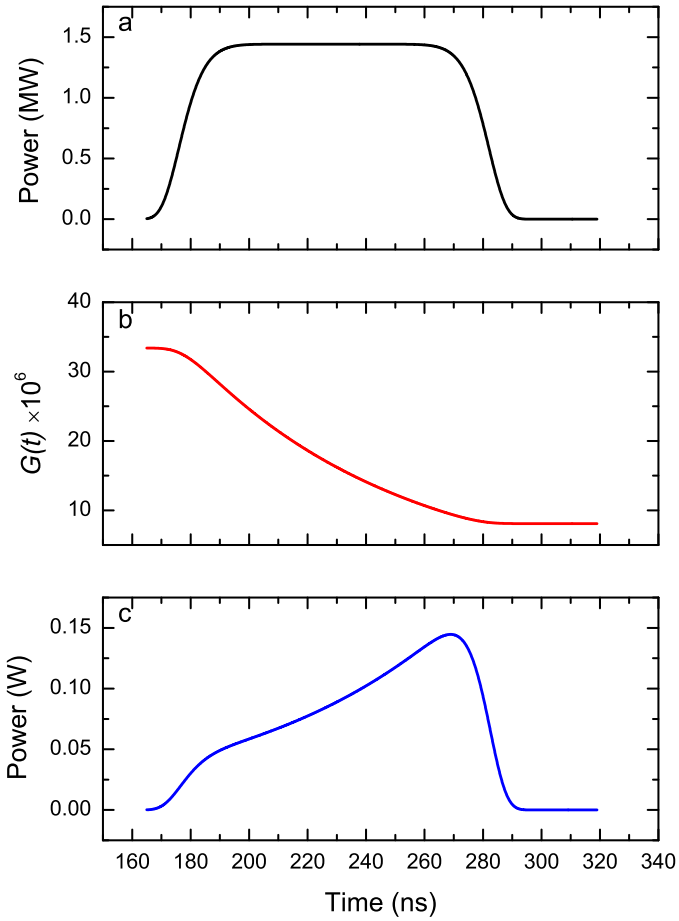

Figure 5.3: (a) The required flat top temporal profile of the amplified pulse, $I_{\text{out}}(t)$, (b) the gain profile $G(t)$ require to give $I_{\text{out}}(t)$ and (c) the input pulse shape $I_{\text{in}}(t)$ required to produce the amplified output beam.

Figure 5.3a shows the desired flat top temporal profile of the amplified beam, $I_{\text{out}}(t)$, figure 5.3b the associated $G(t)$ which would be required to give this output temporal profile and figure 5.3c the calculated temporal profile of the low power input beam, $I_{\text{in}}(t)$ which would produce the required output temporal profile. Of course the instantaneous power as function of time must be converted to the arbitrary values in the pulse shaping software, which can be calibrated using a power meter and photodiode.

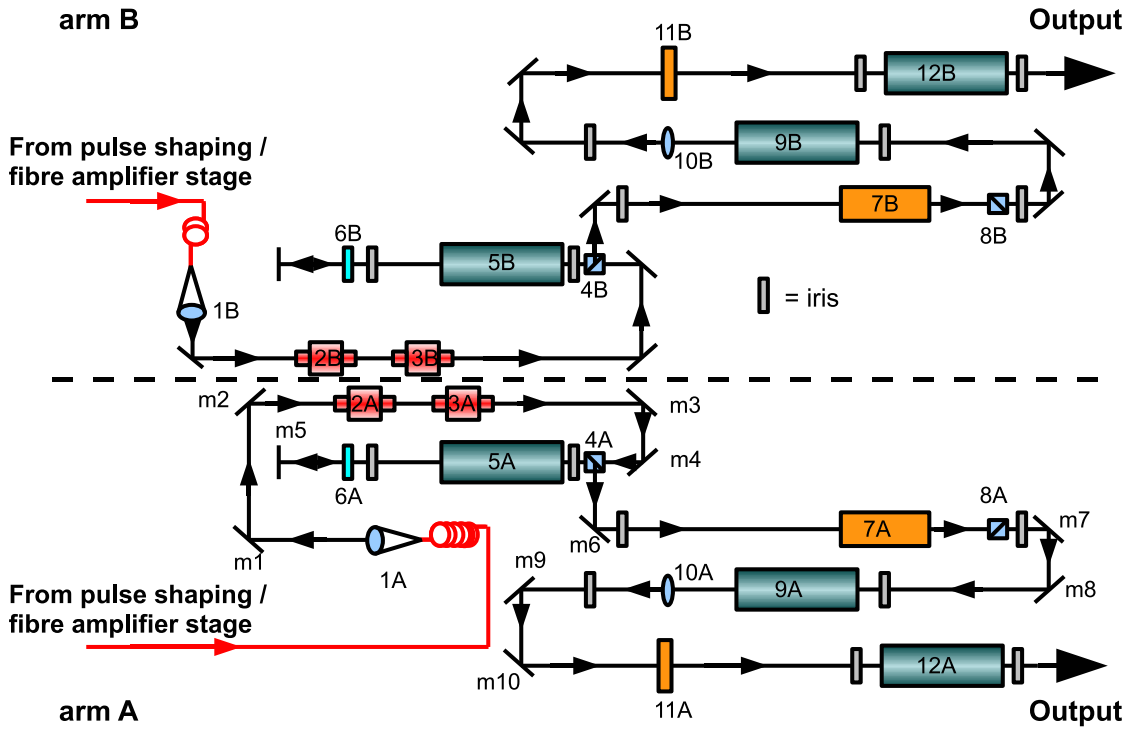

Figure 5.4: Detailed schematic of the Nd:YAG (Continuum) pulsed amplification system, showing both arms used to create the optical lattice.

5.3.5 Alignment Procedures

The output from the optical fibres enters the pulsed amplification stage as shown in figure 5.1. In order to maintain safe and efficient operation, the Nd:YAG pulsed amplification system must be regularly aligned and the output beam profile checked. Small misalignment of the beam through the Nd:YAG rods will result in a reduction in output power and a non-symmetric output beam profile. Larger misalignment is potentially extremely dangerous and could cause damage to the rods or other optics. This can occur because if the beam is clipped by an optic, such as the edge of a rod, it can create a sharp edge to the beam profile. This can cause unwanted diffraction effects, and areas of extremely high intensity at points further down the optical path or at the point of origin due to small back reflections.

Figure 5.4 details the Nd:YAG amplification system. The original custom system designed by Continuum included, in place of the fibre inputs, a single microchip laser (Elforlight) which operated at $\lambda = 1064.1$ nm which was split and then coupled into arms A and B. Since we now require two inputs, which allow us to create a frequency difference between the two arms, the first stage of the system had to be redesigned. As mentioned before, two adjustable lenses (1A, 1B) are fixed to the ends of the fibres in order to create a near collimated, slightly diverging beam and the fibre ends

fixed securely to the optical bread board of the laser. The lenses were chosen so as to create the correct size beam to adequately fill the volume of the Nd:YAG rods, and ensure that the beam does not focus anywhere along the optical path, which given the high intensities involved, could cause damage to the optics.

The rest of the optical path will be described for arm A only since the optical path is essentially identical in arm B. In arm A, the beam is directed by mirrors m1, and m2 through two Faraday isolators (2A, 3A). The paddles are adjusted to correct the polarisation of the light of the fibres using stress induced birefringence, and maximise transmission through the isolators. In total two isolators are required for each arm, to ensure that light can only travel in one direction through the system. A pinhole (10A) is also used before the final stage of amplification to ensure that only light focused at exactly the right spot and on-axis can pass through. This prevents off-axis back reflections, which would focus in a different plane. It also blocks light off-axis.

Mirrors m3 and m4 direct the beam through the first Nd:YAG rod (5A) via polarising beam splitter 4A which allows the light to pass through. The first pair of irises, one after 4A and the other after rod 5A are used for alignment purposes. Firstly, m3 is adjusted to centre the beam on the first iris, then mirror m4 is adjusted to centre the beam on the second iris. This is repeated over many iterations until the beam is aligned centrally through both irises simultaneously. This should ensure that the beam is centred through the amplifying rod. The beam then passes through a quarter wave plate (6A) which rotates the polarisation from linear to circular and is then reflected by a normal incidence mirror m5 where it undergoes another rotation back to linear, however orthogonal to the original polarisation. The beam then passes for a second time through rod 5A, and due to the different polarisation is then reflected by beam splitter 4A where it is directed by mirror m6 through the high voltage Pockels cell (7A).

Mirrors m5 and m6 are then used with the next pair of irises, located after mirror m6 and after polarising beam splitter 8A in the same manner as described before to ensure that the beam is correctly aligned along this path. The high voltage Pockels cell (≈ 1.5 kV), shown as component 7A combined with the polarising beam splitter (8A) ensure that light can only pass once the cell is triggered by a high voltage on the Pockels cell which rotates the polarisation such that the light can pass through the beam splitter. Otherwise, it is rejected on to a beam dump. This ensures that there cannot be a large buildup of amplified spontaneous emission.

Mirrors m7 and m8 direct the beam through the second Nd:YAG rod (9A), where another pair of irises are used to ensure correct alignment. A lens (10A)

with a long focal length ($f \approx 50$ cm) causes the beam to focus at pinhole 11A. Mirrors m9 and m10 direct the beam through pinhole 11A and through the final Nd:YAG rod (12A) which is the final stage of amplification. Another pair of irises are used to ensure correct alignment, where initially pinhole 11A is first removed. Once centrally aligned on both irises, the pinhole is replaced and a piece of white card or lens tissue placed just before the rod (12A). A circular diffraction pattern should appear, caused by the diffraction of the focused beam through the pinhole. The horizontal and vertical position of the pinhole can be finely adjusted with two screws to create a symmetric diffraction pattern, thus ensuring that transmission of the beam waist is maximised. The pulse amplified output is held back by a manually operated shutter to ensure that the high intensity beams are not emitted from the system when not required.

This alignment procedure must then be repeated for arm B, using components 1B to 12B, using the equivalent mirrors and irises. On a weekly basis, one only needs to check the output power, and beam profile to check for misalignment. Often a slight adjustment of the final stage, with mirrors m9 and m10 and pinhole 11A (and the equivalent for arm B) is sufficient to maintain a good Gaussian beam profile and normal operating pulse energies 300-500 mJ / pulse. Generally full alignment of the whole arm was only necessary on a monthly basis.

5.3.6 Beam profile

A typical beam profile is shown by figure 5.5. The vertical diffraction lines and spots on the image are due to the many neutral density filters that had to be placed in front of the camera. This was verified by moving them around and checking which part of the image moved. The unfocused beams are approximately 4-5 mm in diameter at the exit of the pulsed amplifier.

5.4 Timing

One of the major parameters which had to be controlled in this laser system was the timing of the pulses. Firstly, as described in section 5.3.3 on pulse shaping, two pulses were sent through each fibre in such a way that two of the four pulses were temporally overlapped. The high voltage Pockels cells were timed to trigger at the right moment to allow these pulses to be transmitted at the correct time. Their rise time of ≈ 5 ns also allowed for the sharpening of the rising edge of the pulses from each arm.

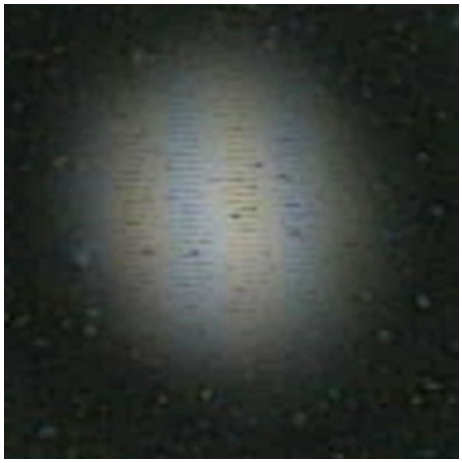

Figure 5.5: A typical beam profile of the pulse amplified output. Beam is $\approx 4-5$ mm in diameter at exit of pulsed amplifier.

A timing diagram for the various triggering events is shown in figure 5.6. All timing for the laser operations and subsequent experiments were carried out with two pulse/delay generators (DG535, Stanford Research Systems Inc.). These devices operate from an internal trigger or can be externally triggered as in our case and can then provide up to four single outputs, A, B, C, D or triggered output pulses of fixed length, A-B, C-D or fixed 'always on' voltages with controllable 'switch-off' pulses of length A-B or C-D. The master trigger t0 was the 10 Hz timing signal from the power supply unit of the Nd:YAG amplification system. An output trigger 108 μs after t0 was used to trigger the Kentech pulse shaper,which is in order to coincide with the build-up in gain of the amplifiers. Approximately 400 ns after this the high voltage Pockels cells were then triggered, which takes into account the time delay for light to pass from one end of the fibres to the other and through approximately 2 m of the pulse amplifier.

5.5 Pulsed outputs for a constant velocity lattice

We now need to verify the behaviour of our pulsed laser system when chirped. Figures 5.7 and 5.8 show the heterodyne (beat) signal, the derived intensity profile, as well as the Fourier transform and mask used to extract the instantaneous phase components and derive the instantaneous frequency of time $f(t)$. The data was taken when a constant velocity lattice was created by the application of a periodic square voltage of 20 V to the e.o. crystal, for the pulsed amplified output. Also shown is the frequency as a function of time $f(t)$ derived from the Fourier transform analysis. In the first case a wider mask is applied which includes frequencies between 220 and

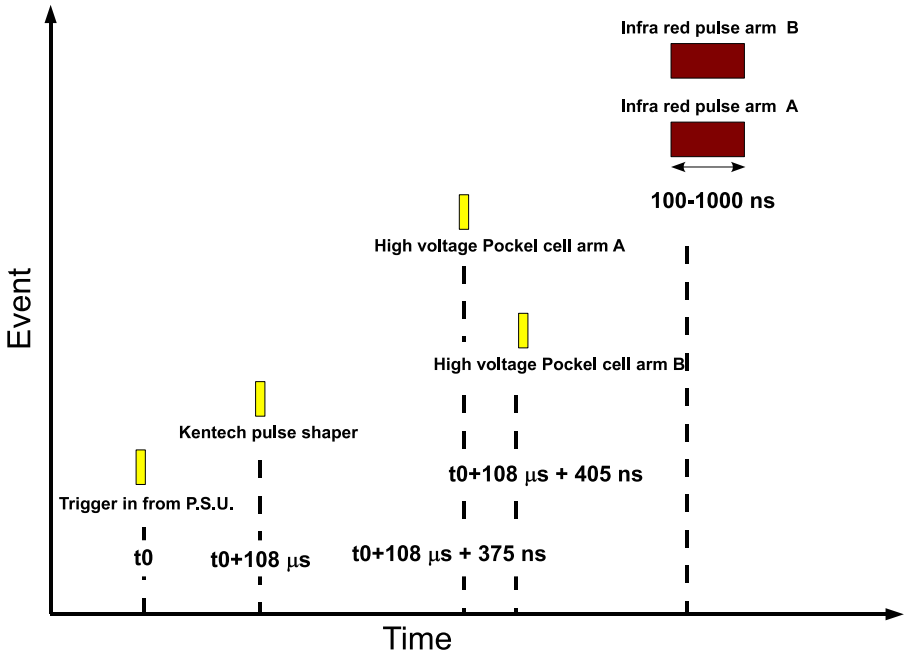

Figure 5.6: Visualisation of the various events that have to be co-ordinated for operation of the laser system and synchronisation of the output laser pulses.

380 MHz. The tunability was calculated to be $f_V = 14.4 \pm 0.4$ MHz/V, given an applied voltage amplitude of 20 ± 0.5 V and a linear fit (applied to central data) to the derived frequency $f(t)$. There is intensity modulation in figure 5.7a (ii) up to 10 % for most of the chirp, comparable to the actual pulse, increasing to 20 % at the beginning of the pulse indicating some overlap between the Fourier components. Oscillations around the predicted frequency in figure 5.7c (i) are, $< \pm$ 10 MHz. The instantaneous phase, $\phi(t)$ shown in figure 5.7c (ii) is without modulation and is linear, as we would expect for a constant frequency $f(t)$, to a slope error of $< 0.1\%$. There are however discontinuties at the beginning and end of the pulse, coinciding with the points at which $f(t)$ deviates greatly from the fit.

The linear fit applied to figure 5.8c (i) implies a tunability of $f_V = 14.6 \pm 0.4$ MHz/V, which is in good agreement with figure 5.7. These are both in good agreement with the tunablities calculated for the low power cw case, where the tunablity was calculated to be 14.6 ± 0.4 MHz/V.

Figure 5.8a (ii) shows intensity modulation up to 10 % for most of the chirp, increasing to 20 % at the beginning of the pulse indicating overlap between the Fourier components. Figure 5.8c (i) shows oscillations of $f(t)$ around the predicted frequency are much smaller, $< \pm$ 2 MHz between 50 and 175 ns than in figure 5.7c (i). The instantaneous phase, $\phi(t)$ shown in figure 5.7c (ii) is without modulation and is linear, as expected for a constant frequency $f(t)$, with slope error of < 0.1 %.

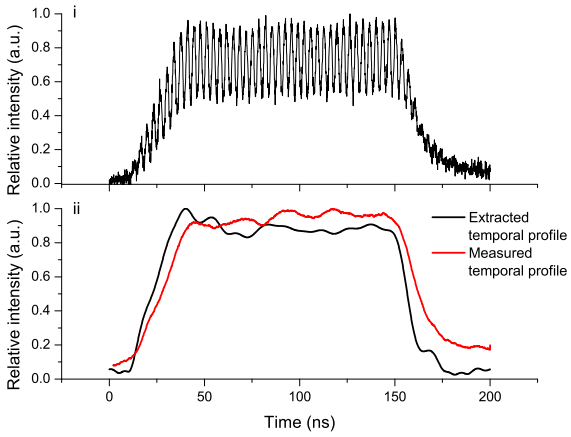

(a)

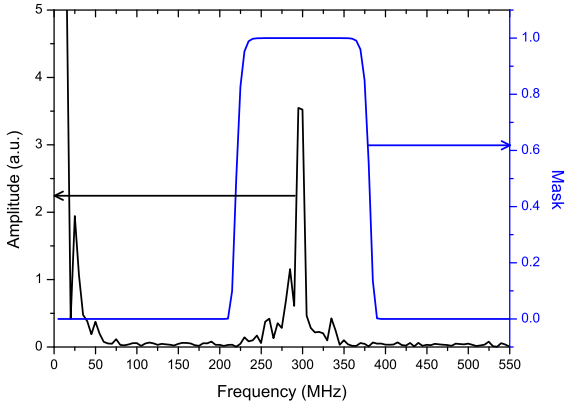

(b)

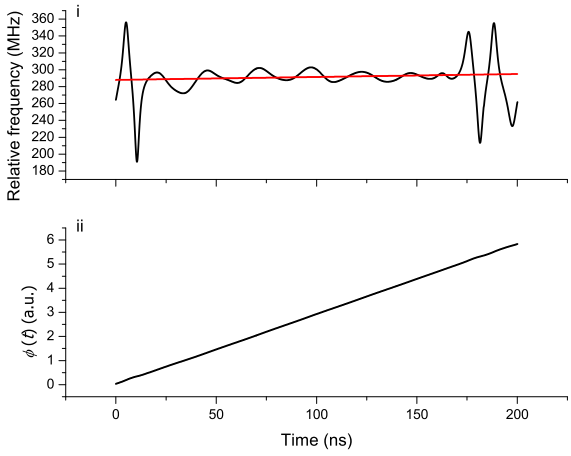

(c)

Figure 5.7: The heterodyne signal measured on a photodiode when a periodic square pulse is applied to the e.o. crystal, to determine the instantaneous frequency difference $f(t)$. (a) i: Heterodyne signal, ii: Extracted intensity temporal profile. The red trace shows the input temporal profile of the beams used to heterodyne. (b) Fourier transform of signal overlaid with super-Gaussian mask including frequencies down to the minimum of $\approx$ 220 MHz up to 380 MHz. (c) i: Derived instantaneous frequency $f(t)$ overlaid with a linear fit (applied to central data), indicating $f_V = 14.4 \pm 0.4$ MHz/V. ii: Extracted instantaneous phase $\phi(t)$.

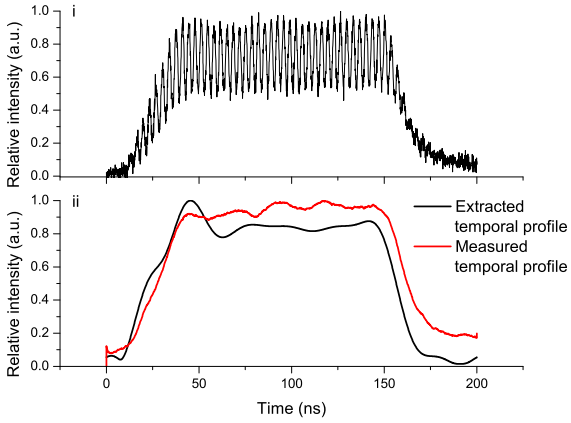

(a)

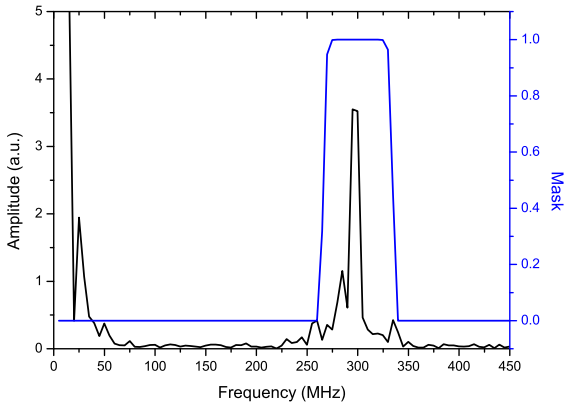

(b)

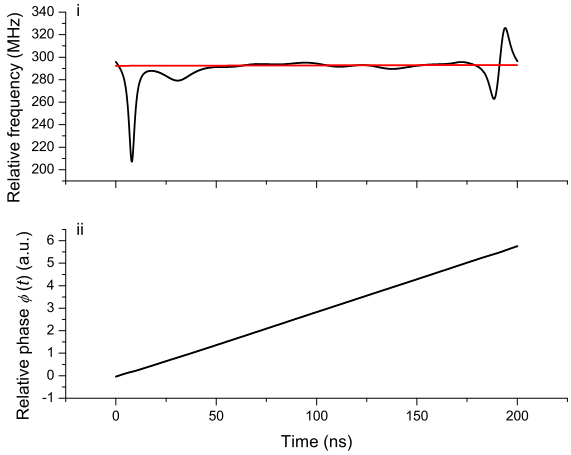

(c)

Figure 5.8: The heterodyne signal measured on a photodiode when a periodic square voltage pulse is applied to the e.o. crystal, to determine the instantaneous frequency difference $f(t)$ with a different width mask. (a) i: Heterodyne signal, ii: Extracted intensity temporal profile. The red trace shows the input temporal profile of the beams used to heterodyne. (b) Fourier transform of signal overlaid with super-Gaussian mask including frequencies down to the minimum of $\approx$ 270 MHz up to 340 MHz. (c) i: Derived instantaneous frequency $f(t)$ overlaid with a linear fit (applied to central data) of 14.6 $\pm$ 0.4 MHz/V. ii: Extracted instantaneous phase $\phi(t)$.

5.6 Linear chirped pulses

Figure 5.9 shows the beat signal, the derived intensity profile, as well as the Fourier transform and mask used to extract the instantaneous phase components, when a periodic triangular voltage with a maximum excursion of 20 V is applied to the e.o. crystal, for the pulsed amplified output. Also shown is the derived frequency as a function of time $f(t)$ derived from the Fourier transform analysis.

Figure 5.9a shows the intensity profile of one of the pulsed beams used to produce the heterodyne signal in Figure 5.9b. The timing is adjusted so that the maximum frequency occurs at the half maximum intensity (24 ns), and zero frequency (162 ns). The instantaneous frequency $f(t)$ is shown in figure 5.9c with a linear fit applied between 27 and 130 ns, omitting the region where the analysis fails due to poor extraction of low frequencies, and at the beginning of the pulse where the intensity is not at maximum. This fit is then extrapolated to include the full range of the chirp. Given that the applied voltage is estimated to be of magnitude 18 $\pm$ 0.5 MHz/V, the tunability is calculated to be, $f_{\mathrm{V}} = 15.3 \pm 0.7$ MHz/V. This is in good agreement with that calculated for the low power cw case.

5.7 A comparison between the pulse amplified and low power cw beam during chirp

Figure 5.10 shows the data taken with a sinusoidal chirp for the pulsed laser, to demonstrate that our laser can be chirped up to the required excursion of ≈ 1 GHz, with figures 5.10a and figure 5.10b showing the intensity profile and heterodyne signal respectively. Figure 5.10c shows the extracted frequency $f(t)$ for the pulsed signal. A fit applied to this data gives a tunability, $f_{\mathrm{V}} = 14.4 \pm 0.2$ MHz/V. For comparison figure 5.10d shows $f(t)$ for the low power cw, where a fit indicates a tunability $f_{\mathrm{V}} = 14.3 \pm 0.2$ MHz/V. These are consistent with each other within the error bounds, demonstrating once again that no additional chirp is imparted during pulsed amplification.

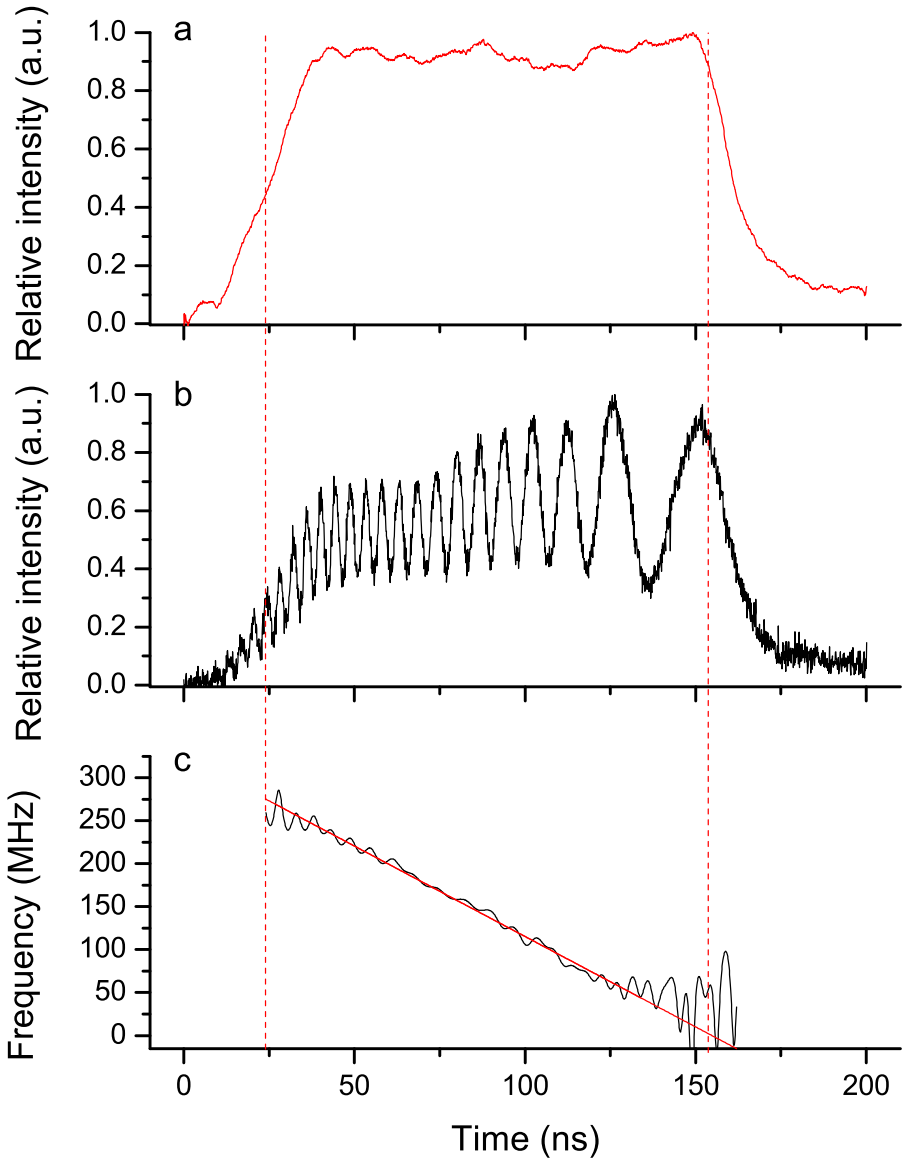

Figure 5.9: The heterodyne signal measured on a photodiode when a periodic triangular voltage pulse is applied to the e.o. crystal, to determine the instantaneous frequency difference $f(t)$. (a) Measured intensity profile of the amplified pulsed used with 50 point adjacent averaging. (b) The heterodyne (beat) pattern when a linear ramp is applied, with the phase of the voltage applied adjusted so that high frequency and zero frequency occur at the half maximum intensity of the pulse, at 24 and 161 ns respectively. (c) The extracted frequency $f(t)$ for the area of interest, from high to zero frequency. A linear fit is applied for the region between 27 and 130 ns before the oscillations. This fit is then extrapolated from 130 - 161 ns, to include the full chirp period of 137 ns. This indicates a relative frequency of -13 MHz at 161 ns and 275 MHz at 24 ns. Given applied voltage of 18 ± 0.5 V, tunability is estimated to be $f_V = 15.3 \pm 0.7$ MHz/V.

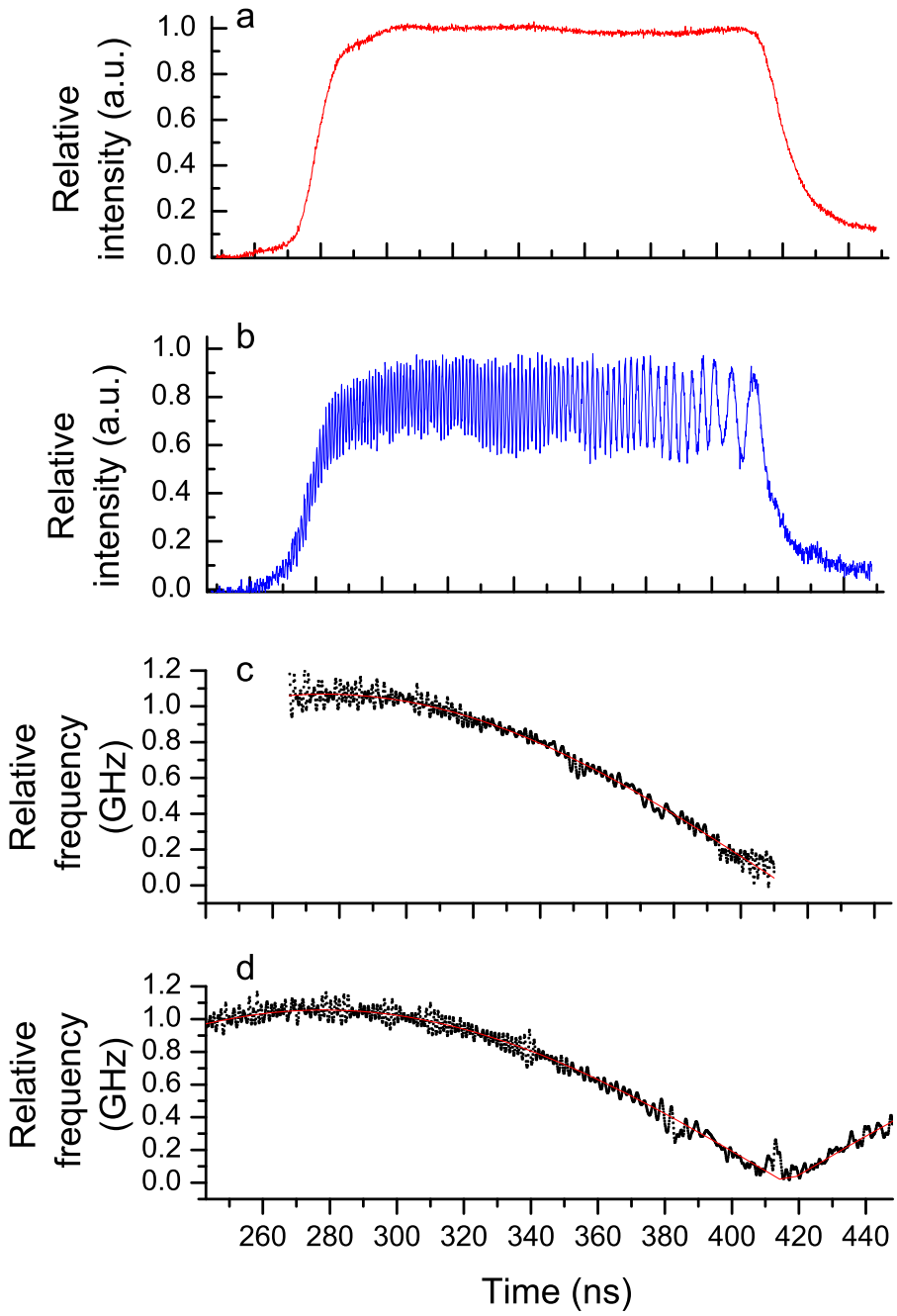

Figure 5.10: The heterodyne signal measured on a photodiode when a sinusoidal voltage pulse is applied to the e.o. crystal, to determine the instantaneous frequency difference $f(t)$. (a) The input profile of one of two pulse amplified laser beams which are heterodyned on a photodiode with 20 point adjacent averaging. (b) The heterodyne beat patten produced by the two pulse amplified beams, detected on a photodiode due to sinusoidal chirp with frequency 1.82 MHz and amplitude 74.0 $\pm$ 0.05 V. (c) Instantaneous frequency as a function of time determined from the data in (b) determined to within an uncertainty of $\pm$ 10 MHz. Applying a fit to this data indicates a tunability of, $f_{\mathrm{V}} = 14.4 \pm 0.2$ MHz/V. (d) Instantaneous frequency as a function of time for identical un-amplified continuous wave case for comparison. The same fit indicates $f_{\mathrm{V}} = 14.3 \pm 0.2$ MHz/V.

5.8 Summary of tunability measurements for low power and pulse amplified cases

Overall, the data taken at a Nd:YVO_4 temperature of 16.95 °C, for the constant and linear ramp lattices, are in good agreement between their respective cw and pulse amplified data and also for the d.c. tunability at the same temperature where $f_V = 14.7 \pm 0.2$ MHz/V. In summary, for a constant velocity lattice, the tunability was calculated to be, $f_V = 14.6 \pm 0.4$ MHz/V, and 14.4 ± 0.4 MHz/V for low power cw and pulse amplified cases respectively. For a linear ramp, $f_V = 15.3 \pm 0.7$ MHz/V, 15.3 ± 0.7 MHz/V for low power cw and pulse amplified cases respectively. The sinusoidal chirp, which also demonstrates the largest frequency excursion, is also in good agreement with the constant velocity case, $f_V = 14.3 \pm 0.2$ MHz/V, 14.4 ± 0.2 MHz/V for low power cw and pulse amplified respectively, however is noticeably lower than the linear case. The bounds for the linear case indicate a slightly higher tunability however it is possible that this is due to the increased error in estimating the tunability for the linear chirping case, where both the frequency sweep and voltage applied are less certain. The other possibility, given that the the crystal characteristics are unlikely to have changed in the time between data readings, is that the response to the voltage of the e.o. crystal is different due to different frequency components in a linear chirp, compared to the d.c. operation or sinusoidal operation. It has already been shown in chapter 3, that the modulation frequency of the applied voltage affects the tunabliity.

The evidence is certainly that, within the limits of accuracy of our data, the very important result that no additional chirp is introduced during pulsed amplification.

Our laser system can produce two laser beams which can be chirped to produce in excess of 1 GHz between them over durations of 100's ns, for a sinusoidally applied voltage with an amplitude of ≈ 70 V and modulation frequency of 1.82 MHz. For other frequency modulations, the tank circuit used to amplify the voltage supplied by the arbitrary frequency generator (limited to 20 V) would need to be adjusted in order to have the appropriate response at the required frequency. We are to produce intensities in the $10^{14} - 10^{15}$ W m^{-2} range and are able to control their temporal profile to a resolution of ≈ 7 ns and use this to produce near flat top pulses which are the most suitable for deceleration or acceleration of molecules.

A linear chirp up to 200 MHz can be produced, with further amplification needed to extend this to the required frequency excursion.

5.9 Non periodic linear chirps

5.9.1 Voltage ramp

We also investigated other linear voltage ramps in order to produce the ideal situation which would include 'flat regions' of no chirp at the beginning and end of the pulse, to allow for the finite rise and fall time of the laser beam intensity. For example, for deceleration we require a region where the lattice velocity, and therefore frequency difference is constant at the beginning so the lattice is moving at the same speed as the molecules as the intensity increases from zero to maximum. We also require a time period after the frequency difference has chirped down to zero, where the chirp has stopped and this 'zero' velocity is maintained whilst the lattice beams are switched off.

We therefore used the arbitrary frequency generator to create a voltage pulse which was not periodic but creates regions of fixed frequency difference at the beginning and end of the pulses. This allows the pulses to switch on and off, similar to that modeled earlier, for example in chapter 2. This was due to the fact that simulations have indicated the importance that the beam intensity has reached the maximum value before the chirp starts, and should then finish, before the beams switch off.

Figure 5.11a shows the voltage trace which was designed for a decelerating lattice, showing the voltage pulse that was applied to the electro-optic crystal (e.o.). The offset in time for arm B is created by the time delay in the fibres. In reality there is only one voltage pulse applied, however as these traces are also proportional to the relative frequency of the two arms, these traces demonstrate the relative frequency between each arm. Up to the start of region 1, the voltage of arm B rapidly rises where it remains flat for ≈ 100 ns, which would create a fixed frequency difference to allow the laser beams to switch on. In region 2, the frequency (voltage) of arm B rapidly chirps down over a duration of 70 ns towards the frequency of arm A, which creates a decelerating lattice. In region 3, the frequencies of the two arms are equal which would represent a stationary lattice, to allow the laser beams to switch off.

Figure 5.11b shows a similar voltage trace applied to the e.o. crystal, designed to create an accelerating lattice. In region 1 the frequencies are equal, which would create a stationary lattice. In region 2, the frequency of arm B chirps up, over a duration of 70 ns which would create an accelerating lattice. In region 3 the frequency of arm B is kept at a constant offset from A, creating a constant velocity lattice.

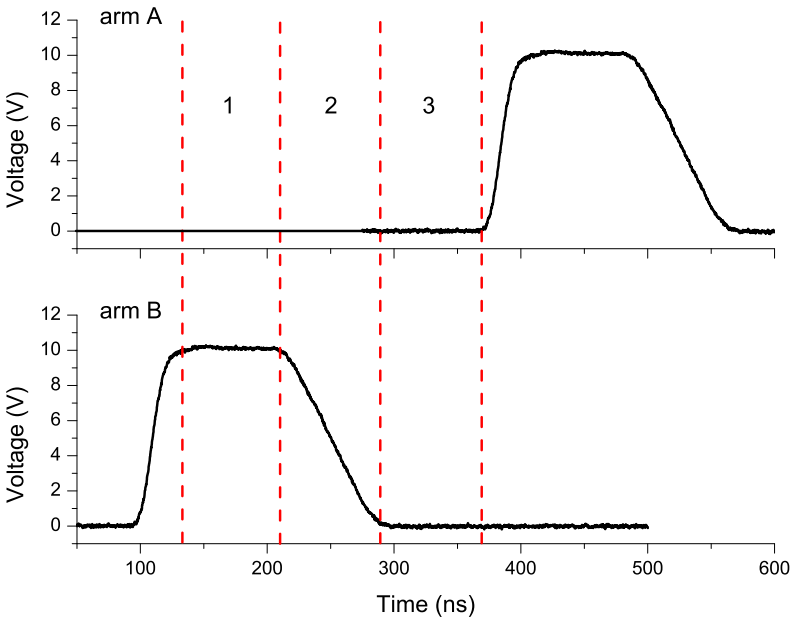

(a) Deceleration

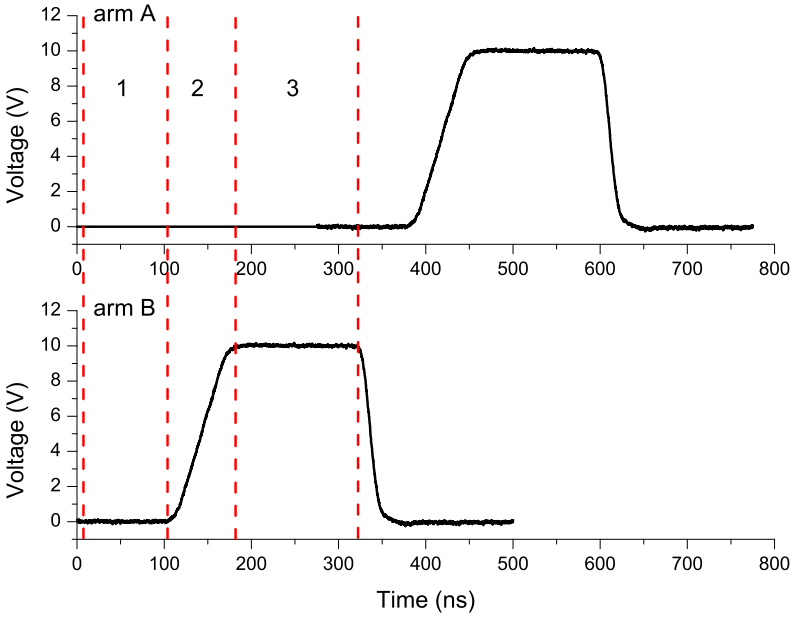

(b) Acceleration

Figure 5.11: The arbitrary waveforms of the applied voltage to the e.o. crystal. A single pulse is applied however the offset between arm A and B is to demonstrate the time delay introduced by the difference in fibre lengths. (a) The function designed for a decelerating linear chirp during region 2, with a region of fixed and zero frequency difference in regions 1 and 3 respectively. (b) The function designed for an accelerating linear chirp during region 2, with a region of zero and fixed frequency difference in regions 1 and 3 respectively.

5.9.2 Heterodyning: a decelerating lattice

We measured the heterodyne signal with the voltage pulse described applied to the e.o. crystal, as shown by figure 5.11a, however with a total voltage excursion of 20 V. Figure 5.12a shows the input temporal profile of one of the pulses, figure 5.12b shows the heterodyne signal and figure 5.12c shows the derived instantaneous frequency $f(t)$.

For this data, an A.O.M was used to offset the frequency of one of the output beams by ≈ 90 MHz. This was done in order to overcome the difficulty in analysing low frequencies. In this way a zero velocity lattice would be observed by a constant 90 MHz beat signal, and the maximum velocity lattice would be offset by the same amount. The timing of the pulse was adjusted so that the chirp region occurred during the flat-top region of maximum intensity and that the regions of constant low and high frequency were at the beginning and end of this flat region during the switch-on and switch-off of the laser beams.

As with previous analysis, a mask was used to separate the frequency components in Fourier space. A linear fit was applied to each region of constant or linearly changing frequency difference. Within the error bounds, the frequency difference remained constant in region 1 at 312 ± 10 MHz, and then chirped over 70 ns down to 98 ± 10 MHz. The fit in region 3 indicates a final frequency difference of 86 ± 10 MHz consistent with the measured A.O.M frequency of 90.7 MHz. This would represent a lattice velocity which changes from ≈ 120 ms^{-1} down to ≈ 0 ms^{-1}.

5.9.3 Heterodyning: an accelerating lattice

We heterodyned the two beams for an accelerating lattice, as shown in figure 5.11b, with a total voltage excursion of 20 V. As before, figure 5.13a and 5.13b show the input temporal profile and heterodyne signal respectively. Figure 5.13c shows the derived instantaneous frequency $f(t)$. As with the previous analysis a mask was used to separate the frequency components in Fourier space. A linear fit was applied to each region. The noise in region 1 required us to use a different mask to reduce the noise at lower frequencies. This data indicates an initial frequency difference of 90 ± 10 MHz in region 1, which is chirped up to 313 ± 10 MHz in region 2 where it remained constant at this value in region 3. This is consistent with the data taken for the decelerating lattice and, taking into account the offset provided by the A.O.M, would represent a lattice velocity that changes from ≈ 0 ms^{-1} up to ≈ 120 ms^{-1}. The tunability for the data taken for the decelerating and accelerating case was calculated to be $\approx 11 \pm 0.5$ MHz/V.

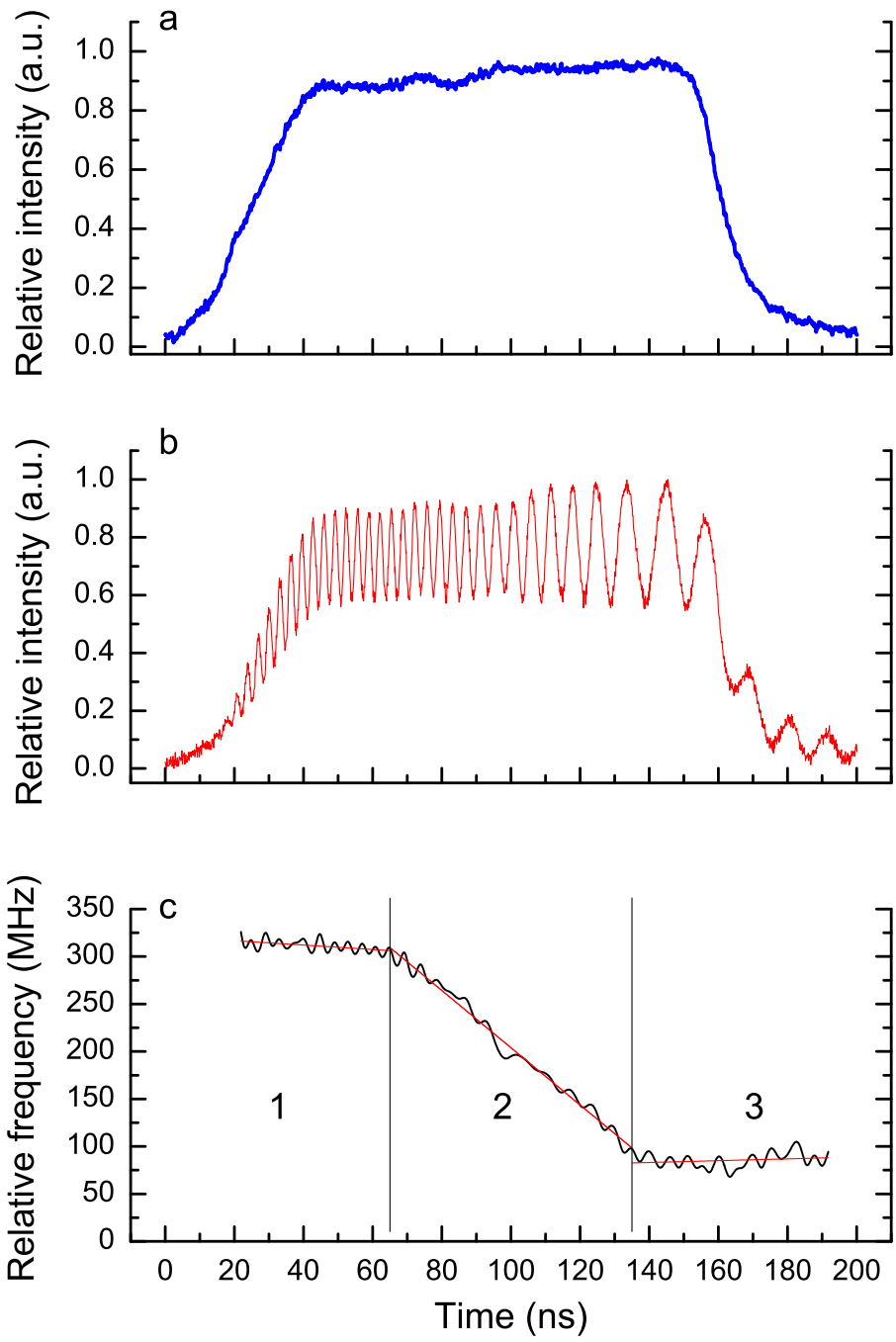

Figure 5.12: The heterodyne signal measured on a photodiode when a 'decelerating' linear voltage ramp is applied to the e.o. crystal. (a) The temporal intensity profile of one of the beams used for heterodyning. (b) The heterodyne signal when an arbitrary voltage ramp, as shown in figure 5.11a is applied to the e.o. crystal. (c) The derived instantaneous frequency $f(t)$. It has been cut up to 20 ns where the intensity was too low to observe clear fringe modulation, as can be seen in (a) and therefore there was excessive noise in $f(t)$. In region 1, a fit is applied after the noisy region, which gives an initial frequency difference from 316 to 308 $\approx \pm$ 10 MHz over the duration of the range. In region 2, a linear fit indicates a chirp rate of $\approx$ 3 GHz/μs, and a change from 308 MHz to 98 $\pm$ 10 MHz. Region 3 indicates a final frequency difference of 83 - 89 $\approx \pm$ 10 MHz over the region, consistent with the A.O.M frequency of 90.7 MHz.

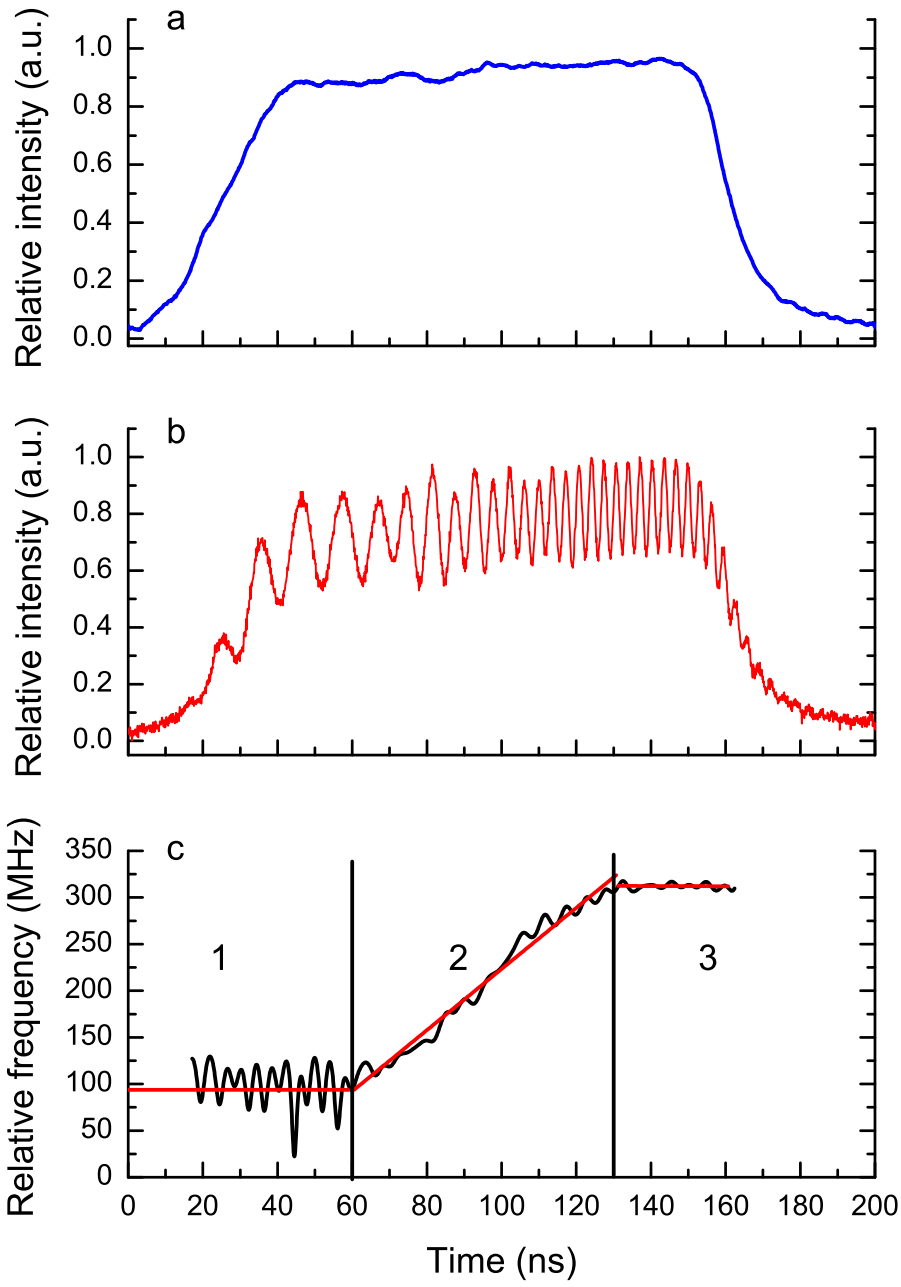

Figure 5.13: The heterodyne signal measured on a photodiode when an 'accelerating' linear voltage ramp is applied to the e.o. crystal.(a) The temporal intensity profile of one of the beams used for heterodyning. (b) The heterodyne signal when an arbitrary voltage ramp, as shown in figure 5.11b is applied to the e.o. crystal. (c) The derived instantaneous frequency $f(t)$. The noise at the beginning of the derived instantaneous frequency is due to the low intensity and poor fringe modulation as can be seen in (a). In region 1, a fit is applied after the noisy region using another mask not shown indicating an initial frequency difference 90 $\approx \pm$ 10 MHz over the duration of the range which is consistent with the offset provided by the A.O.M in one of the beams arms. In region 2, a linear fit indicates a chirp rate of $\approx$ 3 GHz/μs, and a change from 90 MHz to 313 $\pm$ 0.5 MHz. Region 3 indicates a final frequency difference of 313 $\approx \pm$ 10 MHz over the region, consistent with the A.O.M frequency of 90.7 MHz.

This is considerably lower than previously measured. This was based on the applied voltage having an excursion of 20 V. One of the issues with the laser system is that the electrical connections suffer from oxidation and therefore the voltage being applied to the e.o. crystal was lower than indicated by the output of the arbitrary frequency generator.

5.10 Conclusions

We have demonstrated that we can produce pulses with durations of ≈ 100 ns with a near flat-top temporal profile and half-maximum rise times of 10-20 ns.

We can produce a chirp function which remains constant at the beginning and end of the required temporal region, allowing the laser beams to switch on and off. The frequency can then be rapidly chirped over 220 MHz and 70 ns whilst the intensity of the pulse is approximately flat. This represents a chirp rate of ≈ 3 GHz/μs. Currently the limitation with these arbitrary excursions and linear chirps is the maximum voltage excursion of 20 V. Further work is required to amplify the voltage applied to the e.o. crystal to reach frequency excursions up to 1 GHz.

Using a tank circuit to amplify a sinusoidal chirp, we have shown that our laser system can be rapidly chirped in excess of 1 GHz, which is the magnitude required for deceleration from a molecular jet of 400-560 ms^{-1}.

By comparing periodic linear and sinusoidal chirps we have shown the important result that no additional chirp is introduced during pulsed amplification in the Nd:YAG rods.

Chapter 6

Simulations of acceleration/deceleration based on laser system performance

6.1 Introduction

In this chapter we perform numerical acceleration/deceleration simulations based on the laser performance. We use the temporal profiles of actual laser pulses to study the effect of variations in the flat-top temporal profile on the manipulation of molecules and atoms. We also investigated deceleration using non-linear chirps and how this non-ideal chirp can be compensated for by shaping the temporal profile of the pulses.

6.2 Simulations with measured temporal profile and linear chirp

6.2.1 Deceleration of benzene and NO molecules

To improve the accuracy of the simulations in chapter 2, we modelled deceleration using an actual temporal profile from our pulse amplified laser beams. A pulse with a FWHM of ≈ 140 ns was incorporated into the simulation program by interpolating it over the constant time step of our integration.

The linear chirp was modified to have a shorter duration of 100 ns fit within the flat region of the intensity profile. Since the chirp excursion needed to be the same, this meant that the chirp rate would increase. We would therefore expect the minimum (threshold) intensities required for deceleration to increase. The temporal

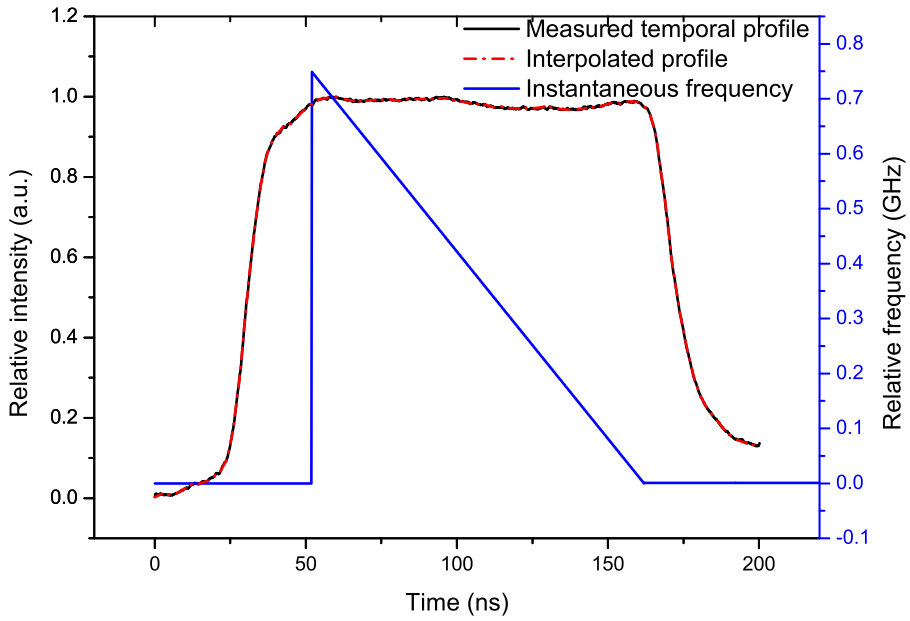

Figure 6.1: A typical temporal intensity profile from our pulsed amplification system and the simulated finite frequency difference between the two lattice beams as a function of time. All intensity fluctuations are up to ≈ 3 %.

profile of a typical pulse from our amplified laser system along with the applied frequency chirp is shown in figure 6.1. The temporal profile displays a small variation in intensity of up to $\approx 3\%$.

Figure 6.2 shows the resultant molecular velocity distribution after the pulse shown by figure 6.1, when a typical temporal intensity profile in the range, $I_{\max} = 1.2 - 0.9 \times 10^{14}$ W m^{-2}, is applied to an ensemble of 20000 benzene molecules at 2 K. $I_{\max} = 1.0 \times 10^{14}$ W m^{-2} is the lowest intensity required for successful deceleration, equivalent to $I_{\max} = 0.75 \times 10^{14}$ W m^{-2} for the slow Gaussian temporal profile. This is consistent with the different chirp rate. The energy spread at this threshold intensity is approximately 4.2 K, much larger than 0.5 K for Gaussian temporal profile case.

For $I_{\max} = 1.2 \times 10^{14}$ W m^{-2}, approximately 3000 (15 %) molecules were decelerated. The FWHM of the velocity spread of ≈ 35 ms^{-1} of all of the simulations is non Gaussian around 0 ms^{-1} representing an energy spread of approximately 5.9 K. For $I_{\max} = 1.1 \times 10^{14}$ W m^{-2} approximately 1800 (9.0 %) molecules were decelerated. The velocity spread was ≈ 30 ms^{-1} representing an energy spread of approximately 4.2 K. For $I_{\max} = 0.9 \times 10^{14}$ W m^{-2} approximately 0 (< 1.0 %) molecules were decelerated.

The fluctuation in intensity in the realistic temporal profile is believed to be responsible for the increased and non-Gaussian velocity/energy spread in the decel-

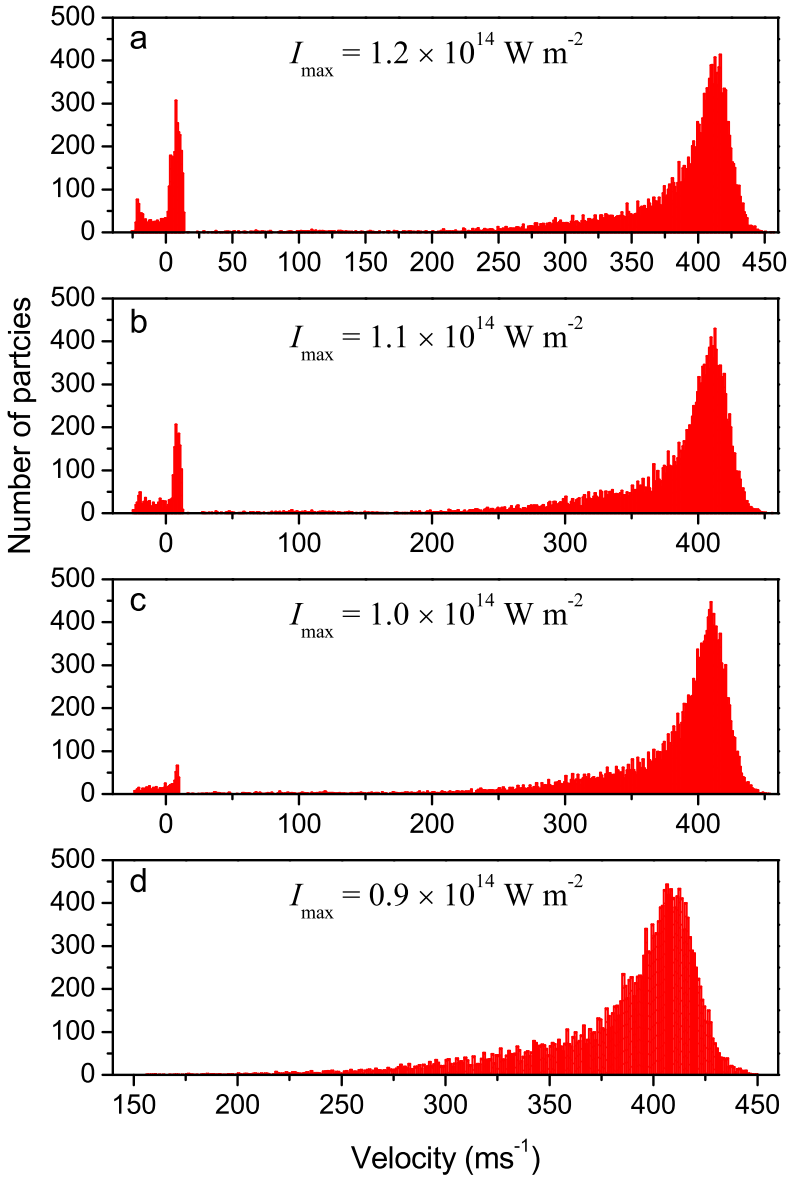

Figure 6.2: The resultant distribution of velocities when the decelerating optical lattice described in figure 6.1 is applied to an ensemble of 20000 benzene molecules at 2 K. (a) $I_{max} = 1.2 \times 10^{14}$ W m^{-2}, (b) $I_{max} = 1.1 \times 10^{14}$ W m^{-2}, (c) $I_{max} = 1.0 \times 10^{14}$ W m^{-2}, (d) $I_{max} = 0.9 \times 10^{14}$ W m^{-2}.

erated distribution. This is due to molecules being lost during deceleration when the intensity at a particular time drops, and then a heating of the residual molecules when the intensity increases again during the course of the pulse.

The same chirp and realistic temporal profile shown in figure 6.1 are then applied to NO molecules at an initial temperature of 2 K and the resultant velocity distributions shown in figure 6.3. Here the threshold intensity is $I_{max} = 2.25 \times 10^{14}$ W m^{-2}, compared to $I_{max} = 1.75 \times 10^{14}$ W m^{-2} for the Gaussian profile, consistent with the increased chirp rate due to the reduced chirp time. Once again there is a much

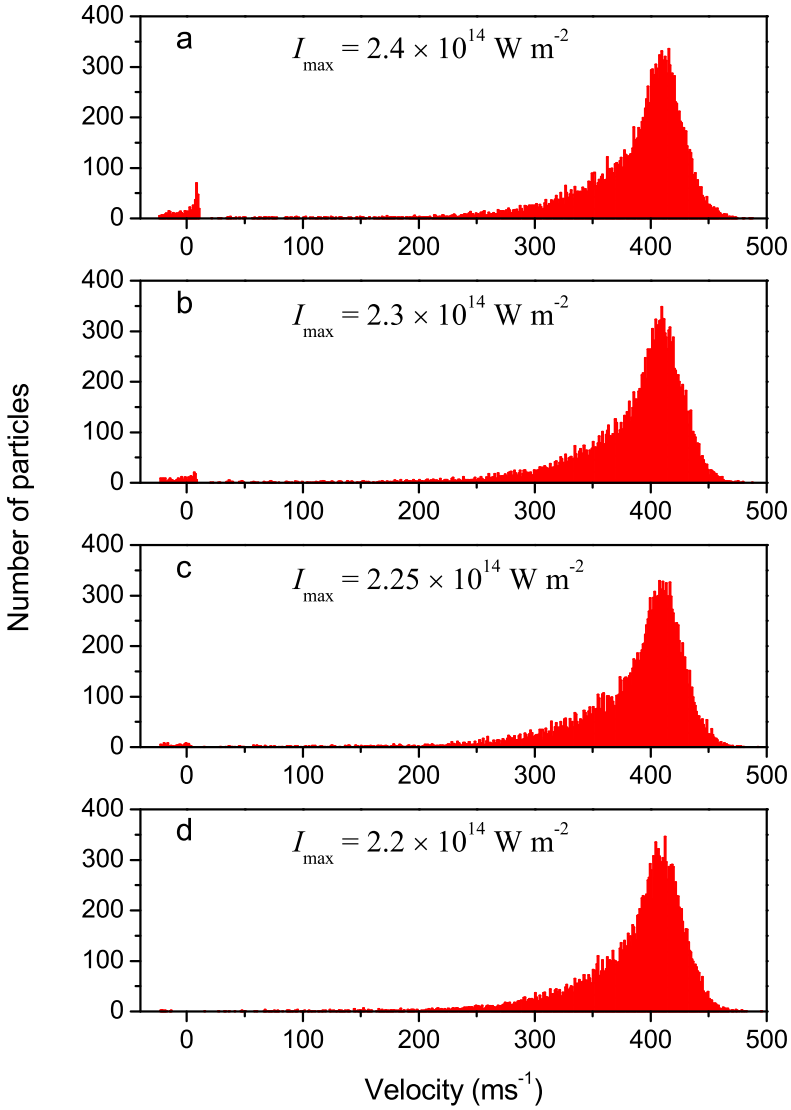

Figure 6.3: The resultant distribution of velocities when the decelerating optical lattice described in figure 6.1 is applied to an ensemble of 20000 NO molecules at 2 K. (a) $I_{\max} = 2.4 \times 10^{14}$ W m^{-2}, (b) $I_{\max} = 2.3 \times 10^{14}$ W m^{-2}, (c) $I_{\max} = 2.25 \times 10^{14}$ W m^{-2}, (d) $I_{\max} = 2.2 \times 10^{14}$ W m^{-2}.

larger velocity spread, with an energy spread of 0.7 K at the threshold intensity, compared to 0.15 K in the Gaussian temporal profile case.

For $I_{\max} = 2.4 \times 10^{14}$ W m^{-2} approximately 520 (2.6 %) molecules were decelerated. The FWHM of the velocity spread was ≈ 35 ms^{-1} representing a temperature of approximately 2.2 K . For $I_{\max} = 2.3 \times 10^{14}$ W m^{-2} approximately 250 (1.3 %) molecules were decelerated. The velocity spread was ≈ 30 ms^{-1} representing a temperature of approximately 1.6 K. For $I_{\max} = 2.2 \times 10^{14}$ W m^{-2} < 10 particles were decelerated.

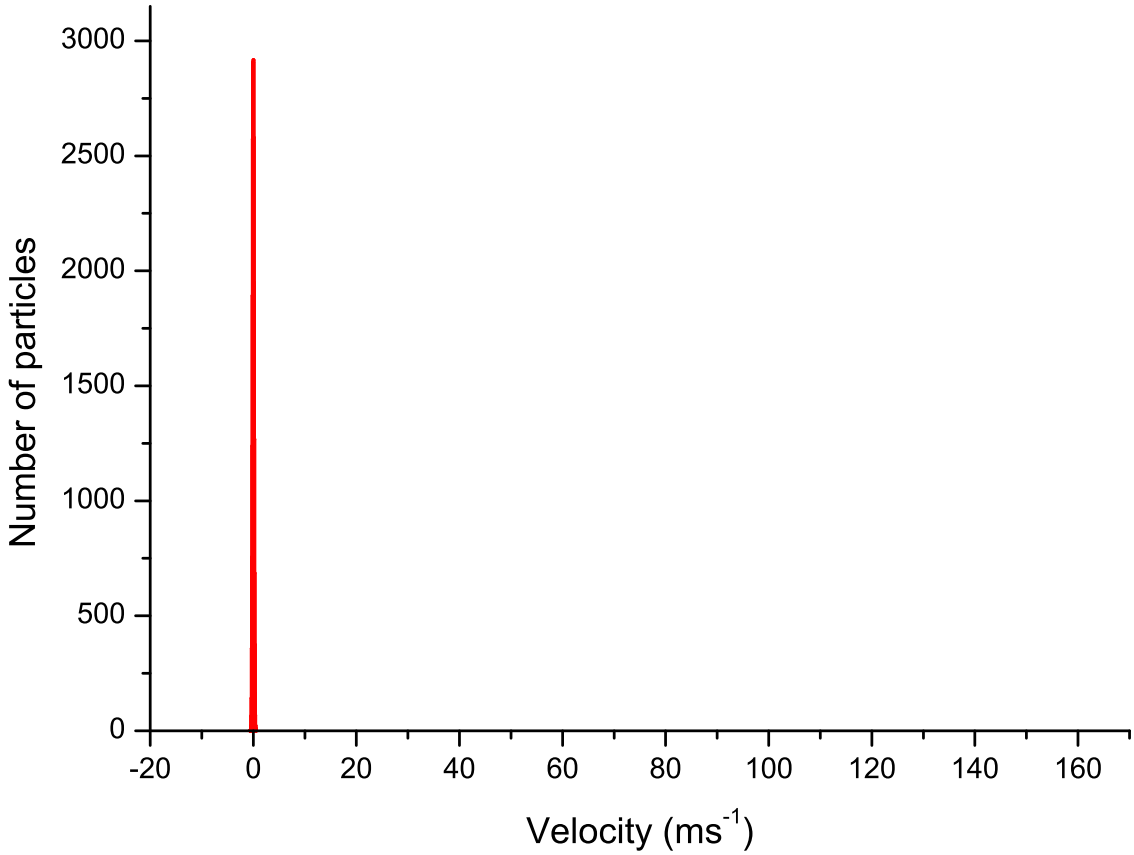

Figure 6.4: Initial velocity distribution of argon atoms at 80 μK. The width of the peak is even narrower than shown due to resolution limits of the image.

6.2.2 Simulating the acceleration of metastable argon atoms

In parallel experiments in the lab, metastable argon atoms with polarisability $\alpha = 47.9 \times 10^{-40}$ C m^2 V^{-1} are being laser cooled and trapped in a MOT with an effective temperature $\approx$ 80 μK and a FWHM velocity spread of $\approx$ 0.3 ms^{-1}. It was therefore decided to model the use of the chirped laser system to accelerate stationary atoms out of the trap. This could have applications in high resolution collision experiments as mentioned in chapter 1 where a polarisable species could be collided at an arbitrary velocity by tuning the velocity of the optical lattice. Because the velocity spread of metastable atoms is much narrower than the benzene and NO molecules in a molecular jet ($\approx$ 2 K) in the deceleration simulations, much lower intensities can be used.

We therefore simulated this acceleration, using a realistic temporal profile for our laser beams. The initial velocity distribution is shown in figure 6.4.

A pulse with a FWHM of $\approx$ 140ns was again interpolated and incorporated into the simulation program. After experimenting with the the simulations by adjusting the relative phase between the chirp and the pulse, it was found that it was important

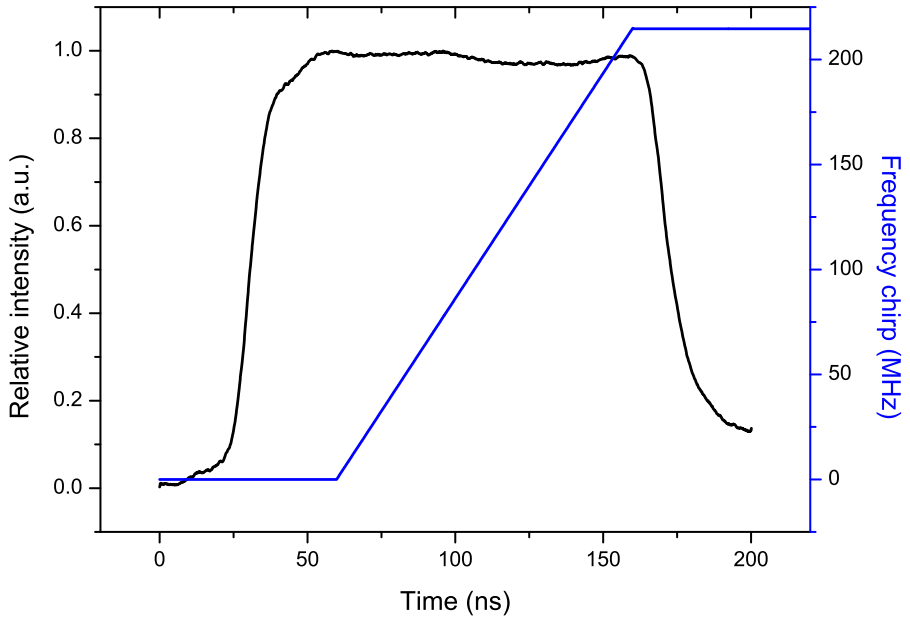

Figure 6.5: Realistic temporal intensity profile of a pulse overlaid with the applied frequency chirp used to simulate the application of an accelerating lattice on the argon atoms.

to hold off the chirp until the maximum intensity was reached. If not the intensity would either be too low to capture any atoms/molecules before the lattice velocity had reached too high a value above the un-accelerated distribution, or if set too high at the beginning would result in excessive heating of the final distribution. The linear chirp used before was therefore modified to have a shorter duration of 100 ns. To ensure the same approximate gradient, the chirp excursion was in turn reduced to $\approx$ 215 MHz, equivalent to 114 ms^{-1} for counter propagating beams, as shown in figure 6.5. The temporal profile displays a small variation in intensity of up to $\approx 3\%$. Figure 6.6 shows the resultant distribution for several intensities.

The accelerated distribution generally has an irregular profile around 122 ms^{-1}, probably due to the longitudinal oscillation time. There is a statistically insignificant 80 atoms (compared to the sample of 20000 in the initial distribution) decelerated at $I_{\max} = 3.6 \times 10^{12}$ W m^{-2}, implying a similar threshold intensity. Generally higher temperatures are observed for the realistic temporal profile, as in the decelerating case, due to intensity variations over the duration of the pulse. There appears to be a periodic depositing of atoms at intervals of $\approx$ 5 ms^{-1}, which is believed to be due to the oscillation in phase space, and variation in intensity, which cause atoms to suddenly drop out at regular intervals.

For $I_{\max} = 3.9 \times 10^{12}$ W m^{-2} approximately 2200 atoms were accelerated with a velocity spread of approximately 5 ms^{-1} representing an energy of 60 mK. For

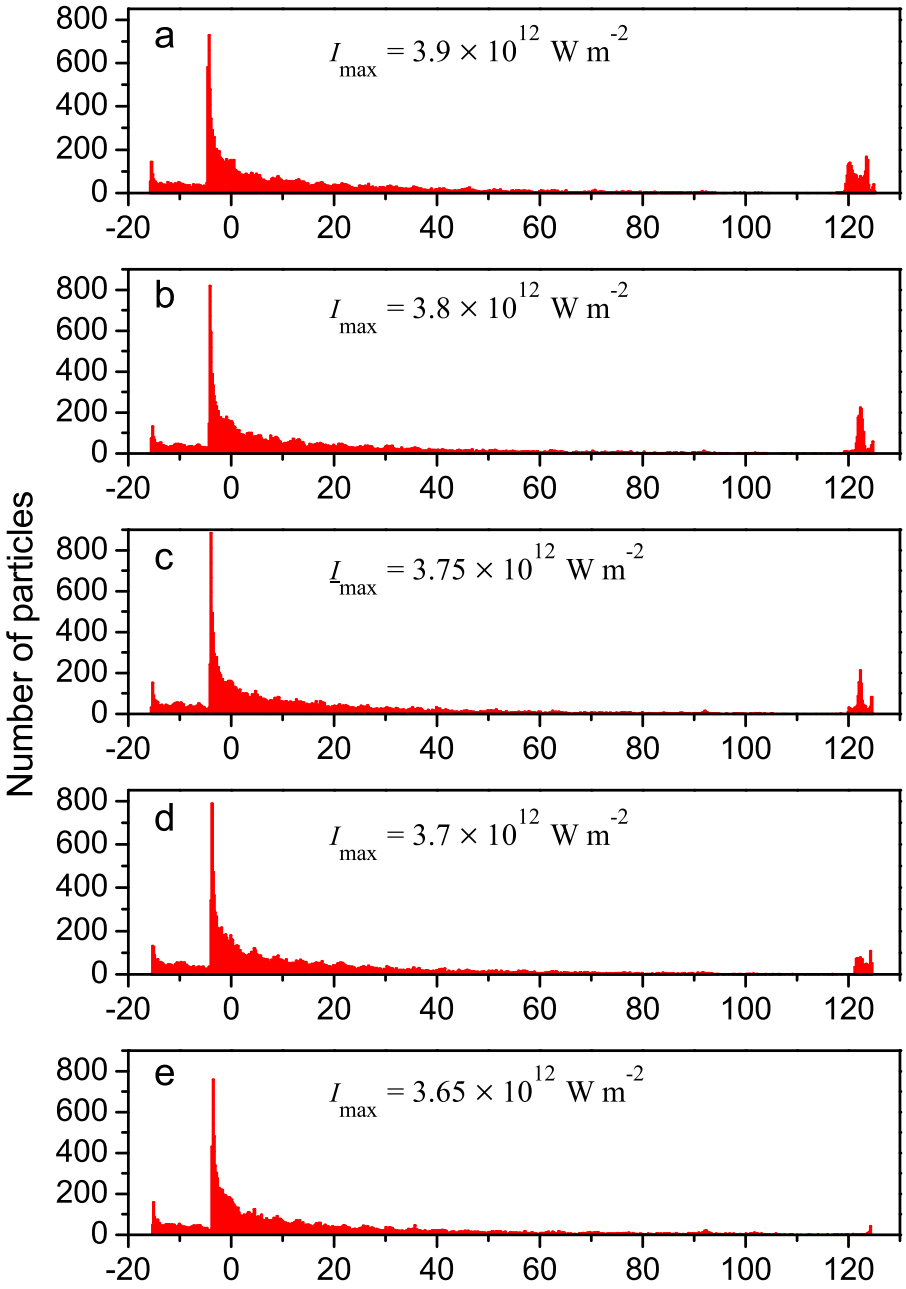

Figure 6.6: The resultant distribution of velocities when the accelerating optical lattice described in figure 6.5 is applied to an ensemble of 20000 metastable Argon atoms. (a) $I_{max} = 3.9 \times 10^{12}$ W m^{-2}, (b) $I_{max} = 3.8 \times 10^{12}$ W m^{-2}, (c) $I_{max} = 3.75 \times 10^{12}$ W m^{-2}, (d) $I_{max} = 3.7 \times 10^{12}$ W m^{-2}, (e) $I_{max} = 3.65 \times 10^{12}$ W m^{-2}.

$I_{\max} = 3.8 \times 10^{12}$ W m^{-2} approximately 2100 atoms were accelerated with a velocity spread of < 5 ms^{-1} representing an energy of < 60 mK. For $I_{\max} = 3.75 \times 10^{12}$ W m^{-2} approximately 1300 atoms were accelerated with a velocity spread of < 5 ms^{-1} representing an energy of < 60 mK. For $I_{\max} = 3.7 \times 10^{12}$ W m^{-2} approximately 1000 atoms were accelerated with a velocity spread of < 5 ms^{-1} representing an energy of < 60 mK. At threshold, $I_{\max} = 3.65 \times 10^{12}$ W m^{-2}, approximately 80 atoms were accelerated with a velocity spread of < 2 ms^{-1} representing an energy of < 10 mK. This is less than 0.5 % of the total number of argon atoms.

6.3 Compensating for non-linear chirps

Since we know that we may not yet be able to produce the required linear voltage ramp for a linear chirp, we therefore investigated whether the varying potential well depth that a non-linear chirp produces, can be compensated for by shaping the temporal profile of the pulses.

We recall from chapter 2 that for a linear chirp we can define the parameter $\psi \equiv \beta/aq$, where β is the chirp rate, a is the maximum force than can be imparted by the optical lattice, and q is the lattice wave vector. This must meet the condition, $\psi < 1$ in order for there to be a potential well which can trap and transport a polarisable species.

We hypothesised that for a non-linear chirp, we should aim to maintain a constant value for the parameter ψ and performed numerical simulations to test this. To keep ψ constant, the intensity of the beams therefore needs to increase if the chirp rate increases and vice versa.

As indicated by equation (2.11) and using the relationship $I(t) = 1/2\epsilon_0 c E^2(t)$, the maximum instantaneous acceleration $a_{\max}(t)$ is given by,

$$a_{\max}(t) = \frac{\alpha q}{m\epsilon_0 c}\sqrt{I_1(t) I_2(t)}. \tag{6.1}$$

We now suppose that instead of being constant, the chirp rate is a function of time, such that $\beta(t) = \frac{\mathrm{d}^2\phi(t)}{\mathrm{d}t^2}$. For a harmonically changing frequency from high to low which we created using the tank circuit, the frequency difference between the two arms is given by, $\omega(t) \equiv \mathrm{d}\phi(t)/\mathrm{d}t = A\cos(\omega_{\mathrm{m}} t)$ and with corresponding chirp,

$$\beta(t) = -A\omega_{\mathrm{m}} \sin\left(\omega_{\mathrm{m}} t\right). \tag{6.2}$$

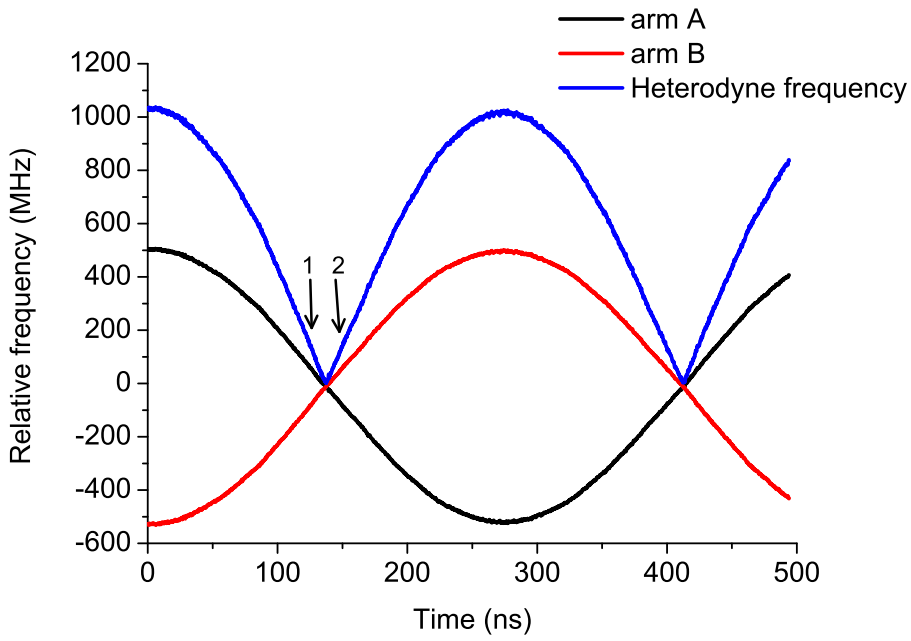

Figure 6.7: Predicted relative frequency between two arms of a time delayed laser to predict beat frequency if the two arms were heterodyned. (1) shows the region of maximum deceleration, and (2) shows the region of maximum acceleration.

In order to keep ψ constant, β must therefore be proportional to the intensities, implying that,

$$\sqrt{I_1 I_2} \propto \sin(\omega_{\mathrm{m}} t)\,. \tag{6.3}$$

The maximum gradient, $\beta(t)$ for a sinusoidal-type waveform $\omega(t) = A\cos\omega_{\mathrm{m}} t$ of angular frequency ω_{m}, period $2\pi/\omega_{\mathrm{m}}$, and amplitude A (the frequency excursion), occurs at $t = \pi/2\omega_{\mathrm{m}}$ and has magnitude $\beta_{\mathrm{max}} = \omega_{\mathrm{m}} A$. For deceleration, the chirp period must occur over a quarter of the period of this waveform, $(\pi/2\omega_{\mathrm{m}})$, where it changes from maximum to zero frequency. We now compare a linear chirp over the same period and frequency excursion with the harmonic chirp. The gradient of the linear chirp, β_{linear} is given by the frequency excursion A divided by the 'quarter period', $\pi/2\omega_{\mathrm{m}}$ which gives, $\beta_{\mathrm{linear}} = A/(\pi/2\omega_{\mathrm{m}}) = 2\omega_{\mathrm{m}} A/\pi$.

The ratio of maximum gradient of the sinusoidally varying function to the constant gradient of the linear case is therefore,

$$\frac{\beta(t)_{\mathrm{max}}}{\beta_{\mathrm{linear}}} = \frac{-\omega_{\mathrm{m}} A}{2\omega_{\mathrm{m}} A/\pi} = \frac{\pi}{2}. \tag{6.4}$$

In the case of a decelerating lattice, the maximum rate of change would occur at the end, for example between 100 and 140 ns (in figure 6.7) and in the case of an accelerating lattice at the beginning of the chirped pulse between 140 and 180 ns.

Using equations (6.3) and (6.4), we predict the temporal profile for a pulse to

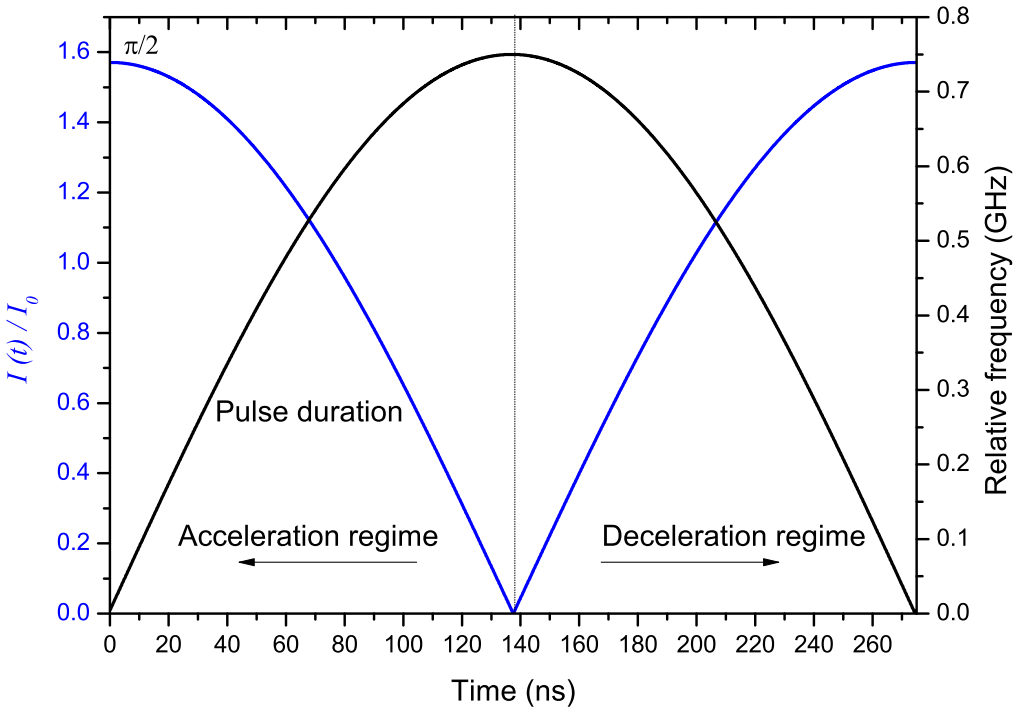

Figure 6.8: Intensity profile shown by the blue profile which would be used to compensate for a non linear chirp shown by the black trace in order to maintain a constant well depth produced by the interaction of a polarisable species with the optical lattice.

compensate for a harmonically varying frequency $\omega(t)$. Figure 6.8 shows a trace of the relative frequency (blue), which is proportional to the lattice velocity created by a sinusoidal voltage applied to the e.o. crystal. Overlaid with this is the temporal profile for the intensity of a pulse which would compensate for the changing rate of deceleration. The left hand side of the figure represents a pulse shape and the portion of the chirp which would be used for the acceleration of particles down to zero velocity. The right hand side of the figure represents the portion that would be used for deceleration from zero velocity.

Equation (6.4) indicates that to scale the intensity of the sinusoidal intensity profile for a sinusoidal chirp to be equivalent to a square temporal profile with a linear chirp, the maximum intensity $I_{\max}$ should be $\pi/2$ times the square temporal profile intensity I_0. The integral over the pulse duration, and therefore the total pulse energy of such a sinusoidal temporal profile with amplitude $I_{\max}/I_0 = \pi/2$ will clearly be the same as a square temporal profile with intensity I_0.

Figure 6.9 shows a simulation of a pulse with a temporal profile and frequency chirp as shown in figure 6.8 with a maximum intensity of $\pi/2$ times the minimum intensity required for deceleration of benzene molecules with an equivalent linearly

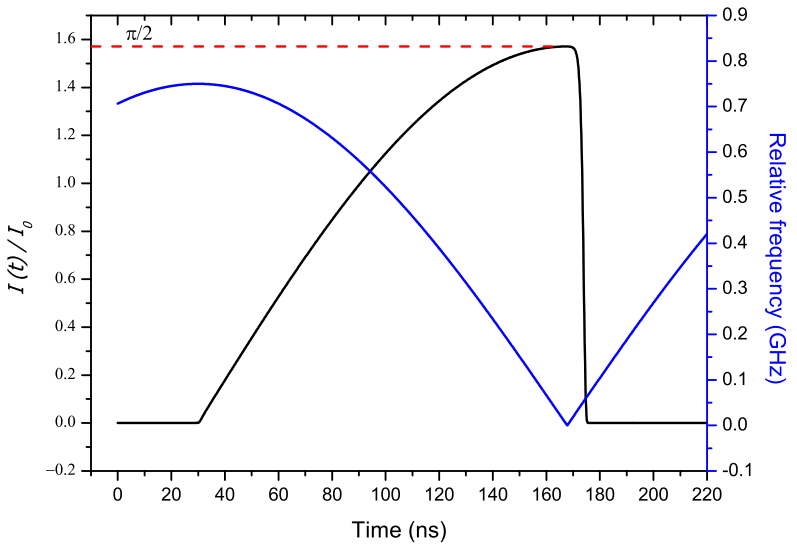

Figure 6.9: A sinusoidal shaped temporal intensity profile applied against a sinusoidally varying frequency chirp for a decelerating lattice, in order to compensate for the changing rate of deceleration and therefore maintain a constant well depth.

chirped pulse, as calculated in chapter 2, i.e. $(\pi/2 \times 0.75) \times 10^{14}$ W m^{-2}. This is compared with two other cases with the usual super-Gaussian temporal profiles, all with the same sinusoidally changing frequency chirp. In the first of these cases, the maximum intensity of the super-Gaussian is 0.75×10^{12} W m^{-2} which would require the same amount of total energy as the sinusoidally shaped pulse described. In the second case a super Gaussian with a maximum intensity of $(\pi/2 \times 0.75) \times 10^{14}$ W m^{-2} is simulated, which for the fastest stage of deceleration at the end of the chirp should be enough to maintain confinement of the same molecules, however would require more pulse energy, which for our laser system is limited. At the beginning of the chirp there would be a greater than threshold well depth, and therefore cause greater heating of the final, accelerated distribution. The total energy of this pulse is $\pi/2$ times the pulse energy in the other two cases.

Figure 6.10 shows the resultant distributions when the pulses described above are applied to the chirp shown in figure 6.9. In (a), the sinusoidally shaped pulse, approximately 120 (0.6 %) molecules have been decelerated. The FWHM of the velocity spread is ≈ 6 ms^{-1} representing an energy of 170 mK. This compares well and offers an improvement on the slow Gaussian profile applied to a linear chirp with the same pulse energy, i.e. $I_{\max} = 0.75 \times 10^{14}$ W m^{-2} where the energy spread was approxiamtely 500 mK, with just 250 benzene molecules decelerated. This demonstrates that if a linear chirp is not available, a similarly efficient deceleration can be achieved by shaping the temporal intensity profile of the pulses accordingly, in order to maintain a constant well-depth for the duration of the pulse. In (b),

where we test the application of a pulse with a super-Gaussian temporal intensity profile with the same pulse energy as (a), no molecules have been decelerated, and have all been lost out at higher velocites, during deceleration. This is as expected, since after $\approx$ 60 ns from the beginning of the chirp (97 ns on the figure 6.9), the gradient of the chirp exceeds the gradient of the linear chirp, and there is insufficent intensity to maintain confinement of the particles.

At 60 ns, the frequency chirp has reached about 580 MHz, corresponding to 310 ms^{-1}, which is approximately at the centre of the molecules which have been decelerated and dropped before the end of the chirp. In (c), where we test the application of a pulse with a super-Gaussian temporal intensity profile with the same maximum intensity as (a) but greater pulse energy as described above, there are two distinguishable distributions which have been decelerated. Approximately 5000 around a mean velocity of 0 ms^{-1} with a spread of $\approx$ 90 ms^{-1} and 4500 around a mean velocity of 100 ms^{-1} with a spread of $\approx$ 60 ms^{-1}, indicating that there has been greater heating, as predicted, during the deceleration process.

6.4 Conclusions

It is clear from simulations with measured intensity profiles for the pulses, that a flat top temporal profile is important in order to maximise the number of decelerated/accelerated particles, and to minimise their velocity spread. A slight decrease causes a loss of population from the optical potential, and then the subsequent increase results in the final transported distribution being heated up.

It is possible to compensate for a non-linear harmonic chirp by shaping the temporal profile of the pulses to compensate. This requires further analysis to determine whether this can be extended more generally to non-linear chirps and intensities.

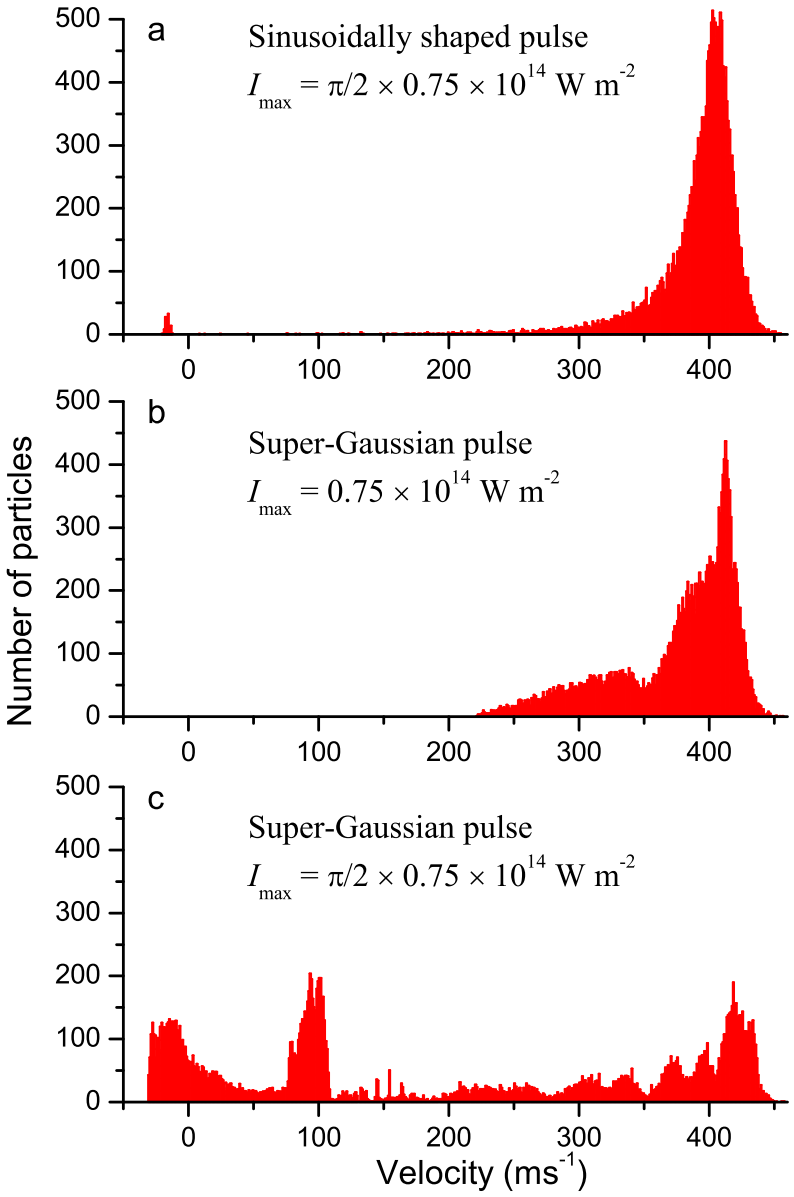

Figure 6.10: Distributions for various intensity profiles. (a) Pulses with temporal profiles as shown by figure 6.9 with a maximum intensity ($\pi/2$) times the minimum intensity required for deceleration of benzene molecules, as indicated in chapter 2, i.e ($\pi/2$) $\times 0.75 \times 10^{14}$ Wm^{-2}. (b) Pulses with super-Gaussian profiles as shown by figure 2.10 with a maximum intensity of 0.75×10^{14} Wm^{-2} and therefore the same pulse energy as (a). (c) Pulses with same super-Gaussian profiles, however with a maximum intensity of $(\pi/2) \times 0.75 \times 10^{14}$ Wm^{-2} and therefore the same maximum well depth as (a) but with $(\pi/2)\times$ the pulse energy as (a).

.

Chapter 7

Lattice alignment by four-wave mixing

7.1 Introduction

To initially test the pulsed amplification system, we performed a type of four-wave mixing (FWM) experiment called coherent Rayleigh scattering (CRS) using the degenerate four wave mixing (DFWM) phase matching configuration. The motivation for coherent Rayleigh scattering is that to produce a signal requires phase matching which in turn requires precise angular alignment and overlap of the 1064 nm beam focii. This therefore would be a useful alignment tool for the creation of the optical lattice used in proposed acceleration and deceleration experiments.

7.2 Coherent Rayleigh scattering

CRS and stimulated Brillouin scattering(BS) [155, 156, 157, 158, 159] are both nonlinear FWM processes which can be performed in gases and liquids using the dipole or electrostrictive force [160] imparted by the applied optical fields. The electrostrictive force creates a density perturbation from which the probe may coherently Bragg scatter. CRS is caused by isobaric density fluctuations, and in the case of a stationary lattice, is at the frequency of the incident light. Brillouin scattering is caused by acoustic waves which are induced by the optical field acting on the medium and therefore the scattered light is shifted in frequency from the incident light by the Doppler effect [159].

Figure 7.1 shows the two counter propagating pumps which interfere to produce a standing wave with wave vector $q = k_1 - k_2$, where $k_{1,2}$ is the wave vector of the pump beams and frequency $\Omega = \omega_1 - \omega_2$, where $\omega_{1,2}$ are the frequencies of the pump

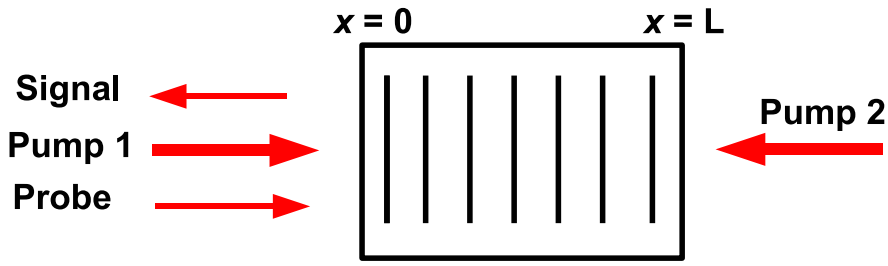

Figure 7.1: Schematic diagram of a four-wave mixing process. The two pumps create a density grating in the distribution of molecules using the optical dipole force. A portion of the probe is scattered from the grating to form the signal.

beams. The induced optical dipole force on the molecules causes the molecules to arrange themselves to form a density grating which the probe then scatters from to create a fourth beam, often called the signal. By conservation of momentum, the signal will have wave vector $k_4 = k_3 - q$, where k_3 is the wave vector of the probe and frequency $\omega_4 = \omega_3 - \Omega$ [155], where ω_3 is the frequency of the probe. For a stationary velocity lattice, where $\omega_1 = \omega_2$ the signal will have the same frequency as the incident radiation. We used the laser setup described in chapter 5 with only one of the arms to produce a constant frequency during the pulse.

7.3 Theory

In order to predict the signal produced we must first consider the one dimensional non-linear wave equation [161],

$$\frac{\partial^2 E(x,t)}{\partial x^2} - \frac{n^2}{c^2}\frac{\partial^2 E(x,t)}{\partial t^2} = \mu_0 \frac{\partial^2 P_{\mathrm{NL}}(x,t)}{\partial t^2}, \tag{7.1}$$

where $E(x,t)$ is the electric field, μ_0 is the permeability of free space and where P_{NL} includes the non-linear polarisabilty, the first two terms of which are, $\epsilon_0\chi^{(2)}E(x,t)^2 + \epsilon_0\chi^{(3)}E(x,t)^3$, where ϵ_0 is the permittivity of free space and χ is the electric susceptibility tensor.

The refractive index n can be related to the number density $N(\mathrm{m}^{-3})$, for far off-resonance fields [161] by,

$$n = \sqrt{1 + \frac{N\alpha}{\epsilon_0}}, \tag{7.2}$$

where N is the number density and α is the polarisabilty of the medium interacting with the optical field. A first order Taylor expansion of this gives, $n \approx 1 + \frac{N_0\alpha}{2\epsilon_0} + \frac{\Delta N(x,t)\alpha}{2\epsilon_0} = n_0 + \Delta n(x,t); |\Delta n(x,t) << n_0|$ [161] where the linear term is given by

$n_0 = 1 + \frac{N_0\alpha}{2\epsilon_0} \approx 1$ and the non-linear change in refractive index due to the optical field, $\Delta n(x,t) = \frac{\Delta N(x,t)\alpha}{2\epsilon_0}$.

Given the assumption $|\Delta n << n_0|$, $n^2 = n_0^2 + 2n_0\Delta n(x,t)$, equation (7.1) can be re-written in terms of the modified refractive index due to an optical field as [161],

$$\frac{\partial^2 E(x,t)}{\partial x^2} - \frac{n_0^2}{c^2}\frac{\partial^2 E(x,t)}{\partial t^2} = \frac{2n_0\Delta n(x,t)}{c^2}\frac{\partial^2 E(x,t)}{\partial t^2}, \tag{7.3}$$

which assumes that the scattering process is due only to the density perturbation due to the linear polarisability and therefore neglects the non-linear polarisability term given in equation (7.1).

To simplify the problem, we consider that the polarisation of the pumps orthogonal to the probe as they do not interfere with each other. The total field, $E_{\rm tot}(x,t)$ is therefore simply the combination of the probe $E_3(x,t)$ and the generated signal $E_4(x,t)$, due to the modified number density of the medium induced due to the pumps $E_1(x,t)$ and $E_2(x,t)$,

$$E_{\rm tot}(x,t) = A_3^0 e^{{\rm i}(k_3 x - \omega_3 t)} + c.c. + A_4^0 e^{{\rm i}(-k_4 x - \omega_4 t)} + c.c., \tag{7.4}$$

where the amplitudes A_3^0, A_4^0 are related to the electric fields according to, $A_3^0, A_4^0 = 1/2\ E_3^0, 1/2\ E_4^0$ respectively and $E_{3,4}^0$ are the amplitudes of the electric fields of the probe and signal respectively.

By substituting (7.4) into (7.3) we produce many terms including first and second derivatives, and terms oscillating at $\omega_3, \omega_4, k_3, k_4$, and $2\omega_3, 2\omega_4, 2k_3, 2k_4$. We can reduce the number by making the slowly varying envelope approximation, $\frac{\partial^2 E(x,t)}{\partial t^2} << 2\omega\frac{\partial E(x,t)}{\partial t} << \omega^2 E(x,t)$ [161], and neglecting terms oscillating at $2\omega_3, 2\omega_4, 2k_3, 2k_4$. Finally, we can produce two sets of coupled differential equations by extracting terms oscillating at ω_3 and ω_4 which describe the evolution of the probe and the generated signal where,

$$\begin{aligned} c^2 k_4 A_4^{'}(x,t) &= {\rm i}n_0\Delta n(x,t)\omega_3^2 A_3(x,t) \\ c^2 k_3 A_3^{'}(x,t) &= -{\rm i}n_0\Delta n(x,t)\omega_4^2 A_4(x,t), \end{aligned} \tag{7.5}$$

where primes indicate d/dx. This assumes that the dynamics of the gas change much more slowly than the field amplitudes. These can solved with the boundary conditions, $A_3(0) = A_3^0,\ A_4(l) = 0$ to give the solutions,

$$A_4(x,t) = \frac{\mathrm{i}\ e^{-\omega_{\mathrm{osc}}x}\left(-e^{2\omega_{\mathrm{osc}}l} + e^{2\omega_{\mathrm{osc}}x}\right)A_3^0}{1+e^{2\omega_{\mathrm{osc}}l}}$$
$$A_3(x,t) = \frac{\mathrm{i}\ e^{-\omega_{\mathrm{osc}}x}\left(\ e^{2\omega_{\mathrm{osc}}l} + e^{2\omega_{\mathrm{osc}}x}\right)A_3^0}{1+e^{2\omega_{\mathrm{osc}}l}}, \tag{7.6}$$

where $\omega_{\mathrm{osc}} = \frac{\Delta n(x,t) n_0 \omega_{\mathrm{opt}}}{c}$, $\omega_{\mathrm{opt}} = 2\pi c/\lambda$ and $l = \lambda/2$ is the fringe spacing for two counter propagating beams. We assume that $k_3 \approx k_4$ and $\omega_3 \approx \omega_4$. A Taylor expansion of equation (7.6) implies that,

$$I_4(x,t) \propto \left(\frac{\Delta n(x,t) n_0 \omega_{\mathrm{opt}}}{c}\right)^2, \tag{7.7}$$

where $A_4^2(x,t) \propto I_4(t)$. We can relate the change in refractive index $\Delta n(x,t)$ to the change in number density $\Delta N(x,t)$ which can be determined from the modified velocity distribution function $g(x,v,t)$ due to the perturbation $g'(x,v,t)$ from the equilibrium $g_0(v)$ where,

$$\Delta N(x,t) = N_0 \int_{-\infty}^{+\infty} g'(x,v,t)dv = \frac{2\epsilon_0 \Delta n(x,t)}{\alpha}. \tag{7.8}$$

To find the perturbed velocity distribution $g(x,v,t)$, we must solve the 1-D Boltzmann equation [155] given by,

$$\frac{\partial g(x,v,t)}{\partial t} + v\frac{\partial g(x,v,t)}{\partial x} + \frac{F(x,t)}{m}\frac{\partial}{\partial v}g(x,v,t) = \left[\frac{\partial g(x,v,t)}{\partial t}\right] \tag{7.9}$$

where $\left[\frac{\partial g(x,v,t)}{\partial t}\right] = \frac{-(g(x,v,t)-g_0)}{\tau_{\mathrm{c}}}$ is the collision term, according to the the BGK. approximation [162], where F is the dipole force due to the interaction of the pump beams with the medium and m is the molecular mass. This simplification to the collision integral assumes that over a relaxation time τ_{c}, the distribution function relaxes to the equilibrium value g_0. We have made the approximation that we are in a 1-D regime since transverse forces are much weaker than in the longitudinal direction, as calculated in chapter 2.

To solve the Boltzmann equation, we make the approximation that $\frac{-(g(x,v,t)-g_0)}{\tau_{\mathrm{c}}} = 0$ which assumes that densities are sufficiently low that collisions do not occur on the time scale of the pump/probe pulse. The mean free path of xenon is 5.4 μm at 293 K, 20 Torr, giving a mean collision time of 24.8 ns. This is comparable to the pulse duration, indicating that there would only be time for one collision to occur on average, partially justifying the collision free regime at this pressure. The mean free path of octane is calculated to be 11.2 μm at 293 K and 10 Torr, giving mean

collision time of 48.0 ns, justifying the collision free assumption, especially as this was the maximum pressure considered. At 1 Torr this collision time increases to 480 ns.

For two counter propagating beams along the x-axis, $F(x,t) = \frac{\alpha}{2}\nabla\left(E_1(x,t)+E_2(x,t)\right)^2$. For weak perturbations, where $(g' << g_0)$, $(\delta g'/\delta v << \delta g_0/\delta v)$ and $\alpha\left|A_1 A_2\right| << k_{\mathrm{B}}T$ this gives the perturbation to the distribution function [155],

$$g'(x,v,t) = \frac{\alpha A_1^0 A_2^0}{k_{\mathrm{B}}T} g_0(v) \times \frac{qv\ \cos(qx-\Omega t) - \cos(qx-qvt)}{qv-\Omega}, \tag{7.10}$$

where A_1^0, A_2^0 are the half amplitudes of the electric fields of the pump beams E_1^0, E_2^0 and $\Omega = \omega_2 - \omega_1$, and ω_1, ω_2 are the frequencies of the pump beams. Equation (7.10) can then be substituted into (7.8), to derive $\Delta n(x,t)$.

To justify the weak perturbation hypothesis we can calculate the well depths for the molecules investigated (octane and xenon) for typical intensities of $I_1^0 \approx 2\times10^{14}$ Wm^{-2}. The maximum well depth in a stationary or constant velocity optical lattice is given by,

$$\Delta U_{\max} = \frac{2ma}{q}, \tag{7.11}$$

where $a = \frac{1}{2}\alpha\frac{qE_0^2}{m}$. Thus,

$$\Delta U_{\max} = \frac{2\alpha I}{\epsilon_0 c} \tag{7.12}$$

For the molecules octane and xenon with polarisabilities 16.8×10^{-40} C m^2 V^{-1} and 4.50×10^{-40} respectively, this gives well depths of 28 K and 8 K respectively. This is relatively small compared to the room temperature (293) K at which the gases were studied

The evolution of the relative change in refractive index, $\Delta n/n_0$ is shown in figure 7.2, for typical intensities of pump, $I_1^0 \approx 1.7\times10^{14}$ Wm^{-2}, and using gaseous xenon, with atomic weight 131 and polarisability $\alpha = 4.5\times10^{-40}$ C m^2 V^{-1}. The intensity of the pump and probe is assumed to be constant so the dynamics of the signal can be observed decoupled from the the effects of the temporal profiles of the pumps/probe that were in fact used. Figure 7.2 indicates a half-maximum induction time of ≈ 1.3 ns, which is much less than the rise time of our pulses, therefore this would not be observable in experiments using our laser system. Once again it should be noted that in this model it is assumed that the force only acts in the x-direction, since in the radial directions perturbations due to the gradient of the laser beam are much smaller than in the longitudinal direction.

We predict a steady state value of $\Delta n/n_0 = 3.8\times10^{-6}$ for xenon, for the intensi-

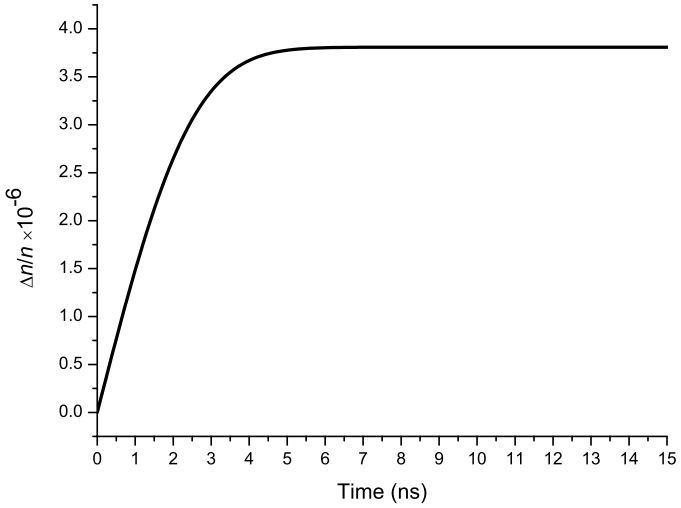

Figure 7.2: Calculated evolution of the change in refractive index ratio $\Delta n/n_0$ as a function of time. The half-maximum time for the molecules to form the diffraction grating after the optical field is switched on is ≈ 1.3 ns at which point $\Delta n/n_0 = 3.8 \times 10^{-6}$.

ties given above. We can substitute $n(x,t)$ at a particular time t into (7.6) to give the predicted evolution of the probe $I_3(x)$ and signal $I_4(x)$ across the interaction region of the laser beams, as shown in figure 7.3. The probe enters the interaction with an initial intensity 6.9×10^{13} Wm^{-2}. As it passes through the medium, the intensity is attenuated by $< 1 \times 10^{-5}$ %, indicating how relatively weak this interaction is. The signal, which is considered to orginate from the opposite side of the interaction region, increases from its inital value of 0 to a maxium of 4.7×10^3 Wm^{-2} where it then leaves the interaction region at this steady state value.

7.4 Experimental setup

Our experimental setup is shown in figure 7.4. This configuration was used as it has the convenience of having a counter propagating probe and pump (pump 2) which can be overlapped at two far points to ensure good alignment. Pump 1 is then sent in at a small angle from the probe. In this configuration, phase matching demands that the signal will be generated with a wave vector $k_4 = -k_1$, so that it will travel along the path of pump 1, in the opposite direction.

A diagram of the experimental setup, including the gas cell and connections employed to connect the rotary pump, gauge and gas cylinder (xenon) are shown in figure 7.5. Before readings were taken, the valve to the vacuum pump was opened to bring the pressure down to the limits of the gauge, ($\pm$ 0.05 Torr). The valve was then closed and the gas released into the cell. In the case of octane, which at

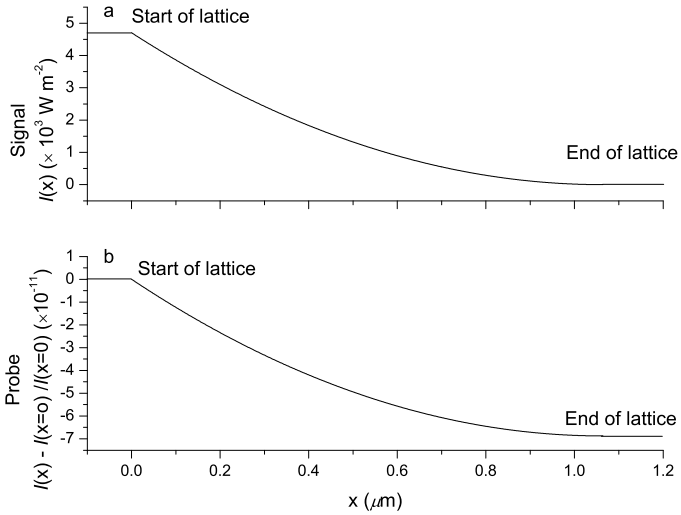

Figure 7.3: (a) The signal at a particular time as a function of position x. We consider the signal to originate from the opposite side of the interaction region to the probe, where it increases from its initial value of 0 to a maximum of 4.7×10^3 Wm^{-2} where it then leaves the interaction region at this steady state value. (b) Evolution of the probe at a particular time, as a function of position x through the interaction region. On the far left the probe enters the interaction with its intensity 6.9×10^{13} Wm^{-2}. As it passes through the medium, the intensity is attenuated by $< 6 \times 10^{-10}$ %, indicating how relatively weak this interaction is.

room temperature is a liquid, a few drops are added by removing the top of the cell and allowing it to form a small reservoir in the bottom of the cell. The top is then replaced and the valve to the pump opened up to pump out the air as described before. As the octane vaporised, the pressure could then be observed to rise again to the vapor pressure of octane ($\approx$ 3.75 Torr), assuming that the pump was not allowed to pump out all of the reservoir.

To produce our two pumps and probe we beam split the output of one of the arms of our laser system to create a constant velocity lattice with a probe of equal frequency. The pulses were attenuated to give energies of $30 - 90$ mJ and FWHM durations of $\approx$ 37 ns (peak intensity for $\approx$ 20 ns). Peak intensities for pump 1 and pump 2 were 2.1×10^{14} W m^{-2} and 1.4×10^{14} W m^{-2} respectively, giving an average pump intensity of 1.7×10^{14} W m^{-2}, and the probe had a peak intensity of 6.9×10^{13} W m^{-2}. The focused spot size ($1/e^2$ radius) of the beams were $\approx$ 50 μm $\pm$ 3 μm, which gives a Rayleigh range of 8 mm. After the beam was split into three, we used a half wave plate to rotate the polarisation of one of them to form the probe. The signal was also orthogonal to the pumps, and therefore we used a polariser to extract the signal from the path of pump 1 and direct it onto a photodiode.

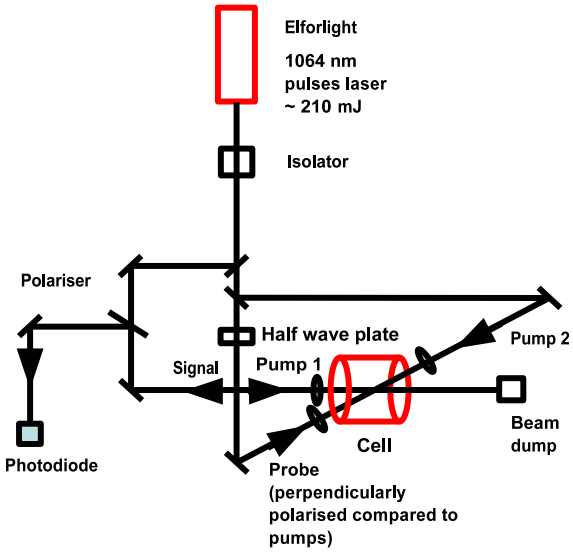

Figure 7.4: Experimental setup for non resonant four-wave mixing. In this configuration the orthogonally polarised probe is counter propagating to pump 2. Pump 1 is at a small angle from the probe. Phase matching requires that the generated signal will be along the path of pump 1, i.e. $k_4 = -k_1$. The signal is extracted by taking advantage of the perpendicular polarisation of the probe/signal and using a polarising beam splitter to direct it onto to a photodiode.

The large intensities of these pulses make small back reflections extremely dangerous, as they can cause runway amplification. To prevent this, an optical isolator was used at the output of the custom amplified beam, as shown in figure 7.4.

7.5 Four wave mixing signals

7.5.1 Xenon

We first performed a four-wave mixing experiment in xenon since it has previously been manipulated by using similar optical lattices. It also has a reasonable polarisability to mass ratio ($\alpha = 4.50 \times 10^{-40}$ C m^2 V^{-1} [100], mass = 131 a.m.u.). Its inert nature also makes it safe to use in an intensity and pressure regime where electronic breakdown of air is a possibility.

Figure 7.6 shows the four-wave mixing signal obtained with xenon at 20 Torr overlaid with the temporal intensity profile of the pulses used to create it. The average peak pump intensity in this case was 1.7×10^{14} W m^{-2}, with a probe intensity of 6.9×10^{13} W m^{-2}. All pulses had the same temporal intensity profile, since they were formed from the same laser beam. To verify that we had a four-wave mixing signal we checked that the signal was only present when both pumps and the probe were present, by blocking each beam in turn.

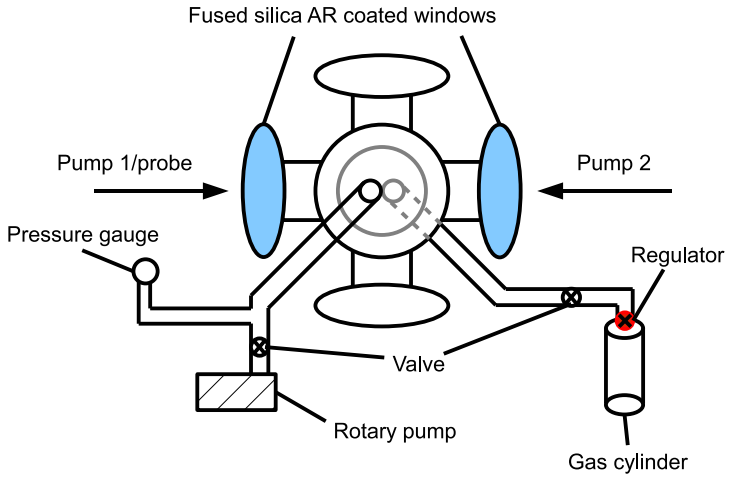

Figure 7.5: The gas cell used for four-wave mixing in octane and xenon. The windows for pumps/probe are AR coated for ($\lambda = 1064$ nm) and are approximately 15 cm apart. Xenon was introduced as shown, and octane was added drop wise via the top and sat in a reservoir in the bottom of the cell.

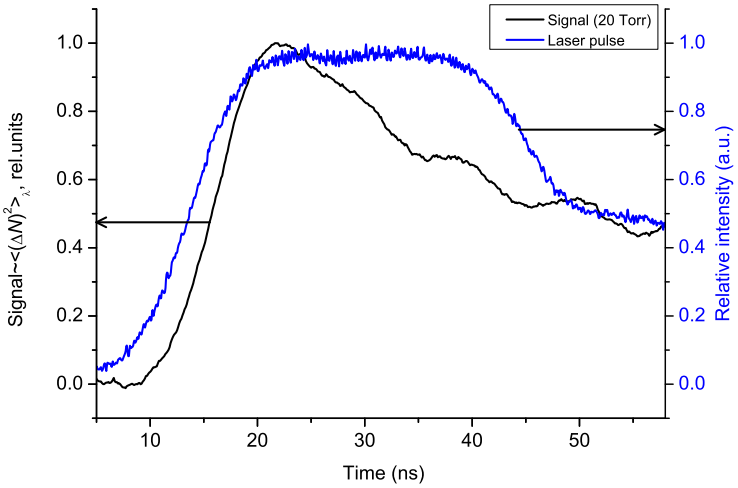

Figure 7.6: The signal obtained with xenon at 20 Torr overlaid with the temporal intensity profile of the pump/probe pulses that were used.

Our simulation is in good agreement with the experimental data during the rise time up to the maximum normalised value of 1 at $\approx$ 25 ns. After this point, the simulated signal stays flat, mirroring the intensity profile of the pulses. The measured signal however, drops away rapidly over 17 ns by $\approx$ 35%, and then continues as the pulse intensity also decreases. This loss of signal whilst the pulse is of a more or less constant intensity indicates that there must be some other mechanism that is attenutating it, or degrading the optical lattice of confined molecules. To study whether it was collisions that were responsible for the decay in signal, lower pressures were investigated. The signal to noise ratio was, however, too low to measure at lower pressures to verify this.

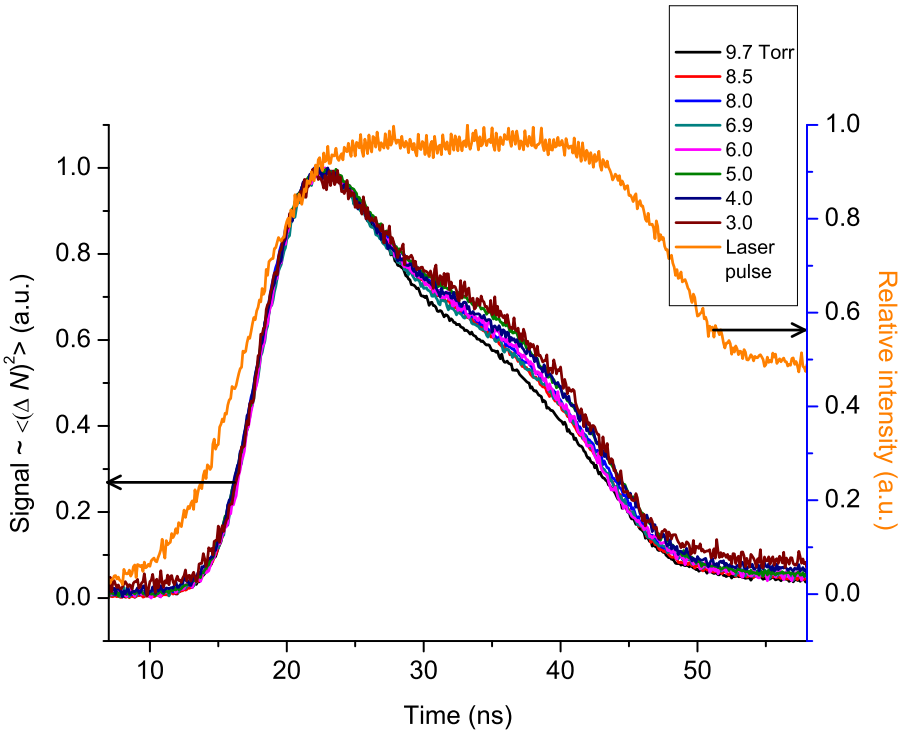

Figure 7.7: The four-wave mixing signals taken with octane, average pump intensities of $\approx 1.7 \times 10^{14}$ W m^{-2}, and a probe intensity of 6.9×10^{13} W m^{-2}, at a variety of pressures from 9.7 to 3.0 Torr.

7.5.2 Octane

Measurements were also performed with octane gas which has a much higher polarisability than xenon and therefore had the potential to offer a better signal to noise ratio at lower pressures, where the mean time between collisions will be longer. Due to its flammability, care was taken not to introduce air into the cell to prevent combustion.

Figure 7.7 show the temporal profile of the pulses overlaid with the four-wave mixing signal recorded with octane gas at a variety of pressures from 3.0 to 9.7 Torr. All are normalised to 1 to compare the time dependence of the signal. Pump and probe intensities were as described before. The figure shows that to within 5% of the mid range pressure there was no difference in the behaviour of the signal, over the duration of the pulse, for the pressures shown. The interactions should therefore be accordingly stronger, with deeper well depths, and therefore a stronger signal to noise ratio at lower pressures than would be expected for xenon.

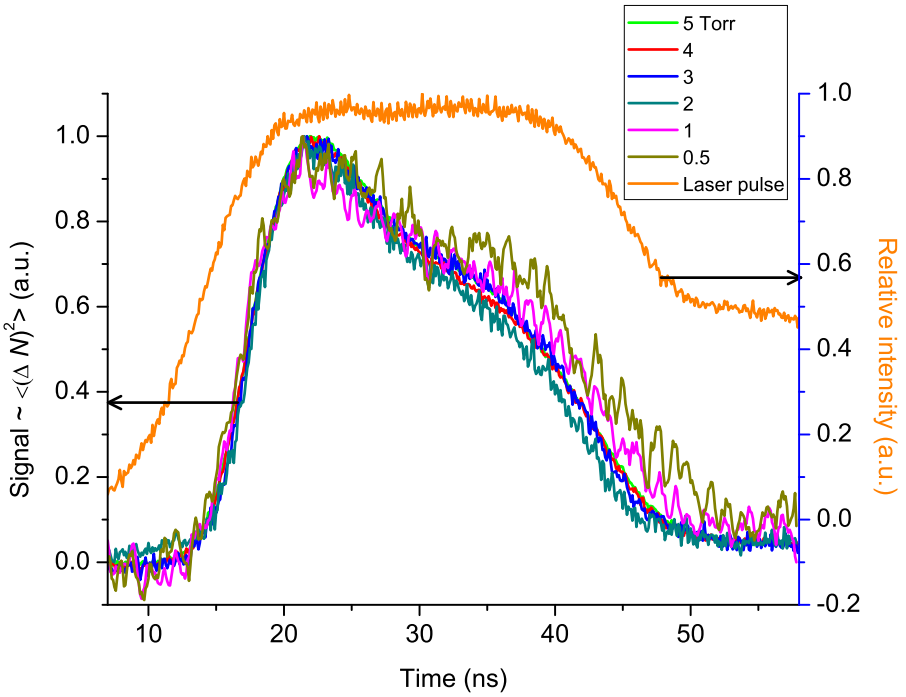

Figure 7.8: The four-wave mixing signals taken with octane, average pump intensities of $\approx 1.7 \times 10^{14}$ W m^{-2}, and a probe intensity of 6.9×10^{13} W m^{-2}, at a variety of pressures from 0.5 to to 5.0 Torr.

Figure 7.8 shows the recorded four-wave mixing signals at a lower range of pressures, from 5 to 0.5 Torr. There is a much poorer signal to noise ratio but within these larger error bounds the behaviour of the signal across the duration of the pulse is independent of pressure. A ten adjacent point averaging has been applied to the data taken at the lowest pressure to reduce the noise.

7.6 The temporal decay of the four-wave mixing signal

Having proved the suitability of the four-wave mixing as an alignment tool, we further studied the decay in the signal beam. To model this, we measured the temporal profile of the pumps/probe used in the experiment and input this into the simulation. This is presented along with the probe/signal temporal profile in figure 7.9 for octane with data taken at 9.7 Torr. Only this pressure is shown here, since the behaviour of the signal over the duration of the pulse was independent of pressure after normalisation. Since the signal is a product of the pumps and probe, which all have the same temporal profile, any change in the pump/probe profile is associated with a much sharper change in signal. For example, the small reduction

of ≈ 5 % in the temporal profile at 25-30 ns is accompanied by a reduction in signal of ≈ 10 %.

It is clear that this model fails to predict the decay in signal after 20 ns. The assumptions of our model is that there are no collisions over the duration of the pulse, no saturation effects of the signal at arbitrarily high intensities and that there is no absorption of the laser pulse energy. We consider that for xenon, at 20 Torr, the mean free collision time is 25 ns as previously calculated. For octane, at 9.7 Torr and 1 Torr, the mean free time between collisions is 48 and 480 ns respectively. For the range of pressures which were studied, a flat top duration of 20 ns, and a FWHM pulse width of ≈ 35 ns, it seems a reasonable assumption that we are in the collision free regime, particularly for the lowest pressures studied.

Saturation effects would occur in the regime in which the perturbation due to the optical lattice cannot be considered small and therefore the velocity distribution of the medium is strongly perturbed.

It is difficult to include possible absorption, collisions or saturation effects in our model. Dr. M. Shneider at Princeton University, uses a hydrodynamic model to study coherent Rayleigh scattering. This uses a series of coupled equations (Navier-Stokes) for conservation of momentum, energy and mass of the fluid subject to an optical lattice, in cylindrical symmetry [163],

$$\begin{aligned}
\frac{\delta r}{\delta t} &= u \\
\frac{1}{\rho} &= \frac{1}{2}\frac{\delta r^2}{\delta m} \\
\frac{\delta u}{\delta t} &= -r\frac{\delta}{\delta m}\left(p + Y\right) \\
\frac{\delta \epsilon}{\delta t} &+ \left(p + Y\right)\frac{\delta}{\delta t}\left(1/\rho\right) = \left[W(r,t) + W_{\text{dipole}}(r,t)\right]/\rho,
\end{aligned} \tag{7.13}$$

where r is position, u is velocity, ρ is momentum, Y is the viscosity, ϵ is the energy of the system, $W(r,t)$ is the laser radiation absorption which is proportional to $I(r,t)$, and W_{dipole} is the dipole heating term. This model assumes that we are in a regime where we can consider our medium to be a fluid, which at the pressures studied is not necessarily a valid assumption. It does however allow for the phenomenological inclusion of laser absorption and collisions.

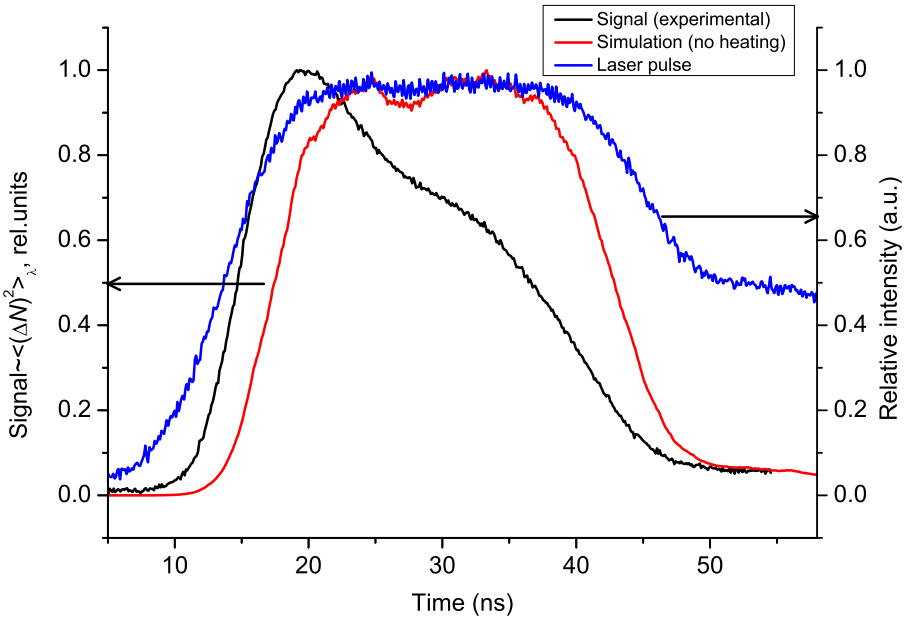

Figure 7.9: The signal obtained with octane at 9.7 Torr overlaid with predicted signal from simulations and temporal intensity profile of pump/probe pulses used.

7.6.1 Comparing the hydrodynamic model with collision free model

We initially compared the hydrodynamic model with calculations performed by Dr M. Shneider, with the collision free model with no laser absorption. The comparison between these simulations is shown in figure 7.10 for octane at 9.7 Torr. The hydrodynamic model (simulation 2) decays more slowly than the collision free model (simulation 1) after 40 ns. This is probably due to the fact that in simulation 2, saturation effects are taken into account, therefore the signal does not decay as fast as expected. Since the pumps and probe all have the same temporal intensity profile $I(t)$, then a drop in intensity at the end of our pulses would in the simplest CRS model, drop according to the relation, signal $\propto \Delta N^2 \propto I^2_{\text{pump}}$. Both simulations predict that during the relatively flat region between 20-40 ns, the signal should also be approximately flat. This is contrary to the decay in signal observed in figures 7.6 - 7.9. There must therefore be some other mechanism for the decay of the density grating.

7.6.2 Heating mechanisms

We then hypothesised that heating, leading to a loss of density modulation would result in the observed signal decay. Free electron heating was dismissed as negligible, given the densities involved. On-resonance absorption of the $\lambda = 1064$ nm light by

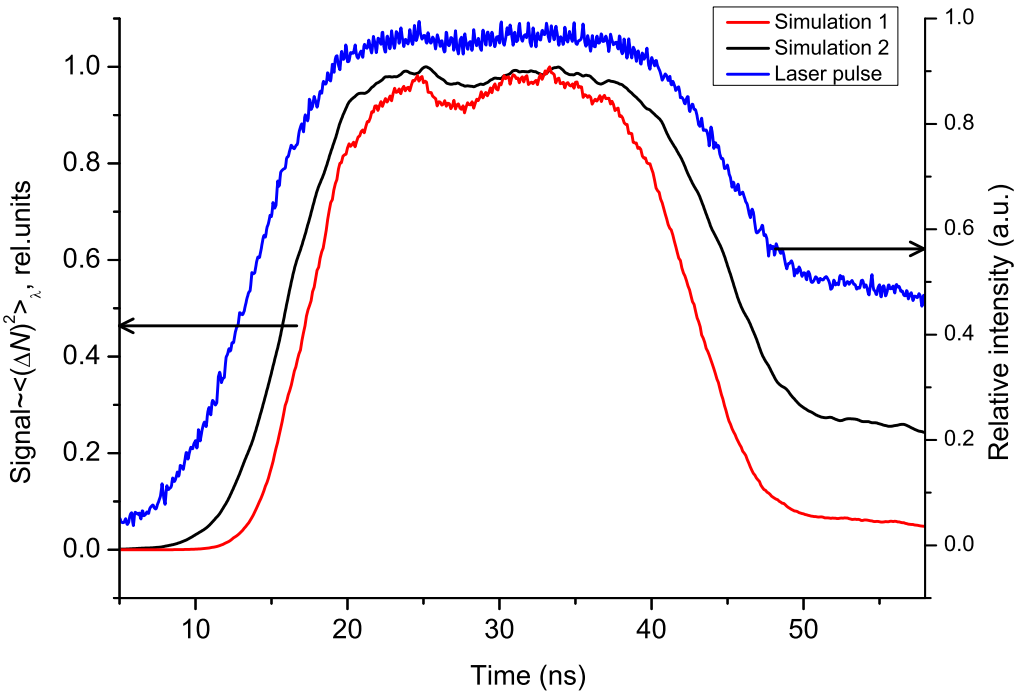

Figure 7.10: A plot comparing the collision free model (simulation 1) to the hydrodynamic model (simulation 2) for octane at 9.7 Torr, with the temporal profile of the laser beams overlaid.

the gas was dismissed since whilst it is more likely to occur in octane, it should not in xenon. Water absorption was then considered and modelled since this may be present in both cases, within the cell as a background gas, perhaps as a contaminant in the gas cylinder, or adsorbed into the material of the cell itself. We were only able to pump down the cell to ≈ 0.1 Torr, therefore it is possible that we were unable to completely remove all of the water which could have been present.

The absorption of the laser by water and the resultant heating, again by collisions, could cause the observed reduction of signal due to the loss of population in the optical lattice. This was then included in the hydrodynamic model and by adjusting the absorption parameters it was possible to find good agreement to the initial drop off in signal consistent with known absorption lines in water.

Figure 7.11a shows the experimental data overlaid with simulations based on the hydrodynamic model with and without phenomenological heating. These are overlaid with the temporal profile of the laser beams. The new hydrodynamic simulation, which includes heating is in reasonable agreement with the observed signal up to 40 ns, following the drop in signal from its maximum at 22 ns. The signal then deviates substantially from the simulation to the end of the pulse.

Figure 7.11b and 7.11c shows similar analysis applied to the data taken with octane at 9.7 and 1.0 Torr respectively. The agreement between the simulation based

on the hydrodynamic model with heating and the experimental data is even better for octane than it was for xenon at both pressures. There is a close relationship over most of the the duration of the pulse for 1 Torr, with a maximum of $\approx 10\%$ discrepency between signal and simulation.

7.7 Conclusions

We have obtained a four-wave mixing signal down to pressures as low as 0.5 Torr with octane and 20 Torr with xenon. This offers the potential as an alignment tool for molecular and atomic deceleration/acceleration experiments. Potential species for molecular deceleration or acceleration such as benzene have similarly large polarisability to mass ratios as octane, therefore it would be possible to produce a similar four wave mixing signal at low pressures. Since producing this signal requires careful alignment and overlap within the focii of the two pumps and probe this would ensure that an optical lattice has been produced and that the third beam, acting as as detection beam in an ionisation scheme, is also overlapped with this lattice. Once a four wave mixing signal is produced at these low pressures, the system could be pumped out further to the required pressures for the deceleration/acceleration experiments. Alternatively, CRS experiments could be performed to produce a 4-wave mixing signal at much lower pressures using an on-resonant probe beam.

Study of the temporal behaviour of the signal showed an unexpected decay in the signal over the flat region of the pulse. A heating mechanism was hypothesised, which may arise from absorption of the pump beams by water which may have been present in the cell. This could affect the density grating and cause a loss of signal. This process is not currently properly understood and requires further analysis. One of the issues with this hypothesis is the lack of time for collisions to occur which would be necessary to conduct heat between water and the gas in our cell. There is also not currently experimental evidence of the presence of sufficient water to account for the laser absorption required for the model to fit the observed signal.

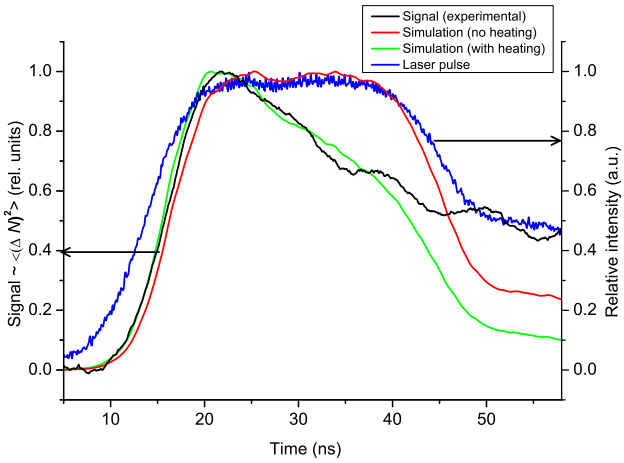

(a)

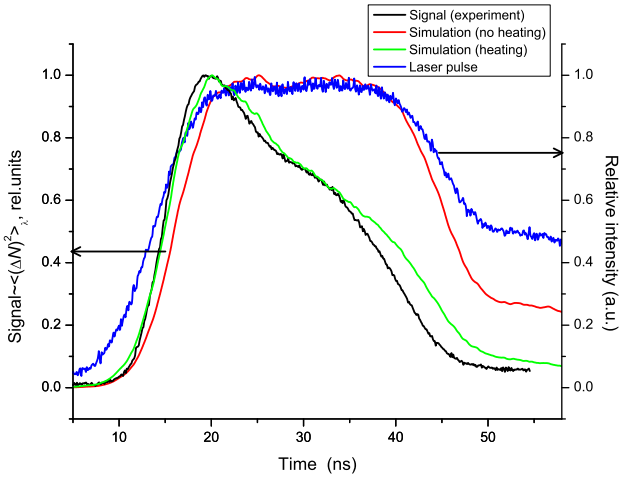

(b)

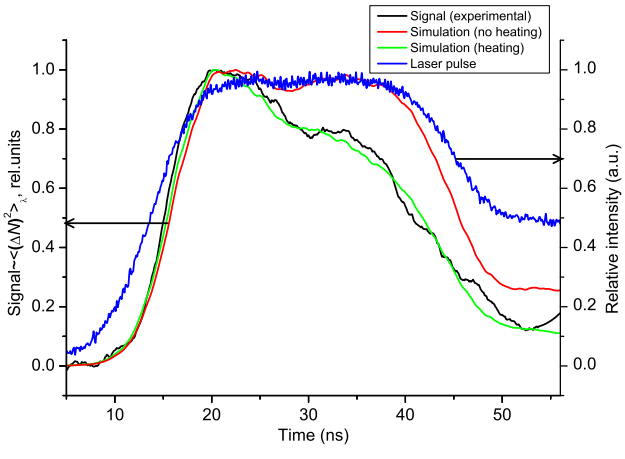

(c)

Figure 7.11: (a) A plot of the observed four wave mixing signal obtained with xenon at 20 Torr. Overlaid is the temporal profile of the pulses used and simulations from the hydrodynamic model with and without heating. (b) As before but with data taken with octane at 9.7 Torr. (c) The same plot but with data taken with octane at 1 Torr.

Chapter 8

Conclusions

8.1 Conclusions

8.1.1 Summary of the laser system

This thesis has presented the development of a unique, high energy, chirped laser system for the deceleration of molecules in a molecular jet. It is capable of being chirped up to 1 GHz over durations of between 20 ns to 10 μs, representing a chirp rate in excess of 10 GHz / μs. The system is capable of producing two overlapped pulses of this duration, which are required to create the deep periodic optical potential ($> 1 - 20$ K) with intensities in the 10^{14} W m^{-2} range. Using a Pockel cell and polarising beam splitter together with computer software, we can produce flat top temporal intensity profiles to a minimum resolution of ≈ 7 ns to produce flat top or any other required profile.

A time delay between the two arms of the laser system, created with optical fibers of different lengths enable the output of a single Nd:YVO_4 master microchip laser to be split and used to produce the two laser beams used to make the optical lattice with a frequency difference when an a.c. voltage is applied to the e.o. ($LiTaO_3$) crystal.

We are able to precisely control the frequency excursion within the 0 to 1 GHz range, its duration and its phase relative to the pulses. This system can therefore be used to decelerate to a non zero velocity as well as to rest, which would be desirable for collisions experiments at arbitrary collision energies. It may also therefore be used for acceleration of a trapped sample of particles to an arbitrary velocity. This would be useful for collision studies.

8.1.2 Improvements to the system

The ultimate limit to the duration of the chirp is the rate that energy can be extracted from the Nd:YAG pulsed amplification system. In our system there is also limit of the maximum time delay between the two arms of the laser system, determined by the difference in fiber lengths. This difference was 55 m, giving a maximum time delay of 275 ns, given a velocity of light of $\approx 2 \times 10^8$ ms^{-1}. A longer difference in fiber length would enable us to chirp over a longer time, however will be limited by the coherence length of the laser.

It would be desirable to have a better voltage amplification system so that we are able to produce the ideal linear voltage ramps up to the required 70 V over the required chirp duration. Although non-linear voltage waveforms can be compensated with a non flat-top temporal intensity profile, a linear change is the simplest to implement in terms of the timing of the chirp to the pulse and also in the setup by the operator.

8.2 Recent results

This laser system has recently been used by my colleagues in the acceleration of metastable argon atoms in a Magneto Optical Trap (MOT).

Figure 8.1 shows the images taken directly from a CCD camera at 30 μs after the application of the optical lattice, when different sinusoidally varying voltages were applied to the e.o. crystal. This is used to produce the distribution of displacement as shown in figure 8.3. It can clearly be seen that as the voltage/frequency increases, so does the final lattice velocity, shown by the increasing displacement of a packet of argon atoms. The other effect is a smearing of the distribution which makes the estimation of the final velocity more difficult for higher values. This is largely due to the long exposure time of the camera (30 μs). Some widening of the velocity distribution is predicted to occur since a sinusoidally shaped chirp has been used in combination with a flat top temporal profile, leading to sub- optimal acceleration.

In theory, for a sinusoidally accelerating lattice, the maximum gradient should be at the beginning of the chirp if the phase has been set correctly. However if not, then particles may be lost early in the chirp and some may have been initially accelerated in the opposite direction. Intensity fluctuation over the duration of the chirp will also cause a loss of particles, particularly at the early part of the chirp where the gradient varies very little. As the gradient decreases towards the end of the chirp, then there will be sub-optimal acceleration and unnecessary heating of the distribution.

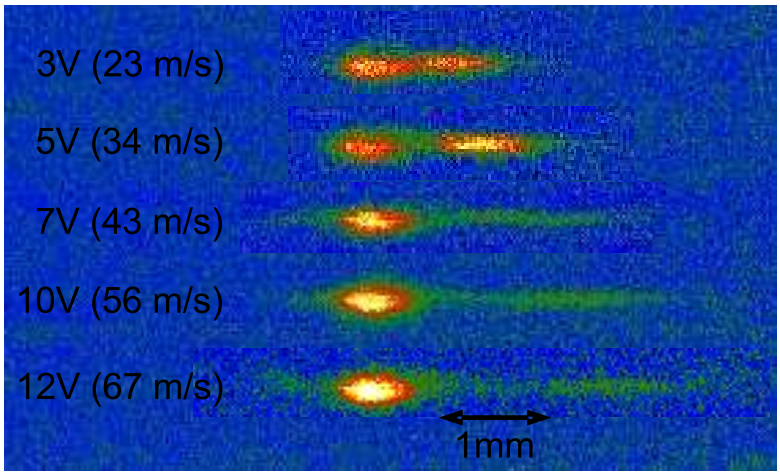

Figure 8.1: Displacement of metastable argon atoms 30 μs after the application of an optical lattice with a sinusoidally varying chirp for various chirp voltages with beams with 20 mJ pulse energy.

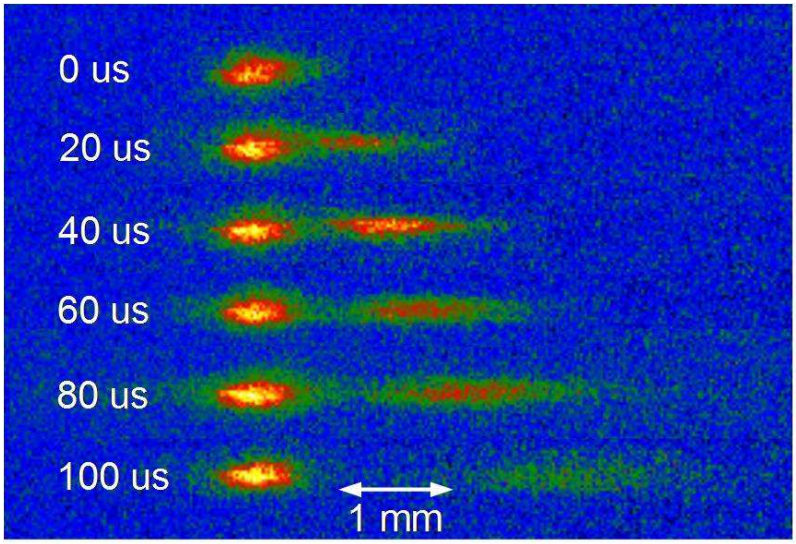

Figure 8.2: Displacement of metastable atoms at various times after the optical lattice was switched off, which were produced with a sinusoidal chirp (5 V amplitude) with beams of 10 mJ pulse energy.

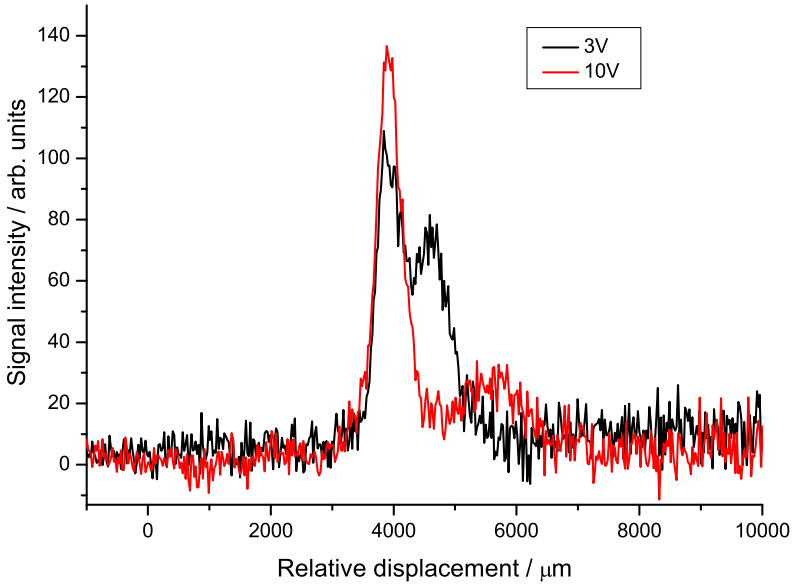

Figure 8.3: Displacement of metastable argon atoms as measured by the signal on a CCD camera taken 30 μs after the switching of an accelerating optical lattice. While switched on the optical lattice was chirped by applying a sinusoidally varying voltage to the e.o. crystal from a zero frequency difference up to various voltages. The red and black traces were taken when the frequency generator was set to 10 and 3 V respectively. An estimation of the final velocity of each accelerated packet gives 59 ± 3 ms^{-1} and 23 ± 2 ms^{-1} respectively.

Figure 8.2 shows the displacement at various times after the optical lattice was switched off. These were produced by a sinusoidal chirp (5 V amplitude). The motion of the accelerated packet of argon atoms can clearly be seen along with a steady smearing of the accelerated distribution.

Figure 8.3 shows the distribution of position of argon atoms taken 30 μs after the switching off of the optical lattice for two different voltage amplitudes applied to the e.o. crystal.

To estimate the final velocity of the atoms, consider that the point in time at which the data is taken is much later than the short acceleration time of ≈ 140 ns therefore the displacement $s = 1/2at_1^2 + vt_2 \approx vt_2$, where t_1 is the duration that the lattice is on and accelerating, and t_2 is the time between the switch off of the lattice and when the CCD data was taken. The approximation is valid for $t_2 >> t_1$.

We estimate the displacement of the accelerated packet of particles by comparing the mid points of the accelerated packet to the mid point of the main distribution. For 10 V this is ≈ 1790 μm and for 3 V this is ≈ 666 μm. Given the 30 μs delay time this gives 59 ± 3 ms^{-1} and 23 ± 2 ms^{-1} respectively, representing, given near counter-propagating beams, a chirp from 0 to 111 $\pm$ 6 and 43 $\pm$ 4 MHz. This indicates a tunablilty $f_V = 11.1 \pm 0.6$ MHz / V for 10 V and $f_V = 14.3 \pm 1.2$ MHz / V for the

3 V chirp. In the case of the 10 V chirp, this tunablity seems quite low compared to other measurements of the laser system. It is known that the tunability is dependent on the electrical connection. Given the fact this data was taken much later, this may explain the change.

The maximum frequency of the chirp in both cases was analysed using the method described in chapter 4 and found to be 90 ± 10 MHz for 10 V, which would in theory give a final velocity of 48 ± 5 ms^{-1}. This is just outside the error bars for the final velocity based on the imaging of the argon atoms. Given the large uncertainties with the position of the phase of the chirp relative to the beginning of the pulse, and in estimating the position of the accelerated packet of argon atoms, this seems a reasonable agreement. These are recent results that have not yet been finalised.

8.3 Future work

The next step is to apply this system to the deceleration of molecules, for example benzene, in a molecular jet down to zero velocity. This will require careful alignment of the optical lattice with the laser required to detect the molecules. A four-wave mixing type experiment, such as described in chapter 7 may offer a good way of ensuring overlap of the two lattice beams as well as the probe beam.

The next step is to load decelerated molecules into an optical trap with cold molecules and then to pursue a sympathetic cooling scheme with rare gas atoms [53, 76] to bring cold molecules closer to the ultra cold regime. Currently metastable argon atoms have been trapped in a MOT with typical trap temperatures of 10 μK. Sympathetic cooling between trapped cold molecules (10 mK) and metastable argon atoms (300 μK) has been modeled using direct Monte Carlo simulations [164]. For hydrogen-argon and benzene-argon these simulations indicate that thermalisation would occur in less than ten seconds and reach final temperatures of 330 ± 30 μK and 600 ± 100 μK

More off-resonance CRS scattering experiments have also been performed recently with this laser system. New spectral features have been observed. These studies were made possible due to the long flat-top pulses which our laser system can produce, with a well defined frequency difference between each arm. The versatility of optical Stark acceleration/deceleration to manipulate the motion of any polarisable species opens up many more areas of research which our group hopes to pursue.

Bibliography

[1] D. W. Chandler, K. E. Strecker, *Chem. Eur. J. of Chem. Phys.* **10**, 751 (2009).

[2] M. Schnell, G. Meijer, *Angewandte Chemie International Edition* **48**, 6010 (2009).

[3] B. Friedrich, J. M. Doyle, *Chem. Eur. J. of Chem. Phys.* **10**, 604 (2009).

[4] J. van Veldhoven, *et al.*, *The European Physical Journal D - Atomic, Molecular, Optical and Plasma Physics* **31**, 337 (2004).

[5] J. J. Gilijamse, *et al.*, *The Journal of Chemical Physics* **127**, 221102 (2007).

[6] S. Y. T. van de Meerakker, N. Vanhaecke, M. P. J. van der Loo, G. C. Groenenboom, G. Meijer, *Phys. Rev. Lett.* **95**, 013003 (2005).

[7] C. Haimberger, J. Kleinert, P. Zabawa, A. Wakim, N. P. Bigelow, *New Journal of Physics* **11**, 055042 (2009).

[8] W. C. Stwalley, H. Wang, *Journal of Molecular Spectroscopy* **195**, 194 (1999).

[9] K. M. Jones, E. Tiesinga, P. D. Lett, P. S. Julienne, *Rev. Mod. Phys.* **78**, 483 (2006).

[10] E. M. Purcell, N. F. Ramsey, *Phys. Rev.* **78**, 807 (1950).

[11] P. A. Bolokhov, M. Pospelov, M. Romalis, *Phys. Rev. D* **78**, 057702 (2008).

[12] R. Bast, P. Schwerdtfeger, *Phys. Rev. Lett.* **91**, 023001 (2003).

[13] S. Jung, J. D. Wells, *Phys. Rev. D* **80**, 015009 (2009).

[14] M. Mark, *et al.*, *Phys. Rev. Lett.* **99**, 113201 (2007).

[15] J. K. Webb, *et al.*, *Phys. Rev. Lett.* **87**, 091301 (2001).

[16] W. J. Marciano, *Phys. Rev. Lett.* **52**, 489 (1984).

[17] V. V. Flambaum, M. G. Kozlov, *Phys. Rev. Lett.* **99**, 150801 (2007).

[18] S. Schiller, V. Korobov, *Phys. Rev. A* **71**, 032505 (2005).

[19] E. R. Hudson, H. J. Lewandowski, B. C. Sawyer, J. Ye, *Phys. Rev. Lett.* **96**, 143004 (2006).

[20] J. Stuhler, *et al.*, *Phys. Rev. Lett.* **95**, 150406 (2005).

[21] M. R. Kutteruf, R. R. Jones, *Phys. Rev. A* **82**, 063409 (2010).

[22] K.-K. Ni, *et al.*, *Science* **322**, 231 (2008).

[23] S. Ospelkaus, *et al.*, *Faraday Discuss.* **142**, 351 (2009).

[24] M. H. Anderson, J. R. Ensher, M. R. Matthews, C. E. Wieman, E. A. Cornell, *Science* **269**, 198 (1995).

[25] A. G. Truscott, K. E. Strecker, W. I. McAlexander, G. B. Partridge, R. G. Hulet, *Science* **291**, 2570 (2001).

[26] M. Greiner, O. Mandel, T. Esslinger, T. W. Hansch, I. Bloch, *Nature* **415**, 39 (2002).

[27] K. Winker, *et al.*, *Nature* **441**, 853 (2006).

[28] M. A. Baranov, M. S. Mar'enko, V. S. Rychkov, G. V. Shlyapnikov, *Phys. Rev. A* **66**, 013606 (2002).

[29] K. Góral, L. Santos, M. Lewenstein, *Phys. Rev. Lett.* **88**, 170406 (2002).

[30] R. Barnett, D. Petrov, M. Lukin, E. Demler, *Phys. Rev. Lett.* **96**, 190401 (2006).

[31] M. Greiner, C. A. Regal, J. D. S., *Nature* **426**, 537 (2003).

[32] C. A. Regal, M. Greiner, D. S. Jin, *Phys. Rev. Lett.* **92**, 040403 (2004).

[33] J. Qian, L. Zhou, K. Zhang, W. Zhang, *New Journal of Physics* **12**, 033002 (2010).

[34] N. Balakrishnan, A. Dalgarno, *Chemical Physics Letters* **341**, 652 (2001).

[35] J. M. Hutson, *Science* **327**, 788 (2010).

[36] S. Ospelkaus, *et al.*, *Science* **327**, 853 (2010).

[37] B. J. Bichsel, M. A. Morrison, N. Shafer-Ray, E. R. I. Abraham, *Phys. Rev. A* **75**, 023410 (2007).

[38] N. Balakrishnan, A. Dalgarno, R. C. Forrey, *The Journal of Chemical Physics* **113**, 621 (2000).

[39] J. Hutson, *International Reviews in Physical Chemistry* **26**, 1 (2007).

[40] E. Bodo, *International Reviews in Physical Chemistry* **25**, 313 (2006).

[41] D. Skouteris, *et al.*, *Science* **286**, 1713 (1999).

[42] R. T. Skodje, *et al.*, *Phys. Rev. Lett.* **85**, 1206 (2000).

[43] G. Hall, K. Liu, M. J. McAuliffe, C. F. Giese, W. R. Gentry, *The Journal of Chemical Physics* **81**, 5577 (1984).

[44] R. G. Macdonald, K. Liu, *The Journal of Chemical Physics* **91**, 821 (1989).

[45] D. M. Sonnenfroh, R. G. Macdonald, K. Liu, *The Journal of Chemical Physics* **94**, 6508 (1991).

[46] J. J. Gilijamse, S. Hoekstra, S. Y. T. van de Meerakker, G. C. Groenenboom, G. Meijer, *Science* **313**, 1617 (2006).

[47] B. C. Sawyer, B. K. Stuhl, D. Wang, M. Yeo, J. Ye, *Phys. Rev. Lett.* **101**, 203203 (2008).

[48] T. V. Tscherbul, Z. Pavlovic, H. R. Sadeghpour, R. Côté, A. Dalgarno, *Phys. Rev. A* **82**, 022704 (2010).

[49] J. C. Flasher, R. C. Forrey, *Phys. Rev. A* **65**, 032710 (2002).

[50] A. Mack, *et al.*, *Phys. Rev. A* **74**, 052718 (2006).

[51] T. Köhler, K. Góral, P. S. Julienne, *Rev. Mod. Phys.* **78**, 1311 (2006).

[52] R. Fulton, A. I. Bishop, M. N. Shneider, P. F. Barker, *Nature Physics* **2**, 465 (2006).

[53] P. Barletta, J. Tennyson, P. F. Barker, *Phys. Rev. A* **78**, 052707 (2008).

[54] J. T. Bahns, W. C. Stwalley, P. L. Gould, *The Journal of Chemical Physics* **104**, 9689 (1996).

[55] E. S. B. Shuman, D. J. F. DeMille, *Nature* **467** (2010).

[56] P. O. Fedichev, Y. Kagan, G. V. Shlyapnikov, J. T. M. Walraven, *Phys. Rev. Lett.* **77**, 2913 (1996).

[57] J. M. Vogels, *et al.*, *Phys. Rev. A* **56**, R1067 (1997).

[58] P. Courteille, R. S. Freeland, D. J. Heinzen, F. A. van Abeelen, B. J. Verhaar, *Phys. Rev. Lett.* **81**, 69 (1998).

[59] Z. Li, R. V. Krems, *Phys. Rev. A* **75**, 032709 (2007).

[60] T. Köhler, K. Góral, P. S. Julienne, *Rev. Mod. Phys.* **78**, 1311 (2006).

[61] J. Cubizolles, T. Bourdel, S. J. J. M. F. Kokkelmans, G. V. Shlyapnikov, C. Salomon, *Phys. Rev. Lett.* **91**, 240401 (2003).

[62] K. M. Jones, E. Tiesinga, P. D. Lett, P. S. Julienne, *Rev. Mod. Phys.* **78**, 483 (2006).

[63] C. Haimberger, J. Kleinert, M. Bhattacharya, N. P. Bigelow, *Phys. Rev. A* **70**, 021402 (2004).

[64] A. N. Nikolov, *et al.*, *Phys. Rev. Lett.* **84**, 246 (2000).

[65] J. M. Sage, S. Sainis, T. Bergeman, D. DeMille, *Phys. Rev. Lett.* **94**, 203001 (2005).

[66] S. Azizi, M. Aymar, O. Dulieu, *The European Physical Journal D - Atomic, Molecular, Optical and Plasma Physics* **31**, 195 (2004).

[67] A. Trottier, D. Carty, E. Wrede, *Mol. Phys.* **5**, 725 (2011).

[68] D. Egorov, T. Lahaye, W. Schöllkopf, B. Friedrich, J. M. Doyle, *Phys. Rev. A* **66**, 043401 (2002).

[69] D. Egorov, *et al.*, *The European Physical Journal D - Atomic, Molecular, Optical and Plasma Physics* **31**, 307 (2004).

[70] R. deCarvalho, *et al.*, *The European Physical Journal D - Atomic, Molecular, Optical and Plasma Physics* **7**, 289 (1999).

[71] R. Krems, W. Stwalley, B. Friedrich, *Cold molecules: theory, experiment, applications* (CRC Press, 2009).

[72] J. D. Weinstein, R. deCarvalho, T. Guillet, B. Friedrich, J. M. D. Doyle, *Nature* **395**, 148 (1998).

[73] F. Schreck, *et al.*, *Phys. Rev. A* **64**, 011402 (2001).

[74] G. Modugno, *et al.*, *Science* **294**, 1320 (2001).

[75] P. S. Żuchowski, J. M. Hutson, *Phys. Rev. A* **78**, 022701 (2008).

[76] P. Barletta, J. Tennyson, P. F. Barker, *New Journal of Physics* **11**, 055029 (2009).

[77] W. Lu, Y. Zhao, P. F. Barker, *Phys. Rev. A* **76**, 013417 (2007).

[78] P. Maunz, *et al.*, *Nature* **428**, 50 (2004).

[79] Y. Zhao, W. Lu, P. F. Barker, G. Dong, *Faraday Discuss.* **142**, 311 (2009).

[80] A. Andre, *et al.*, *Nature Physics* **2**, 636 (2006).

[81] M. Wallquist, P. Rabl, M. D. Lukin, P. Zoller, *New Journal of Physics* **10**, 063005 (2008).

[82] H. L. Bethlem, G. Berden, G. Meijer, *Phys. Rev. Lett.* **83**, 1558 (1999).

[83] S. Y. van de Meerakker, N. Vanhaecke, G. Meijer, *Annual Review of Physical Chemistry* **57**, 159 (2006).

[84] H. L. Bethlem, A. J. A. van Roij, R. T. Jongma, G. Meijer, *Phys. Rev. Lett.* **88**, 133003 (2002).

[85] S. Earnshaw, *Trans. Camb. Phil. Soc* **7**, 97 (1842).

[86] D. Auerbach, E. E. A. Bromberg, L. Wharton, *The Journal of Chemical Physics* **45**, 2160 (1966).

[87] E. D. Courant, H. S. Snyder, *Annals of Physics* **3**, 1 (1958).

[88] T. E. Wall, *et al.*, *Phys. Rev. A* **80**, 043407 (2009).

[89] H. L. Bethlem, G. Berden, G. Meijer, *Phys. Rev. Lett.* **83**, 1558 (1999).

[90] S. D. Hogan, C. Seiler, F. Merkt, *Phys. Rev. Lett.* **103**, 123001 (2009).

[91] E. Vliegen, F. Merkt, *Journal of Physics B: Atomic, Molecular and Optical Physics* **38**, 1623 (2005).

[92] E. Vliegen, F. Merkt, *Journal of Physics B: Atomic, Molecular and Optical Physics* **39**, L241 (2006).

[93] K. Enomoto, T. Momose, *Phys. Rev. A* **72**, 061403 (2005).

[94] T. Junglen, T. Rieger, S. A. Rangwala, P. W. H. Pinkse, G. Rempe, *The European Physical Journal D - Atomic, Molecular, Optical and Plasma Physics* **31**, 365 (2004).

[95] S. A. Rangwala, T. Junglen, T. Rieger, P. W. H. Pinkse, G. Rempe, *Phys. Rev. A* **67**, 043406 (2003).

[96] E. Narevicius, *et al.*, *Phys. Rev. A* **77**, 051401 (2008).

[97] R. Fulton, A. I. Bishop, M. N. Shneider, P. F. Barker, *Journal of Physics B: Atomic, Molecular and Optical Physics* **39**, S1097 (2006).

[98] R. Fulton, A. I. Bishop, P. F. Barker, *Phys. Rev. Lett.* **93**, 243004 (2004).

[99] H. Sakai, *et al.*, *The Journal of Chemical Physics* **110**, 10235 (1999).

[100] R. Fulton, A. I. Bishop, P. F. Barker, *Phys. Rev. A* **71**, 043404 (2005).

[101] A. I. Bishop, L. Wang, P. F. Barker, *New Journal of Physics* **12**, 073028 (2010).

[102] P. F. Barker, M. N. Shneider, *Phys. Rev. A* **66**, 065402 (2002).

[103] R. B. Horne, M. P. Freeman, *Journal of Computational Physics* **171**, 182 (2001).

[104] R. Fulton, A. I. Bishop, M. N. Shneider, P. F. Barker, *Nature Physics* **2**, 465 (2006).

[105] P. F. Barker, M. N. Shneider, *Phys. Rev. A* **64**, 033408 (2001).

[106] A. E. Siegman, *Lasers* (University Science Books, Mill Valley, Calif., 1986).

[107] P. Tipler, *Physics for scientists and engineers* (W.H. Freeman/Worth Publishers, 1999).

[108] J. J. Zayhowski, A. Mooradian, *Opt. Lett.* **14**, 618 (1989).

[109] J. J. Zayhowski, A. Mooradian, *Opt. Lett.* **14**, 24 (1989).

[110] L. Levin, *Opt. Lett.* **27**, 237 (2002).

[111] C. J. Hawthorn, K. P. Weber, R. E. Scholten, *Review of Scientific Instruments* **72**, 4477 (2001).

[112] J. Troger, L. Thévenaz, P. Robert, *Opt. Lett.* **24**, 1493 (1999).

[113] C. E. R. III, M. J. Wright, J. L. Carini, J. A. Pechkis, P. L. Gould", *J. Opt. Soc. Am. B* **24**, 1249 (2007).

[114] B. Boggs, C. Greiner, T. Wang, H. Lin, T. W. Mossberg, *Opt. Lett.* **23**, 1906 (1998).

[115] B. Wacogne, J.-P. Goedgebuer, H. Porte, *Opt. Lett.* **19**, 1334 (1994).

[116] J.-P. Goedgebuer, S. Gurib, K. Porte, *Quantum Electronics, IEEE Journal of* **28**, 1414 (1992).

[117] J. Bakos, *et al.*, *Optics and Lasers in Engineering* **47**, 19 (2009).

[118] J. S. Bakos, *et al.* (2007).

[119] Y. Li, S. M. Goldwasser, P. Herczfeld, L. M. Narducci, *IEEE Journal of Quantum Electronics* **42**, 208 (2006).

[120] M. J. Wright, S. D. Gensemer, J. Vala, R. Kosloff, P. L. Gould, *Phys. Rev. Lett.* **95**, 063001 (2005).

[121] E. Luc-Koenig, R. Kosloff, F. Masnou-Seeuws, M. Vatasescu, *Phys. Rev. A* **70**, 033414 (2004).

[122] A. S. Arnold, J. S. Wilson, M. G. Boshier, *Review of Scientific Instruments* **69**, 1236 (1998).

[123] L. Ricci, *et al.*, *Optics Communications* **117**, 541 (1995).

[124] T. Hof, D. Fick, H. J. Jänsch, *Optics Communications* **124**, 283 (1996).

[125] K. Liu, M. G. Littman, *Opt. Lett.* **6**, 117 (1981).

[126] K. S. Repasky, G. W. Switzer, J. L. Carlsten, *Review of Scientific Instruments* **73**, 3154 (2002).

[127] K. D. Merkel, W. R. Babbitt, *Opt. Lett.* **23**, 528 (1998).

[128] L. Eldada, *et al.*, *Lightwave Technology, Journal of* **13**, 2034 (1995).

[129] O. Kazharsky, *et al.*, *Optics Communications* **137**, 77 (1997).

[130] M. Wright, P. Gould, S. Gensemer, *Rev. Sci. Instrum.* **75**, 4718 (2004).

[131] A. Sudbø, *Quantum Electronics, IEEE Journal of* **22**, 1006 (1986).

[132] J. Zayhowski, J. A. Keszenheimer, *IEEE J. Quantum Electron.* **28**, 1118 (1992).

[133] L. Ménager, L. Cabaret, I. Lorgeré, J.-L. L. Gouët, *Opt. Lett.* **25**, 1246 (2000).

[134] M. Duval, G. Fortin, M. Piché, N. McCarthy, *Appl. Opt.* **44**, 5112 (2005).

[135] B. V. Zhdanov, G. P. Andersen, R. J. Knize, *American Journal of Physics* **68**, 282 (2000).

[136] Y. Ma, *et al.*, *Opt. Express* **16**, 18702 (2008).

[137] T. Taira, A. Mukai, Y. Nozawa, T. Kobayashi, *Opt. Lett.* **16**, 1955 (1991).

[138] A. Sennaroglu, *Optics Communications* **164**, 191 (1999).

[139] P. L. Hansen, C. Pedersen, P. Buchhave, T. Skettrup, *Optics Communications* **127**, 353 (1996).

[140] V. J. A. Bramati, J.-P. Hermier, E. Giacobino, *The European Physical Journal D - Atomic, Molecular, Optical and Plasma Physics* **19**, 421 (2002).

[141] Y. S. Kim, R. T. Smith, *Journal of Applied Physics* **40**, 4637 (1969).

[142] D. Hum, *A dissertation submitted to Stanford University* (2007).

[143] U. P. Oppenheim, M. Naftaly, *Appl. Opt.* **23**, 661 (1984).

[144] S. Valling, B. Ståhlberg, A. Lindberg, *Optics and Laser Technology* **39**, 82 (2007).

[145] S. Kobayashi, T. Kimura, *IEEE Journal of Quantum Electronics* **17**, 681 (1981).

[146] R. Hayes, D. Persechini, *Photonics Technology Letters, IEEE* **5**, 70 (1993).

[147] K. Williams, D. Tulchinsky, *Holey Fibers and Photonic Crystals/Polarization Mode Dispersion/Photonics Time/Frequency Measurement and Control, 2003 Digest of the LEOS Summer Topical Meetings* (2003), pp. TuC3.4/51 – TuC3.4/52.

[148] M. S. Fee, K. Danzmann, S. Chu, *Phys. Rev. A* **45**, 4911 (1992).

[149] C. Wieman, T. W. Hänsch, *Phys. Rev. A* **22**, 192 (1980).

[150] R. Fulton, Atomic and molecular manipulation, Ph.D. thesis (2006).

[151] R. T. White, Y. He, B. J. Orr, M. Kono, K. G. H. Baldwin, *J. Opt. Soc. Am. B* **21**, 1577 (2004).

[152] C. Pan, *IEEE Transactions on Signal Processing* **49**, 444 (2001).

[153] H. Schröder, H. Blume, *One and Multidimensional Signal Processing* (Wiley, 2000).

[154] B. Liu, ed., *Digital Filters and the Fast Fourier Transform* (Halsted Press, 1975).

[155] J. H. Grinstead, P. F. Barker, *Phys. Rev. Lett.* **85**, 1222 (2000).

[156] J. V. Leyendekkers, *The Journal of Physical Chemistry* **83**, 347 (1979).

[157] X. Pan, M. N. Shneider, R. B. Miles, *Phys. Rev. Lett.* **89**, 183001 (2002).

[158] R. W. Boyd, *Nonlinear Optics,Third Edition* (Elsevier, 2008).

[159] W. Hubschmid, B. Hemmerling, A. Stampanoni-Panariello, *J. Opt. Soc. Am. B* **12**, 1850 (1995).

[160] R. W. Boyd, *Nonlinear Optics,Third Edition* (Elsevier, 2008).

[161] M. N. Shneider, P. Barker, *Optics Communications* **284**, 1238 (2011).

[162] P. L. Bhatnagar, E. P. Gross, M. Krook, *Phys. Rev.* **94**, 511 (1954).

[163] T. Faber, *Fluid dynamics for physicists* (Cambridge University Press, 1995).

[164] P. Barletta, J. Tennyson, P. F. Barker, *New Journal of Physics* **12**, 113002 (2010).